UC Riverside
UC Riverside Electronic Theses and Dissertations

Title
Investigation of Spin-Based Phenomena in Candidate Spintronic Materials by Molecular Beam Epitaxy

Permalink
https://escholarship.org/uc/item/6ct6h0pd

Author
Swartz, Adrian

Publication Date
2013

Peer reviewed|Thesis/dissertation

eScholarship.org Powered by the California Digital Library
University of California

UNIVERSITY OF CALIFORNIA
RIVERSIDE

Investigation of Spin-Based Phenomena in Candidate Spintronic Materials by Molecular Beam Epitaxy

A Dissertation submitted in partial satisfaction
of the requirements for the degree of

Doctor of Philosophy

in

Physics

by

Adrian Grant Swartz

March 2013

Dissertation Committee:
Dr. Roland Kawakami, Chairperson
Dr. Jing Shi
Dr. Vivek Aji

Copyright by
Adrian Grant Swartz
2013

The Dissertation of Adrian Grant Swartz is approved:

____

____

____

Committee Chairperson

University of California, Riverside

ACKNOWLEDGEMENTS

I am eternally grateful to all the people who have helped me during my time at UC Riverside. In particular, I would like to thank Prof. Roland Kawakami, my research advisor. I have developed significantly as a scientist and researcher and I owe much of that progress to your hard work. Further, the environment you create in the group allowed for me to grow and achieve great things. I would also like to thank my dissertation committee for their helpful discussions.

Also, I am greatly indebted to the Kawakami group members who preceded me. To the older students, Yan Li and Keyu Pi who not only trained me when I was a young grad student but also helped create a great research group. Also, I will very much miss the other three of the '4 of us' - Wei Han, Jared Wong, and Kathy McCreary. Those years we worked together were an incredibly exciting and fun time.

I also want to thank my wife, Jaclyn DeMartini. It meant everything to me that we were able to go through this together and I owe so much to you. To my parents and family, you have always been completely supportive of me and I am deeply thankful to have you in my corner.

ABSTRACT OF THE DISSERTATION

Investigation of Spin-Based Phenomena in Candidate Spintronic Materials by Molecular Beam Epitaxy

by

Adrian Grant Swartz

Doctor of Philosophy, Graduate Program in Physics
University of California, Riverside, March 2013
Dr. Roland Kawakami, Chairperson

Spin-based electronics, or spintronics, seeks to utilize the electron degree of freedom in order to perform logic, computation, or information storage. Proximity based interactions between nearby systems (i.e. films, adsorbates, molecules) and candidate spintronic materials (i.e. GaAs, graphene) could lead to the realization of novel phenomena. Such effects, which rely on atomic orbital overlap, require highly controlled surfaces and interfaces which can be achieved using molecular beam epitaxy (MBE). Here, this dissertation examines the feasibility of integrating high quality single crystal ferromagnetic insulators with oxide interfaces, the semiconductor GaAs, and graphene. Graphene, a single atomic layer of sp^2 bonded carbon with conducting π orbitals that extend out of the plane, is highly surface sensitive and can be considered an ideal material for investigating novel spin-based proximity related be-

havior. In particular, the interactions of functional oxides or adsorbates with graphene could lead to induced exchange splitting, magnetism, and spin-orbit coupling.

High quality crystalline deposition of the ferromagnetic insulator EuO is investigated with the primary focus of realizing high quality abrupt interfaces between the functional oxide and the spintronic material of choice. In this dissertation, stoichiometric EuO films are investigated on a wide variety of substrates including the spintronic relevant materials GaAs, 2-D planes of TiO_2, and sp^2 bonded carbon. The integration of EuO on these materials is a key advance towards experimental observation of the exchange proximity effect.

The atomic scale control over deposition provided by MBE allows for the investigation of submonolayer adsorbates (adatoms) and their interactions with graphene. In order to understand the effect of the adsorbates on spin-based properties and phenomena, we have performed systematic *in-situ* deposition of adatoms onto graphene non-local spin valves. Atomic hydrogen induces magnetic moments in graphene that couple via exchange to the injected spin current. This coupling results in an exchange field which causes the spins to precess rapidly with an effectively enhanced electron g-factor. These results demonstrate the power of molecular beam epitaxy in realizing novel graphene properties and functionality through careful control over the key interfaces and proximity materials.

Contents

List of Figures **xii**

1 Spintronics **1**

1.1 Introduction 1

1.2 Graphene for Spintronics 13

1.2.1 Introduction to Graphene 13

1.2.2 Spin Transport in Graphene 17

1.3 Spin Transport in Candidate Materials 26

1.4 Conclusion 28

2 Molecular Beam Epitaxy **31**

2.1 Introduction to Thin Film MBE 31

2.2 MBE Basics 33

2.2.1 Introduction to Vacuum Chambers 33

2.2.2 Vacuum Basics 35

2.2.3 The Manipulator 42

2.2.4 Evaporators 44
2.3 Surface Characterization Techniques for Thin Films 48
2.3.1 RHEED 48
2.3.2 Auger 54
2.4 Adatom Doping of Graphene by MBE 55
2.4.1 Effect on Charge Transport 56
2.4.2 Effect on Spin Transport 67
2.5 Conclusions and Outlook 71

3 The Ferromagnetic Insulator EuO 73

3.1 Historical Perspective 73
3.2 Electrical, Magnetic, and Optical Properties of EuO 76
3.3 Reactive Molecular Beam Epitaxy (rMBE) of EuO 89

4 Spin-Based Proximity Induced Phenomena 94

4.1 Induced Proximity Effects in Thin Film Systems 94
4.1.1 Introduction 94
4.1.2 EuO/GaAs 96
4.1.3 EuO/$LaAlO_3$ 97
4.1.4 EuO/Graphene 99
4.2 Induced Magnetism in Graphene by Dopants and Defects 100
4.2.1 Introduction to p_z-orbital Defects in Graphene 100

4.2.2 Experimental Progress on Magnetism in Graphene by Localized Defects . . . 105
4.3 Conclusion . . . 107

5 Epitaxial EuO Thin Films on GaAs 109

5.1 Introduction . . . 109
5.2 Experimental Determination of Eu Distillation Off Lattice Matched YSZ(001) 111
5.3 MgO as a Diffusion Barrier for Deposition of EuO on GaAs . . . 114
5.4 Conclusion . . . 117

6 TiO_2 as an Electrostatic Template for Epitaxial Growth of EuO on MgO(001) 118

6.1 Introduction . . . 118
6.2 Methods . . . 120
6.3 Electrostatic Considerations at the EuO/MgO(001) Interface . . . 121
6.4 Results and Discussion . . . 126
6.5 Conclusion . . . 132

7 Integration of the Ferromagnetic Insulator EuO with graphene 134

7.1 Introduction . . . 134
7.2 Results and Discussion . . . 137
7.3 Conclusion . . . 148
7.4 Experimental Methods . . . 149

8 Magnetic Moment Formation in Graphene Detected by Scattering of Pure Spin Currents 151

8.1 Introduction 151

8.1.1 The Proposed Experiment 153

8.2 Spin Transport in Pristine Graphene 154

8.3 Hydrogen Doping of Graphene Spin Valves 157

8.4 Origin of the Dip in R_{NL}: Control Experiments 158

8.4.1 Excluding Field-Dependent Resistivity Effects 159

8.4.2 Excluding Nuclear Spin Effects 162

8.4.3 Excluding Changes in Magnetization of the Electrodes 166

8.5 Effective Exchange Field Model 169

8.5.1 Single Spin-Moment Model 169

8.5.2 Interaction of an Electron Spin With Many Induced Moments 170

8.6 Application of the Exchange Field Model to Experimental R_{NL} and Hanle Data 175

8.7 Magnetic Moments Generated by Lattice Vacancies 184

8.8 Properties of the Exchange Field 185

8.8.1 Exchange Field and Narrowing of the Hanle Curve 186

8.8.2 Gate Dependence and Accuracy of g_e^* 194

8.9 Conclusion 196

9 Effect of *in-situ* Deposition of Mg Adatoms on Spin Relaxation in Graphene 199

9.1 Introduction 199

9.2 Results and Discussion 201

9.3 Conclusion 210

10 Appendix A: Growth Recipes 211

10.1 Introduction 211

10.2 Mg Distillation and MgO Homoepitaxy 211

10.2.1 A (Recent) Growth Perspective on MgO 211

10.2.2 Mg Distillation 213

10.2.3 MgO Homoepitaxy by rMBE 215

10.2.4 Recipes for MgO Homoepitaxy 218

10.3 MgO on Semiconductors by e-beam Deposition 221

10.3.1 MgO on GaAs(001) 221

10.3.2 MgO on Si(001) for Al/Fe/MgO/Si Collaboration with OSU 225

10.4 EuO Growths on Various Substrates 234

10.4.1 EuO/YSZ(001) 235

10.4.2 EuO/MgO/GaAs(001) 238

10.4.3 EuO/TiO_2/MgO(001) 240

10.4.4 EuO/HOPG(0001) 243

10.5 Co/Pd Superstructures for Perpendicular Media 246

Bibliography 256

List of Figures

1.1 DOS for Ferromagnetic and Non-magnetic Materials. 2
1.2 Giant Magnetoresistance (GMR). 3
1.3 Tunneling Magnetoresistance (TMR). 5
1.4 The Datta-Das SpinFET. 6
1.5 Spin Injection at FM/NM Interface. 7
1.6 The Johnson-Silsbee Experiment of Non-local Spin Transport. 8
1.7 Non-local Spin Transport in Metallic Spin Valves. 9
1.8 Hanle Spin Precession in Non-local Metallic Spin Valves. 12
1.9 Graphene Lattice and Band Structure. 15
1.10 Ambipolar Field Effect Behavior and Quantum Hall Effect in Graphene. . . . 17
1.11 Demonstration of Spin Transport in Graphene. 18
1.12 Linear Scaling Between Spin Relaxation and Momentum Scattering Through Field Effect Spin Transport Measurements in Graphene. 19
1.13 Atomically Smooth MgO on Graphene with TiO_2 Seed Layer. 22
1.14 Tunneling Spin Injection into SLG at RT. 23

1.15 Comparison of Hanle Spin Precession Measurements for Tunneling, Ohmic, and Pinhole Contacts to Graphene. 25

2.1 Typical MBE Chambers. 35

2.2 Contaminant Deposition Rate Caused by Background Pressure in MBE. . . . 39

2.3 Pumping Systems Relevant for UHV. 41

2.4 Thermal Evaporator. 45

2.5 Bending Magnet e-beam Evaporator Schematic 46

2.6 e-beam Rod Evaporator Schematic 47

2.7 Reflection High Energy Electron Diffraction 2D View 50

2.8 Reflection High Energy Electron Diffraction 3D View 51

2.9 Direct and Reciprocal Lattice of the MgO Surface 51

2.10 RHEED example: MgO 53

2.11 Auger Electron Spectroscopy (AES) Example: HOPG. 55

2.12 Electron-Hole Puddles in Graphene on SiO_2/Si Substrate 58

2.13 Role of the Contacts on Graphene. 59

2.14 Observation of Electric Fields at the Contacts to Graphene Due to Interfacial Dipole and Charge Transfer. 59

2.15 Graphene as a Gas Sensor. 60

2.16 Systematic Doping of Graphene with Potassium. 61

2.17 The *in-situ* Measurement System. 62

2.18 Sample Platen and Paddles for *in-situ* Measurement System 63

2.19 Transition Metal Doping of Graphene. 64

2.20 Effect on Graphene Mobility and Charge Neutrality Point by TM Doping. . . 65

2.21 Au Doping of Graphene at 18 K. 67

2.22 Clustering of Au on Graphene. 68

2.23 Au doping of Graphene Non-local Spin Valves with Ohmic Contacts. 69

3.1 Crystal Structure of EuO 75

3.2 Energy Levels of Atomic Orbitals in EuO 77

3.3 Absorption Spectrum of EuO 78

3.4 Band Levels and Density of States for EuO 79

3.5 Temperature Dependence of 5d Band Splitting in EuO 79

3.6 Diagram of Adsorption-controlled Growth Regime 93

4.1 Proximity Effect in EuO/Al 95

4.2 Spin Polarized 2DEG at the EuO/LAO$_3$ Interface 98

4.3 Exchange Interaction for Spin Manipulation in a SFET 100

4.4 Single p_z-orbital Defects in Graphene. 101

4.5 Spin-dependent DOS of Graphene with Exchange Split Quasi-localized Defect States 103

4.6 Spatial Distribution of the Quasi-localized Induced Magnetic Moment 104

4.7 Spin-1/2 Paramagnetism in Graphene. 106

5.1 Investigation of EuO on YSZ(001) and MgO(001). 112

5.2 Integration of EuO on GaAs(001). 115

5.3 Magnetic Characterization of EuO/Mgo/GaAs(001). 116

6.1 Various Crystal Structure Schematics of EuO on MgO. 122

6.2 RHEED Images for EuO/TiO_2/MgO(001). 125

6.3 Time Evolution and Magnetic Properties of EuO Growth on TiO_2/MgO and MgO. 129

6.4 Magnetic Characterization of Ultrathin EuO. 131

7.1 Auger Spectroscopy of Eu Deposited on HOPG at Several Different Substrate Temperatures. 138

7.2 Characterization of EuO Thin Films on HOPG. 140

7.3 Schematic of EuO Crystal on Graphene 142

7.4 Temperature Dependence of the Magnetization of EuO/HOPG. 143

7.5 EuO Thin Films Deposited on Exfoliated Graphene Flakes. 145

7.6 Gate Dependent Resistivity for EuO/graphene. 147

7.7 MOKE for EuO Grown on CVD Graphene. 147

8.1 Schematic of the *in-situ* Deposition of H and Interaction with the Spin Current. 154

8.2 The Effect of Hydrogen Exposure on Charge and Spin Transport in SLG at 15 K. 155

8.3 Investigating the Source of the Dip Measured in R_{NL}: Changes in Resistivity. 161

8.4 Comparison of Percent Change for R_{NL} and Resistivity. 161

8.5 Test of Nuclear Spin Effects. 162

8.6 Reversibility of effects due to hydrogen doping of SLG. 165

8.7 Magnetoresistance of Co Wires Before and After Hydrogen Exposure at T=10 K. 168

8.8 Minor Loop of Hydrogen-doped Graphene and Analysis of R_{NL}. 169

8.9 The Effect of Lattice Vacancies on Charge and Spin Transport in SLG at 15 K. 184

8.10 Conductivity and Calculated Diffusion Coefficient for Pristine and Hydrogen-doped SLG at 15 K. 187

8.11 Conventional Hanle Fitting Assuming g_e^*=2 (No Exchange Field). 188

8.12 Comparison of the Spin Lifetimes. 192

8.13 Gate Dependence of the Enhanced Precession due to the Exchange Field. . . 193

8.14 Analysis of Hanle Spin Precession Data Without Consideration of R_{NL} Data. 196

9.1 Spin Transport in Pristine Graphene 202

9.2 Effect on Charge Transport by Mg Doping. 205

9.3 Effect on Spin Transport by Mg Adatoms. 207

10.1 Homoepitaxy of e-beam MgO on MgO(001). 213

10.2 Evolution of Mg Distillation. 215

10.3 Homoepitaxy of Reactively Grown MgO on MgO(001). 216

10.4 Comparison of Spin Lifetimes by TRKR on Different GaAs Substrates. . . . 222

10.5 RHEED and Auger of Si. 226

10.6 RHEED and Auger of e-beam MgO/Si. 232

10.7 RHEED and Auger of Al/Fe/MgO/Si. 234

10.8 Comparison of Magnetic Behavior of Different Co/Pd Superlattices. 251

10.9 Co/Pd layers on MgO/GaAs(001) Characterization for Future Spin Injection. 254

Chapter 1

Spintronics

1.1 Introduction

Spin-based electronics, or spintronics, seeks to utilize the electron degree of freedom in order to perform logic operations or information storage. Over the years, many significant advances have been made in the field towards realizing commercial applications that can work either in place of or in conjunction with standard Si based electronics. In particular, the discovery of giant magnetoresistance (GMR) (Nobel Prize in Physics 2007) [1, 2] and tunneling magnetoresistance [3, 4, 5, 6] has revolutionized magnetic sensing technology and increased hard drive storage many orders of magnitude [7]. In practice, much of the current spintronics field is founded upon taking advantage of the built in spin polarized nature of ferromagnetic materials. In recent years there has been a push in trying to realize control over spins and spin dynamics in systems such as NV diamond centers [8, 9, 10] and quantum

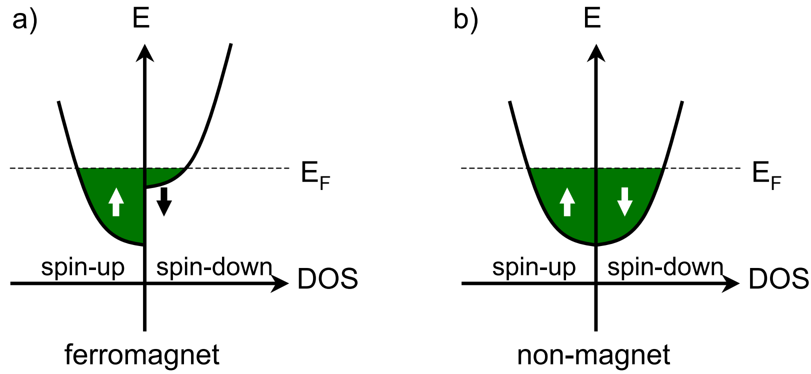

Figure 1.1: DOS for Ferromagnetic and Non-magnetic Materials. a) Spin-dependent density of states (DOS) for a ferromagnetic material. b) Spin-dependent density of states for a non-magnetic materials. Number of spin up and spin down the below the fermi level and at the fermi level are equal for a non-magnetic material.

dots [11, 12, 13] to try to realize logic operation by coupling the spin degree of freedom with optical control [14]. There are several excellent reviews on the current status of spintronics [15, 16, 17, 18, 19, 20, 21, 22, 14, 23, 24, 25].

A simple model for a ferromagnetic material is displayed in Fig. 1.1 and compared with a non-magnetic material. In the Stoner-Wohlfarth picture [26], a ferromagnet can be understood in terms of the spin-dependent density of states (DOS), for which there is a spin imbalance when the number of up spins ($N_\uparrow$) exceeds the number of down spins ($N_\downarrow$). In this model, spontaneous magnetism arises from a spin imbalance in the net spin-dependent DOS ($N_\uparrow - N_\downarrow$) and the properties for spin injection are determined by the difference in the density of states at the Fermi level ($N_\uparrow(E_F) - N_\downarrow(E_F)$), where E_F denotes the Fermi level in the material. This model works satisfactorily for understanding d-orbital based ferromagnets such as Co and Fe. In Rare earth based ferromagnetic materials, the magnetic moment lies in

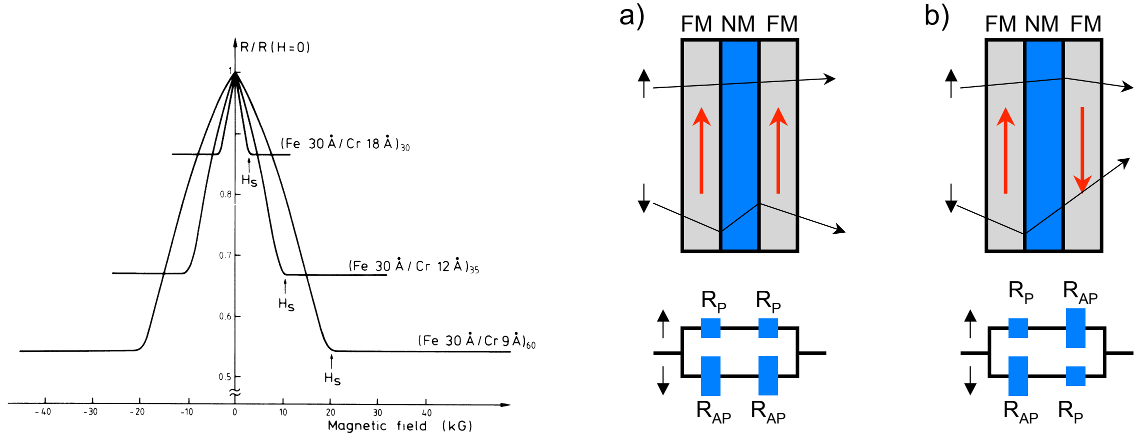

Figure 1.2: Giant Magnetoresistance (GMR). **Left column**: Adapted from [1]. GMR effect in Fe/Cr superlattices. **Right column**: Cartoon schematic of GMR effect. a) Parallel configuration for two metallic ferromagnetic thin film layers with a non-magnetic metallic interlayer. Current path for resistance measurement is perpendicular to the plane (CPP). b) Antiparallel (AP) configuration of the GMR device generating a high resistance state.

the highly localized $4f$ shell. Rare earth magnetism and exchange will be discussed further in Chapter 3.

Fig. 1.2 (left column) displays the magnetoresistance effect in molecular beam epitaxy (MBE) grown Fe(001)/Cr(001) superlattices grown on GaAs(001). MBE is a materials growth technique that allows for high purity thin film materials with control at the atomic scale and is discussed in more detail in Chapter 2. The resistance is measured by driving a current perpendicular to the plane (CPP) of the superlattice. Focusing on the 9 Å thick Cr superlattice, the resistance is maximum at zero field and decreases as a magnetic field is applied. This behavior can be understood in terms of RKKY coupling [26] between the ferromagnetic layers. Itinerant electrons within the non-magnetic layer can couple the magnetizations of the adjacent ferromagnetic layers through exchange coupling, $H_{ex} = -J(\vec{M}_1 \cdot \vec{M}_2)$. The coupling favors parallel or antiparallel configurations depending on the sign of the exchange

coupling term, J. According to RKKY theory [26], J depends strongly on the thickness (d) of the of the non-magnetic layer and can oscillate between positive and negative values depending on d, following the equation $J \propto \cos 2k_F d$. A cartoon schematic explaining the GMR effect in such exchange coupled FM/NM/FM superlattices is displayed in Fig. 1.2 (right column). Consider two channel (spin up or spin down) transport through this structure. A spin channel which is parallel (P) to the magnetization of a ferromagnetic layer will experience less scattering than a spin channel that is antiparallel (AP) to the magnetization. This can be modeled in a simple high (low) resistor circuit for AP (P) configuration. When the magnetizations, M_1 and M_2 are in an AP configuration there is an overall increase in the resistance compared to a P configuration for M_1 and M_2. Accordingly, the Fe/Cr superlattice with 9 Å of Cr has antiferromagnetically coupled Fe layers at zero applied field and therefore demonstrates a maximum in the resistance of the structure.

A related phenomena, known as tunneling magnetoresistance (TMR), occurs in similar structures for which the nonmagnetic metallic interlayer is replaced with an insulating material such as Al_2O_3 or MgO. For these heterostructures, transport is strongly dependent upon the spin-dependent tunneling probability between the two ferromagnetic layers [3]. This is schematically depicted in Fig. 1.3. The insertion of single crystal MgO(001) tunnel barriers into TMR devices proved to be a revolutionary advance in the field of magnetic head sensors. This is due to the special Δ_1 spin filtering associated with Co/MgO, Fe/MgO, and CoFeB/MgO interfaces which can yield large TMR values above 400% [6, 5, 27]. Such large changes in the resistivity combined with advances in nanofabrication processes has made

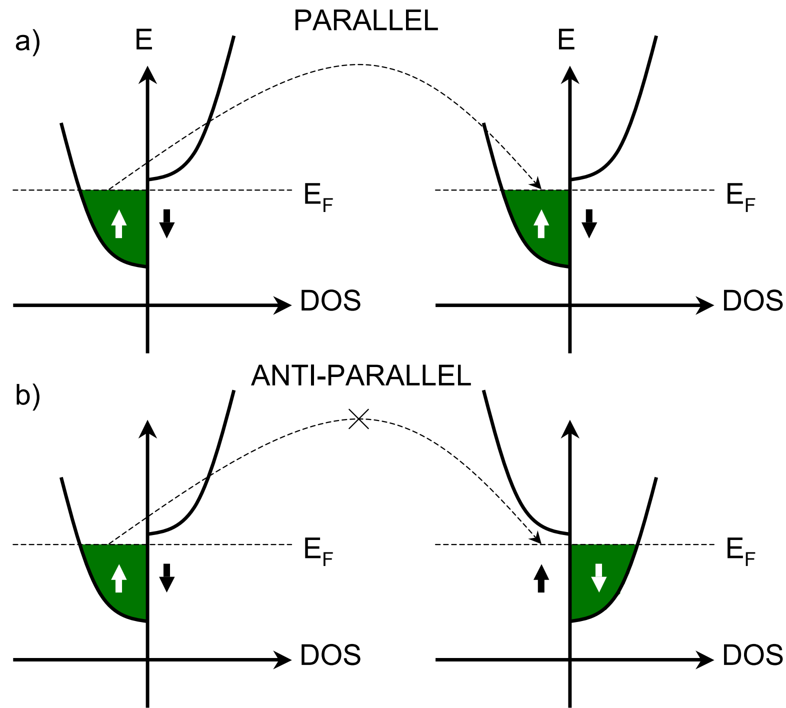

Figure 1.3: Tunneling Magnetoresistance (TMR). a) Spin-dependent DOS for two adjacent ferromagnetic materials separated by an insulating layer in the parallel configuration. Tunneling probability is determined by spin-dependent DOS at the Fermi level. b) Spin-dependent DOS for two adjacent ferromagnetic materials separated by an insulating layer in antiparallel configuration. Tunneling probability is minimal due to the lack of available states to tunnel into at the Fermi level. *Note:* This is a simplified picture assuming 100% spin polarization at the Fermi level. Standard ferromagnetic materials (Co, Fe) have much lower polarization at the Fermi level when compared to half metallic materials such as EuO_{1-x}, LSMO, and Fe_3O_4.

TMR devices extremely important for the hard drive industry and have since replaced GMR as the industry mainstay.

As discussed above, spintronic devices are extremely important for for data storage in industrial applications. However, spintronics for information processing is still being investigated from a fundamental point of view. The standard premise for a functional spin-based transistor consists of spin injection into a non-magnetic channel, transport along the chan-

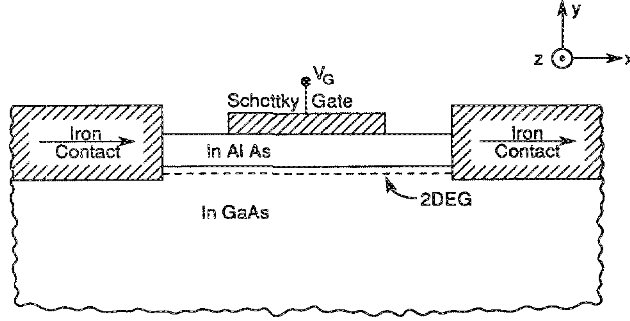

Figure 1.4: The Datta-Das SpinFET. Adapted from [28].

nel, spin manipulation in transit, and spin detection. Such a device was first proposed by Datta and Das in 1990 [28] and is shown in Fig. 1.4. In this novel device, the proposed spin transport channel is the two dimensional electron gas (2DEG) that forms at InAlAs/InGaAs interfaces. One Fe contact provides a source for spin injection, while the other acts as an analyzer for spin detection in analogy to an electro-optic modulator. Due to inversion symmetry breaking, there exists Rashba type spin-orbit (SO) coupling at this interface. The Datta-Das spin field effect device (SpinFET or SFET) is based on the idea that spins in transit can be modulated through an applied gate voltage which can tune the Rashba SO coupling. Much of the work contained in this dissertation is aimed at trying to realize materials systems and routes for control over spin transport beyond the simple Datta-Das Rashba model.

First, spin injection from a ferromagnet into a non-magnetic material must be discussed. Fig. 1.5 shows the junction between a ferromagnetic metal and a non-magnetic metal. Spin-dependent properties within the FM and NM magnetic layers are best described by the spin-dependent chemical potentials ($\mu_{FM,\uparrow,\downarrow}$, $\mu_{NM,\uparrow,\downarrow}$) and average chemical potential ($\mu_{FM} = \frac{1}{2}(\mu_{FM,\uparrow} + \mu_{FM,\downarrow})$). Under an applied bias, the problem can be discussed in terms of Ohm's

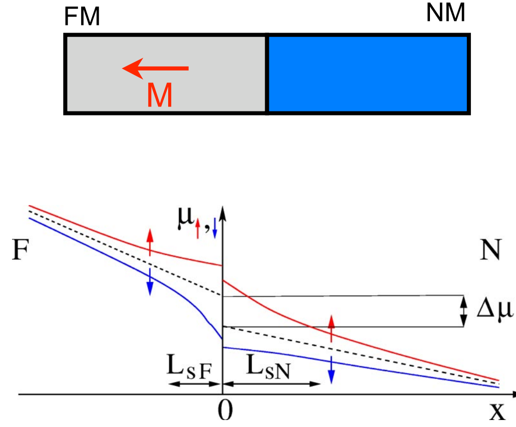

Figure 1.5: Spin Injection at FM/NM Interface. **Top panel**: Schematic of the interface between a ferromagnetic metal (FM) and a non-magnetic metal (NM). **Bottom panel**: Adapted from [16]. Spin-dependent chemical potentials as a function of position at the interface of FM and NM materials.

law and the continuity equation [16, 26]. At the interface, the average chemical potential is discontinuous due to a difference in the spin chemical potentials between the two materials caused by the presence of a polarization current. This potential drop at the interface is often called spin accumulation and relies on the principle of two different spin conduction channels and two materials with different electrical conductivities. Away from the interface, the spin-dependent chemical potentials decay exponentially with characteristic length-scales. This is the spin diffusion length, $\lambda_{sf} = \sqrt{D\tau_s}$, where D is the diffusion constant of the respective materials and τ_s is the spin lifetime. In figure 1.5, the spin diffusion length, λ_{sf}, is denoted L_{sF} and L_{sN} for the ferromagnetic and non-magnetic materials, respectively. Away from the interface, $\mu_{NM,\uparrow}$ and $\mu_{NM,\downarrow}$ approach μ_{NM} as the spin population relaxes with characteristic time that is τ_s and characteristic length-scale, λ_{sf}. It is of fundamental importance to better understand the nature of spin-relaxation in different materials in order to realize applicable SFET behavior.

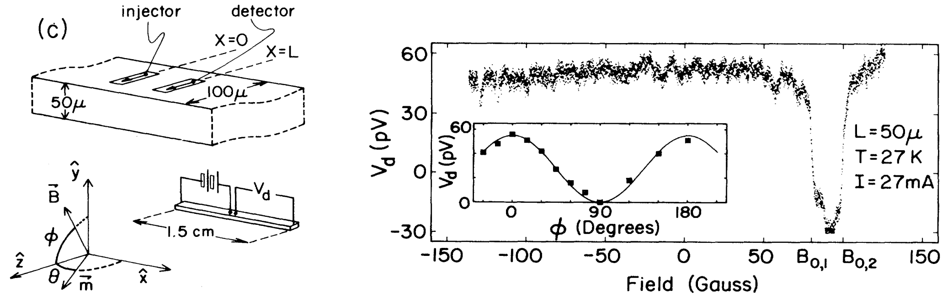

Figure 1.6: The Johnson-Silsbee Experiment of Non-local Spin Transport. Adapted from [29].

In a pioneering experiment, Johnson and Silsbee [29] demonstrated a working lateral spin valve using permalloy (Py) electrical contacts to an Al channel in a non-local geometry (See Fig. 1.6). The picture of FM/NM spin injection based on spin-dependent chemical potentials discussed above is directly relevant for multiterminal electrical measurements. In particular, the CPP GMR measurements can also be understood in this way [26, 7]. The Johnson-Silsbee experiment for non-local spin transport was revisited in 2002 by Jedema (van Wees group) [30]. The non-local geometry has a particular advantage over other electrical measurements in that it separates out contributions from spin and charge transport and can probe the spin properties (λ_{sf}, τ_s) of the transport channel.

Fig. 1.8 (left column) a) displays a scanning electron microscope (SEM) image from the Jedema experiment of a non-local spin valve fabricated using modern e-beam lithography techniques [30]. The device uses Co electrodes contacted to an aluminum channel with Al_2O_3 tunnel barriers inserted between the Co and Al. The electrical schematic for the measurement is displayed in Fig. 1.8 (left column) b). In the four terminal non-local measurement, the current path is separated from the voltage detection points. As shown in

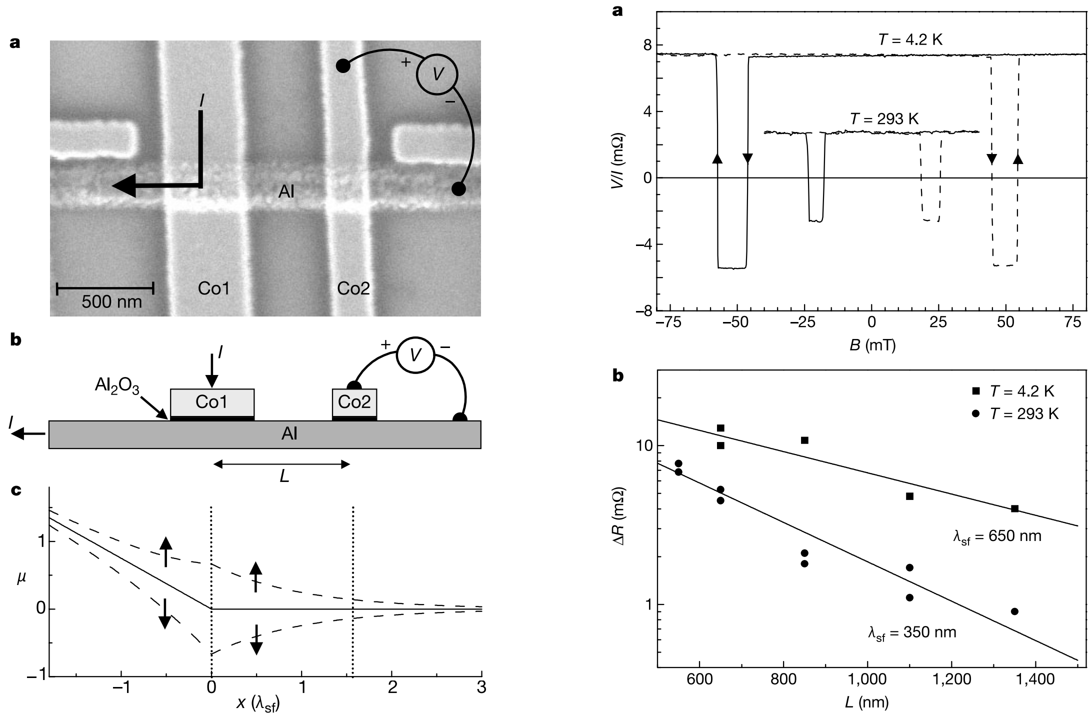

Figure 1.7: Non-local Spin Transport in Metallic Spin valves. Adapted from [30]. **Left column**: a) SEM image of non-local spin valve with Co contacts to an Al channel. b) Cross sectional schematic of device and electrical connections. c) Spin-dependent chemical potentials as a function of position along the Al channel. **Right column**: a) Non-local magnetoresistance data demonstrating spin injection, transport, and detection. b) Non-local magnetoresistance for several different Al channel spacings, L. Log scale dependence yields the spin diffusion length at T=4.2 K and T=293 K of 0.65 μm and 0.35 μm, respectively.

the figure, Current is injected through one of the inner ferromagnetic electrodes and flows to the left. Underneath the ferromagnetic contact, spins are injected into the Al channel. The picture for spin injection and accumulation is comparable to the one discussed previously. Below the contact there is a positional dependence of the spin-dependent chemical potential. For any quantity that exhibits a gradient in the concentration as a function of position, diffusion can be expected to occur. Thus, to the left, spins undergo drift and diffusion. To the right, pure spin diffusion occurs along the Al channel. Since the detection measurement is an

electrical probe, it is sensitive only to voltages underneath the contacts. By employing ferromagnetic contacts, the voltage measurement probes the spin-dependent chemical potential depending on the relative orientation of the dominant spin axis and the magnetization vector of the ferromagnetic electrode.

Fig. 1.8 (left column) c) displays the spin dependent chemical potential (dashed lines) and the averaged chemical potential (solid line) as a function of position in the Al channel. $x = 0$ corresponds with the location of the injector electrode. The detector is located a distance, L, away from the injector electrode. To the left of the injector electrode ($x < 0$), the chemical potential exhibits a linear slope due to presence of an applied bias in the current loop. To the right, the averaged chemical potential is a flat line because there is no net electrical current being driven. However, as discussed previously, there is a net non-zero imbalance in the spin dependent chemical potential due to spin injection at $x = 0$. This is characterized by the spin injection polarization in the Al at $x = 0$ and depends on the spin polarization and the injection efficiency across the junction.

Spins are transported along the channel in the positive x direction due to diffusion. During transit, the spin population can relax with a characteristic time scale, τ_s, and the spin-dependent chemical potential decays exponentially as $\mu_{\uparrow,\downarrow} \propto e^{-L/\lambda_{sf}}$. Therefore, the ferromagnetic electrode at $x = L$ measures the spin voltage that has decayed relative to $x = 0$. Nevertheless, a voltage can be measured as long as the ration L/λ_{sf} is not too large. The spin dependent chemical potential at $x = L$ is experimentally measured in reference to another voltage probe located at $x \to \infty$. If the magnetization of the injector electrode is parallel

(antiparallel) to the magnetization of the detector, then a positive (negative) voltage will be measured. Due to the shape anisotropy of the Co wires, the magnetization vector points in plane along the axis (y-axis) of the wire. An applied field along the wire axis (y-axis) can control the magnetization of the electrode, which switches its magnetization at the coercive field, H_C. If the two ferromagnetic electrodes (injector and detector), are made to have different widths, then the will have different coercivity as the shape anisotropy has been altered. A narrower wire will have a larger coercivity than a wider wire. By engineering the coercivities of the injector and detector, there exists an applied field range in which there will be both parallel and antiparallel alignment of the magnetization vectors. Therefore, measurements of the non-local voltage as a function of in plane field (y-axis sweep) will generate characteristic two state spin voltage signals, V_P and V_{AP}, for parallel and antiparallel, respectively. This is demonstrated in Fig. 1.6 and 1.8 (right column) a). A non-local resistance can be defined as $\Delta R_{NL} = (V_P - V_{AP})/\mathrm{I}$, where I is the injected current. In relatively thin films or 2D transport layers such as graphene, the non-local spin transport is well described by the Takahashi and Maekawa 1D equation [31],

$$R_{NL}^{(P/AP)} = \pm 2R_S e^{\frac{-L}{\lambda_{sf}}} \prod_{i=1}^{2} \left(\frac{P_J \frac{R_i}{R_S}}{1 - P_J^2} + \frac{P_F \frac{R_F}{R_S}}{1 - P_F^2} \right) \times \left[\prod_{i=1}^{2} \left(1 + \frac{2 \frac{R_i}{R_S}}{1 - P_J^2} + \frac{2 \frac{R_F}{R_S}}{1 - P_F^2} \right) - e^{\frac{-2L}{\lambda_{sf}}} \right]^{-1} \quad (1.1)$$

where $R_S = \rho \lambda_{sf}/w$ is the spin resistance of transport layer, ρ is the channel resistivity, w is the channel width, $R_F = \rho_F \lambda_F / A_J$ is the spin resistance of the ferromagnet, ρ_F is the ferromagnet resistivity, λ_F is the ferromagnet spin diffusion length, A_J is the junction area,

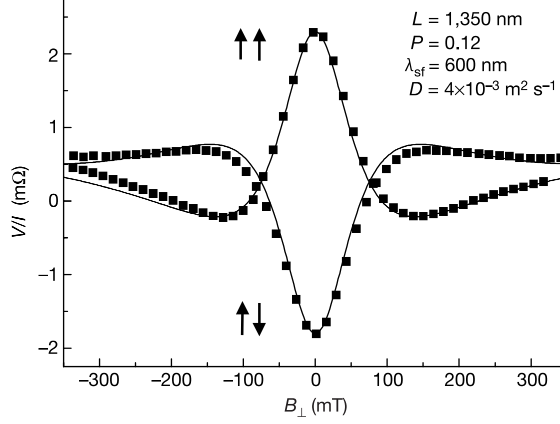

Figure 1.8: Hanle Spin Precession in Non-local Metallic Spin Valves. Adapted from [30]. Hanle curve of non-local spin signal due to spin injection from Py into Al at T=4.2 K.

P_F is the spin polarization of ferromagnet, P_J is the spin injection polarization, R_1 and R_2 are the contact resistances of the spin injector and detector.

Instead of sweeping an in-plane magnetic field, application of an out-of-plane field causes the injected spins to precess as they diffuse along the channel. This technique is called Hanle spin precession. Since the transport is a diffusive process, there is a distribution of arrival times at the detector electrode which gives a distribution of relative spin orientation at the detector. The voltage measurement is not sensitive to individual spins at each arrival time, but instead measures the entire packet distribution and essentially averages the net spin orientations. Therefore, at high applied fields, the entire spin population is dephased leading to zero spin signal. Such spin precession measurements can be fit using the non-local Hanle equation [32, 25, 33, 34],

$$R_{NL} = S \int_0^\infty \frac{e^{-L^2/4Dt}}{\sqrt{4\pi Dt}} \cos\left(\frac{g_e \mu_B}{\hbar} B_{app,z} t\right) e^{-t/\tau_s} dt \tag{1.2}$$

provides values of spin lifetime (τ_s), diffusion coefficient (D), Hanle amplitude (S), and spin diffusion length ($\lambda_{sf} = \sqrt{D\,\tau_s}$).

Using the non-local technique, the spin diffusion lengths have been determined for Al, Ag, Cu, Au, and Pt. The corresponding diffusion lengths at room temperature are $\lambda_{sf,Al} \sim 350$ nm [30], $\lambda_{sf,Ag} \sim 300$ nm [35, 36], $\lambda_{sf,Cu} \sim 350 - 400$ nm [37, 38], $\lambda_{sf,Au} \sim 100$ nm [39], and at T=4 K, $\lambda_{sf,Pt} \sim 10$ nm [40]. Typical spin lifetimes range between 1 and 10 ps [26, 30]. For ferromagnetic metals (Fe, Co, Ni, Py), the spin diffusion lengths are generally in the range of 5 to 50 nm [26].

1.2 Graphene for Spintronics

1.2.1 Introduction to Graphene

Graphene is a two dimensional sheet of carbon atoms arrayed in a honeycomb lattice and is based on the same sp^2 bonded layers that make up graphite. In 2004, graphene was first isolated by a mechanical exfoliation technique developed by Novoselov and Geim [41] and was subsequently shown to have excellent mechanical and electrical properties [42, 43, 41, 44, 45, 46]. For these advances in the field of 2D materials, Novoselov and Geim were awarded the 2010 Nobel Prize in Physics [47]. The mechanical exfoliation technique cleaves ultrathin graphite and graphene from highly oriented pyrolitic graphite (HOPG) or Kish graphite. Due to the weak interplane van der Waals force, sheets of graphene can be readily removed by a simple peeling technique with scotch tape and has since become known

as the 'scotch-tape' method. The graphene sheets can then be placed on SiO_2/Si substrate which due to special optical properties of the 300 nm SiO_2 layer, allows for the graphene flake to be viewed under an optical microscope, despite being 1 atom thick with weak absorption of light in the visible range [42]. This technique has the advantage of providing high quality single crystal and relatively clean flakes for device fabrication. In such FET devices, the SiO_2 acts as a dielectric layer for the heavily p-doped Si back gate. Alternative to mechanical exfoliation, there have been recent advances in production of large area graphene (LAG) through chemical vapor deposition (CVD) [48, 49], which has greatly increased graphene's viability for commercial applications.

The graphene lattice is displayed in Fig. 1.9 (top center). Graphene made of carbon atoms arrayed in a triangular lattice, where each carbon atom in the A sublattice has a corresponding basis carbon atom in a triangular B sublattice. A carbon atom in the A (B) sublattice is covalently bonded to 3 nearest neighbor carbon atoms in the B (A) sublattice. The electronic properties of graphene are well described through tight-binding model [43]. In this model, electronic transport is determined by hopping energies, t and t', for nearest neighbor atoms and next-nearest neighbors (NNN), respectively. Solutions to the tight binding Hamiltonian [43] yield the electronic dispersion,

$$E(k) = \pm\hbar t\sqrt{3 + 2\cos\sqrt{3}k_y a + 4\cos\frac{3}{2}k_x a} + \mathcal{O}(t') \tag{1.3}$$

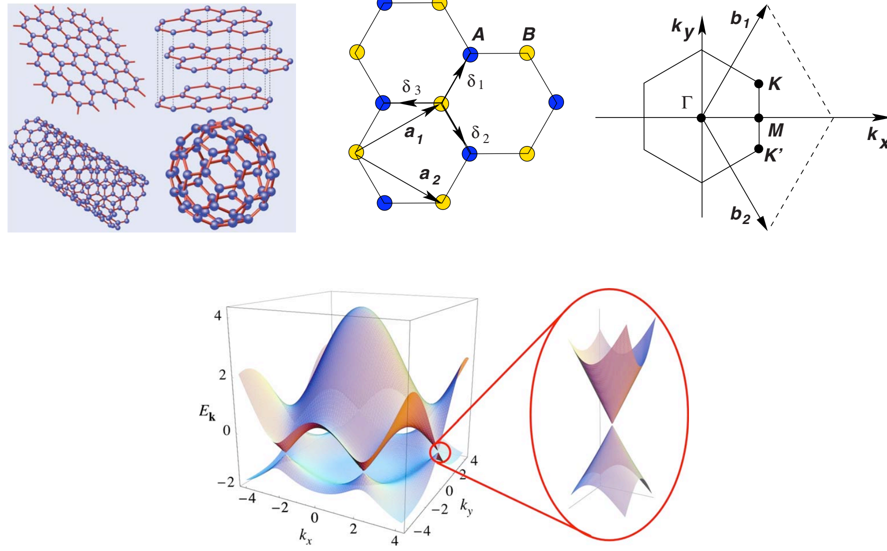

Figure 1.9: Graphene Lattice and Band Structure. Adapted from [43]. **Top left**: Graphene is the basic building block for other important sp^2 bonded carbon materials. Stacking of graphene produces graphite, rolling graphene produces carbon nanotubes, and wrapping produces fullerenes. **Top center**: Real space diagram of the graphene in a triangular lattice. Yellow atoms represent the A sublattice and blue atoms represents the B sublattice. **Top right**: First Brillouin zone of graphene in reciprocal space. Dirac cones exist at the K and K′ prime points that are related to the AB sublattice. **Bottom**: The band structure of graphene in reciprocal space. Around the K and K′ points the band structure is characterized by cones with linear dispersion.

where a=1.42 Å is the magnitude of one of the real space lattice vectors. The NNN hoping term, t', is thought to be 1 to 2 orders of magnitude smaller than t and is generally ignored. The dispersion is displayed in Fig. 1.9 (bottom) and vanishes at the six corners of the Brillouin zone. These points are the K and K′ points, which arise due to the AB sublattice. Expanding equation 1.3 around the K or K′ yields,

$$E(k) = \pm\hbar\frac{3ta}{2}k = \pm\hbar v_F k \tag{1.4}$$

which is known as the Dirac equation for graphene. $v_F = 1 \times 10^6$ m/s is the Fermi velocity and is independent of both energy and momentum, which is a unique property of Dirac materials. Notably, the dispersion is linear and sweeps out a circular cone in k space around the K and K$'$ points as shown in Fig. 1.9. The top Dirac cone represents the conduction band, while the lower band is the valence band. There is no band gap, which suggests that graphene is best described as a semimetal. Under an applied gate voltage the Fermi level can be tuned from electron to hole type carriers. This effect is demonstrated in Fig. 1.10 a). Due to the large Fermi velocity, is reasonably expected that graphene should have relatively high mobility. Indeed, it has been found that typical graphene FET devices exfoliated on SiO_2 have mobilities in the range of 1000 to 20,000 cm^2/Vs [41, 50, 51]. Recently, the mobility of graphene devices has been dramatically improved by either suspending the graphene or by placing the graphene on hBN, which has yielded mobilities upwards of 500,000 cm^2/Vs [52, 53, 54, 55, 56].

Because the dispersion does not depend on mass, electron or hole type carriers are thought to behave as relativistic, massless Dirac fermions. Therefore, graphene serves as a platform for investigating 'tabletop' relativistic physics. In particular, there have been exciting reports of the integer quantized Hall effect (QHE) [44, 45], fractional QHE [52, 57], and Klein tunneling [58, 59, 60]. The observation of the quantum Hall sequence in graphene by the Geim and Kim groups in 2005 [44, 45] was the first conclusive evidence for massless Dirac fermions in graphene (see Fig. 1.10 b)). The Hall conductivity for graphene follows the

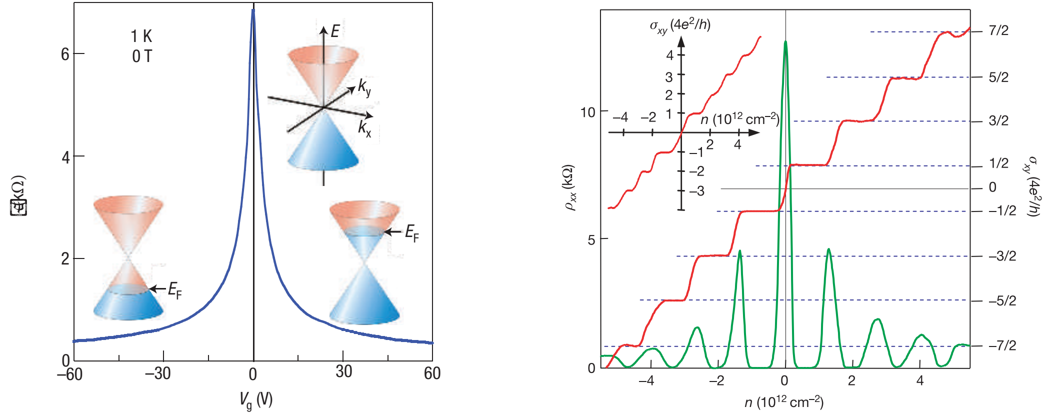

Figure 1.10: Ambipolar Field Effect Behavior and Quantum Hall Effect in Graphene. a) Resistance of a graphene field effect device as a function of back gate voltage. Maximum resistance corresponds to the Dirac point where the Fermi level is expected to cross from electron to hole type carriers. Adapted from [42]. b) Quantum Hall effect in graphene. Anomalous quantization of the Hall conductivity is evidence for 2D massless Dirac fermions in graphene. The inset shows the QHE sequence for bilayer graphene. Adapted from [44].

equation, $\sigma_{xy} = (n + \frac{1}{2})4\frac{e^2}{h}$, with QHE sequence of ±2, ±6, ±10 in conductance units of e^2/h.

1.2.2 Spin Transport in Graphene

As discussed above, the linear dispersion of graphene produces interesting and unique properties that are attractive for electronic devices including ambipolar FET behavior and high mobility. From a spin transport point of view, graphene, which is made up of a light element material, is expected to have weak spin orbit coupling [61, 62, 63]. Further, there is low abundance of ^{13}C nuclear carbon [64], which would suggest weak hyperfine coupling as well. The low intrinsic spin-orbit coupling and weak hyperfine coupling, combined with

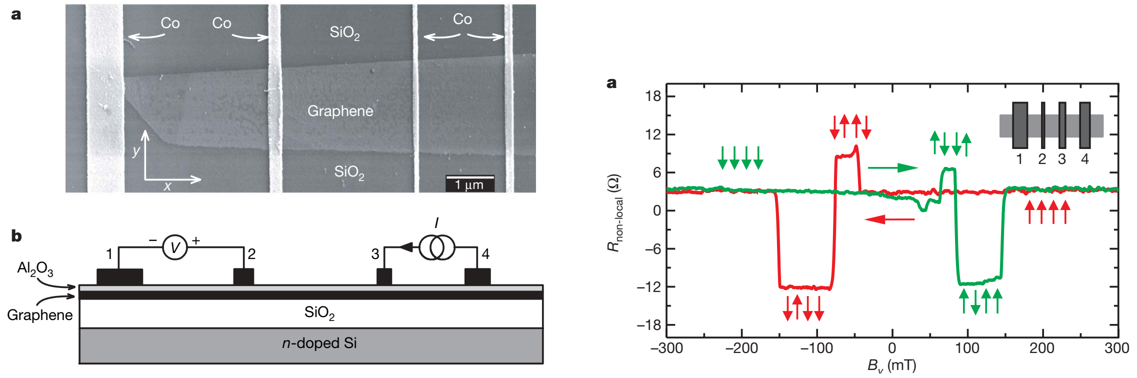

Figure 1.11: Demonstration of Spin Transport in Graphene. Adapted from [32]. **Left column**: a) SEM image of an exfoliated graphene flake contacted with Co ferromagnetic electrodes. Electrodes fabricated using e-beam lithography. b) Cross section schematic indicating the SiO_2/Si substrate, graphene flake, Al_2O_3 layer, Co contacts, and electrical connections for the non-local measurement. **Right column**: Non-local magnetoresistance demonstrating spin transport in single layer graphene.

high mobility, gives graphene great potential for long spin lifetimes and long spin diffusion lengths.

The foundational work in the field of graphene spintronics is the Tombros 2007 paper from the van Wees group [32]. Around this time, there were three other reports suggesting spin transport in graphene in two terminal (local) spin valves [65, 66, 67]. However, in the local geometry, it is difficult to distinguish a real graphene signal from an artifact such as anisotropic magnetoresistance (AMR). The big success of the Tombros paper, was the demonstration of room temperature local *and* non-local spin transport along with Hanle spin precession measurements. It was found that graphene had a relatively long (compared to metals and semiconductors at room temperature) spin diffusion length, $\lambda_{sf} = 1 - 2\ \mu$m. Further, the spin-lifetime was determined to be in the range of 100 to 170 ps. In the same time period, the Fuhrer group demonstrated non-local spin transport at low temperatures in

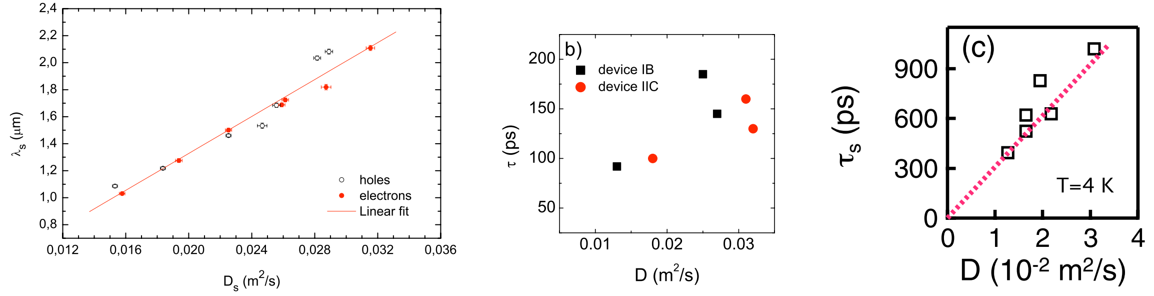

Figure 1.12: Linear Scaling Between Spin Relaxation and Momentum Scattering Through Field Effect Spin Transport Measurements in Graphene. a) Adapted from [70]. b) Adapted from [69]. c) Adapted from [72].

narrow graphene channels for which the data was interpreted in terms of quantum transport behavior [68]. These five works constitute the beginning of the field of graphene spintronics, while the Tombros paper [32] is generally considered to represent the best evidence for spin transport.

Since the original work by the van Wees group, there have been several experimental milestones in the field over the past 5 years. This includes studies of spin relaxation mechanisms in single layer graphene (SLG) on SiO_2 [69, 70, 71, 72, 73], electron hole asymmetry [74], tunneling spin injection [71], spin transport in bilayer [72, 75] and multilayer graphene [67, 76], spin transport in CVD grown graphene [75] and epitaxial graphene [77, 78, 79], as well as spin transport and relaxation in suspended graphene [80, 81] and graphene on hBN [82].

Much of the focus has been on trying to understand why the spin lifetimes are so short. While the spin diffusion length at room temperature is the longest in any material, it is still much shorter than expected and owes it's large value mainly to graphene's high mobility, which yields a relatively high diffusion constant, D. Following the Tombros paper, spin

relaxation mechanisms in graphene on SiO_2 were investigated by taking advantage of the FET behavior [69, 70, 72, 73]. Control over the back gate allows for the carrier density in graphene to be tuned. At higher carrier concentrations, the conductivity increases. The conductivity, σ is directly related to the diffusion constant, D, through the Einstein relation,

$$D = \frac{\sigma}{e^2 \nu} \tag{1.5}$$

where e is the electron charge and ν is the graphene two dimensional DOS. Further, D is directly related to momentum scattering time. Therefore, by simply sweeping the back gate it is possible to realize different charge scattering conditions in the graphene layer. Measuring the spin lifetime at different gate voltages allows for momentum scattering to be compared with what happens in the spin properties of the graphene. Indeed, as shown in Fig. 1.12, several experiments have investigated the relationship between the spin lifetime and the diffusion constant using the FET properties of graphene [69, 70, 72]. The data of Han [72] and Popinciuc [69] clearly demonstrate a linear relationship between τ_s and D, while the data of Jozsa [70] indicates a sublinear dependence of τ_s on D. Regardless, the FET technique clearly demonstrates a positive correlation between the spin lifetime and the momentum scattering.

There are two mechanisms for spin relaxation that are thought to be important for graphene [75, 72, 83, 84, 85, 86, 87, 88, 70, 69, 89]. They are the Elliot-Yafet (EY) [90, 91] and D'yakonov-Perel (DP) mechanisms [92]. The EY mechanism can be understood in terms of a finite probability for spin-flip scattering due to the presence of some scattering source

[90, 91, 20]. There are many possible sources of spin relaxation including charged impurity (CI) scatterers [83, 84], Rashba SO coupling due to adatoms [85, 93, 86], ripples [87, 88], and edge effects [84]. For EY, each scattering event will cause momentum scattering and some probability for the spin to flip. Therefore, the more scattering sources that exist in the sample (i.e. increased defects), there will be increased momentum scattering and spin-flip events, which generates a linear relationship between the spin lifetime and the momentum scattering.

The DP mechanism stems from the presence of a spin-orbit field [92, 20] as opposed to relying on spin flipping during a scattering event. In this picture, a spin is continuously precessing due to the spin orbit field and the precession depends on the electron k vector. Such a spin-orbit field tends to cause dephasing of an ensemble spin polarization. Scattering events which do not conserve momentum, cause the spin to precess around a different spin-orbit field axis. As the scattering events are increased and due to the randomness of the momentum scattering process, the spin polarization can be conserved. Thus, the momentum scattering can be related to the spin lifetime by the relation, $\tau_s \propto 1/\tau_p$.

Therefore, the FET experiments discussed above [70, 69, 72], which demonstrate a positive correlation between τ_s and D suggest that the EY mechanism is important for graphene. However, it has been shown by Ochoa et al. [84] that $\tau_s = (E_F)^2\tau_p/(\Delta_{SO})^2$, where E_F is the Fermi level, Δ_{SO} is the spin orbit coupling. τ_p is the momentum scattering time and represents the time between scattering collisions, which is related to the diffusion constant. Thus, there is a fundamental issue with the principle of tuning momentum scattering through the

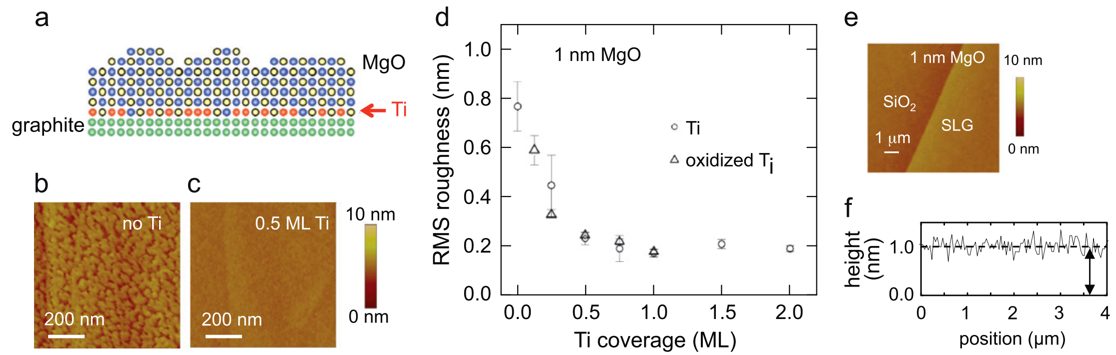

Figure 1.13: Atomically Smooth MgO on Graphene with TiO_2 Seed Layer. Adapted from [25].

back gate voltage and this is because the fermi level is also being modified. Further, several recent theoretical reports have called the FET technique into question and suggest that the DP mechanism should dominate over EY in graphene [88, 89, 84]. The issue of spin relaxation in graphene is taken up in Chapter 9.

A milestone in the field of graphene spintronics was the development of smooth MgO films for tunneling spin injection into SLG [67, 71, 34]. As shown in Fig. 1.13 b), MgO deposited onto graphene results in rough films with many pinholes. On the other hand, by depositing a 0.5 ML Ti seed layer (Fig. 1.13 a)), the subsequent MgO film becomes atomically smooth as shown in the AFM image in Fig. 1.13. It was also demonstrated that the post oxidation of such Ti seed layers also results in atomically smooth MgO with the added advantage of insulating behavior, which is crucial for application in a tunnel barrier. Transport measurements conclusively demonstrated that submololayers of oxidized Ti do not introduce significant charge transfer (doping) or a large decrease in the mobility [94]. Oxide growth on graphene is a challenging field due to graphene's chemically inert nature and low surface en-

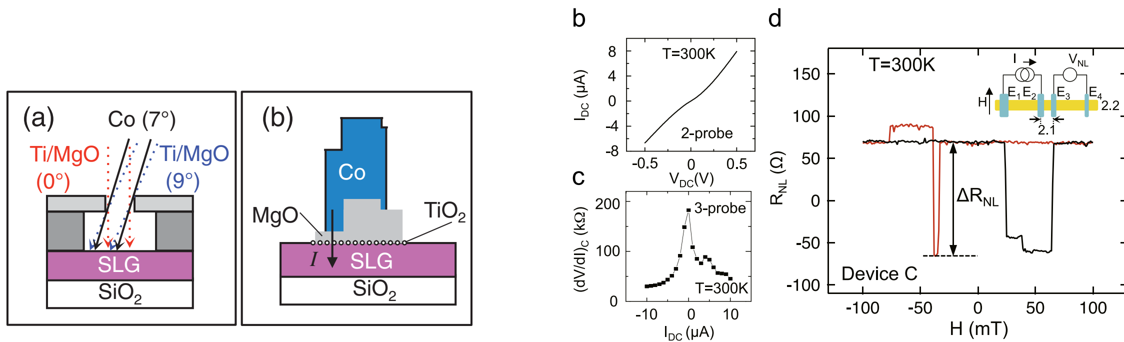

Figure 1.14: Tunneling Spin Injection into SLG at RT. **Left panel**: Adapted from [71]. a) Schematic of the fabrication of high quality tunnel barriers and Co ferromagnetic electrode. Angle evaporation into the undercut using a thick MgO masking layer grown at normal incidence allows for decreased tunneling spin injection area. The final grown structure for the tunnel barrier is shown in b). **Right panel**: b) 2 probe I-V curve using tunneling contacts to graphene. Non-linear I-V is characteristic of non-ohmic behavior. c) 3 terminal contact resistance measurement demonstrates sharp tunneling behavior with a junction resistance at low bias above 100 kΩ. d) Demonstration of non-local spin transport with tunneling spin injection at room temperature. The non-local signal, ΔR_{NL}, is 130 Ω, the largest of any material.

ergy. The issue of oxides on graphene is critical to trying to realize new phenomena through spin based proximity interactions and is taken up in Chapters 4 and 7.

In 2010, Wei Han demonstrated tunneling spin injection into single layer graphene [71]. Fig. 1.14 (left panel) shows the special growth using angle evaporation and the TiO_2 seed layer. In order to achieve high materials quality and control over thicknesses in the sub-monolayer range, MBE is employed as it allows excellent control over materials at the atomic scale. Angle evaporation of a thin MgO layer (0.9 nm) at an angle of 9° into the undercut of the MMA/PMMA bilayer and a second evaporation step of 3 nm MgO at normal incidence creates an MgO tunnel barrier structure that will be dominated by tunneling only in a small junction area near the undercut. Evaporation of the ferromagnetic electrode, in this case Co, into the undercut at 7° ensures that spin will be injected through the thin 0.9 nm MgO

layer but keeps the Co from direct contacting the graphene. The I-V characteristics of such contacts are shown in Fig. 1.14 (right panel) b) and c). Two probe I-V shows non-linear behavior indicating that the contacts are non-ohmic. A three terminal measurement can shed light on the contact resistance of the contacts. Following the schematic in the inset of Fig. 1.14 d), the three terminal configuration consists of passing current from electrode E_2 to E_1, with E_1 acting as electrical ground. A voltage can be measured between E_2 and E_4. Thus, Only the Co wire and tunnel barrier share the current path and voltage detection, which yields a resistance measurement that is sensitive to the contact resistance of E_2. Applying an AC current and sweeping a DC current bias while measuring the AC voltage response using lock-in techniques, is a differential measurement and can be plotted as (dV/dI) in kΩ against the DC current bias, I_{DC}. Fig. 1.14 (right panel) c) displays the dV/dI contact resistance measurement typical for a tunneling contact using the special angle evaporation, TiO_2 seed layer, and MBE growth. Subsequently, devices with such contacts were shown to have the largest non-local magnetoresistance at room temperature of any material, ΔR_{NL}, is 130 Ω. Accordingly, the spin injection efficiency was greatly improved. Previously, typical devices were characterized by $P_J < 0.15$, whereas the tunneling contacts demonstrated $P_J = 0.3$, which is approaching the intrinsic polarization value in Co ($P_F = 0.35$). At low temperatures, both local and non-local spin transport can be observed.

Tunneling, or high resistance contacts, have important implications in spin relaxation measurements [71, 72]. Fig. 1.15 shows the Hanle spin precession measurements performed on devices with ohmic, pinhole, and tunneling contacts. Ohmic and pinhole contacts gener-

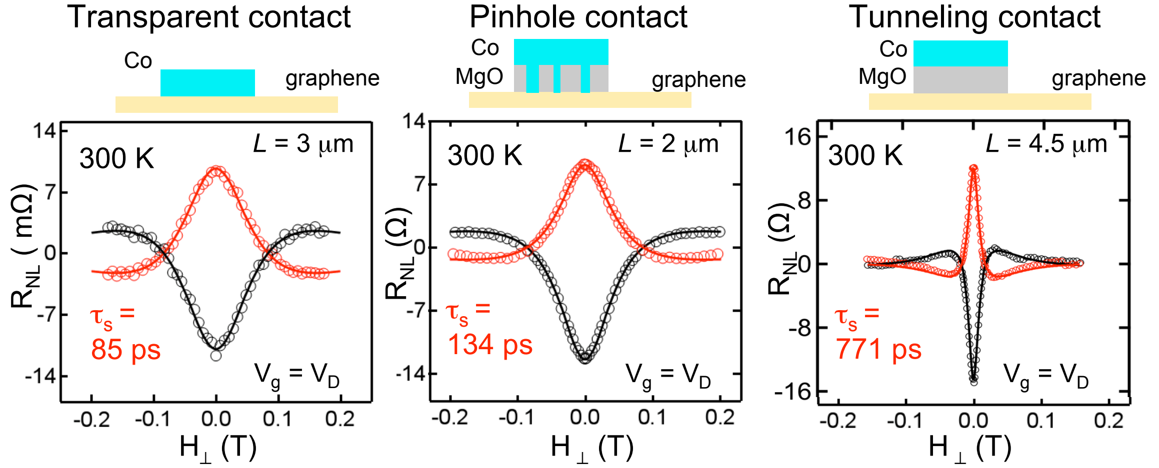

Figure 1.15: Comparison of Hanle Spin Precession Measurements for Tunneling, Ohmic, and Pinhole Contacts to Graphene.

ally yield spin lifetimes in the range of 80 - 200 ps. On the other hand, long spin lifetimes up to 1 ns can be realized with the tunneling contacts developed by Wei Han [71]. This indicates that for ohmic and pinhole contacts that there exists extra contact induced spin relaxation which appears to generate low spin lifetimes in Hanle measurements. For Co directly in contact with the graphene layer, injected spins can readily flow back into the Co contacts due to the lower spin resistance of the ferromagnet compared to the graphene [71, 25]. This is often discussed in terms of an escape time such that the total spin lifetime, τ_{total}, is given by, $(\tau_{total})^{-1} = (\tau_{sf})^{-1} + (\tau_{escape})^{-1}$. There is also the possibility of additions spin-flip scattering underneath the ferromagnetic contact. Insertion of a tunnel barrier eliminates the back flow of spins into the ferromagnet and yields longer spin lifetimes [71, 95] and should also reduce spin-flip scattering due to Co at the interface. There is also the possibility that stray magnetic fields caused by roughness of the bottom Co interface introduces additional dephasing under the contacts. This issue is known to be important for semiconductors [96],

but it's relevance for graphene is unclear and likely depends on the Co/MgO interface. In the case of the TiO_2 seeded MgO, the MgO surface is atomically smooth which should limit the stray field dephasing. Contact induced spin-relaxation is still remains a highly debated topic [71, 72, 34, 25, 97, 76, 77, 80, 82, 95]. Tunneling spin valves as developed by Wei Han [34] are used exclusively for this thesis in chapters Chapters 4 and 7.

1.3 Spin Transport in Candidate Materials

Beyond metals and semimetals, there is extensive interest in understanding spin injection and transport in other candidate materials including semiconductors [15, 19, 20, 98, 99, 100, 101, 102], carbon nanotubes, organics, and oxide interfaces. In particular, semiconductor spintronics has been a highly active field partly due to their importance in modern information processing, which makes them ideal for integrating spintronics with charge based processing. Further, semiconducting materials have demonstrated long spin lifetimes [15, 103, 19, 20]. From a fundamental point of view, semiconducting materials exhibit a wide variety of spin-related properties which motivate new and exciting physics including optical orientation [104], polarization of nuclear spins [104, 105], interfacial states, band bending, and spin-orbit coupling [100]. In particular, GaAs has a direct band gap which allows for optical probes of the spin state [104, 103, 98, 99, 106, 101], has long spin lifetimes despite the presence of a strong nuclear bath and large spin-orbit coupling, and was also the first material to demonstrate the spin hall effect [100]. Further, spin injection can be achieved both

electrically [98, 99, 101, 102] and through orientation of photoexcited carriers due to the optical selection rules [104, 103]. Spin injection into GaAs has been detected through optical probes using the Faraday or Kerr effect [103, 101], electrically [102, 107], and through spin polarized emission using a quantum well structure (spin LED) [98, 99, 108].

Semiconductor spintronics is a rich field for which spin injection and detection have been intensively studied, but control over spin properties during transit remains a difficult problem. While graphene readily exhibits FET behavior due to it's 2D nature, electric field control over spin transport in semiconducting channels is generally discussed in terms of Rashba SO coupling. Indeed, this is the fundamental idea proposed by Datta and Das in 1990 [28]. Since that time there has been an exciting experimental report demonstrating a functioning spin-FET [109]. In this dissertation, it is proposed that control over spin transport can be achieved through exchange coupling between the GaAs transport channel and a ferromagnetic insulator. Use of the ferromagnetic insulator as a gate dielectric could potentially lead to control over either the carrier density at the interface or wavefunction overlap. Thus, it is important to develop FMI/SC materials systems. Few ferromagnetic insulators exist, particularly when compared with the abundance of metallic ferromagnets and oxide antiferromagnets. Here it is proposed to use the ferromagnetic insulator EuO as the gate dielectric. Chapter 3 discusses the properties of EuO and in Chapter 5 the growth of high quality single crystal EuO on GaAs is presented.

2D oxide interfaces are an emerging system of interest for spintronics and spin transport [110, 111, 112, 113]. In 2004, Ohtomo and Hwang realized charge transport with high

mobility at the interface of $LaAlO_3$ and $SrTiO_3$ which has been attributed to the polar catastrophe mechanism [110]. Since then the $LaAlO_3$/$SrTiO_3$ quasi-2D system has demonstrated many interesting phenomena including superconductivity [114, 115]; gate-tunable transport properties including superconductivity [114], mobility [116], confinement [116], and spin-orbit coupling [117, 118]; and the coexistence of magnetism and superconductivity [119]. Low dimensional conductive channels have been realized in other oxide systems including the Mg_xZnO_{1-x}/ZnO [120] and δ-doped $SrTiO_3$ [121, 122]. To date few spin-based studies in these systems exist. There have been predictions for low spin-orbit coupling and long spin lifetimes [123] as well as interesting predictions for a 100% spin-polarized 2DEG at the interface of $LaALO_3$ and EuO [124, 125]. Experimentally, there exists a single study of three terminal Hanle spin injection from Co into localized states inside the $LaAlO_3$ layer of the $LaAlO_3$/$SrTiO_3$ system. Chapter 6 discusses the growth of high quality EuO on TiO_2 perovskite planes which is of direct relevance to the field of spintronics and opens up many possibilities for future spintronics applications in oxide systems.

1.4 Conclusion

Here I present my dissertation on trying to realize novel spin-based phenomena in candidate spintronic materials including graphene, oxide systems, and graphene by taking advantage of the atomic scale control provided by MBE. In Chapter 1, I have introduced the field of spintronics with a focus on the topics that are directly relevant to the chapters that follow.

In particular I have discussed non-local spin transport and Hanle spin precession with a focus on graphene spintronics. I have also introduced GaAs as an important spin transport material and discussed routes towards trying to realize spin manipulation. Spin-based phenomena in low dimensional oxide interfaces is an emerging field with few theoretical and experimental results but shows great promise as a future materials system for studies of spins. Spin-based phenomena and magnetism depend fundamentally on interactions driven by quantum mechanics, leading to fascinating new behavior as the size of designed heterostructures and devices approaches the length scale of the relevant interactions.

To achieve these new and exciting behaviors, it cannot be emphasized enough that atomic scale control over materials synthesis is absolutely critical. Molecular beam epitaxy (MBE) is a materials growth technique which renders growth quality and control on this scale. In Chapter 2, I introduce MBE and discuss basic experimental details as well as thin film characterization techniques and probes of graphene properties through adatom deposition, which will serve as necessary background information for the subsequent chapters. Chapter 3 introduces the ferromagnetic insulator EuO. Chapter 4 discusses spin-based proximity induced phenomena. My work on realizing high quality growth of EuO on GaAs is presented in Chapter 5. Next, I present in Chapter 6, a progressive materials achievement towards realizing interesting spin-based behavior at low dimensional oxide interfaces by templated growth of EuO on TiO_2 perovskite planes. Next, in Chapter 7, I demonstrate epitaxial and atomically smooth growth of the ferromagnetic insulator EuO on HOPG and graphene. After examining the potential for realizing high quality materials growth and integrating EuO onto candidate

spintronics materials, the focus shifts towards investigating novel spin behavior in graphene though submonolayer MBE deposition. In these studies non-local spin valves are used to probe the spin properties of the graphene layers. Chapter 8 presents groundbreaking work on magnetic moment formation in graphene through hydrogen adsorbates and lattice vacancies. Amazingly, these systems exhibit exchange coupling to the conduction electron spins and for the first time, demonstrates exchange fields in graphene. Last, spin relaxation mechanism in graphene are discussed in Chapter 9.

Chapter 2

Molecular Beam Epitaxy

2.1 Introduction to Thin Film MBE

Molecular Beam Epitaxy (MBE) is a materials synthesis technique that allows for excellent control over atomic scale growth. It can be thought of as spray painting atom by atom and can therefore be used to create high quality crystalline films that are easily controlled at the most basic level. Epitaxy is concerned with achieving the ordering of deposited overlayers relative to a crystalline substrate. This technique, developed in the 1960's and 1970's, began by investigating ways of growing semiconducting films for the fast growing electronics industry [126, 127, 128, 129, 130, 131, 132, 133]. One of the key foundational works by Arthur in 1969 investigated the growth of GaAs films and found that flux matching between Ga and As, when the substrate is held at elevated temperatures, does not determine the growth process [129, 126]. In fact, above ~400 °C, As readily desorbs from the GaAs

surface, allowing for a regime in which by simply overpressuring with As, the entire Ga flux would bond and form GaAs. This technique, now called distillation, was one of the first works in the field of MBE, before that term had even been coined and before *in-situ* diffraction techniques had been developed that could monitor the crystal surface during growth. Key achievements in the following time period included graded doping and the development of GaAs/$Al_xGa_{1-x}As$ heterostructures which eventually led to the realization of quantized electronic structures [132]. In particular, such developments were directly responsible for many scientific advances in condensed matter physics and nanoscience including the samples which demonstrated the fractional quantum Hall effect [134, 132, 133].

At the time, the combination of growth process with surface characterization such as Auger spectroscopy and reflection high energy electron diffraction (RHEED), which can investigate thin film properties, was a major breakthrough in the field. Since then, serious advances have been made particularly by the development of atomic scale microscopy techniques such as scanning tunneling microscopy (STM) along with scanning tunneling spectroscopy (STS) and its relatives atomic force microscopy (AFM), conductive tip AFM, and magnetic force microscopy (MFM). These techniques have scaled down the range of study from the thin film layer-by-layer growth to investigating the growth process within a single film from nucleation of islands to adsorbates as well as offering direct information on adsorbates, passivation, defects, and reconstructions. Further, STM is a powerful tool capable of detecting the electronic structure at the atomic scale and evidence of its capability is demonstrated in the 1992 discovery of the quantum corral [135] which was able to directly

image electronic wavefunctions on surfaces with atomic scale spatial resolution. MBE began as an experimental technique to investigate the potential for semiconductor transistors and has since blossomed into a diverse and important tool for oxides, organics, metals, semiconductors. This is especially crucial in light of downward scaling in size of electronic devices calling for the need to engineer and understand novel heterostructures and two dimensional systems. In particular, the field of oxide growth and heterostructures has blossomed in the last 15 years [136, 137, 112]. Understanding growth at the atomic scale in these materials systems and engineered heterostructures is important for many applications including electronics, spintronics, opto-electronics, plasmonics, chemical self-assembly, and the integration of these diverse fields.

2.2 MBE Basics

2.2.1 Introduction to Vacuum Chambers

Molecular Beam Epitaxy relies on several key ideas: Ultra high vacuum (UHV), vapor phase 'beams' of material to deposit, a substrate mount capable of heating, and *in-situ* characterization techniques. UHV refers to pressures less than 1×10^{-9} Torr. MBE is mainly concerned with realizing epitaxial growth of ordered films on top of crystalline substrates. A typical MBE system is shown in Fig. 2.1. A standard MBE system should consist of three separate chambers, two of which should be considered UHV. The 'main chamber' contains the growth evaporators, gas sources, mechanical shutters to block the beams, substrate

mount ('manipulator') capable of positioning the sample and heating the substrate. The substrate should be able to face the evaporators and rotate (90 ° or 180 °) for sample transfer. The main chamber in the Kawakami group also has a cryo-panel behind the manipulator to allow for the beams to condense. Also, the chamber has a deposition monitor mounted on a UHV linear stage that can be placed in front of the sample to take the deposition rate of the evaporated material. Lastly, the main chamber is equipped with a characterization tool capable of monitoring the growth in real time such as RHEED. An adjacent chamber, sometimes called the buffer, characterization, or analysis chamber, exists to isolate the main chamber from the 'load lock' as well as house any desired surface analysis techniques such as Auger electron spectroscopy (AES), low energy electron diffraction (LEED), μLEED, x-ray photoemission spectroscopy (XPS), and possibly x-ray diffraction (XRD) or angle-resolved photoemission spectroscopy (ARPES). Also, the buffer chamber may be equipped with a heater for degassing of sample holders and substrates, and possibly a sample storage stage. The buffer chamber should be UHV or nearly UHV. Lastly, the load lock is a high vacuum system capable of pumping to 1×10^{-8} Torr for which samples can be easily loaded or removed by venting the chamber. When pumped down, the load lock should be well evacuated to minimize the introduction of water vapor and other undesirable residual gases to the buffer chamber, which could then subsequently enter the main growth chamber. Important companies for UHV related parts and equipment are: MDC vacuum, Kurt J Lesker, Thermionics, Nor-Cal Products, Gamma Vacuum, Varian, Pfeiffer (Germany), VST, Heat Wave Labs, Alfa Aesar, American Elements, HEFA Rare Earth (China, Canada), Lakeshore, Omega, Hosi-

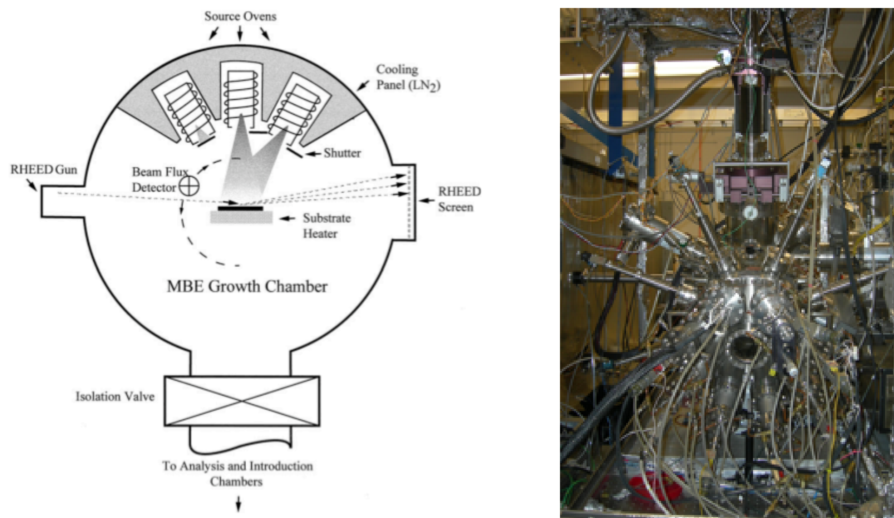

Figure 2.1: Typical MBE Chambers. a) Schematic of a typical MBE chamber. Adapted from [126]. b) The MBE chamber in the Kawakami group as viewed from the back where the evaporator cells are located.

trad (Netherlands), UHV Design Ltd., Advanced Research Systems, Admat Inc., ESPI, New Metals and Chemicals Ltd. (UK), Reade, Goodfellow, Thermo Shield, McAllister, Ferrovac (Switzerland) , MBE-Komponenten GmbH (Germany), Infinicon, œrlikon Leybold (Germany), Omicron (Germany), Tectra (Germany), Staib Instruments, Momentive, Kyocera, MPF Products, Swagelok, Faztek, Grainger, and McMaster-Carr.

2.2.2 Vacuum Basics

An MBE chamber consists of a stainless steel enclosed space of varying size, usually between roughly 1 ft. and 5 ft. in diameter for standard research applications. Our two main chambers have been custom designed for particular capabilities and then manufactured by Thermionics or MDC Vacuum. Here I discuss vacuum chamber basics that are relevant

for the Kawakami group main chamber where chamber parts and materials must be able to handle moderate temperatures and oxygen environments ($P_{O_2} < 5 \times 10^{-7}$ Torr). In regards to materials that are generally used for building of chamber parts, it is recommended that only stainless steel (SS), tantalum, molybdenum, titanium, and ceramics are used for building UHV grade parts. Ta, Moly, and Ti should be of relatively high quality. While aluminum is easy to machine, it readily outgases under vacuum and makes it impossible to reach ideal UHV pressures. Stainless steel works well as chamber walls and most chamber parts but cannot be used for parts that are heated. Standard ceramics are alumina and pBN. Access to the inside of the chamber is achieved through extrusions called ports, which are terminated by a flange. A flange is a connecting location where UHV parts come together and provide access within the chamber and between chambers. Flanges come in many sizes (in inches) and are defined by the outer diameter (OD) of the flange. Some common sizes are: mini (1.33 OD), 2 3/4, 3.33, 4.5, 4.625, 6, 8, 10. On the face of every flange is a knife edge, which is an angled protrusion extending from the face and encircling the through hole of the flange (the part inside the vacuum). A cross section of the knife edge looks like a right triangle that comes to a sharp point. It is very important that the knife edge is never damaged (scraped, scratched, dented, etc...) as the knife edge is critical for achieving UHV grade seals between connecting parts on the chamber. A seal is made between two flanges by inserting a copper gasket of appropriate size. Bolting together the two flanges causes the knife edge on each flange to cut into the soft copper material and create an excellent metal on metal seal. This type of seal is called Con-Flat (CF) or Del-Seal by some companies. CF gasket seals are

significantly better for reaching UHV pressures compared to Viton or rubber O-ring style seals such as Kwik (Quick) Flange (KF). KF is best used on high vacuum (HV) ($\sim 1 \times 10^{-6}$ – $\sim 10 \times 10^{-8}$) systems such as load locks and cryogenic systems.

There are two other important types of seals that are worth mentioning, but are not relevant for UHV chamber building. These are VCR and swagelok and are best used for 'plumbing' of liquids and gases. These serve as excellent ways to pipe in gases or chilled water to parts inside the chamber, but are not integrated onto the chamber ports in such a way that they are responsible for maintaining UHV. Swagelok is a reusable metal on metal seal that does not involve gaskets and is capable of maintaining pressures down to $\sim 1 \times 10^{-6}$. VCR is also a metal on metal seal, but uses a soft aluminum or copper gasket to seal and in principle can hold pressure in the UHV range. Swagelok is reusable and easy to use, and so is most commonly used for fluid plumbing. While VCR is more difficult due to the need to weld VCR male/female adaptors on any piping and the non-reusable nature of gaskets, but offer excellent base pressure which is important for gases and gas lines involved in growth processes.

Chamber base vacuum pressure is of key concern for the quality of a growth process. The rate of residual gas molecules impinging on the sample surface is given by [126],

$$\frac{dn}{dt} = \frac{P}{\sqrt{2\pi m k_B T}} \tag{2.1}$$

where P is the chamber pressure in Torr, m is the atomic mass of the residual gas particles, k_B is Boltzmann's constant, and T is the substrate temperature in K. The unit for dn/dt is cm^{-2}s^{-1}. The quantity dn/dt is directly related to the number of contaminants that could be introduced at the surface and can be thought of as a deposition rate of contaminants. A clean system should have a residual gas pressure that gives an contaminant concentration to be less than 1×10^{-6} or 1 part in a million. If we take the background pressure to be made up of a standard air mixture, we can expect a residual gas mass of roughly 26 g. Taking two cases, room temperature (RT) at 25 °C and an elevated growth temperature of 500 °C, we get $dn/dt = \sim 5 \times 10^{20} \times P$ for RT and $dn/dt = \sim 2 \times 10^{20} \times P$ at 500 °C. Fig. 2.2 a) displays dn/dt vs. chamber pressure for 25 °C and 500 °C. For instance, a typical surface has roughly 10^{14} – 10^{15} atoms cm^{-2}. Therefore, at a vacuum of 10^{-6} Torr, the number of contaminants impinging on the sample surface is roughly equal, while a typical deposition rate would be close to 1 monolayer (ML) per couple of minutes. The comparative rate in $dn/d(ML)$ in units of cm^{-2}ML^{-1} for a typical deposition rate of material is shown on the right axis of Fig. 2.2 a). The contaminant rate is clearly larger than the deposition rate. However, this is really overstating the problem as only a fraction of the rate dn/dt will react with the substrate surface. A very important tool to aid in this problem is called 'bake-out'. Bake-out consists of heating up the entire vacuum chamber above 100 °C and desorbing undesirable contaminants from the chamber walls such as water vapor, acetone, and IPA. Another important technique is to degas the evaporator cells and cell material. After proper bake-out and degassing, the chamber background pressure (even in the range 10^{-10} Torr) is largely due to the vapor pres-

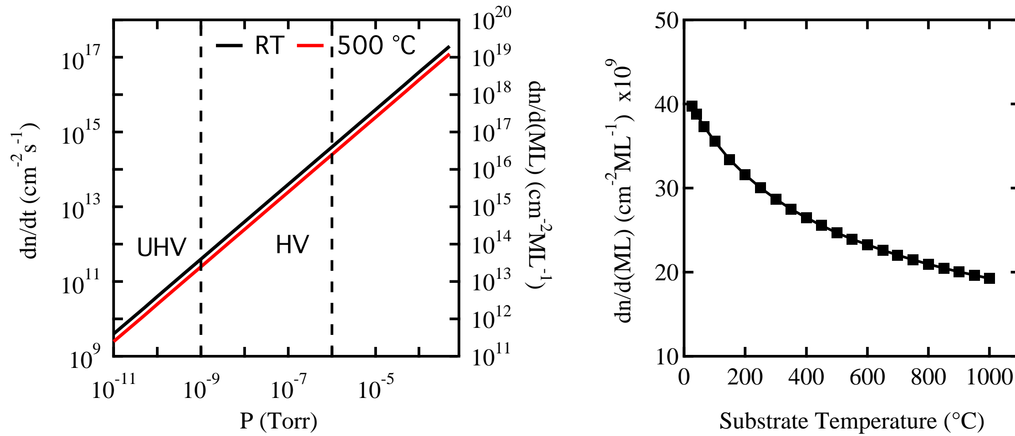

Figure 2.2: Contaminant Deposition Rate Caused by Background Pressure in MBE. a) Contaminant deposition rate, dn/dt, caused by residual gas in a vacuum chamber. b) $dn/d(ML)$ rate as a function of substrate temperature at $P = 1 \times 10^{-10}$ Torr.

sure of the cell materials and not from reactive contaminants. Lastly, Fig. 2.2 b) displays the comparative rate of contaminants to materials deposited, $dn/d(ML)$ as a function of temperature at $P = 1 \times 10^{-10}$ Torr. The contaminant rate decreases some as the temperature is increased, but not as dramatically compared to the effect of base pressure. However, the increase of deposited contaminants with decreasing pressure, is the underlying principle behind the cryo-pump and cryo-panel. Cooling to cryogenic temperatures can increase dn/dt roughly one order of magnitude.

There are several types of pumping systems that operate in different ranges and are necessary for realizing UHV pressures. The most basic pump is the roughing pump which is capable of pumping at high flow (L/s) and is generally only used for pumping down a vented system to less than 1×10^{-3} Torr. A roughing pump is also used in series with a turbo-molecular pump to rough on the turbo, which cannot operate at pressures greater than 1×10^{-3} Torr. A standard roughing pump is the Alcatel oil pump, which is relatively cheap

and easy to maintain. The main (and serious) drawback of an oil pump is the possibility of contaminating the UHV chamber with hydrocarbon contaminants. A better option is the oil-free, mechanical scroll pump. Leybold offers a very good, reliable scroll pump. While a roughing pump can get you part way to achieving high vacuum, the turbo pumping range is between 1×10^{-3} Torr and 1×10^{-9} Torr and thus a combination of a turbo and roughing pump can give you a relative good high vacuum system. Many evaporation deposition chamber rely on such a system. However, for the cleanliness required for UHV, a simple roughing/turbo system is insufficient.

There are three other pumps that are key for realizing UHV and they each have their own specialties. They are: the ion pump, the titanium sublimation pump (TSP), and the cryopump. After a chamber has been evacuated with a roughing/turbo system, an ion pump can reach pressures of 1×10^{-11} Torr. An ion pump consists of a system of metallic plates coated in chemically active material (i.e. titanium) for the application of large electric fields and a uniform DC magnetic field. The system acts as a trap for ions which are attracted to high voltage (HV) points in the pump. The impact of the ions onto the cathode can effectively sputter the chemically active coating (Ti) into the chamber (and onto the chamber walls) and act as a sorption pump. Over time, it can become necessary to regenerate the titanium coating. Some residual gases are difficult to ionize, such as H_2, He, and Ar, are difficult for an ion pump to handle. A chamber should not be vented using Ar or He gas. It is best to use pure N_2 gas, which helps reduce the introduction of water vapor into the system. A titanium sublimation pump is a very useful tool in an MBE chamber, especially for systems in which molecular

Figure 2.3: Pumping Systems Relevant for UHV. a) Oil free scroll pump. b) A Varian turbo pump. c) A Gamma Vacuum ion pump. d) A titanium sublimation pump (TSP).

oxygen is used frequently. A TSP is a simple system that is closely related to the principles of thermal evaporators. A TSP functions based on the heating of filaments connected in series to a large amount of Ti material. When high current is passed through the filament (and the Ti material), the Ti heats up considerable and begins to sublime. Sublimation, a key concept in MBE, occurs when a solid material reaches very high temperature while under high vacuum (or UHV) condition and the temperature needed for evaporation (related to vapor pressure) falls below the melting temperature. In that case, there is a phase transition to the vapor phase in the absence of melting. A TSP evaporates Ti on the chamber walls. The Ti is highly reactive, particularly with hydrogen and oxygen. When residual gas reaches the chamber walls at a rate dn/dt, the gas will react with the Ti and the new reacted material will stick to the chamber walls and the process is irreversible. Lastly, a cryo-panel, when positioned in the line of sight of the evaporation cells but behind the manipulator, can physisorb the residual gas and decrease the amount of gas that could be reflected back towards the evaporators. A variation of the cryo-panel is the cryo-trap pump, which can be placed anywhere on the chamber and operates under the same principles. A cryo-pump is very good at reducing the pressure in the chamber, but can only do so while the pump is kept at liquid

nitrogen temperatures. Since physisiorption is a reversible process, once the pump warms to room temperature, the pressure will increase. All three pumps used in combination increases the vacuum quality and allows for a system that is capable of reaching base pressures in the 1×10^{-12} Torr range. Good companies for pumps are: Leybold for scroll pumps, Varian and Pfeiffer for turbo-molecular pumps, and Gamma Vacuum for ion pumps and TSP's.

2.2.3 The Manipulator

Samples are mounted on 'pockets' (Thermionics platen) or 'paddles' by laying them flat on the surface an using Ta foil strips to cover the corners and hold the samples down. Pockets and paddles and foil should be made of high purity Ta material. The Ta foil strips are spot welded (Ametek power supply) to the pocket. A thermocouple mounted on the pocked face can monitor the temperature very close to the sample. The purpose of a manipulator is to orient the sample in the desired direction, hold the sample in place, allow for easy transfer in and out of the system, enable *in-situ* heating and temperature sensing, and possibly have water cooling or liquid nitrogen cooling. Substrate temperature is extremely important for any growth process. A wide variety of temperatures are achievable for MBE growth from cryogenic (nitrogen) up to above 1200 °C. Depending on the substrate material, the surface properties (energy, reactivity, kinetics, diffusion, etc...) will vary drastically. It is critical to understand the effects of temperature in any growth process. A standard manipulator heater is a simple radiative heating element. Electrical feedthroughs ($\sim$15 Amp) at the top of the manipulator enable an external power supply (Sorensen) to drive current through the heater.

Additional feedthroughs for thermocouples (generally type K) are also located at the top of the manipulator.

The sample positioning is enabled through an XYZ stage on he manipulator. Above the XYZ stage are two rotational platforms, one with internal gears and one with external gears. An external rotational stage allows for sample rotation control so that the sample can face any direction in the chamber. Rotational motion control is used to orient the sample face at any angle relative to the cells. This is particularly important for the angle evaporation used in Co/MgO/TiO_2 tunneling contacts for non-local graphene spin valves as discussed in Chapter 1 and more thoroughly in [34]. Rotation by 90 ° or 180 ° allows for sample transfer. Second, in-plane rotation of the sample can be achieved through a set of internal gears within the chamber that are connected to an external rotation control. Because of the internal gears, the manipulator has a special compartment around surrounding a section which contains internal to external mechanical components. This joint between gears can cause leaks and the chamber will not pump to UHV if this surrounding compartment is not differentially pumped.

In some applications is is desirable to have water (or liquid nitrogen) cooling capability to act as a bath for the sample during growth. It is not always necessary to have cooling water (CW), as a manipulator can function without it, but CW will allow for faster cooling from elevated temperatures. CW is also important for growth on substrates involving resists, such as in the case of growth of Co electrodes for graphene spin valves. Deposited material often lands on the sample surface at elevated temperatures. In order to keep the resist from

hard baking and degassing into the chamber, water cooling can maintain a reasonable sample temperature ($\sim 60°$C).

2.2.4 Evaporators

Evaporators are one of the most important components of the MBE chamber and basically consist of high purity source material and some heating apparatus that causes the source material to evaporate. Due to the low chamber pressure, the mean free path for the vapor molecules/atoms is very long. This means that when material is evaporated, in the time and distance it takes to reach the sample, it does not interact with any residual gas allowing for the deposition of high purity materials. Thus, the vapor is essentially a 'beam' of atoms and hence the name molecular beam epitaxy. In MBE, the rate of deposition is very slow, on the order of $\sim$ Å/min and it can take $\sim$ 2 minutes (roughly) to deposit one monolayer (ML) of material. Therefore, the cleanliness provided by UHV and the slow rate allows for high purity atomic scale control over the materials deposited. We have primarily used thermal evaporators and e-beam evaporators.

Thermal Sources

An example high temperature thermal evaporator is shown in Fig. 2.4. For more information on construction of these homemade cells for both the low temperature and high temperature design see reference [138]. As can be seen in 2.4 a), the functional part of the cell consists of an alumina (or pBN) ceramic crucible surrounded with tungsten (or tantalum)

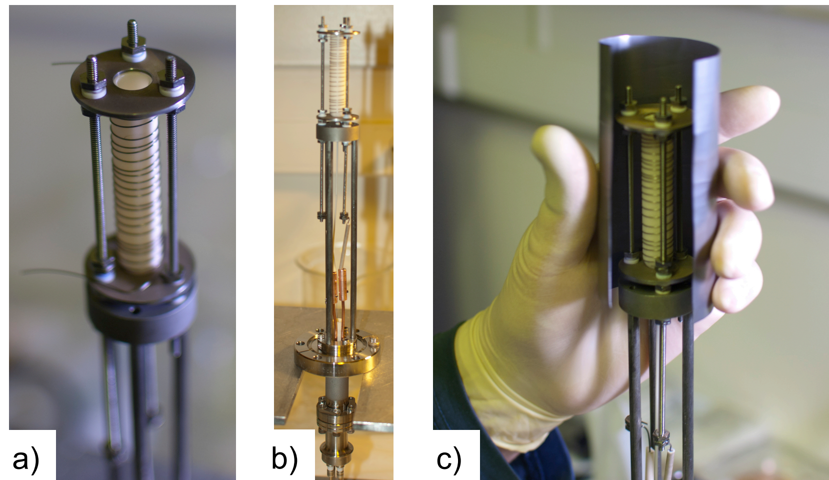

Figure 2.4: A thermal evaporator during construction. This design is for a high temperature cell (i.e. Ni, Au, Co, Fe).

wire. When high current is passed through the wire, I^2R heating causes the filament temperature to increase and emit radiation. This will cause the crucible to heat up along with the source material inside the crucible. At UHV pressures, the source material vapor pressure decreases significantly, which allows for sublimation at achievable temperatures. For instance, at atmospheric pressure, Fe must undergo a phase transition through the liquid phase ($\sim$1500 °C) before turning into a vapor ($\sim$2700 °C). However, in vacuum, the temperature needed to reach the vapor phase decreases as the pressure drops. Therefore, at UHV pressures, Fe can sublime at approximately 900 °C, while the melting point remains fixed at $\sim$1500 °C.

e-beam Sources

There are two kinds of e-beam sources used in this dissertation to evaporate the desired source material. Both rely on the principle of electron bombardment to increase the temperature of the source material for evaporation. The first is called bending magnet e-beam and

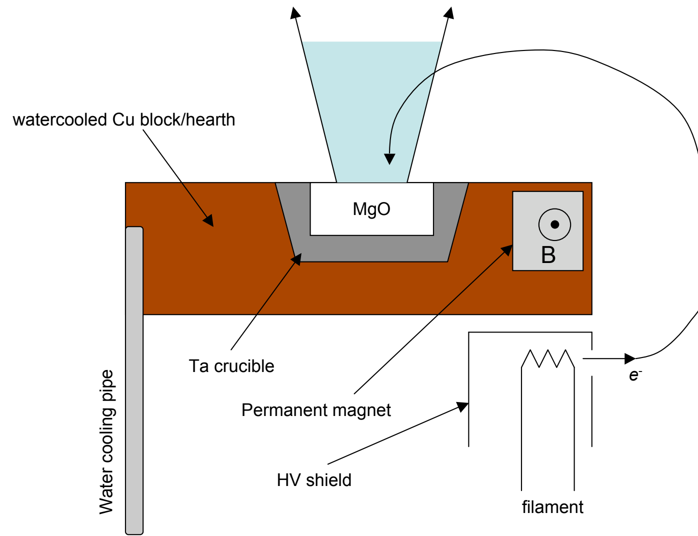

Figure 2.5: Bending Magnet e-beam Evaporator Schematic.

the second is a rod fed, three-terminal e-beam. The bending magnet e-beam source consists of a Cu hearth that is water cooled through a feedthrough connected to a water recycling and heat exchanger system (see Fig. 2.5). The Cu block has a cutout in which a Ta crucible fits semi-loosely. It is not a press fit. For horizontal mounting to the growth chamber, it might be necessary place a thin Ta foil strip over the edge of the crucible to maintain it in place and ensure that the crucible doesn't fall out. For this dissertation, the source material was single crystal MgO(001) cylinder from the MTI corporation. A filament is located below the copper block out of the line of sight from the source MgO material. The filament is heated by I^2R heating in order to emit electrons which are then accelerated outward through a hole in the filament shielding maintained at high voltage. A permanent magnet located within the copper block causes the emitted electrons into a circular trajectory and then impact the source material. Since the electrons have a high kinetic energy, the MgO material heats up

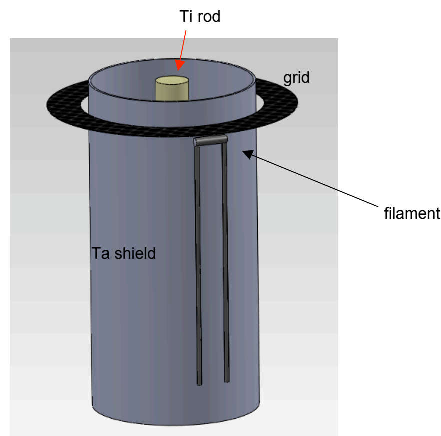

Figure 2.6: e-beam Rod Evaporator Schematic.

and then evaporates. The impact location of the electron beam onto the source material can be tuned by adjusting the high voltage. A commercial MDC bending magnet e-beam cell is used throughout this study to evaporate MgO. This MDC cell operates at 4.8 kV and between 8 and 17 mA emission current. An emission current above 15 mA could risk evaporation of the Ta crucible and samples may be contaminated. This can be confirmed through Auger spectroscopy (see section 2.3.2) in the adjacent buffer chamber.

The e-beam rod design does not take advantage of a magnetic field to direct the electrons onto the source material. Instead, this design employs a ‘grid’ to focus the beam towards the source material which is maintained at high voltage in order to attract the electrons towards it, which then impact at high velocity. The design is displayed as a schematic in Fig. 2.6. The centrally located source material is in the shape of a rod or thick wire, usually about 1/4 inch in diameter or smaller. The rod is placed into a Ta foil tube which provides an equipotential for the rod HV as well as electrical support. This Ta tube is mounted to a structural support

consisting of a central Molybdenum disk and three Molybdenum support legs. The rod is connected to an electrical HV feedthrough, but isolated from the central molybdenum disk and legs. Around the rod, a concentric Ta shield protects the source material from line of sight to the filament. The filament consists of two 0.01 inch diameter Ta wires that are twisted (4x) and attached on each side of the source to 2-56 molybdenum threaded rods and electrically isolated from the rest of the source. The molybdenum threaded rods are then connected to 15 Amp Cu power feedthroughs. The two Ta foil filaments are connected just below a circular Tantalum mesh grid that rings the Ta shield protecting the rod source material. Standard power operation is as follows. First the power is applied to the filament of approximately 6-10 V and 5-8 Amps depending on the resistance of the Ta foil filaments and one side of the filament should be electrically grounded. The grid should then be turned up to approximately 200 V and the rod to 1.5 - 3 kV. Typical emission currents on the grid range from 20 - 80 mA, and 10 - 30 mA for the rod source material. Throughout this dissertation, most growths in which Ti was used, employed this e-beam source. Specifically, this source was used for the growths in Chapter 6 and for the tunneling spin valve contacts in Chapters 8 and 9.

2.3 Surface Characterization Techniques for Thin Films

2.3.1 RHEED

Reflection high energy electron diffraction (RHEED) is one of the primary characterization tools for gaining feedback on MBE growths [139]. RHEED is a structural characterization

tool that probes the crystallinity of the sample structure and can be placed within the growth chamber, which allows for *in-situ* information during any growth process (deposition, annealing, etc...). It is important to note that RHEED is a diffraction technique, which means that the observed RHEED pattern, depends on the quality of the crystallinity of the surface, as opposed to the flatness. For instance, it is possible to have crystalline nano-pillars and obtain a RHEED pattern. On the other hand, it is also conceivable to have a surface that is very smooth, but amorphous, and therefore nor RHEED pattern is obtained. The RHEED gun used in our lab is from Staib Instruments. Figures 2.7 and 2.8 demonstrate the principle of diffraction using the electron beam to generate an image that can be monitored in real time.

An electron gun emits a collimated electron beam at grazing incidence to the sample surface, usually at an angle of $\sim 1^{\circ}$. Thus, the beam samples the surface crystal structure and only penetrates the first few monolayers. RHEED is a diffraction technique and is therefore fundamentally dependent on the 2D surface reciprocal lattice. In the case of a surface square lattice, the reciprocal lattice is also a simple square of dimension $2\pi/a$ and is schematically displayed in Fig. 2.7 a). Since this is a 2D structure in real space, in the reciprocal space, rods extend along the z-axis (out of plane) as depicted in Fig. 2.7 b). The condition for coherent diffraction is met when these rods intersect the Ewald sphere of radius k_0, which is determined by the wavelength of the electron beam. Fig. 2.8 shows a three dimensional schematic of these k-space vectors and their projection onto a photoluminescent phosphorous screen. A CCD camera located behind the screen can record the resulting image on the

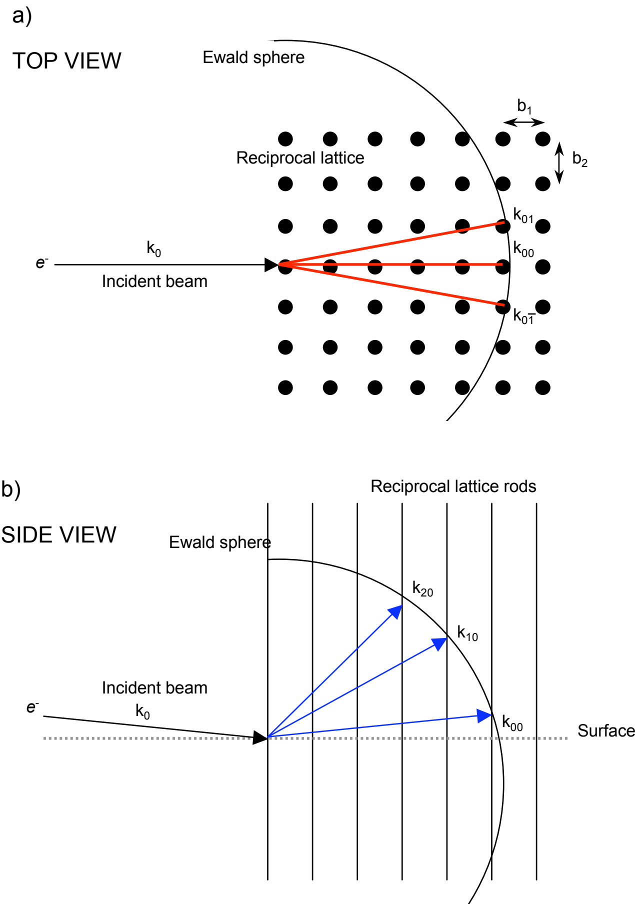

Figure 2.7: Reflection High Energy Electron Diffraction 2D View. a) Top view of surface which is represented as a 2D reciprocal lattice separated by reciprocal lattice constants b_1 and b_2. The Ewald sphere has the diameter of the incoming electron beam momentum wavevector, k_0, which is related to the wavelength of the incoming electron beam. b_2 is the parallel component that determines the scattering angle for the vectors that intersect the Ewald sphere and are labeled k_{00}, k_{01}, and $k_{0\bar{1}}$. b) Side view of the reciprocal lattice rods that intersect the Ewald sphere. Coherent diffraction condition is met at intersecting points of the Ewald sphere and the reciprocal lattice rods. This intersection is determined by the wavelength of electron beam and the reciprocal lattice constant, b_1.

detector screen. By accurately determining the position of the screen from the sample, the location of the diffraction spots/streaks can be related to reciprocal space vectors.

A simple RHEED example can be found by examining the surface of MgO(001) substrate. MgO is a rock salt oxide which is an FCC lattice with a basis of oxygen atoms (see

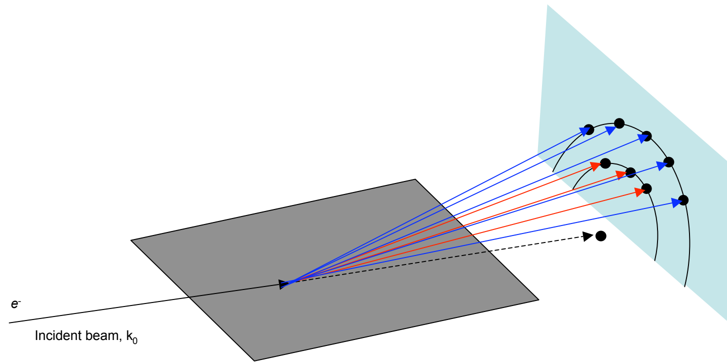

Figure 2.8: Reflection High Energy Electron Diffraction 3D View. Diffraction of the electron beam and projection onto a photoluminescent screen which serves as an imaging detector.

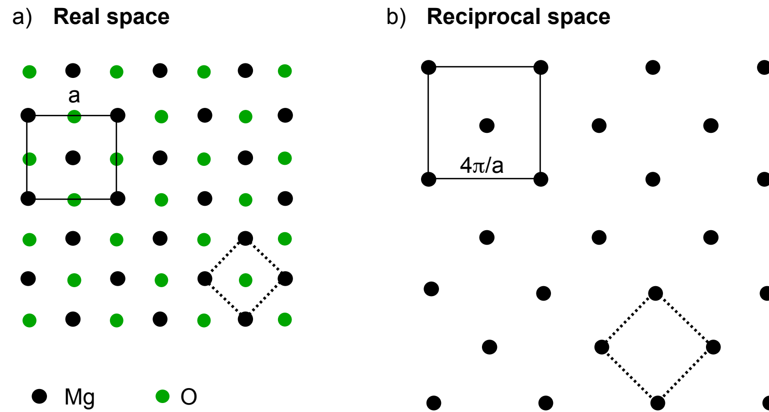

Figure 2.9: Direct and Reciprocal Lattice of the MgO Surface. a) Direct lattice of the surface of MgO(001). b) Reciprocal lattice for the surface of MgO(001).

Fig. 2.9 a). The surface in not a simple square, but a face centered square with lattice constant $a = 4.2$ Å. The primitive unit cell is outlined with dashed lines and has sides of length $\sqrt{2}a/2$. The reciprocal lattice is also a face centered square but with length $4\pi/a$, as shown in Fig. 2.9 b). The primitive cell for the reciprocal lattice is shown with dashed lines and has sides of length $2\sqrt{2}\pi/a$.

An incident electron beam along the [100] or [110] directions sweep out an Ewald sphere of radius k_0, and is shown in Fig. 2.10 a) and 2.10 b), respectively. Along the [100] direc-

tion, the sphere intersects diffraction rods with k-space reciprocal lattice vectors along the direction perpendicular to the beam of length $4\pi/a$ which is twice the MgO k-space length of $2\pi/a$. In the 2D reciprocal surface, there is no rod that exists at the $2\pi/a$ lattice spacing, which leads to what appears to be a missing streak in the MgO(001) [100] RHEED pattern as shown in Fig. 2.10 c). The streaks labeled $0\overline{2}$ and 02 in Fig. 2.10 c) correspond to the reciprocal lattice vectors $k_{0\overline{2}}$ and k_{02} of Fig. 2.10 a). Fig. 2.10 b) shows the [110] direction, for which the sphere intersects diffraction rods with k-space reciprocal lattice vectors along the direction perpendicular to the beam of length $\sqrt{2}2\pi/a$. Therefore, the [110] MgO RHEED pattern (Fig. 2.10 d)) contains the diffraction streaks $\overline{22}$, $\overline{11}$, 11, and 22.

It should be noted here that the Ewald sphere shown in Figs. 2.7, 2.8, and 2.9 are vastly dramatized. Typical e-beams of energies between 10 keV and 30 keV would sweep out an Ewald sphere approximately 50 - 100 times the size of a reciprocal lattice vector [139]. Therefore, the Ewald sphere is more of a plane across the unit cells shown in the figures. Further, there are several important features worth discussing for understanding a realistic experimental RHEED pattern. Much information beyond the lattice spacings can be gained from RHEED patterns. These include layer-by-layer growth from RHEED oscillations, reconstructions, broadening of diffraction streaks due to terracing of a certain length scale, Kikuchi lines, as well as information on morphology in the surface growth such as islanding, twinning, and disorder. In general however, the quality of the crystallinity of a growth is simply determined by the sharpness of the RHEED pattern and whether or not the RHEED spots translate as the substrate rotates. There are three basic RHEED patterns: no image,

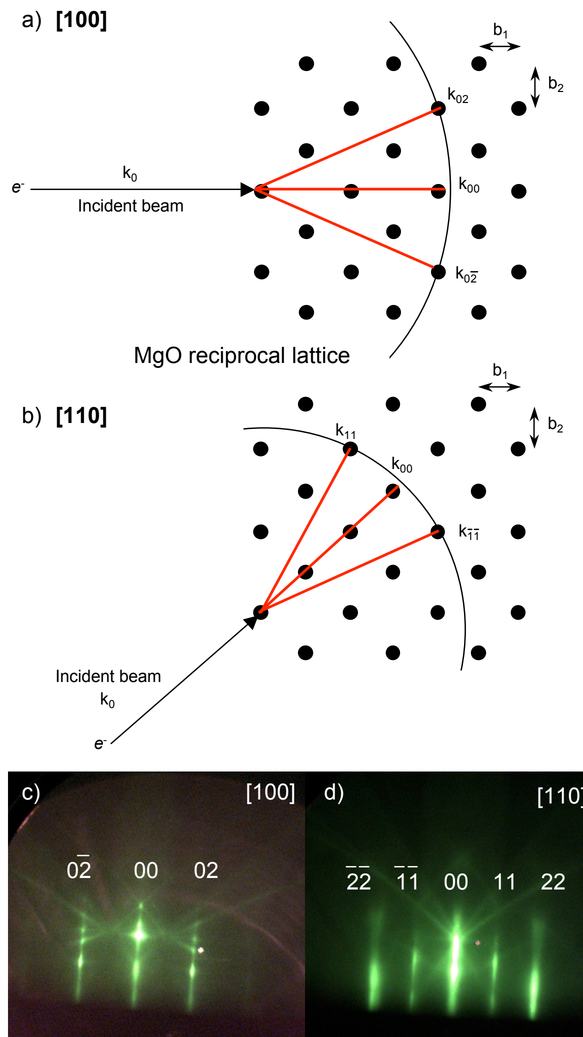

Figure 2.10: RHEED Example: MgO. a) and b) Top view of the reciprocal lattice surface and Ewald sphere for MgO(001) with incident electron beam along [100] and [110], respectively. c) RHEED pattern for MgO(001) along [100] with the appropriate reciprocal lattice diffraction vectors. d) RHEED pattern for MgO(001) along [110] with the appropriate reciprocal lattice diffraction vectors.

rings, and one with well defined spots and streaks. Spots and streaks indicate an ordered crystalline structure, while rings indicate a polycrystalline surface, and no image means that the material is amorphous.

2.3.2 Auger

Auger electron spectroscopy (AES) is a widely used surface science technique [140]. Many MBE systems consist of a three chamber configuration: the main growth chamber, the characterization/analysis chamber, and a load lock. RHEED is almost always placed in the main chamber for *in-situ* feedback on the growth process as it happens. On the other hand, the nearby characterization chamber usually contains a surface analysis tool such as XPS or AES. The Auger tool in our lab doubles as a diffractometer, but uses lower energy electrons compared to RHEED, and therefore this type of diffraction is called low energy electron diffraction (LEED). LEED is a useful technique, but since there is no LEED data presented in this dissertation, it will not be discussed.

AES is a low energy technique in that typical systems are in the energy range below 5 keV. As opposed to RHEED, for which the electron beam grazes the sample across the surface, in Auger, the low energy electrons are directed at normal incidence to the sample surface. The electrons ionize the core level electrons which can then relax and emit an Auger electron. Since the orbitals are element specific, analyzing the emitted electrons provides information about the composition of the surface. For instance, an Auger scan of highly-oriented pyrolitic graphite (HOPG) surface will yield a peak at 272 eV, which is characteristic for carbon. The AES system in the Kawakami group is an omicron SPECTALEED combined LEED and Auger system which uses a LaB_6 filament, has an energy range up to 3 keV, and is located in the buffer chamber with a base pressure of 1×10^{-9} Torr. A typical AES scan of HOPG is shown in Fig. 2.11.

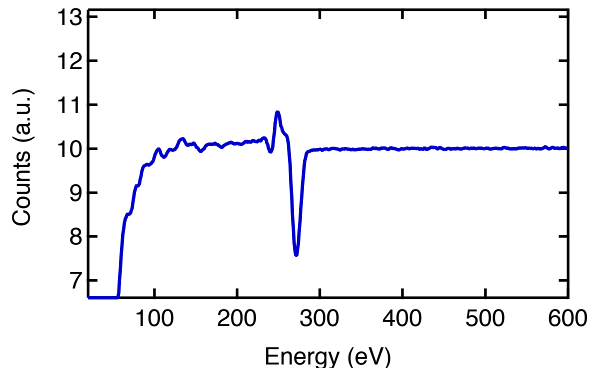

Figure 2.11: Auger electron spectroscopy (AES) example data set of highly oriented pyrolitic graphite (HOPG) with a characteristic peak associated with carbon at 272 eV.

2.4 Adatom Doping of Graphene by MBE

The above sections describe the basics of MBE and several important surface science techniques that are employed in this dissertation. These sections are mostly geared towards the growth and characterization of thin films deposited on relatively large substrates (usually, 1 cm by 1 cm). However, this dissertation is not solely concerned with growth and characterization from a fundamental point of view towards achieving a better understanding of functionally relevant materials for inducing novel-spin based phenomena. While this is of crucial importance, we must also develop ways of investigating the induced behavior in the material of choice. In this dissertation, graphene is employed as a candidate spin transport material due to its low intrinsic spin-orbit coupling, weak hyperfine coupling, and high mobility, which gives graphene excellent potential for realizing long spin lifetimes and long spin diffusion lengths [61, 62, 63, 32, 71]. Perhaps even more important, is the fact that graphene consists of a single atomic layer of sp^2 bonded carbon with p_z-orbitals that extend out of the

plane of the graphene sheet [43]. These p_z orbitals contain one electron each and generate the linear dispersion bands at the K and K' points in the brillouin zone. The transport properties of graphene (spin and charge) are entirely determined by this band of p_z orbitals called the π band. Thus, due to it's two dimensional nature, the transport properties of graphene are extremely sensitive to the local environment. For example, nearby molecules [141, 142, 143], adatoms [51, 144, 94], organics [145, 146, 147], and films [148, 46, 149, 150, 151] will dramatically effect the electronic response of the graphene layer . This is in stark contrast to buried 2D transport materials such as the AlGaAs/GaAs and $LaAlO_3$/$SrTiO_3$ structures, for which the transport layer is not at the surface.

2.4.1 Effect on Charge Transport

Before discussing the effect on charge transport through the careful introduction of defects and dopants by MBE, the nature of graphene on SiO_2 substrate must first be considered. Use of heavily p-doped Si substrate with a 300 nm SiO_2 amorphous overlayer is a nice substrate to use for the placement of graphene (either by mechanical exfoliation or by supported transfer of CVD grown graphene). This is due to the convenient optical visibility of graphene on 300 nm SiO_2 and the ease of using the Si substrate as a global back gate, which allows for the easy tuning from electron or hole type carriers. However, it is known that the SiO_2 surface is not particularly flat and is often littered with local charge impurities [152, 153]. Such disorder can greatly impact the electronic properties of the graphene layer [53]. In 2007, the Yacoby group measured large spatial variations in the charge density at a back gate voltage that

corresponded with the charge neutrality point [152]. These so-called electron-hole puddles are due to the inhomogeneity and doping profile of the underlying SiO_2 substrate. It has been estimated that approximately 5×10^{11} cm^{-2} carriers are doped into the graphene/SiO_2 system [152, 53, 154]. For this reason, the voltage at which the conductivity is minimized is usually referred to as the charge neutrality point (CNP) as opposed to the Dirac point. Near the CNP, the density of states (DOS) is no longer vanishing, but instead approaches a constant value at the CNP. An energy broadening parameter can be employed to effectively smear the intrinsic graphene DOS and yield realistic DOS for graphene on SiO_2 [70]. This is discussed further in Chapter 8. Recently, there has been much effort in trying to replace SiO_2 with atomically flat, insulating, and charge impurity free substrates such as hBN or by suspending the graphene [55, 52, 53, 54]. However, as these techniques are outside the scope of this dissertation, they will not be discussed further.

Here we seek to develop the tools necessary to measure the properties of the graphene layer *in-situ* in an MBE chamber with full deposition capability. Therefore, the devices are fabricated into charge or spin-type field effect transistor (FET) devices. These devices require the use of metal contacts for electrical injection/detection. Thus the role of the contacts on graphene are important to understand. It was reasonably expected [148] that since graphene is a semimetal without a band gap, that there should not be any band bending, Schottky barrier formation, Fermi level pinning, or any other semiconductor-like energy band behavior. Instead, it was suggested, primarily based on differences in the relative work functions between the graphene and metallic contacts, that charge should be transferred in a predictable

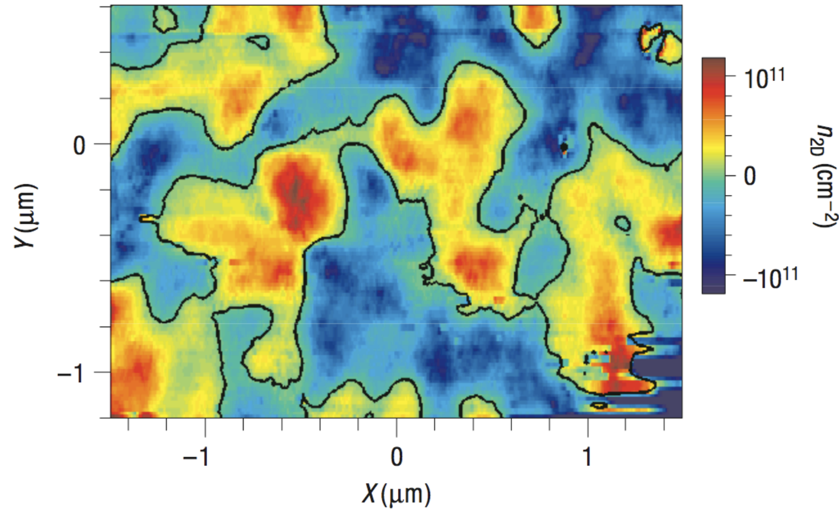

Figure 2.12: Electron-Hole Puddles in Graphene on SiO_2/Si Substrate. Adapted from [152]. Observation of spatial inhomogeneity in in the carrier density in single layer graphene. These puddles were then correlated with electric potential variations in the underlying SiO_2 substrate. The disorder is thought to exist on a scale of approximately 30 nm.

manner [148]. The electron transfer then creates an interfacial dipole that creates an electric field at the location of the contacts as schematically shown in Fig. 2.13. This was verified through several scanning photocurrent experiments which showed significant photocurrent mainly at the location of the metal contacts (see Fig. 2.14) [46, 155, 156, 157]. The large signal at the contacts is attributed to the electric field present which drives a current of photoexcited carriers. Within the graphene channel, the photocurrent response is small due to the weak absorption of graphene and lack of an electric field to sweep carriers away.

There have been several landmark experiments that investigated graphene's sensitivity to the environment. In an experiment from the Manchester group, the electrical properties of a graphene FET device were measured before and after exposure to various gaseous chemicals (NO_2, NH_3, H_2O and CO). The experiment was performed as follows: The device was placed

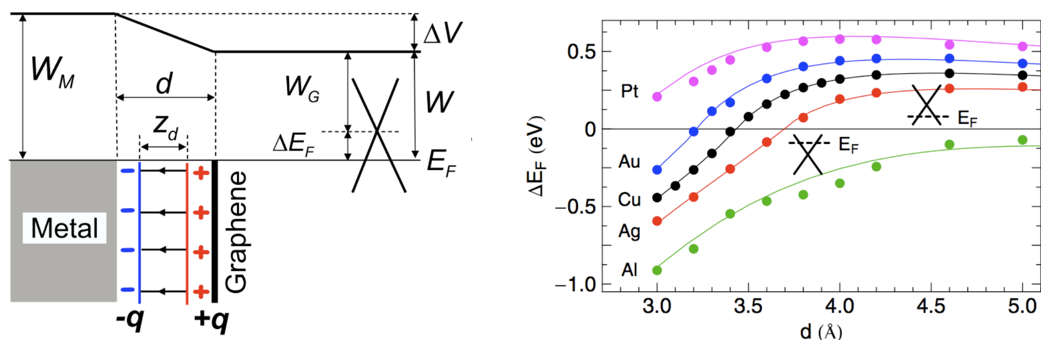

Figure 2.13: Role of the Contacts on Graphene. Adapted from [148] a) Energy band diagrams for metal contacts to graphene. b) Predicted element specific doping to graphene depending on the interfacial dipole and distance.

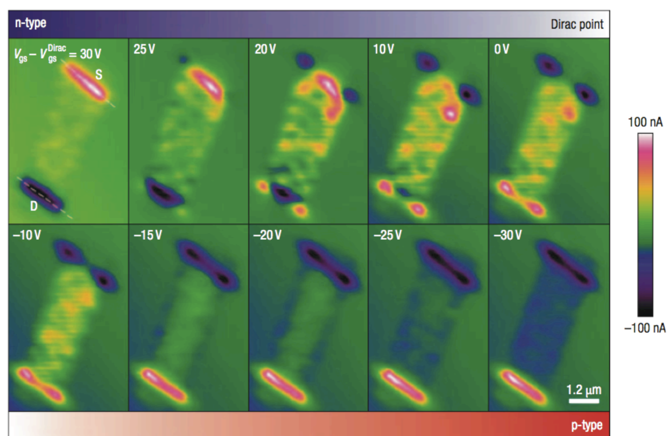

Figure 2.14: Observation of Electric Fields at the Contacts to Graphene Due to Interfacial Dipole and Charge Transfer. Adapted from [46]. Scanning photocurrent microscopy scans at several gate voltages. Color scale indicates the measured photocurrent. Largest signal is observed at opposite electrodes due to the presence of an electric field which sweeps away photoexcited carriers.

in a standard transport measurement cryostat with an attached pumping and flushing line connected to a glass container which held low concentrations of these chemicals diluted with either Nitrogen or Helium. Under exposure to NO_2 and H_2O, devices exhibited p-type shifts in the Fermi level, while NH_3 and CO demonstrated n-type doping. In all cases the mobility decreased. The experiments also demonstrated a dependence on the concentration

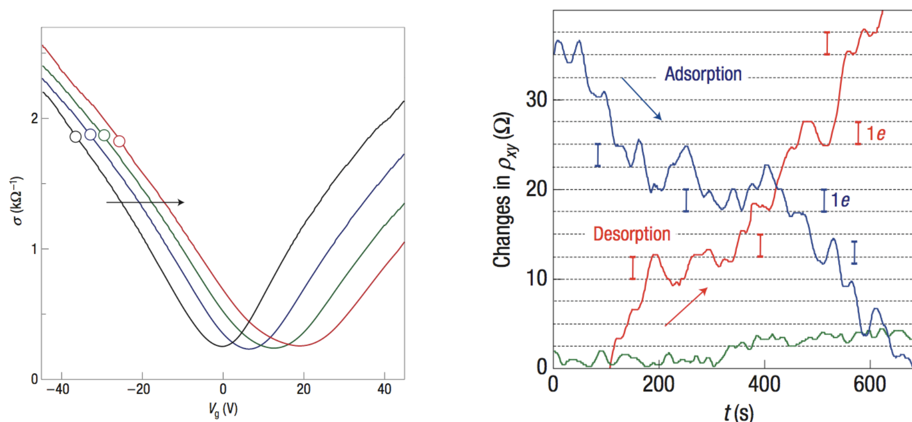

Figure 2.15: Graphene as a Gas Sensor. Adapted from [141] a) Exposure of graphene FET device to NO_2 gas. The gate dependent conductivity curves indicate a shift in the Fermi level towards higher positive gate voltages, which is associated with p-type doping. Second, the gate dependent conductivity curves demonstrate broadening of the region around the charge neutrality point and a decrease in the slope of σ vs. V_G, which indicates a decrease in the mobility. b) NO_2 gas adsorption and desorption curves for graphene demonstrating single electron charge transfers of magnitude $1e^2/h$.

of the gasses and a time dependence for adsorption and desorption. In the adsorption and desorption data the researchers were able to show that graphene FET devices are capable of measuring single electron transfer of charge (see Fig. 2.15 b)).

Soon after this work, the Fuhrer and Ishigami groups investigated the nature of charged impurity scattering in graphene through careful introduction of potassium dopants under UHV conditions [158]. This was the first *in-situ* UHV experiment to look at doping of graphene and had several significant advantages over previous studies because of the high level of control and cleanliness associated with UHV. As highlighted in Fig. 2.16, potassium doping shifts the Fermi level n-type and also induces increased charge impurity scattering which causes the mobility to decrease. Because the doping was performed systematically in a well controlled environment at cryogenic temperatures, it was possible to correlate small

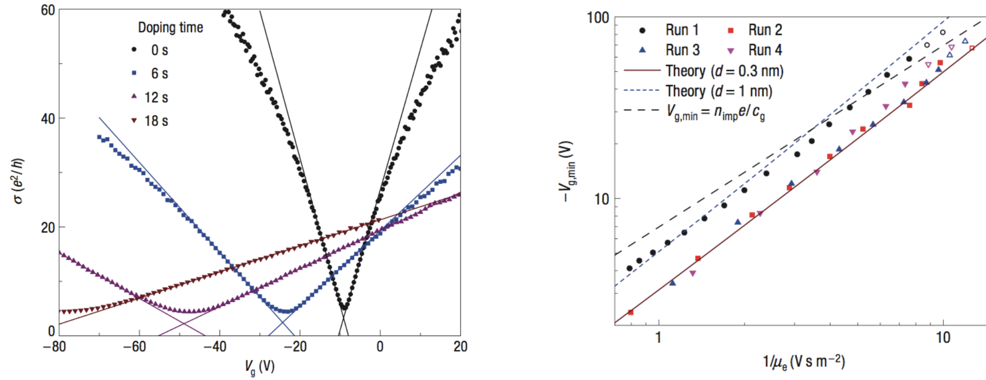

Figure 2.16: Systematic Doping of Graphene with Potassium. Adapted from [158] a) Systematic K doping under UHV conditions demonstrating n-type charge transfer and a decrease in the mobility b) Log plot of the shift in the charge neutrality point, $-V_{CNP}$ vs. the inverse mobility, $1/\mu$. Data indicates a linear relationship between charge doping and momentum scattering suggesting that charge impurity scattering is important for graphene.

changes in the gate voltage shift with changes in the mobility. Under these conditions, the authors were able to show that potassium adsorbs on graphene acts as a point-like charge impurity scattering potential site. In particular, the charge impurity concentration (n_{imp}) was shown to vary inversely with the mobility, following the equation $\mu = \frac{5\times10^{15}\ \mathrm{V^{-1}s^{-1}}}{n_{imp}}$, which agrees with the theory expected for charge impurity scattering [159, 160]. In general, it is currently believed that charge impurity scattering is the dominant mechanism for charge scattering and the limited mobility for graphene devices on SiO_2.

In a related experiment, the Fuhrer and Ishigami groups investigated the irradiation of graphene with Ne^+ ions which is believed to produces single lattice-vacancies when performed at cryogenic temperatures under UHV conditions [161]. Interestingly, introduction of this type of disorder had a very different impact on the graphene behavior compared to charged impurities. Instead, the data indicated strong decrease in the minimum conductivity and much larger changes in the mobility (approximately 4x). However, the authors claims

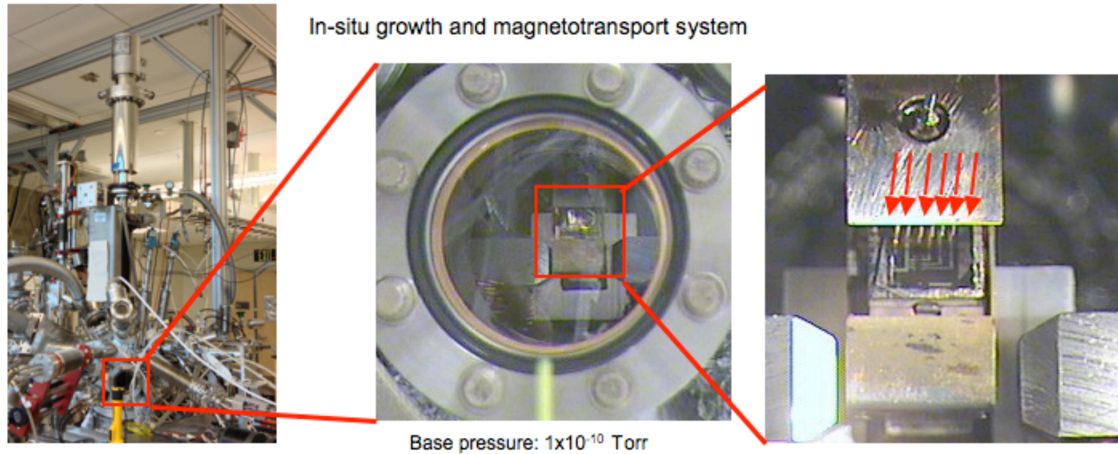

Figure 2.17: The *in-situ* Measurement System.

of potential gap opening and metal-insulator transition have since not been well established. Notably, Raman spectroscopy demonstrated the appearance of a D band peak after exposure to Ne^+, which is associated with the presence of resonant type scattering. Resonant scattering can be understood in terms of intervalley scattering that arises from the creation of what we now call p_z-orbital defects. These defects effectively remove a π electron from the band structure at a localized site in the form of a lattice vacancy or sp^3 hybridization. Other experiments also demonstrated similar resonant scattering through hydrogen [162, 163, 164], fluorination [165, 166], ozone [167], and plasmas [164, 168].

It is the aim of this dissertation to introduce adsorbates and defects on graphene's surface in a highly controlled and systematic manner to investigate the feasibility of inducing interesting spin-based phenomena through proximity effects. Keyu Pi designed and built a special MBE chamber [169] (see Fig. 2.17) equipped with several front facing 2 3/4 inch ports for materials deposition, a quartz crystal monitor, a wedge mask system, several gas sources, an

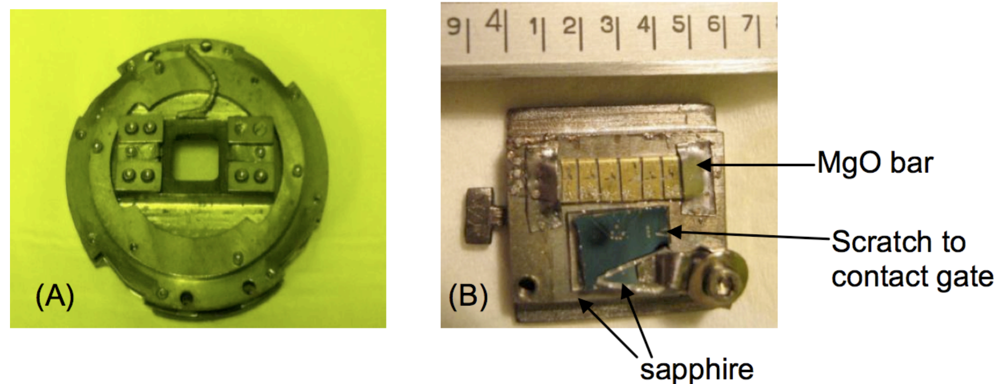

Figure 2.18: Sample Platen and Paddles for *in-situ* Measurement System. a) Thermionics sample platen for transfer of sample paddle in UHV chamber system. b) Sample paddle with graphene device on SiO_2/Si chip held down with Ta clip system and Al_2O_3 spacer for electrical isolation. The top rectangle in the image is the MgO bar with Ti/Au evaporated on the top surface in strips that line up with electrical probes located on the cryostat inside the MBE chamber.

ion gauge, a turbo-mechanical pump, and an ion pump. The base pressure of the system is less than 1×10^{-10} Torr. Also the manipulator is a Thermionics 3-axis XYZ motion stage (with 6 inch Z motion travel) plus an additional rotation stage and is differentially pumped with a roughing/turbo system. The manipulator supports the cryostat and cold finger, which extends into the middle of the chamber. The ports are focused onto the center point of the chamber for deposition onto graphene samples, which are mounted on sample 'paddles'. These paddles (see Fig. 2.18) can be electrically contacted *in-situ* without breaking vacuum. A key and hinge system, which can be manipulated using a Ferrovac wobble stick, can lower electrical probes onto the MgO bar. The MgO bar is connected to electrical contact pads for the graphene devices through Al wirebonds. The wirebonding is performed ex-situ, before loading the sample paddle into the UHV system. Also inside the chamber is a homemade iron core electromagnet capable of fields up to approximately 1200 Oe. Therefore, variable tem-

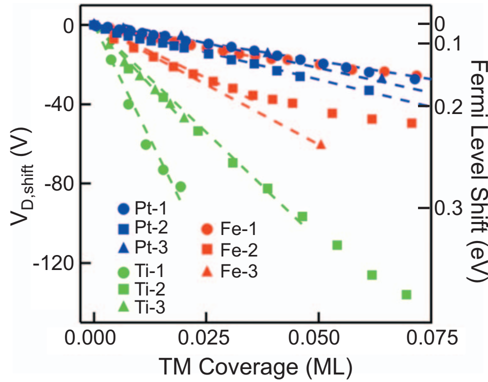

Figure 2.19: Transition Metal Doping of Graphene. Adapted from [51]. Data indicated n-type doping of graphene during systematic deposition of the transition metals titanium, iron, and platinum. Generally, behavior in doping efficiency tracks the relative work functions of the TM materials.

perature magnetotransport measurements can be performed inside the MBE chamber before and after adsorbates and defects are introduced to the graphene samples without ever exposing the sample to air. Device fabrication for graphene four terminal resistance measurements, Hall bars, and non-local spin valves is discussed thoroughly elsewhere [71, 169, 34, 33].

Using the *in-situ* measurement system, Keyu Pi and Kathleen McCreary studied the effect on graphene's electrical properties by transition metal (TM) doping at room temperature [51, 33]. In the UHV system, they systematically introduced Ti, Fe, and Pt in intervals of a few percent of a monolayer and then measured gate dependent resistance curves. Considering only the work functions (WF) of the different materials, it could be reasonably expected that only Ti (WF=4.3 eV) and Fe (WF=4.7eV) should act as electron donors to graphene (WF=4.5 eV), while Pt (WF=5.9 eV) should act as an electron acceptor, and as predicted by Giovannetti [148]. As shown in Fig. 2.19, it was found that all three doped the graphene n-type, with Ti donating approximately 0.1 electrons/Ti adatom, and Pt being the weakest donor of elec-

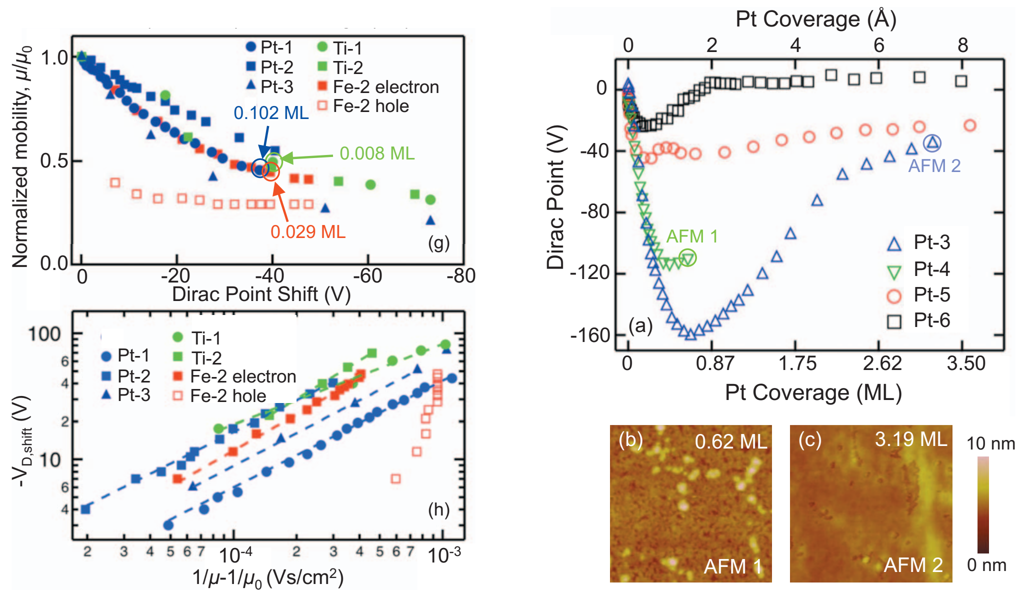

Figure 2.20: Effect on Graphene Mobility and Charge Neutrality Point by TM Doping. Adapted from [51]. **Upper left panel**: average electron and hole mobility normalized to the initial pristine mobility plotted against the shift in the charge neutrality point (Dirac point) for Ti, Fe, and Pt dopants. Generally, the mobility demonstrates a universal curve that depends on Dirac point shift as opposed to the amount of material deposited, as indicated by the circled points which indicates the amount in ML deposited. **Lower left panel**: Plot of the Dirac point shift vs the inverse of the mobility. Power law fits indicate a linear relationship. **Upper right panel**: Effect on the Dirac point as a function of high coverage for Pt doping. At high coverages, the dirac point shifts back towards lower values (less n-type doping), as the films become more uniform. This is due to a decrease in doping efficiency for clusters of metallic material and the formation of an interfacial dipole as predicted theoretically [148]. **Bottom right panel**: AFM of Pt deposited on graphene for the coverages indicated in the upper right panel.

trons by giving approximately 0.02 electrons/Ti adatom, with the electron doping efficiency tracking the relative work functions of the TM material. Interestingly, as shown in Fig. 2.22 (right upper panel), with increased coverage, Pt doping can demonstrate n-type or weakly p-type doping, which is in agreement with the theoretical predictions [148] for the formation of an interfacial dipole. It was also found that the mobility decreased as coverage increased due to the increased charge impurity scattering. More specifically, the mobility was shown

to depend on the shift in the charge neutrality point as opposed to the relative amount of TM coverage (see Fig. 2.22 (left upper panel)). To better understand the nature of the charge impurity potential, the shift in charge neutrality point can be plotted against $1/\mu - 1/\mu_0$, where μ is the average of the electron and hole mobilities and μ_0 is the average electron and hole mobility for pristine graphene (see Fig. 2.22 (left bottom panel). The dashed lines are power law fits of $-V_{\text{Dshift}} \propto (1/\mu - 1/\mu_0)^b$, for which values of $1.2 < b < 1.3$ indicates a $1/r$ scattering potential for point-like scatterers. For the transition metal doping, it was found that the power law dependence is best fit with a power law exponent between 0.64–1.01, which indicates significant clustering for TM deposition at RT. This was confirmed by AFM studies at partial coverage as shown in Fig. 2.22 (bottom right panel). The above analysis of charge transfer vs. momentum scattering as probed by the mobility will be revisited in Chapter 9.

In a related experiment, Kathleen McCreary investigated the low temperature deposition of Au adatoms onto graphene [144, 33]. Theoretically, it had been thought that clustering may play a significant role in the charge transfer behavior of metals on the graphene surface [170]. As shown in figure 2.21 a) and b), Au deposition at cryogenic temperatures resulted in n-type doping of graphene and efficient charge impurity scattering. This is due to the point like scattering potentials created from isolated Au adatoms (Fig. 2.21 c)). Further, upon warming, it was shown that Au tends to form clusters roughly on the size of 50 - 80 nm in size. This decreases the n-type doping and increases the mobility. This can be understood as a crossover regime between point like Au impurities and large clusters which behave partially like an electrode. The doping of the graphene takes place at the edges of the clusters only and

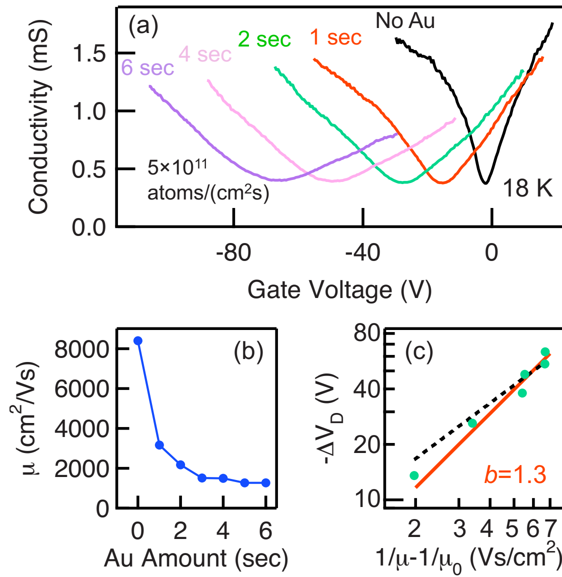

Figure 2.21: Au Doping of Graphene at 18 K.. Adapted from [144]. a) Gate dependent conductivity of graphene for pristine graphene and at several doping coverages of Au deposited at 18 K. b) Change in the mobility due to Au deposition. c) Power law fit to the shift in the Dirac point as a function of $1/\mu$ demonstrating point like behavior of Au adatoms deposited at cryogenic temperatures.

as the size of the clusters increase, the number of Au atoms participating in doping decreases causing the Dirac point to shift to reflect less n-type doping and the mobility to increase.

2.4.2 Effect on Spin Transport

In Chapter 1 section 1.2, several experiments investigating spin injection and transport in graphene were discussed [32, 71, 74, 25, 73, 70, 69]. In these experiments, it was reported that the main mechanism for spin relaxation in graphene was due to the Elliot-Yafet (EY) spin relaxation mechanism [70, 69]. The authors were able to come to this conclusion by taking advantage of the gate tunability of graphene, which allows for control over the carrier concentration in the graphene channel. It is known that the diffusion constant changes

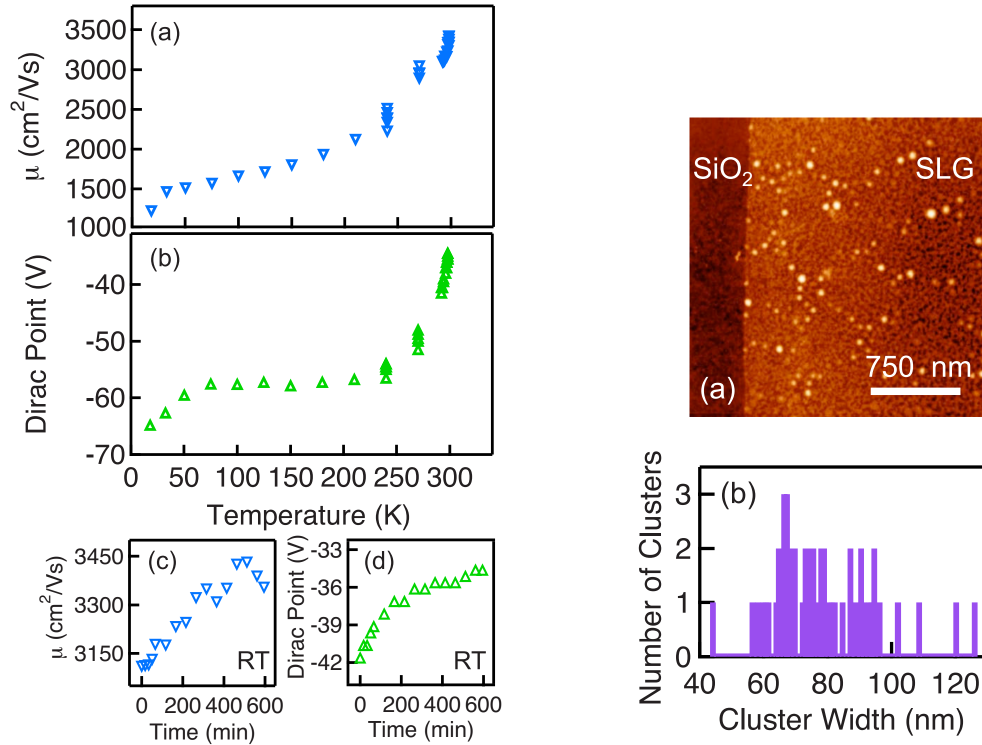

Figure 2.22: Clustering of Au on Graphene. Adapted from [144]. **Left column**: a) Temperature dependence of the graphene mobiilty after Au deposition at 18 K b) Temperature dependence of the Dirac point. c) Time dependence of the mobility at room temperature after Au deposition at cryogenic temperatures. d) Time dependence of the Dirac point at room temperature corresponding to the mobility data in c). **Right column**: a) AFM image of Au clusters on graphene. b) Histogram for the average diameter of Au clusters on graphene.

linearly with increased carrier density, and it was found that the spin lifetime changed linearly as the back gate voltage was tuned to higher carrier density, leading to the conclusion for EY scattering. Therefore, it is reasonably expected that momentum scattering should be very important for spin relaxation in graphene [69]. Since, as discussed above, the dominant source of momentum scattering in graphene is due to the presence of charged impurities [152, 158, 159, 160, 51, 144, 33], CI scattering should be important for spin transport and relaxation in graphene.

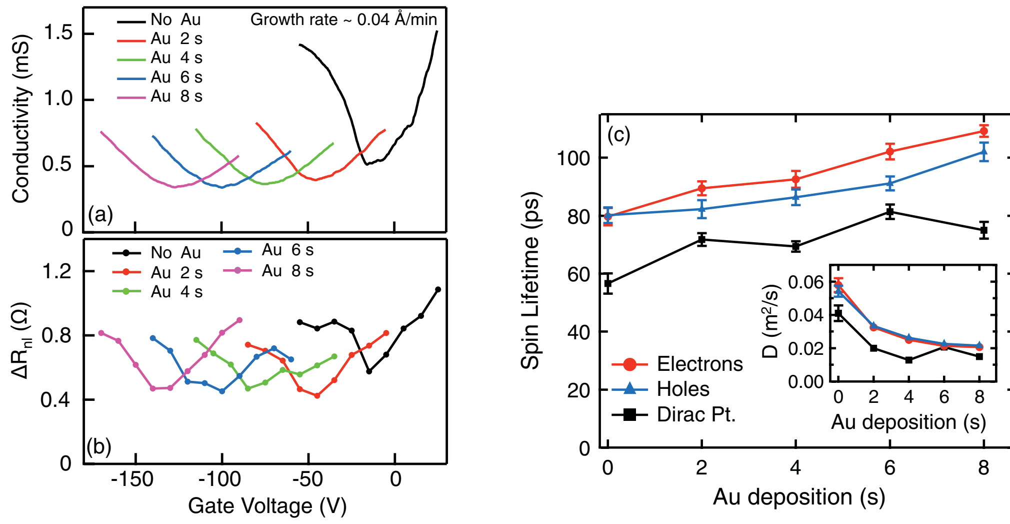

Figure 2.23: Au doping of Graphene Non-local Spin Valves with Ohmic Contacts. Adapted from [171]. a) Gate dependent conductivity curves for several Au doping exposures at 18 K. Reproduces result of [144]. b) Effect on the non-local resistance for several gate voltages and increasing Au coverage. c) Spin lifetime as a function of Au deposition at 18 K. Spin lifetime is obtained by fits to the Hanle equation (eq. 1.2). Inset shows the corresponding diffusion constants obtained by Hanle fitting.

Using the *in-situ* measurement system, Keyu Pi investigated the spin transport and relaxation in non-local graphene spin valves during systematic deposition of Au adatoms at cryogenic temperatures in UHV [171]. Non-local graphene spin valves were fabricated using standard one-step lithographic procedures with Co electrodes. The contacts were specially fabricated using angle evaporation in an MBE chamber and using an MgO masking layer and taking advantage of the MMA/PMMA bilayer undercut. This technique results in Co directly contacted to the graphene layer with but with reduced contact area. These contacts, developed by Wei Han [74, 25, 34], result in robust non-local spin valve devices with a relatively high device yield. Key characteristics of these devices includes the linear relationship between the measured non-local resistance and the graphene channel conductivity. This is

shown explicitly in Fig. 2.23 b) for pristine graphene on SiO_2 and at several different Au depositions. Interestingly, the non-local resistance was not significantly modified by the deposition of Au adatoms despite the large effect on the mobility (see for example Fig. 2.21). This is surprising since the non-local voltage depends strongly on the spin diffusion length (see equation 1.1), which can be related to momentum scattering through the Einstein relation (equation 1.5).

Further, Pi, et al, [171] measured Hanle spin precession curves at several different Au adatom coverages. By fitting the spin precession data to the non-local Hanle equation (eq. 1.2), the spin lifetimes could be obtained. As shown in 2.23 c), the spin lifetime determined by the Hanle fits increased slightly from about 80 ps upwards of 120 ps. While the reason for the increase in spin lifetime was not clear, the fact remained that the spin-lifetime was certainly not decreasing as would be expected if CI scattering was not the dominant spin relaxation mechanism. Further, the lack of a decrease in the spin lifetime is particularly perplexing in light of Au's large atomic weight, which could possibly induce large spin-orbit coupling in the vicinity of the adatom. It was suggested that, while the relationship for EY ($\tau_s \propto D$) is not obeyed in the case of Au adatoms and CI scattering, that this does not necessarily argue against EY as other mechanisms such as phonons, edges, and short range impurity potentials may play a significant role in spin relaxation for non-local spin valves with spin lifetimes in the range of 100 ps. Recently, the progressive work of Wei Han has conclusively demonstrated that ohmic contacts to graphene spin-valves results in increased spin relaxation, which is caused by back flow of spins into the ferromagnetic contacts [71].

Currently, by employing tunneling contacts, spin lifetimes in graphene are roughly an order of magnitude higher than ohmically contacted graphene. The Pi experiment remains the only work, previous to this dissertation, which systematically studies the effects on the spin lifetime in graphene in a UHV environment by adatom deposition as opposed to changing the carrier density by tuning the back gate.

2.5 Conclusions and Outlook

MBE is a powerful technique that, due to the high purity and slow rate of growth, allows for excellent control over materials growth at the atomic scale. MBE is an excellent method for single crystal epitaxial growth of thin films, monolayers, and submonolayers. This thesis seeks to demonstrate the power of MBE in investigating novel-spin based phenomena in candidate spintronics materials through a proximity effect. From an MBE point of view, this thesis is divided into two parts, but each with the same focus. The first discusses high quality MBE growth of thin films of functional ferromagnetic insulators onto interesting spin transport materials for the future potential application of realizing exchange fields and other interesting spin based phenomena induced in the non-magnetic material. In particular, Chapter 5 investigates thin film growth of EuO on GaAs and Chapter 7 studies the integration of EuO onto HOPG and graphene. These are two of the most important materials for spintronics applications due to their long spin lifetimes. Also, Chapter 6 investigates the feasibility of growing ultra thin ferromagnetic EuO onto TiO_2 perovskite planes. This is of direct rele-

vance for the nascent field of spin polarized transport and proximity induced phenomena in the quasi-two dimensional correlated oxide materials.

The second part of the thesis is oriented on investigating spin based behavior induced through proximity effects to adsorbates and defects introduced through submonolayer depositions by MBE. As discussed above, many interesting experiments have taken advantage of graphene's unique surface sensitivity in combination with its tunable Fermi level to examine the effect on charge transport by various gases, adsorbates, and substrates in terms of charge impurity scattering and resonant scattering. This dissertation aims to build on these foundational works and investigate the effect on spin transport of both charge impurity scattering and defects by employing tunneling non-local spin valves. In particular, Chapter 8 investigates the effect of atomic hydrogen and lattice vacancies on the spin transport in the *in-situ* measurement system. Chapter 9 builds on the work of Keyu Pi and investigates the effect on the spin lifetime by systematically introducing charge impurities to non-local spin valves with tunneling contacts which avoids the conductivity mismatch problem.

Chapter 3

The Ferromagnetic Insulator EuO

3.1 Historical Perspective

The first fabrication of EuO samples in 1961 by Matthias was motivated by a standing problem concerning strange magnetic behavior in $EuIr_2$ and Eu_2O_3 [172, 173]. The problem was simple: trivalent Eu should not be magnetic. Yet, in experiments, these materials exhibited ferromagnetism with identical Curie temperatures. It was suggested that trace amounts of EuO could be the reason. After the first synthesis and measurements of EuO [172], an entire class of important materials, the chalcogenides, was born. Since its initial discovery, EuO has demonstrated many remarkable properties [174]. It is the first rare-earth oxide to demonstrate ferromagnetism. It is also characterized by the largest magnetization per unit volume of any oxide [172, 175], fantastically large Faraday rotation [176], and a highly spin split 5d conduction band [174]. However, early samples were typified by oxygen deficiencies leading the

discovery of unusual (interesting) behavior such as a metal-insulator transition (MIT) [177], colossal magnetoresistance (CMR) [178], half-metallic behavior [179], and the anomalous Hall effect [180]. Thereafter, EuO was the subject of intense theoretical and experimental research regarding its electrical, optical, and magnetic properties that is thoroughly reviewed in Mauger and Goddart 1985 [174] and Steeneken's Ph.D. Thesis 2002 [181].

Following an intense research period in which the properties of EuO (and related metals EuO_{1-x} and doped $M_xEu_{1-x}O$) became well understood, EuO evolved into a fundamental example for understanding phenomena in the spinels, other multifunctional oxides, and dilute magnetic semiconductors, whose fields were beginning to gain significant momentum [174]. Interest in EuO began to fade as physicists lost interest and engineers saw no use in a material with an ordering temperature of 69 K. Around the turn of the century, EuO resurfaced for three reasons: 1) spintronics, 2) modern characterization techniques, and 3) advances in materials synthesis. For spintronics, which seeks to realize novel routes for information processing and storage by taking advantage of the electron's spin degree of freedom, insulating EuO offered a route towards realizing electrical control over magnetism and spins in solids. In particular, EuO's large magneto-optic response could be applied to laser-assisted writing of the magnetization. Also, it is thought to be a prime candidate for realizing novel magnetic control over spins and spin transport. This is evident by over 50 related theoretical publications since 2008 on the topic of inducing spin-based phenomena in graphene [182, 183, 184, 185, 186, 187, 188, 189, 190, 191, 192, 193, 194, 195, 196, 197, 198, 199, 200, 201, 202, 203, 204, 205, 206, 207, 208, 209, 210, 211, 212, 213, 214, 215, 216, 217, 218, 219, 220, 221,

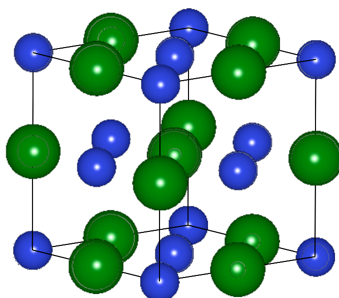

Figure 3.1: Crystal Structure of EuO. EuO crystallizes in the rock-salt structure represented with blue Eu atoms and green Oxygen atoms. Generated using VESTA software ([245]).

222, 223, 224, 225, 226, 227, 228, 229, 230, 231, 232, 233, 234, 235, 236, 237, 238, 239]. Also, after 30 years since EuO fell out of favor, there have been significant advances in synchrotron sources and electron spectroscopy as well as the realization of new surface techniques such as scanning tunneling microscopy (STM). Lastly, the importance of advances in materials synthesis cannot be understated as thin film UHV technology has replaced furnace based bulk crystal growth for achieving technologically relevant materials. The first generation of EuO research relied entirely on production of crystals through thermodynamic reduction processes [172, 174, 181]. Currently, EuO is almost exclusively grown by reactive MBE [181, 240, 241, 242, 243, 244]. In the modern growth era (since 2002 [181]), EuO has been thoroughly re-examined as an interesting system from a growth perspective and as a potential material for spintronics applications. EuO is precluded from industrial applications due to it's low Curie temperature, but from a research point of view, a low T_C is desirable as it allows for easy tuning of the system from the ferromagnetic to paramagnetic state.

3.2 Electrical, Magnetic, and Optical Properties of EuO

EuO has the rock-salt crystal structure (a = 5.14 Å) based on FCC Eu atoms each with an associated oxygen atom that forms an FCC oxygen sublattice as shown in Fig. 3.1. Eu is the 63rd element in the periodic table with an electronic structure of $[Xe]4f^7 5d^0 6s^2$, while oxygen has $1s^2 2s^2 2p^6$. Therefore, when Hund's rules are applied to trivalent (Eu^{3+}) Europium oxide (Eu_2O_3), we obtain a S=6/2 and L=-3, resulting in total angular momentum J=0 and a non-magnetic material. However, in the case of divalent (Eu^{2+}) Europium monoxide, S=7/2, L=0, and J=7/2 is maximized. Fig. 3.2 shows a schematic of the meaningful energy bands for the Eu and O atoms when forming EuO [174]. The first several columns take into account the electron affinity, the Madelung electrostatic lattice energy, and polarization effects [246, 247, 248]. The last column takes into account crystal field splitting of the 5d bands and optical absorption data (see Fig. 3.3) to make final corrections to the energy spacings. The schematic in Fig. 3.2 is useful in understanding the relative contributions to energy scales in EuO, but are essentially an approximation in the atomic limit from tight binding theory. The O 2p shell drops down below the Eu 4f and 5d shells to form the EuO fully occupied valence band due to the ionic contribution of two electrons from the Eu atoms. The Fermi level sits in the middle of the 4f shell, which is half occupied and highly localized. Because of this strong localization of the 4f state (typical for the first occupied atomic n level), it does not contribute to transport despite being a partially filled band.

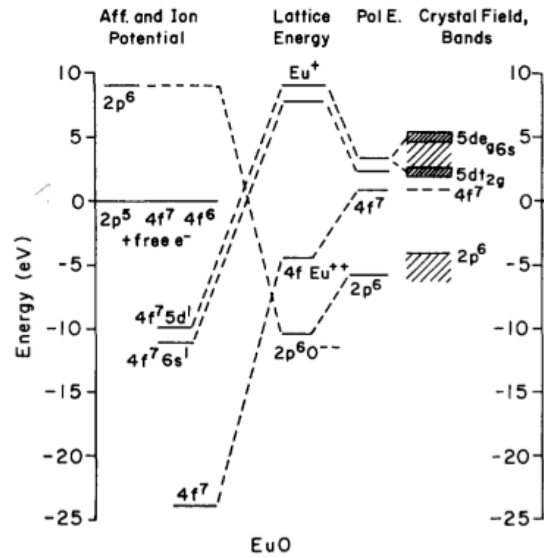

Figure 3.2: Energy Levels of Atomic Orbitals in EuO. Adapted from [174].

The unoccupied 5d band is highly delocalized and is the conduction band. Below the Curie temperature, EuO orders ferromagnetically which breaks time reversal symmetry and causes crystal field splitting which lifts the degeneracy of the 5d band into 5d t_{2g} and 5d e_g. The 'e_g' and 't_{2g}' represent the cubic symmetry for the FCC lattice and the 5d e_g consists of the d_{z^2} and $d_{x^2-y^2}$ orbitals, while the 5d t_{2g} consits of the three d_{xy}, d_{xz}, and d_{yz} orbitals. These 5d states are themselves linear combinations of the more traditionally known solutions to the hydrogen atom with l=2. The d_{z^2} has orbital angular momentum of zero (m_l=0), while the d_{xz}, and d_{yz} are linear combinations of the $m_l = \pm 1$ states, and the $d_{x^2-y^2}$ and d_{xy} states are linear combinations of the $m_l = \pm 2$ states. Another schematic representation of the band alignments and the DOS is shown in 3.4 a), which shows the EuO band gap of 1.1 eV at room temperature. In the ferromagnetic state as T $\rightarrow$ 0 K, the 5d bands are split by an amount Δ_{EX}

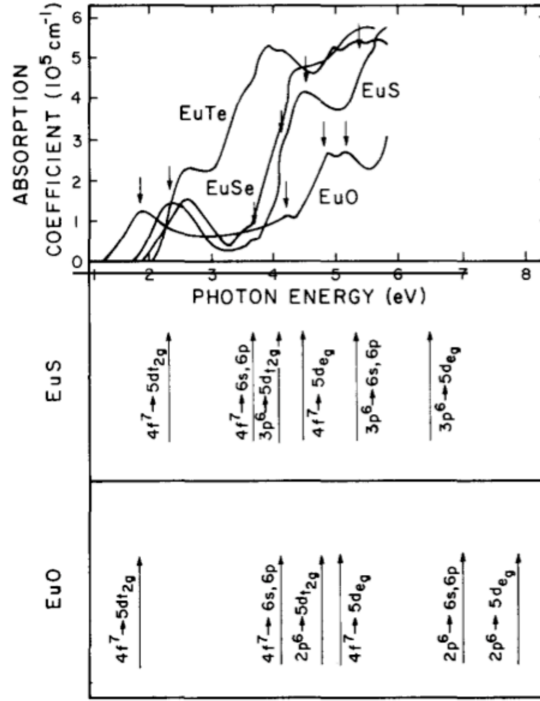

Figure 3.3: Absorption Spectrum of EuO. Adapted from [249].

and the band gap decreases to 0.8 eV as schematically shown in 3.5. Lastly, a more realistic DOS is shown in 3.4 b), calculated using LDA+U theory [250].

Magnetism in 4f rare earth materials obeys Hund's rules very well, while magnetism in the transition metals, which exists based on spins from the 3d-orbitals, tends to be highly complex due to strong hybridization of the spin carrying 3d wavefunctions and orbital quenching [26]. On the other hand, the highly localized 4f shell is essentially isotropic, which is why EuO can be considered as the model example for a perfect Heisenberg ferromagnet, described by the Heisenberg spin-spin Hamiltonian,

$$H_{ex} = -J\vec{s}_i \cdot \vec{s}_j. \tag{3.1}$$

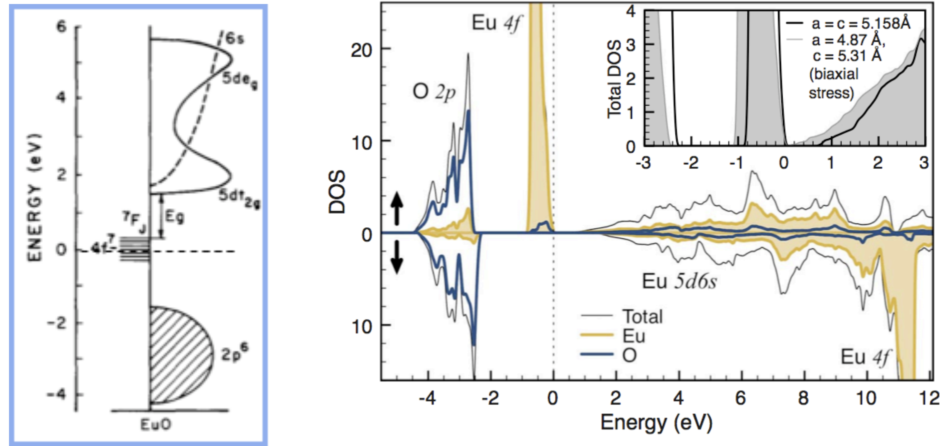

Figure 3.4: Band Levels and Density of States for EuO a) Simple schematic of the band locations and DOS for the band insulator EuO with the Fermi level in the middle of the highly localized 4f shell. Adapted from [174]. b) Detailed spin resolved density of states for EuO. Adapted from [250].

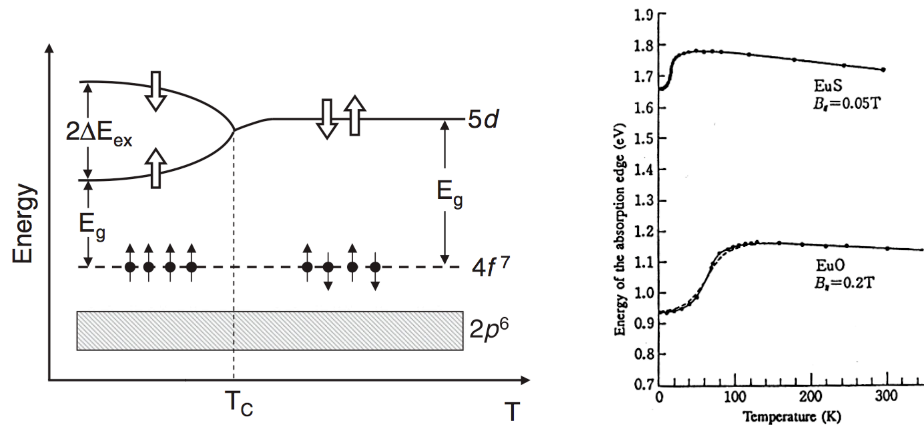

Figure 3.5: a) Temperature Dependence of 5d Band Splitting in EuO. Adapted from [251]. b) Absorption measurements demonstrating 5d band edge shift in EuO. Adapted from [252]

On the surface, this equation looks amazingly simple in explaining ferromagnetic ordering [253, 254, 255, 26] and gives the appearance that magnetism is easily explained by a spin-ordering phenomena, in which spins of electrons interact either parallel or antiparallel depending upon the sign of the scaling factor, J. The term J is known as the exchange integral. However, equation 3.14 is an effective and simplified Hamiltonian that is reduced from the

full Hamiltonian of a solid with 10^{23} interacting electrons in a periodic lattice. In fact, such a system is subject to the Pauli exclusion principle and therefore, since electrons are fermions and cannot be in the same state, their wavefunctions must be antisymmetrized [255]. Also, and importantly, the full Hamiltonian includes the interactions of electrons through their Coulomb interaction. If we take the simple problem of two interacting electrons through a Coulomb potential, we arrive at the standard single electron Hamiltonian that depends only on the interactions of a single electron and the lattice along with the kinetic energy as,

$$H_{single} = KE + V(R_k) \tag{3.2}$$

where $V(R_k)$ denotes the interaction of the electron with an atomic potential at position R_k. Solutions to the single electron Hamiltonian yield the well known s,p,d, and f atomic orbitals. However, taking into account electron-electron interactions, results in an extra interaction term,

$$H_{int} = \frac{e^2}{|r_1 - r_2|} \tag{3.3}$$

which is just the electron-electron coulomb energy for two electrons a distance $|r_1 - r_2|$ away from each other. In the case of a two electron system, there are two electrons at positions labeled $\vec{r}_1$ and $\vec{r}_2$, with two possible states, ψ_i and ψ_j. The two electrons can have their orbital wavefunctions written in terms of symmetric and antisymmetric single particle

wavefunctions,

$$\psi_+ = \psi_i(\vec{r}_1)\psi_j(\vec{r}_2) + \psi_i(\vec{r}_2)\psi_j(\vec{r}_1) \tag{3.4}$$

$$\psi_- = \psi_i(\vec{r}_1)\psi_j(\vec{r}_2) - \psi_i(\vec{r}_2)\psi_j(\vec{r}_1) \tag{3.5}$$

and the spin part is given by,

$$\chi_+ = \chi_{1\uparrow}\chi_{2\uparrow} + \chi_{1\downarrow}\chi_{2\downarrow} \tag{3.6}$$

$$\chi_- = \chi_{1\uparrow}\chi_{2\downarrow} - \chi_{1\downarrow}\chi_{2\uparrow} \tag{3.7}$$

where $\chi_{1\uparrow}$ represents an electron at $\vec{r}_1$ with spin $+1/2$. The total electron wavefunction must comprise both the orbital and spin components and be antisymmetric, leading to

$$\psi_{+,-} = [\psi_i(\vec{r}_1)\psi_j(\vec{r}_2) + \psi_i(\vec{r}_2)\psi_j(\vec{r}_1)]\,[\chi_{1\uparrow}\chi_{2\downarrow} - \chi_{1\downarrow}\chi_{2\uparrow}] = \psi_+\chi_- \tag{3.8}$$

$$\psi_{-,+} = [\psi_i(\vec{r}_1)\psi_j(\vec{r}_2) - \psi_i(\vec{r}_2)\psi_j(\vec{r}_1)]\,[\chi_{1\uparrow}\chi_{2\uparrow} + \chi_{1\downarrow}\chi_{2\downarrow}] = \psi_-\chi_+ \tag{3.9}$$

For this two electron Heitler-London problem, there are two energy eigenvalues determined by examining the quantities $\psi^* H_{total}\psi = \psi^*(H_{single} + H_{int})\psi$. The solutions of which are

$$E_+ = E_{KE} + E_V + E_{e-e} + J_{ij} \tag{3.10}$$

$$E_- = E_{KE} + E_V + E_{e-e} - J_{ij} \tag{3.11}$$

where E_{e-e} and J_{ij} are given by

$$E_{e-e} = \int \int \psi_i^*(\vec{r}_1)\psi_j^*(\vec{r}_2)\frac{e^2}{\vec{r}_1 - \vec{r}_2}\psi_i(\vec{r}_1)\psi_j(\vec{r}_2)dV_1 dV_2 \tag{3.12}$$

$$J_{ij} = \int \int \psi_i^*(\vec{r}_1)\psi_j^*(\vec{r}_2)\frac{e^2}{\vec{r}_1 - \vec{r}_2}\psi_j(\vec{r}_1)\psi_i(\vec{r}_2)dV_1 dV_2 \tag{3.13}$$

and the integral is taken over the spacial volume. The only difference between equations 3.12 and 3.13 is that the states ψ_j and ψ_i are swapped in the second half of the integral. This can be understood as follows. The first term, E_{e-e} represents the electron-electron interaction term between single electron states $\psi_i^*(\vec{r}_1)\psi_i(\vec{r}_1)$ at $\vec{r}_1$ and $\psi_j^*(\vec{r}_2)\psi_j(\vec{r}_2)$ at $\vec{r}_2$. On the other hand, the second term, which is the exchange integral mentioned previously, is so named since it couples the swapped electron states.

The eigenvalue solutions E_+ and E_- are associated with the spin states χ_+ and χ_-, respectively. χ_+ is the "ferromagnetic" state with total spin S = 1/2 + 1/2 = 1, while χ_- is the "anti-ferromagnetic" state with spin S = 1/2 - 1/2 = 0. Therefore, simply based on symmetrization of the wavefunction and Coulomb interactions, there is a forced requirement that the two electron spins must either align or anti-align. The exchange term, which relies fundamentally on the Pauli exclusion principle and Coulomb interactions between electrons allows for the problem to be reduced to the simple form of the exchange Hamiltonian (3.14) which can be ferromagnetic or anti-ferromagnetic depending upon the precise nature of the overlap of the wavefunction and Coulomb term. This examination of the Heitler-London problem serves to demonstrate how exchange leads to magnetism. For real materials, for which the

exchange is much more complex by involving virtual transitions and multiple orbitals, the basic principle of exchange remains, along with the usefulness of the phenomenological Hamiltonian 3.14.

In the case of the 4f magnetic metals, such as Gd, direct exchange via nearest neighbors is negligible due to the localized nature of the 4f shell. Instead, the exchange mechanism is either through double exchange or by exchange using the delocalized conduction electrons to mediate the interaction [256]. However, in the 4f magnetic insulator EuO, the 5d conduction band is unoccupied, which means that free electrons cannot mediate the exchange interactions responsible for magnetism. Exchange in EuO can be thought of to have two main contributions, J_1 and J_2 related to the interactions between nearest neighbors and next nearest neighbors,

$$H_{ex} = -\sum_{nn} J_1 \vec{s}_i \cdot \vec{s}_j - \sum_{nnn} J_2 \vec{s}_i \cdot \vec{s}_k \tag{3.14}$$

as discussed in [174, 257, 258]. Experimentally it has been determined from neutron scattering measurements that $J_1/k_B = +0.606$ K, and $J_2/k_B = +0.119$ K [174, 259], which are in good agreement with the theoretically calculated values by Kasuya [258, 174] of $J_1/k_B = +0.406$ K, and $J_2/k_B = +0.163$ K. It should be noted here, that the calculated values for Heisenberg exchange are an approximation in that they do not employ realistic 5d density of states or momentum-dependent wavefunctions. Nevertheless, a great success of the calculations of Kasuya were the predictions for ferromagnetic J_2 for EuO and antiferromagnetic J_2 for the other europium chalcogenides (EuS, EuSe, and EuTe).

Currently, it is generally thought that there is one majority exchange mechanism for J_1 and several competing exchange mechanisms that contribute to J_2 [258, 174, 181]. Ferromagnetic J_1, which involves nearest neighbor Eu-Eu 4f electrons arises from the following process: an Eu 4f electron at one Eu atom undergoes an excitation (dipole transition) to the delocalized 5d conduction band and experiences exchange with a 4f electron on the nearest Eu atom. Subsequently, the excited electron undergoes a second transition back down to the first Eu 4f atom, thus resulting in an exchange process through dipole transitions, but which have net energy of zero and are therefore called virtual transitions.

On the other hand, J_2, consists of exchange mechanisms involving the next nearest neighbor Eu atoms through the intervening oxygen p orbitals. This type of exchange is commonly called superexchange. There are three important contributions to J_2 for EuO and they are the Kramers-Anderson superexchange (J_{K-A}), the d-f superexchange (J_{d-f}), and the "crossed" exchange term (J_c) [258, 174]. The Kramers-Anderson superexchange involves mediation of 4f-4f next nearest neighbor exchange via oxygen p orbitals and is almost always antiferromagnetic as is true for for the entire class of europium chalcogenides. The value for K-A exchange calculated by Kasuya is $J_{K-A}/k_B = -0.0058$ K. The d-f superexchange mechanism involves transferring an Eu 4f electron through the oxygen anion p state to the next nearest neighbor 5d conduction band where 5d-4f exchange takes place. This is the key mechanism for J_2 in EuO as it was found to be ferromagnetic [258] ($J_{d-f}/k_B = +0.075$ K). In the other EuX materials, the d-f superexchange mechanism is an order of magnitude larger and antiferromagnetic. In those materials, the lattice constant increases with increas-

ing size of the anion atom from S to Te, which causes the nearest neighbor exchange J_1 to decrease and be dominated by the antiferromagnetic superexchange terms J_{K-A}, and primarily, J_{d-f}. Lastly, the crossed exchange term, which arises from interference between the Kramers-Anderson mechanism and the d-f superexchange mechanism, is also ferromagnetic in EuO and is estimated to be $J_c/k_B = +0.95$ K.

More recently, EuO has been theoretically revisited by several authors [260, 261, 262, 263, 264, 265, 250, 266, 267, 268] in order to improve upon the simple exchange model employed by Kasuya. In particular, with the advent of more advanced band calculations such as density functional theory (DFT), theorists have improved upon the simple s-like approximation for modeling the 5d band and 5d-4f exchange [260, 261, 262, 264, 265, 250, 267, 268, 269]. Unfortunately, it is a known problem that DFT local density approximation (LDA) calculations cannot account for the observed band gap between the itinerant 5d band and localized 4f states. This is can be dealt with by taking the 4f states as core levels to obtain realistic 5d states, or by adding in an onsite coulomb (Hubbard-like) energy U (so called LDA (or LSDA) + U models) that can then account for the band gap and provide realistic 5d DOS. This allows for the calculation of J_1 an J_2 exchange constants that are in relatively good agreement with those experimentally determined from neutron scattering experiments [259]. In particular, key issues that have come under debate in recent years concern fundamental understanding of the nature of the exchange interactions, including the role of 4f-2p hybridization [250, 265, 270, 271, 267], momentum dependence of the

5d states [270, 260], and limiting factors in realizing an increase in the Curie temperature [250, 265, 272, 266, 271, 273, 274, 275, 276, 277, 278, 279].

Interestingly, a recent Monte Carlo study of EuO exchange constants [266], determined that the mean field relationship of T_C with J_1 and J_2 is inaccurate, calling into question the entire understanding of the nature of exchange (and superexchange) in EuO as originally proposed by Kasuya in 1970 [258]. In many experiments, the measurable quantity is $J = J_1 + J_2$, and J_1 and J_2 values are determined by the mean field relationship [259, 266],

$$T_C = \frac{2}{3}S(S+1)(12J_1 + 6J_2)/k_B \tag{3.15}$$

which is used to determine the values listed above ($J_1/k_B = +0.606$ K, and $J_2/k_B = +0.119$ K [174, 259]). Subsequent theoretical treatments have mainly worked within this frame work, while improving upon the the Kasuya approximations by including more realistic 5d DOS [260, 261, 262, 264, 265, 250, 267, 268], relativistic effects [261], and hybridization [250, 265, 270, 271, 267]. However, the Monte Carlo method indicated that equation 3.15 underestimates J_1 significantly and calculated $J_1/k_B \sim 1.2$ K, almost double the mean field value. In this picture, for which the experimentally determined $J = J_1 + J_2 = 0.755$ is accepted as valid, the implication is that the J_2 must be antiferromagnetic, as opposed to the prediction of Kasuya. This has recently been supported by an experiment that induces tensile strain in EuO through epitaxial growth on CaF_2. These authors observed an enhancement in the Curie temperature, which is unexpected for ferromagnetic J_2 as shown by Ingle [250],

as well as observing strong hybridization effects between the Eu 4f and O 2p states. Thus, the 'simple' issue of exchange in EuO remains a matter of contentious debate evan after 40 years of intense research. Yet, if we only consider the basic properties of a ferromagnetic isotropic system with J_{total}, EuO can still be considered a model system for understanding Hund's rules and the Heisenberg Hamiltonian.

So far, only the basic properties of EuO have been discussed. However, there are several variations on EuO, including insulating stoichiometric EuO, Eu rich EuO (EuO_{1-x}), and substitutionally doped $X_xEu_{1-x}O$. In XEuO, Eu is replaced with small amounts of another cation, usually Gd, or La [274, 278, 269, 276]. However, experiments have also been performed with X= Ce, Lu, and Fe [280, 281, 282]. Interestingly, these dopants demonstrate an enhanced Curie temperature up to ~ 200 K for Gd doping. Also, such samples are known to exhibit a unique 'double dome' M-T curve. Several factors have been proposed to explain the T_C enhancement and M-T curve shape, including magnetic bound polaron, strain, and enhanced exchange due to donor doping [174, 276, 278]. A key difference in behavior for EuO_{1-x} and substitutionally doped $X_xEu_{1-x}O$ is the deviation from insulating behavior in stoichiometric EuO. In fact, both Eu_{1-x} and XEuO exhibit an electrical phase transition, known as the metal to insulator transition (MIT), around the ferromagnetic ordering temperature and changes in resistance of over 8 orders of magnitude have been observed [174, 181, 269]. Strikingly, as the nature of exchange is a many-body effect that involves electron correlations, large colossal magneto resistance (CMR) is typical for these materials[178]. The field of doped EuO has been a very active research field in the last decade, mainly due to

the recent advances in growth techniques. It is now possible to accurately control the growth process and doping through MBE to obtain stoichiometric, doped, or Eu rich films. However, for the purpose of a magnetic gate dielectric for spintronics applications, it is crucial to maintain the insulating properties of EuO. Thus, this thesis is concerned with achieving stoichiometric films.

Much of the work regarding EuO concerns the bulk properties, but almost all modern day growth produces thin films at the nanometer scale. Thus, it is essential to understand EuO thin films from this perspective. There have been theoretical suggestions of interesting phases such as a surface induced MIT [263]. Otherwise, there is little existing material discussing the potential effects of nanoscaling EuO. Experimentally, there have been conflicting reports as to the magnetic nature of thin EuO films ($<$ 10 nm). It has been shown that at these reduced thicknesses, that the magnetic quality decreases along with a reduction in the Curie temperature [283, 284, 285]. On the other hand, it has also been demonstrated by several other groups that, even down to just a couple unit cells, EuO demonstrates the bulk Curie temperature [243] and is supported by structural investigations by STM [286] and RHEED oscillations [241]. These contradictory results appear to originate from differences in growth methods, conditions, and regimes. This is an important issue since the proximity exchange interaction discussed in this dissertation requires high quality magnetic behavior at the interface, even for ultrathin films. In this dissertation, it is shown that the special growth regime (discussed below), in which stoichiometry is maintained, produces high quality EuO films with bulk T_C values.

3.3 Reactive Molecular Beam Epitaxy (rMBE) of EuO

High quality stoichiometric EuO can be reliably grown thanks to a special growth regime that is called 'distillation and oxygen-limited' or equivalently, 'adsorption-controlled' [181, 269, 240, 241, 242, 243, 244]. Fundamentally, this regime is analogous to the one discussed in Chapter 2 regarding the early growths and development of GaAs films. The Ph.D. dissertation by P. G. Steeneken [181] (L. H. Tjeng group) provided the first experimental guide to growing high quality EuO films in a way that could maintain stoichiometry. In this work, stoichiometric EuO was shown to grow on YSZ, Al_2O_3, and MgO. Growth on YSZ and MgO were shown to grow epitaxially, while growth on Al_2O_3 was polycrystalline. This growth regime centers on the principle of flux distillation. In typical MBE growth, an elemental Eu flux is incident on a substrate causing the growth of a Eu film. However, Eu is a low temperature growth material with an evaporation temperature close to 400 °C under UHV conditions. Therefore, it is possible that if the substrate temperature is raised above the evaporation temperature of Eu, the sticking probability of the Eu flux will be zero. Therefore, the incident material will not be adsorbed onto the surface, but will be re-evaporated (distillation). This can be confirmed by monitoring the *in-situ* RHEED pattern. Next, to commence the growth of EuO, a small amount of oxygen can be introduced to the chamber. As long as the incident Eu flux exceeds the oxygen flux, then stoichiometric EuO will form. If the flux ratio Eu:O favors oxygen content, even slightly, then Eu_2O_3 or Eu_3O_4 will form. This is due to the ther-

modynamic stability of Eu_2O_3 compared to EuO [287]. This growth regime is presented in Fig. 3.6.

Further, Steeneken showed that by simply controlling the substrate temperature (as opposed to the flux ratio), that the oxygen vacancies could be carefully introduced into the sample. The first published paper in a peer reviewed journal that employed the adsorption-controlled regime investigated the exchange splitting in EuO_{1-x} with a strong MIT [269]. These seminal works in the field of EuO growth were not immediately recognized for what they were. In 2008, the Schlom group published a milestone paper on the growth of EuO on well lattice-matched $YAlO_3$ and termed the name for this kind of growth as adsorption-limited. One year later, Sutarto (Tjeng group) published a thorough investigation of the growth of EuO on lattice-matched YSZ [241]. Remarkably, it was shown that EuO can be grown on YSZ *without* introducing oxygen into the chamber. Instead, the Eu flux can steal oxygen from the substrate. This phenomenon is now called substrate-supplied oxidation or substrate-assisted oxidation. Interestingly, the growths on different oxide substrates exhibited noticeable differences including minimum substrate temperature for distillation, crystallinity, ability for substrate supplied oxidation, magnetic behavior, and electrical properties.

However, to this point, all growths taking advantage of this regime, involved oxide substrates. In particular the growth on lattice-matched substrates $YAlO_3$ and YSZ (with substrate-supplied oxidation) had been thoroughly investigated and shown to be of superb quality [240, 241]. On the other hand, growth on MgO had been demonstrated but generally with varying results, which was mainly attributed to the large lattice mismatch [288, 241]. MgO is

an important oxide for spintronics due to it's ubiquitous use as a growth substrate [289] and spin filter tunneling [6, 27, 5]. In this dissertation, Chapter 5, section 5.2 briefly summarizes the first growth experiments in our group that reproduce the work of the Tjeng group in the Sutarto paper [241, 242]. Chapter 5 goes on to present the growth of EuO on GaAs. This is the first demonstration of the growth of high quality stoichiometric EuO on GaAs, and the first demonstration of the adsorption-limited growth regime on any semiconductor.

Through this work it was discovered that the growth quality of EuO on MgO is not reliable. While it is possible to growth single crystal EuO on MgO, two substrates prepared exactly the same way, may result in entirely different films when grown under the same conditions. After a careful and systematic debugging of the growth chamber, it was determined that the this was a real growth mode issue relating to the MgO surface. A general trend was found that smoother MgO films ($>$10 nm e-beam MgO buffer layer), demonstrated the poor growth regime. On the other hand, films grown with either a very thin buffer layer of e-beam MgO ($<$ 10 nm) or directly on the bare MTI corporation MgO substrate, would sometimes result in highly ordered epitaxial films with cube-on-cube orientation. The question of contamination or roughness was not determined and these growth results are unpublished and only of preliminary status. However, this led to the work presented in Chapter 6 which demonstrates high quality growth on MgO through a special TiO_2 electrostatic template which alleviates the growth problems associated with MgO substrate. The results presented in Chapter 6 are directly relevant for the growth of EuO on perovskite planes and opens the door for possible studies of growth on perovskite materials such as $LaAlO_3$ and $SrTiO_3$. This is an important

direction due to the prediction of a spin-polarized 2-D electron gas at the interface of EuO and $LaAlO_3$, due to the polar catastrophe effect [125, 124].

Graphene is a promising spintronics materials as it has the longest spin diffusion length at room temperature and should theoretically have long spin lifetimes. However, oxide growth on graphene is nontrivial due to the low surface energy of sp^2 bonded carbon materials [290]. Chapter 7 presents the integration of EuO onto graphene. The primary aim of this dissertation is to provide original research towards realizing novel spin-based phenomena in a candidate spintronic material via a proximity effect. The growth and integration of EuO onto GaAs, TiO_2 perovskite planes, and graphene provide a major advance in the field toward realizing these goals.

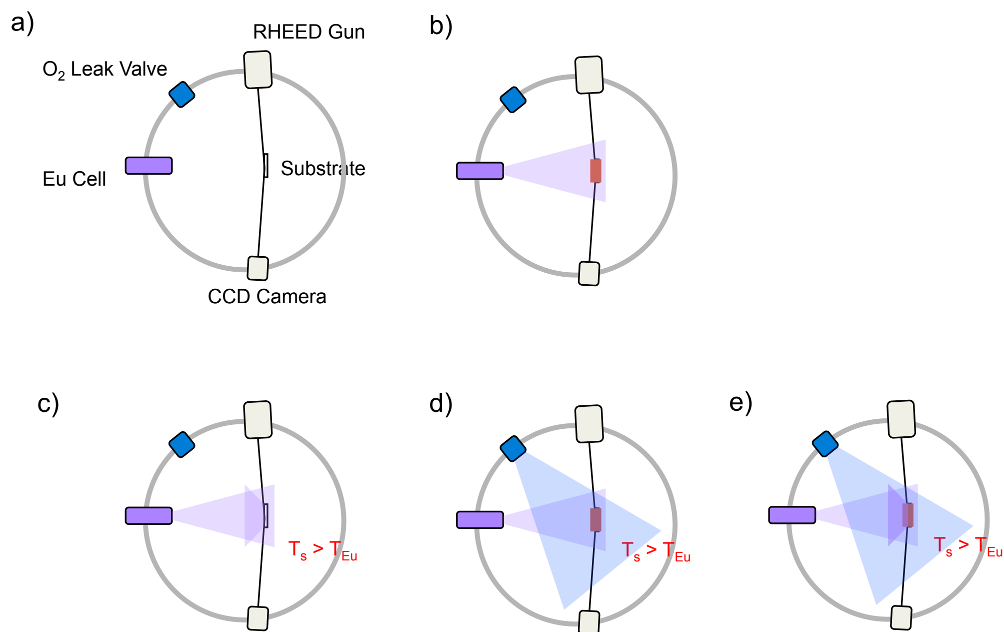

Figure 3.6: Diagram of Adsorption-controlled Growth Regime. a) Simplified schematic of a standard MBE chamber equipped with a Eu effusion cell, O_2 molecular leak valve, RHEED electron gun, and CCD camera for monitoring the RHEED pattern *in-situ*. The black line connecting the RHEED gun to the CCD camera signifies the electron beam path. The substrate is mounted in the center of the chamber facing the Eu source and can be radiatively heated. b) Typical MBE growth when the substrate is maintained at room temperature. The Eu material is sublimed from the source cell and due to the long mean free path in the chamber, the flux extends out as an atomic beam resulting in the growth of a thin Eu film (shown in red). Lower panel (c) - e)): Schematic of adsorption-limited regime. c) Schematic of the Eu flux distillation. When the substrate is maintained at an elevated temperature for which the sticking probability of Eu atoms on the substrate surface is zero, then the Eu flux re-evaporates. This effect is highly substrate and temperature dependent. d) Schematic of the growth of EuO under distillation condition at perfect flux matching, Eu:O 1:1. In this case, all the incident Eu is converted to EuO. However, due to the difficulty of perfect flux matching between Eu and O, combined with the thermodynamic favorability to form Eu_2O_3 for flux ratios where O>Eu, leads to the requirement that the Eu flux always exceed the O flux. However, this does not form Eu rich EuO (EuO_{1-x}) due to the distillation condition as excess Eu is re-evaporated, as is shown in e).

Chapter 4

Spin-Based Proximity Induced Phenomena

4.1 Induced Proximity Effects in Thin Film Systems

4.1.1 Introduction

Control over (nanoscale) magnetism is not a new field and there have been many discoveries particularly in trying to realize electric field control over magnetism [291]. Such achievements include electric field control over interfacial anisotropy [292, 293], exchange bias [294], magnetoresistance [295, 296], spin transport [109], and correlated phase transitions [297]. However, induced magnetism or spin-based phenomena through a proximity effect is also of great interest, but has been more difficult to achieve and study. In 1971 Mersevey and Tedrow [4] demonstrated that when a superconductor is brought into contact

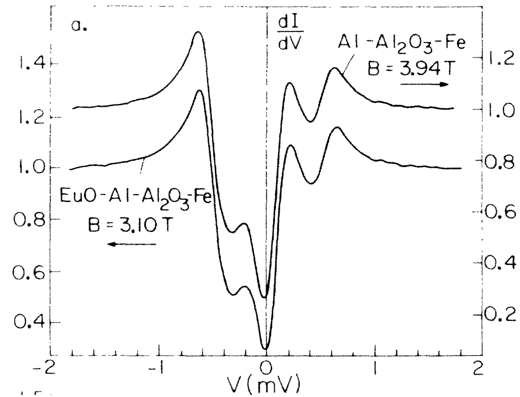

Figure 4.1: Proximity Effect in EuO/Al. Adapted from [298].

with a ferromagnet, that interesting behavior stemming from the ferromagnet can be detected in the superconducting current. In particular, due to the overlap of wavefunctions, an exchange field can be penetrate some small depth into the superconductor. Tedrow went on to demonstrate evidence for a proximity induced magnetic field in the superconducting layer due contact with EuO [298]. This technique has become useful in measuring the spin polarization of the conduction band of the ferromagnetic metal, as was demonstrated with La doped EuO for which a spin polarization close to 100% was measured [179]. Very recently, the issue of proximity induced magnetism has resurfaced in the metallic bilayer systems that are used in inverse spin Hall measurements [299]. In this case, it is suspected that the spin Hall layer (Pd, Pt) is polarized some thickness near the interface, but accurate measurements on the nature of the magnetic interface, importance of growth quality, as well as the effect of such proximity effects on interfacial angular momentum transfer remain open questions.

Here, it is proposed to take advantage of exchange overlap of wavefunctions, an electronic effect, which has the potential for gate tunability, and attempt to induce new behavior

in candidate spin transport materials. In this dissertation two approaches along this theme are investigated. First, the growth of epitaxial ferromagnetic insulators is studied. EuO is the ferromagnetic insulator of choice as it is discussed extensively as a possible material to induce exchange by a proximity effect. Further, EuO behaves as a model isotropic Heisenberg ferromagnet with excellent properties. Since overlap of wavefunctions will require high quality materials at the atomic scale, MBE is used to grow EuO in a special growth regime on several non-magnetic candidate spin transport materials (GaAs, oxide interfaces, graphene).

4.1.2 EuO/GaAs

There exists no theoretical predictions, experiments, or even materials growth studies for the EuO/GaAs system. However, GaAs is a great spin system due to its long spin lifetimes and direct band gap. There are several possible ways to study induced phenomena at the interface. One is to use ultrathin GaAs layers and use electrical measurements. The second involves taking advantage of the optical access provided by the direct band gap [104] and investigate the spin dependent properties at the interface for which there have been significant advances in interfacial optical probes including second harmonic generation [300, 301] and ferromagnetic proximity polarization [105, 302, 303]. In Chapter 5, I demonstrate for the first time, the epitaxial growth of EuO on GaAs.

4.1.3 EuO/$LaAlO_3$

Correlated oxide interfaces have generated new and interesting phenomena not present in the bulk constituent materials [112, 113]. Further, these systems have demonstrated fascinating conducting behavior due to the polar catastrophe effect [304]. In this picture, due to the buildup in electric potential, charge is transferred from the surface to the interface in order to reduce the electric field built-up inside the polar oxide material. The charge transferred to the interface lies in a surface conducting channel provided by the non-polar band insulating material. This was observed for the first time at the $SrTiO_3$/$LaAlO_3$ interface in 2004 [110]. This system can be considered quasi-2D and demonstrates Subnikov de-Haas (SdH) oscillations [110], is confined to a region approximately 2 nm near the interface [305], demonstrates gate tunable confinement and mobility [116], and possibly has two or more conducting channels [306]. Further, there have been reports of gate tunable superconductivity [114] and the coexistence of dilute magnetic moments and superconductivity [119]. From a spin transport point of view, there have been reports for gate tunable spin orbit coupling [118], but few discussions of potential as a spin transport layer. There exists one study of spin injection into this system by three terminal Hanle method [111]. In this technique spins are injected from a Co contact into interfacial states in the $LaAlO_3$ tunnel barrier and detected there. Clear demonstration of spin injection and transport in this system is lacking. There have also been amazing reports of fully 2D interfacial transport in MgZnO/ZnO which has demonstrated SdH oscillations but also the quantized Hall effect (a clear signature of 2D transport) [120], as well as the fractional quantized Hall effect [307]. Further, since interface

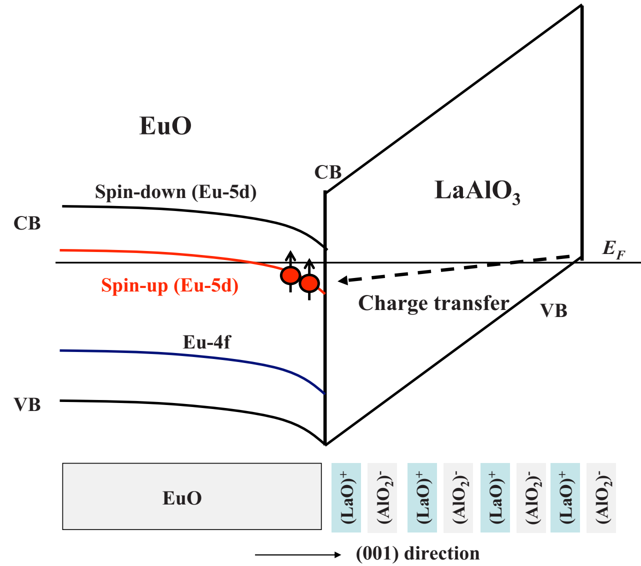

Figure 4.2: Spin Polarized 2DEG at the EuO/LAO_3 Interface. Adapted from [124].

properties in these systems are strongly driven by broken symmetries (inversion, time, gauge) [113], which depends strongly on the materials of choice and correlated behavior, there exists great potential for realizing unique and exciting behavior.

There have been exciting predictions [125, 124] for the formation of a spin-polarized 2D conducting channel at the interface of EuO and $LaAlO_3$ due to the polar catastrophe effect. Because of the electric potential build up in the polar LaO interface, charge is transfered from the surface to the interface and causes band bending in the EuO at the interface. If there is enough band bending, the conduction band can drop below the fermi level which creates a populated conduction channel at the interface as is shown in Fig. 4.2. Because of the strong spin splitting in the EuO 5d conduction band, the conduction channel created at the interface is expected to be strongly spin polarized as predicted by DFT calculations [125, 124]. There has been one experimental work suggesting the possibility of a proximity

effect [308], but more experiments are needed. Chapter 6 presents the high quality epitaxial growth on specially templated TiO_2 planes which are the building blocks of perovskite structures. It is demonstrated that ultrathin EuO films with bulk like T_C can be realized. This is highly promising for potentially realizing spin-polarized 2DEGs as the material structural and magnetic quality can be maintained at the interface.

4.1.4 EuO/Graphene

As briefly mentioned in Chapter 3, there have been many theoretical predictions for induced spin-based phenomena in graphene which require an exchange field in graphene [182, 183, 184, 185, 186, 187, 188, 189, 190, 191, 192, 193, 194, 195, 196, 197, 198, 199, 200, 201, 202, 203, 204, 205, 206, 207, 208, 209, 210, 211, 212, 213, 214, 215, 216, 217, 218, 219, 220, 221, 222, 223, 224, 225, 226, 228, 229, 230, 231, 232, 233, 234, 235, 236, 237, 238, 239]. In 2007, Semenov et al., [210] proposed a variation of the Datta-Das spin transistor. In this scheme (see Fig. 4.3) the method of spin manipulation originally proposed by Datta and Das (Rashba spin-orbit coupling) is replaced with a gate tunable exchange interaction induced through a proximity effect. Subsequently, a simple calculation by Haugen et al., [190] based on the Tedrow experiments with EuO predicted a 5 meV spin splitting induced in the graphene layer through the exchange proximity interaction (EPI). There have since been some interesting device applications including graphene mediated exchange bias, spin torque, and gate tunable magnetoresistance. Despite the extensive interest in this system, there has yet to be any experimental progress in this direction. Part of the reason for this is graphene's

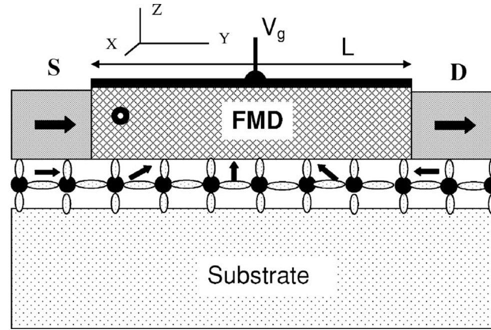

Figure 4.3: Exchange Interaction for Spin Manipulation in a SFET. Adapted from [210].

chemically inert nature, which makes epitaxial oxide growth very difficult. Effective gate dielectrics require pinhole free, relatively flat and uniform oxides on graphene. Further, the EPI also has stringent requirements on the materials quality at the interface. In Chapter 7, I demonstrate epitaxial growth of EuO on graphene and demonstrate that the growth of these films leaves the graphene in good condition.

4.2 Induced Magnetism in Graphene by Dopants and Defects

4.2.1 Introduction to p_z-orbital Defects in Graphene

Magnetism in graphene is an emerging field [309] but difficult to achieve since intrinsic pristine graphene is magnetically uninteresting. This is due to low intrinsic spin-orbit coupling [61, 62, 63], low abundance of nuclear carbon [64], and graphene produced in experiments by CVD and mechanical exfoliation can be single crystal and defect free [310, 48]. It is

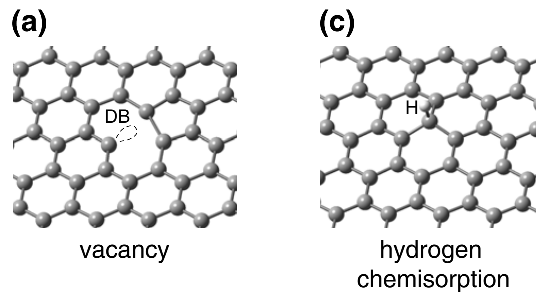

Figure 4.4: Single p_z-orbital Defects in Graphene. Adapted from [309]. a) Single lattice vacancy in graphene. Removal of a carbon atom leaves three σ dangling bonds and removes an electron from the p_z band locally. c) Single hydrogen atom generates sp^3 hybridization which effectively removes an electron from the p_z band locally.

exactly for these reasons that graphene has such great potential as a spin transport layer with long spin lifetimes [32, 71]. However, some interesting spintronics devices and fundamental physics can be realized in magnetic graphene [213, 226, 228, 204, 202, 200, 199, 185]. Two ways in which magnetic graphene can be realized is through proximity to a ferromagnetic insulator [190, 210], as discussed above, or through p_z-orbital defects [309]. Such defects can be chemically and structurally distinct, so long as they effectively remove a p_z-orbital electron from the band structure. Fig. 4.7 displays two scenarios that can create these kind of defects. One is through adsorption of adatoms that cause sp^3 hybridization. Another is through actual lattice vacancies. The vacancy picture is more complicated since there are also remainder dangling bonds in the σ band. However, a general picture for magnetic moment formation through p_z-orbital defects can be understood for both cases.

The creation of magnetic moments by localized defects has been studied extensively by theorists [309]. Localized defects, such as vacancies and sp^3 bonded adsorbates, remove a p_z electron locally which creates a defect state close to the Fermi energy [311, 312]. On-site

coulomb interactions generates spin-splitting of the defect state and is therefore an electron-electron correlated effect. This is a variation of the Hubbard model and has been studied from first principles [313, 314, 315, 316] and from the point of view of mean-field Hubbard exchange [317, 318, 319, 320]. Fig. 4.5 a) and b) presents the calculated spin-resolved DOS for graphene with hydrogen adsorbates and single lattice vacancies, respectively. In the case of p_z-orbital vacancies (Fig. 4.5 a)) there are two clear peaks in the DOS near the Fermi energy on top of the intrinsic graphene band structure for tight binding theory. Notably, the two defect states are spin split in energy, with one state lying above the Fermi energy and the other lying below. Thus, the state is half occupied and has a net spin, $S = 1/2$ and 1 μ_{B} per defect site is expected. The phenomenon can be understood even more generally in terms of Lieb's theorem [321] which states that, for such a two-part (A and B sublattice) lattice with on-site Hubbard exchange, there should be a net spin-moment in the system given by $2S = |N_A - N_B|$ [309, 319]. This connects local defects and p_z-orbital defects with nanostructured graphene such as islands and ribbons with magnetism. In fact, this same physics is the foundation for the prediction of magnetism in specially patterned structures and edge magnetism in graphene nanoribbons [322, 323].

The case of single lattice vacancies in graphene is more complicated as demonstrated in the spin-resolved DOS shown in Fig. 4.5 b). For lattice vacancies the picture of exchange splitting of defect states for the removal of a p_z orbital remains and these states are appropriately labeled in Fig. 4.5 b). However, the removal of a carbon atom to form the vacancy leaves dangling σ bonds which also experience on-site coulomb repulsion [315]. These dan-

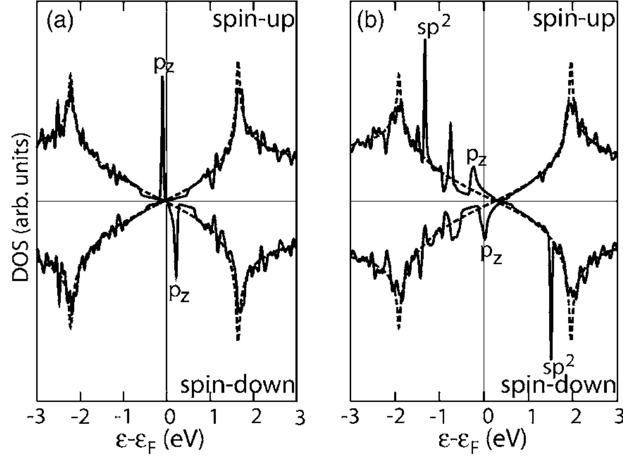

Figure 4.5: Spin-dependent DOS of Graphene with Exchange Split Quasi-localized Defect States. Adapted from [315]. a) DOS for hydrogen induced sp^3 bonding with quasi-localized defect state near the Fermi level that is spin split by on-site exchange interaction. b) DOS for single lattice vacancy showing both the quasi-localized defect state near the Fermi level and the strongly exchange split defect states arising from the σ band dangling bonds.

gling bonds also generate a defect state which is also subject to an on-site coulomb exchange interaction. These states are labeled sp^2 in Fig. 4.5 b) and the exchange interaction for the dangling bonds is large compared with the p_z defect states. Thus, the magnetic moment arising from the σ band dominates in the case of vacancies [315, 319]. Because there are two bands contributing defect spin-split defect states, the expected moment per defect is between 1.1 and 1.5 μ_B per defect state [309]. As depicted in Fig 4.5 b), the quasi-localized p_z-orbital defect state is suppressed in the vacancy case compared to the hydrogen case due to electronic reconstruction of the vacancy [315].

For the A sublattice, according to Lieb's theorem, a defect should generate spin, $S = +1/2$, while on the B sublattice the sign should be reversed. Further, the quasi-localized state extends radially several unit cells and the total magnetic moment is correspondingly

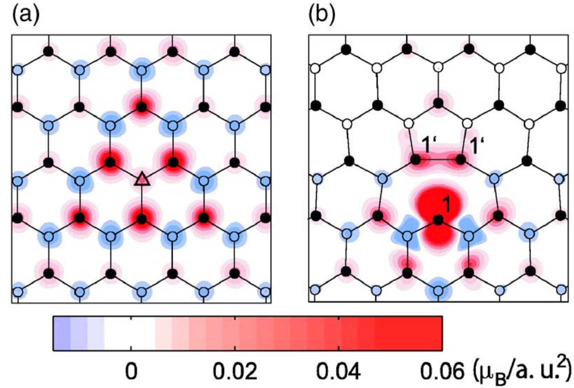

Figure 4.6: Spatial Distribution of the Quasi-localized Induced Magnetic Moment. Adapted from [315]. a) Distribution of magnetic moment for the quasi-localized state for hydrogen adsorbed onto graphene. A and B sublattice have opposite signs of the induced moment. b) Distribution of magnetic moment for the quasi-localized state a single lattice vacancy in graphene.

distributed with spin texture that is positive and negative depending on the sublattice. This is shown in Fig. 4.6 for both chemisorbed hydrogen and for a single lattice vacancy [315].

Regarding interactions between localized moments, the coupling is expected to be of the RKKY nature since graphene is a semimetal [317]. However, for graphene this is expected to be very weak and magnetic ordering might only be realized low temperatures [309]. In the limit of relatively dilute local moments, there is a general consensus that both type of defects should generate spin-half paramagnetism [319]. At high concentration of defects, the localized moment is actually quenched due to strong interactions between the quasi-localized states [319, 316]. In the intermediate regime, it has been shown that for a realistic defect topography, which places single defects randomly and on each sublattice, the coupling should be antiferromagnetic [319]. Ferromagnetic order is only expected for defects on a single sublattice, which is not possible to realize in typical experiments [309].

4.2.2 Experimental Progress on Magnetism in Graphene by Localized Defects

There have been many experimental studies of magnetism and magnetic order in graphene and it's allotropes. Much of the progress in this field has revolved around investigations of defected graphite by magnetometry measurements [309, 324, 325, 326, 327, 328, 329, 330, 331]. In particular, there have been several reports of ferromagnetic ordering in graphene and graphite [324, 325, 326, 327, 328, 329]. As discussed above, there is a universal explanation for the production of magnetic moments in defected graphene, defected carbon nanotubes, defected fullerenes, defected graphite, and nanostructured graphene. This is based on the fact that all these systems have the A-B sublattice and are subjected to Lieb's theorem. However, it has also been discussed that ferromagnetic ordering is unlikely to be observed since all the defects must exist on only one sublattice in order to realize ferromagnetic coupling [309]. Further, it is known that magnetometry measurements are prone to artificial signals of magnetism due to the fact that the whole magnetic signal is measured and the signal is not sensitive locally. Recently, a careful study [330] showed that many types of commercial HOPG substrates are littered with Fe and other magnetic impurities which give ferromagnetic results at room temperature. The authors go on to show that carefully constructed graphene 'laminates' derived from high quality HOPG from SPI (does not demonstrate ferromagnetism) exhibits spin-1/2 paramagnetism when fluorinated or proton irradiated irradiated. To date,

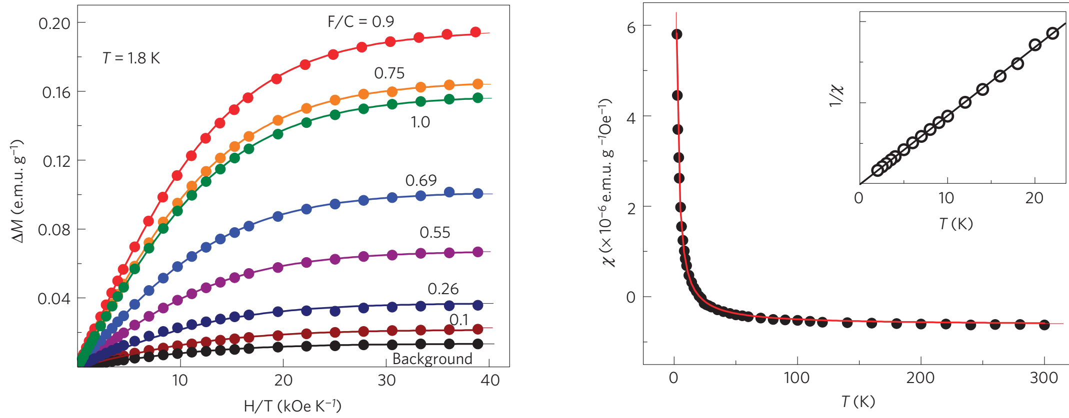

Figure 4.7: Spin-1/2 Paramagnetism in Graphene. Adapted from [330]. a) SQUID magnetometry measurements of fluorinated graphene 'laminates' derived from HOPG. Authors report observation of diamagnetism before fluorination. After fluorination, clear onset of S=1/2 paramagnetism is observed with increasing net magnetization increasing with increasing concentration. Solid lines are best fits with J=1/2 Brillouin function. Not shown: Fits with other values for J do not satisfactorily match the observed behavior. b) Temperature dependent magnetic susceptibility demonstrates that the observed moment disappears above 20 K, with the diamagnetic signal returning.

this is the most clear evidence for magnetic moment formation in agreement with the theoretical considerations discussed above.

Further, there have been several transport experiments regarding magnetism in graphene. This has the advantage of locally probing the graphene flake, but does not directly probe the magnetic degree of freedom. In 2011, Candini et al., [332] observed hysteretic magnetoresistance in narrow graphene ribbons and Hong et al., [165] observed negative colossal magnetoresistance and weak (anti)localization in dilute fluorinated graphene. Notably, Chen et at., [333] reported the observation of gate tunable Kondo effect in defected graphene through measurements of the temperature dependent resistance which demonstrated a possible logarithmic dependence that could be suggestive of the Kondo effect. This claim was disputed by Jobst and Weber [334]. To date, Kondo in graphene remains a controversial topic.

4.3 Conclusion

Induced magnetism in graphene is an interesting and exciting problem that is just emerging from an experimental point of view. There have been many theoretical works that have investigated both induced magnetism through proximity to a ferromagnetic insulator and through localized defects. In the former case, most theoretical works have taken induced exchange splitting for fact, and suggested new and novel spintronics applications for the FMI/graphene materials system. The standing prediction of 5 meV splitting through contact by EuO with graphene is possibly large enough to have implications for transport experiments. However, to date, the field is lacking in concrete experimental works that try to realize the EPI. The current problem is that the FMI graphene system does not exist and meet the materials quality at the interface necessary to realize the EPI. Chapter 7 discusses a significant materials advance in this field by demonstrating the epitaxial integration of EuO onto graphene.

On the other hand, induced magnetism in doped and defected graphene appears to have an excellent theoretical grounding but careful experiments are lacking. Essentially, the problem of generating induced magnetism in graphene on a local scale, is highly related to inducing the exchange proximity interaction (EPI) by a ferromagnetic insulator. In both cases, the mechanism for induced magnetism is the exchange interaction. Further, both require high quality surfaces and interfaces to be realized. The reports of ferromagnetic ordering in defected graphene and graphite have motivated significant interest. The work of Nair et al., which demonstrates S=1/2 paramagnetic behavior for initially diamagnetic graphene lami-

nates agrees well with the theoretical predictions but is in stark contrast with the rest of the field. Transport measurements are able to locally probe the graphene flake but must rely on localization models or observations of hysteretic behavior in the resistance which could stem from various causes. Further, the recent report of Kondo complicates these reports. Clear experiments that can take the advantages of both of these techniques is necessary. In Chapter 8 this issue is revisited. By employing non-local spin valves in the unique *in-situ* UHV measurement system, the spin degree of freedom can be directly probed locally on the graphene flake immediately before and after defects are carefully introduced to the sample. This work represents a significant advance in the field towards understanding induced magnetic behavior in graphene.

Chapter 5

Epitaxial EuO Thin Films on GaAs

5.1 Introduction

Stoichiometric EuO is an attractive material for spintronics because it is a ferromagnetic insulator with a large exchange splitting of its conduction band [251], as well as having the largest magneto-optic response of any oxide [176], and large magnetic moment of 7 Bohr magnetons (μ_{B}) per Eu atom [174]. When used as a tunnel barrier, the EuO is an effective spin filter [251] due to its spin dependent barrier height. EuO's insulating nature enables its use as a gate dielectric for which it is predicted to generate a gate tunable exchange field for spin manipulation [190]. Historically, the growth of stoichiometric EuO has been notoriously difficult to achieve. For reactive molecular beam epitaxy (MBE), the growth requires fine-tuning of the Eu and O_2 fluxes because a low oxygen flux results in the formation of Eu-rich EuO (EuO_{1-x}) [288, 179]. On the other hand, a high oxygen flux leads to the formation of

non-magnetic Eu_2O_3, which is more thermodynamically favorable [287]. While EuO_{1-x} is interesting for its metal-insulator transition and colossal magnetoresistance, its ferromagnetic phase is metallic and therefore does not possess the unique properties of a ferromagnetic insulator.

Recently, the high quality and reliable epitaxial growth of stoichiometric EuO on oxide substrates has been accomplished using a high temperature, adsorption-controlled growth mode [181, 335, 240, 241]. In this regime, the Eu flux is set to be much higher than the O_2 flux and a high substrate temperature ($\sim$450 °C) is maintained to re-evaporate any excess Eu. Only Eu atoms that have paired with an oxygen atom remain on the sample, leading to a stoichiometric EuO film whose growth rate is controlled by the adsorption of the oxygen gas. Furthermore, the europium overpressure inhibits the formation of Eu_2O_3.

The integration of a magnetic insulator, such as EuO, with semiconductors is important for spintronic devices since semiconductors are the mainstay of the current electronics industry. While there has been great progress in the MBE growth of EuO_{1-x} on silicon and GaN [179, 336], the growth of stoichiometric EuO on a semiconductor has yet to be achieved. We are particularly interested in EuO/GaAs because GaAs is well suited for optical probes of the spin polarization and spin dynamics [105, 101, 106]. However, the direct growth of stoichiometric EuO on GaAs presents significant challenges. It is well known that elemental rare-earths grown on GaAs(001) result in highly reacted interfacial phases [337]. In addition, the elevated substrate temperatures required for stoichiometric growth will enhance the interface reaction and also promote interdiffusion. This suggests that a diffusion barrier will

be necessary for the integration of stoichiometric EuO with GaAs, similar to the approach utilized for integrating epitaxial oxides onto silicon [336, 338, 339, 340].

Here, we report the epitaxial growth of EuO films on GaAs(001) in the adsorption-controlled regime using an MgO diffusion barrier. EuO is deposited on yttrium-stabilized cubic zirconia (YSZ) and MgO substrates to demonstrate high quality, adsorption-controlled growth. When deposited directly onto GaAs, EuO exhibits poor crystalline structure and weak or no ferromagnetic behavior. To solve this problem, we employ MgO diffusion barriers on GaAs(001) and subsequently deposit EuO overlayers in the adsorption-controlled regime. These samples exhibit high quality single-crystal structure and possess good magnetic properties including a Curie temperature (T_C) of 69 K (equal to bulk T_C [174]), hysteresis loops with substantial remanent magnetization, and a large magneto-optic Kerr rotation of 0.57 degrees.

5.2 Experimental Determination of Eu Distillation Off Lattice Matched YSZ(001)

Samples are grown by MBE in an ultrahigh vacuum chamber with a base pressure of 1×10^{-10} Torr. For all samples, pure Eu metal (99.99%) is evaporated from a thermal effusion cell at a rate of 7.4-7.8 Å/min. For all EuO depositions, the samples are held at 450 °C for the re-evaporation of Eu. Growths are initiated with Eu flux, followed by molecular oxygen gas (99.994% pure) that is leaked into the chamber to a stable pressure of 1.0×10^{-10} Torr.

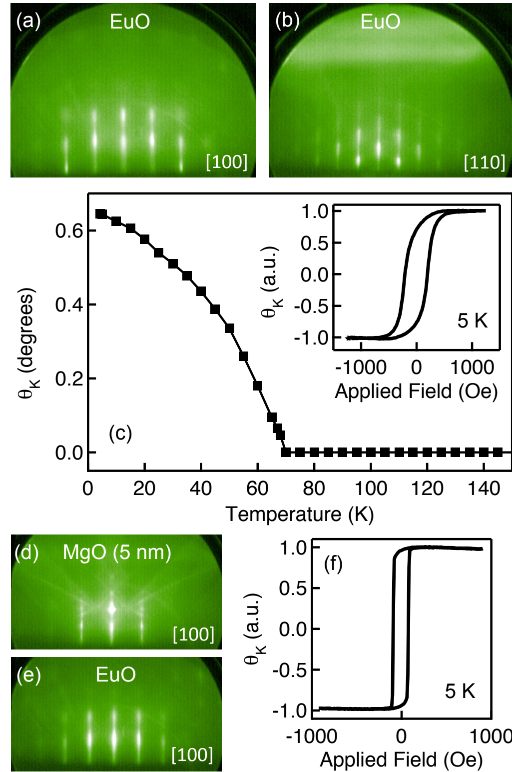

Figure 5.1: Investigation of EuO on YSZ(001) and MgO(001). a) and b) EuO RHEED patterns on YSZ(001) along [100] and [110], respectively. c) Temperature dependence of the Kerr rotation at saturation for EuO/YSZ(001). Inset: longitudinal MOKE hysteresis loop at 5 K. d) RHEED pattern of 5 nm MgO buffer layer on MgO(001). e) RHEED pattern of EuO/MgO(5 nm)/MgO(001) along [100]. f) MOKE hysteresis loop of EuO/MgO(5 nm)/MgO(001)

For all samples, the growth time is 30 minutes and is terminated by closing the oxygen leak valve and then closing the Eu shutter within 30 s. Samples are capped with 3 nm MgO from an electron beam source to protect the EuO from further oxidation. For growth on GaAs, GaAs(001) substrates with GaAs buffer layers are prepared by III-V MBE and capped with As. After transferring in air to the EuO/MgO MBE system, the As cap is desorbed to yield a 2×4 GaAs(001) surface. An atomic force microscopy (AFM) profile scan of a sample grown under these conditions gives a film thickness of 5.54 ± .07 nm, for which a

saturation magnetization value of 6.93 $\pm$0.26 μ_B/Eu atom is measured by vibrating sample magnetometry at 5 K (not shown). Within the error, this is nearly identical to the theoretical value of 7 μ_B/Eu atom for EuO.

The epitaxy of EuO on YSZ(001) (Y_2O_3:ZrO 8% mol) serves as a reference for the adsorption-controlled growth due to the excellent lattice match of 0.3% (a_{EuO}=5.140 Å, a_{YSZ}=5.125 Å) [241]. Fig. 5.1 a) and Fig. 5.1 b) show typical reflection high energy electron diffraction (RHEED) patterns for EuO/YSZ(001) along the [100] and [110] directions, respectively. RHEED oscillations (not shown) are seen up to eight monolayers (ML) independent of the oxygen partial pressure, indicating that the initial growth is substrate assisted in agreement with previous reports [241]. Samples are characterized by longitudinal magneto-optic Kerr effect (MOKE) (635 nm, 150 μW) in an optical flow cryostat with an angle of incidence of 45 ° and *p*-polarized incident beam. The inset of Fig. 5.1 c) shows a typical MOKE loop for EuO/YSZ measured at 5 K. The coercive field (H_C) is 202 Oe, the ratio of the remanent magnetization to saturation magnetization (M_R/M_S) is 0.69, and the measured Kerr rotation is 0.65 °. The remanent Kerr rotation as a function of temperature (Fig. 5.1 c)) indicates a T_C of 69 K, in agreement with the bulk T_C. These magnetic properties indicate the growth of high quality EuO.

Following the growth on YSZ(001), we deposit EuO on both As- and Ga-terminated surfaces of GaAs(001) at 450 °C. In all cases, RHEED patterns are nonexistent and MOKE characterizations show either weak or no ferromagnetic behavior. The high temperature likely aides in the out-diffusion of As and the formation of reactive phases. A possible method to

suppress the interdiffusion and interface reaction is to employ a thin MgO diffusion barrier (i.e. EuO/MgO/GaAs).

5.3 MgO as a Diffusion Barrier for Deposition of EuO on GaAs

To systematically develop the MgO diffusion barrier, we grow EuO on an MgO(001) substrate because the large lattice mismatch of 22.5% (a_{EuO}=5.140 Å, a_{MgO}=4.212 Å) makes the epitaxial growth non-trivial and magnetic quality uncertain. Prior to growth, the MgO substrates are annealed at 600 °C in an oxygen environment (1×10^{-7} Torr), followed by a 5 nm MgO buffer layer deposited at 350 °C [289] in an oxygen environment (8×10^{-8} Torr). The RHEED pattern of the MgO buffer layer is shown in Fig. 5.1 d). At the onset of EuO growth, the RHEED pattern fades, with only the central peak remaining. After approximately 2 nm, the pattern reappears (Fig. 5.1 e)), and the side diffraction streaks are shifted by 22% (compared to MgO), indicating high quality epitaxy and cube-on-cube growth. Longitudinal MOKE loops (Fig. 5.1 f)) taken at 5 K indicate excellent magnetic properties with an H_C of 58 Oe and M_R/M_S of 0.97.

Since it is well known that the epitaxy of MgO on semiconductors is highly temperature dependent [338, 341, 342], we next investigate the growth of MgO diffusion barriers on GaAs(001) and optimize the quality of e-beam deposited MgO by systematically varying the growth temperature. Starting with a 2×4 GaAs(001) surface (Fig. 5.2 a) and 5.2 b)), 2 nm

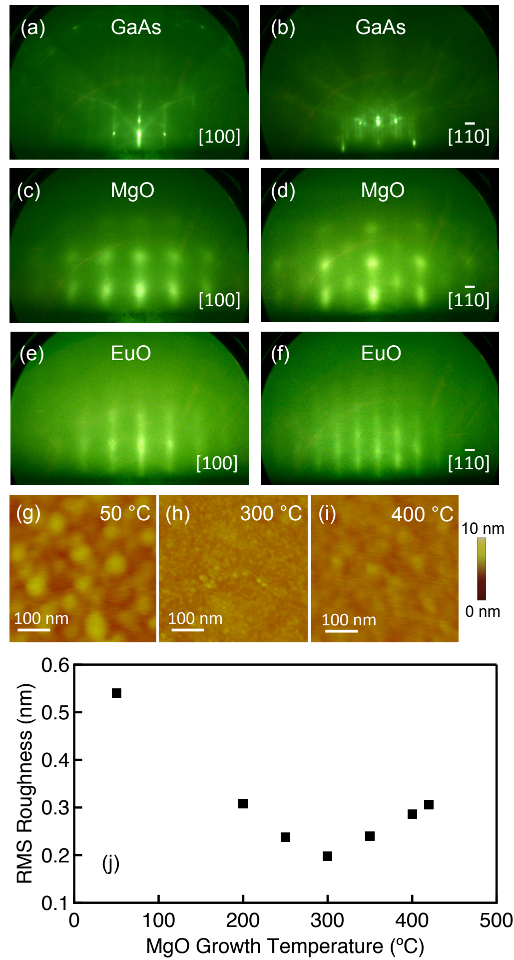

Figure 5.2: Integration of EuO on GaAs(001). a)-f) RHEED patterns of the GaAs substrate with 2×4 reconstruction and subsequent growths of 2 nm MgO grown at 300 °C and EuO grown at 450 °C. The left column is in the [100] direction and the right column is in the [1$\bar{1}$0] direction. g)-i) AFM measured at RT on 2 nm MgO grown at 50 °C, 300 °C and 400 °C, respectively, on 2°4 reconstructed GaAs. j) RMS roughness of 2 nm MgO on GaAs displayed as a function of growth temperature.

MgO films are grown in an oxygen environment (8×10^{-8} Torr) at substrate temperatures ranging from 50 °C to 420 °C (the limit for 2×4 reconstruction). Because the adsorption-controlled growth of EuO requires a substrate temperature of 450 °C, the MgO films are subsequently annealed for 30 minutes at 450 °C. After post annealing, samples are removed for ex situ AFM. Figures 5.2 g), 5.2 h), and 5.2 i) show AFM scans of MgO films grown

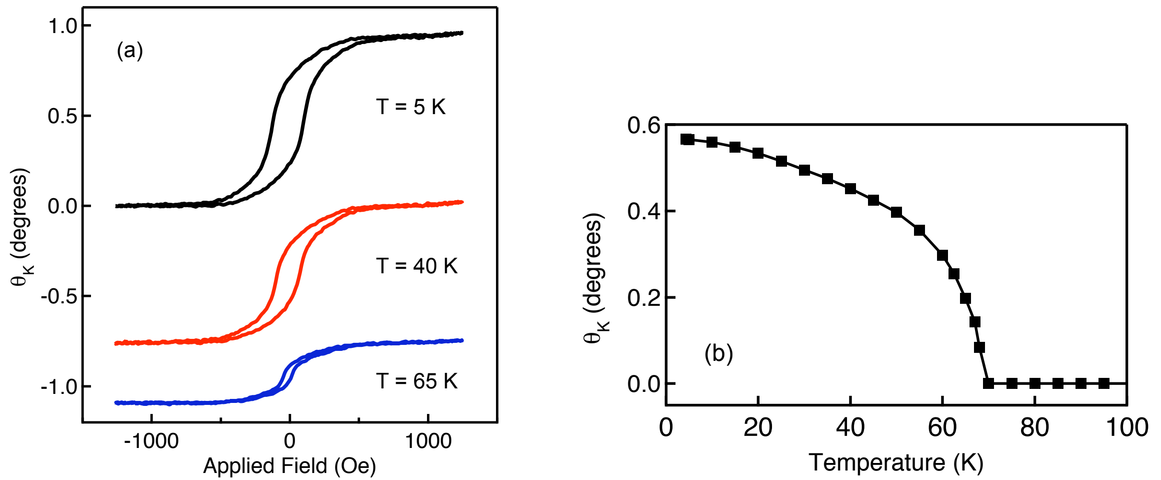

Figure 5.3: Magnetization Characterization by MOKE on EuO /MgO(2 nm)/GaAs (001). a) Longitudinal MOKE hysteresis loops taken at 5 K, 40 K, and 65 K. b) Temperature dependence of the Kerr rotation at saturation.

at 50 °C, 300 °C, and 400 °C, respectively. As summarized in Fig. 5.2 j), AFM scans yield RMS roughness values between 0.540 nm and 0.198 nm, with the optimal growth of MgO on GaAs at 300 °C. The corresponding RHEED patterns of the optimized MgO are shown in Fig. 5.2 b) and 5.2 c) for [100] and [1$\bar{1}$0], respectively, and indicate good single-crystal structure. Lastly, adsorption-controlled EuO is deposited on MgO/GaAs(001) at 450 °C with an optimized MgO diffusion barrier. RHEED patterns, as shown in Fig. 5.2 e) and 5.2 f) along [100] and [1$\bar{1}$0], respectively, indicate that the growth of EuO is single crystal and cube-on-cube.

Fig. 5.3 a) shows longitudinal MOKE hysteresis loops taken at 5 K, 40 K, and 65 K. At 5 K, the H_C is 102 Oe, M_R/M_S is 0.44, and the saturation Kerr rotation is 0.57 °. With increasing temperature, both H_C and the Kerr rotation decrease monotonically as expected for magnetic thin film behavior. Figure 5.3 b) shows a detailed measurement of the remanent Kerr rotation

as a function of temperature. The measured Curie temperature, T_C=69 K, agrees with the bulk value. Comparing these properties to the EuO films on YSZ(001) and MgO(001) substrates indicates that the magnetic properties of EuO/MgO/GaAs(001) are weaker but still very good.

5.4 Conclusion

In conclusion, we have grown EuO on YSZ(001), MgO(001), and GaAs(001) in the adsorption-controlled regime. For growth on GaAs(001), an MgO diffusion barrier is employed to suppress the interface reaction and interdiffusion between the EuO film and GaAs substrate. All films exhibit a T_C of 69 K, large MOKE signals, and relatively square hysteresis loops. The growth of single-crystal, stoichiometric EuO films on GaAs enables alternative approaches for injecting, detecting, and manipulating spin in GaAs.

Chapter 6

TiO_2 as an Electrostatic Template for Epitaxial Growth of EuO on MgO(001)

6.1 Introduction

The spin filter effect [251], possible use as a magnetic gate dielectric [190, 242], and a large magneto-optic response [176], makes stoichiometric EuO, a ferromagnetic insulator, promising for spin-based applications [15]. Also of great interest are doped and nonstoichiometric EuO due to their demonstration of a metal-insulator transition [177], colossal magnetoresistance [178], half metallic behavior [179], and the anomalous Hall effect [180]. The recent resurgence of interest in EuO is largely due to the advances in synthesis of high quality EuO films by reactive molecular beam epitaxy (MBE) [242, 335, 240, 241]. More specifically, the stoichiometric growths have been reliably achieved only within an adsorption-controlled

growth regime [335, 240]. Two separate conditions determine this regime. First, the substrate is maintained at an elevated temperature, which allows for Eu re-evaporation (distillation) from the substrate. Second, a carefully maintained oxygen partial pressure determines the growth rate and chemical composition (Eu_xO_y).

MgO is an important oxide for spintronics due to its Δ_1 band spin filtering in magnetic tunnel junctions [6, 5, 27] and its effective use as a tunnel barrier for spin injection into semiconductors and graphene [343, 344, 345, 71]. Also, MgO has long served as a popular commercially available substrate for the deposition of a wide variety of materials such as transition metals, perovskites, and spinels [6, 346, 347]. Several authors have reported successful deposition of EuO on MgO [241, 288] and cube-on-cube growth with a magnetization of 7 Bohr magnetons per Eu atom despite the large lattice mismatch of $\sim$22% (($a_{EuO}-a_{MgO}$) / a_{MgO} = (0.514 nm$-$0.421 nm) / 0.421 nm = 22.1%) [242]. However, while single crystal deposition on MgO(001) is possible, the initial stages of the growth have yet to be fully investigated and require further exploration [241, 286].

Here, I present the results of high quality EuO epitaxy on MgO by the introduction of a TiO_2 interfacial layer. Conceptual electrostatic arguments are introduced to explain why TiO_2 alleviates many of the problems associated with rock salt heteroepitaxy. Time evolution of the growths are compared and the TiO_2 surface is shown to produce single crystal EuO in the monolayer regime by inducing a 45° in plane rotation, which decreases the lattice mismatch, and by serving as an electrostatic template for which like-ion repulsion is alleviated. On the other hand, direct epitaxy of EuO on MgO is shown to be of reasonable quality only after

2 nm. Interestingly, ultrathin EuO can be produced without the introduction of oxygen partial pressure through substrate-supplied oxidation to yield films in the monolayer regime. Such ultrathin films are ferromagnetic with bulk Curie temperatures.

6.2 Methods

In this study, 10 mm x 10 mm x 0.5 mm double-side polished MgO(001) substrates are first rinsed in DI water, then loaded into a MBE system with a base pressure $\sim 1 \times 10^{-10}$ torr. The crystal surface quality of the sample is monitored throughout the annealing and subsequent layer growths with *in-situ* reflection high energy electron diffraction (RHEED). The substrate is annealed for 60 minutes at 600 °C as measured by a thermocouple located near the sample. The substrate is then cooled to 350 °C for the deposition of a 10 nm MgO buffer layer grown by e-beam evaporation at a typical rate of ∼1 Å/min [289]. The MgO buffer layer smoothes the substrates surface, indicated in the RHEED pattern as sharpened streaks and Kikuchi lines (Fig 6.2 a) and 6.2 b)). To create the TiO_2 layer, Ti is first deposited from an e-beam source onto the MgO buffer layer at room temperature (RT). The Ti thickness is chosen according to the number of desired surface Ti atoms corresponding to 1, 1.5, or 2 monolayers of lattice matched 2×2 reconstructed TiO (chemical composition TiO_2) as described more fully in the following section. The Ti layer is exposed to molecular oxygen (5×10^{-8}) at 500 °C for 30 minutes. For subsequent growths on either the TiO_2 or directly on the MgO buffer layer, EuO films are produced by reactive MBE where a high purity metal

source is sublimed and allowed to react with a molecular oxygen partial pressure. Typical stoichiometric growth in the adsorption-controlled (distillation and oxygen-limited) regime proceeds as follows. 99.99% pure Eu metal is evaporated from a thermal effusion cell and the flux (∼8 Å/min) is incident upon the heated substrate which is maintained at 500 °C. Next, molecular oxygen is leaked into the chamber with a partial pressure of 1×10^{-8} torr enabling the growth of stoichiometric EuO [242, 240, 241]. Such films on bare MgO have been shown to be approximately 5 nm thick for a 30 minute growth time by AFM profiling giving a growth rate of 0.17 nm/min [242].

6.3 Electrostatic Considerations at the EuO/MgO(001) Interface

Heteroepitaxy between insulating oxides, such as of large cation oxides on MgO, is greatly determined by interface electrostatics [346]. Purely structural considerations are insufficient to fully understand the EuO/MgO interface. The cube-on-cube (EuO(001)[100] // MgO(001)[100]) growth on MgO [242, 241] suggests that some structural arrangement (i.e. either 1:1, 3:4, 4:5, etc) is favored. A 3:4 spacing has a reduced lattice mismatch of 8.4% and a 4:5 spacing has a mismatch of 2.3%. For a clearer picture, a 4:5 (EuO:MgO) stacking, displayed using VESTA software [245], is shown in Figure 6.1 a). An examination of the 4:5 stacking shows that while the center Eu^{2+} ion has a favorable position above an O^{2-} ion, at

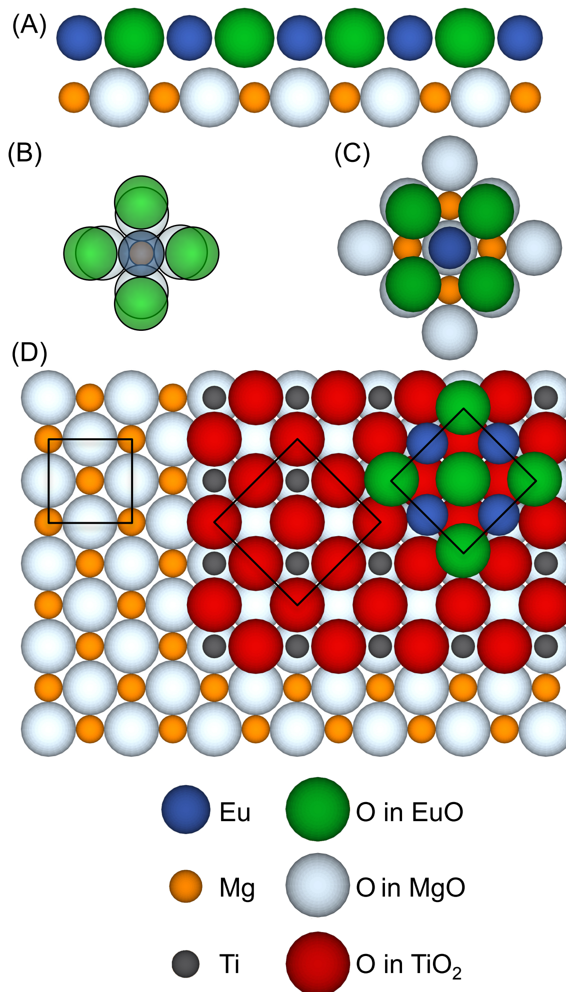

Figure 6.1: Various Crystal Structure Schematics of EuO on MgO. a) Schematic of cube-on-cube EuO/MgO(001) in a 4:5 (EuO:MgO) configuration at the interface. Ions are represented as follows: the Mg ions are shown as small spheres (orange), the O in MgO ions are large white spheres, Eu ions are the medium spheres (blue) and O in EuO are the large dark spheres (green). b) Shows the ion size effect for cube-on-cube growth of EuO (transparent over layer) on MgO (under layer). c) Configuration for a 45° rotated EuO over-layer on MgO demonstrating the anion-anion overlap between the oxygen ions of the EuO and MgO. d) Structure of the EuO/TiO_2/MgO layers. Ti ions are the smallest gray spheres and O ions in TiO_2 are the large gray spheres (red). Boxes show the unit cells for each oxide. For a)-d), the ions in each schematic are sized according to their ionic radius. The MgO and TiO_2 are drawn to scale with the bulk MgO lattice parameter while all EuO layers correspond to the bulk EuO lattice constant.

the left edge, the first Eu^{2+} ion is sitting above an Mg^{2+} ion and the first O^{2-} ion is above another O^{2-} ion.

This is repeated at the right edge of the 4:5 configuration. From an electrostatic point of view, strong Coulomb repulsion between like ions suggests that such a stacking is not ideal despite the improved lattice match and would certainly lead to surface roughening at the interface. Another concern for the cube-on-cube growth mode for direct heteroepitaxy is the ion-size difference effect [346], which is related to the difference in size between the Mg-O bond and the Eu-O bond. The Mg^{2+} ionic diameter, 0.130 nm, combined with two Oxygen (O^{2-}) ionic radii of 0.140 nm, forms a nearly close- packed system with the ions spanning 97% of the lattice constant [348]. Figure 6.1 b) illustrates that replacing the Mg^{2+} ion with a Eu^{2+} ion changes the cation ionic diameter to 0.234 nm and increases the O-O nearest neighbor bond by 22% from 0.298 nm to 0.363 nm. Effectively, the deposition of an atomically flat EuO layer on a pristine MgO(001) surface is equivalent to 100% substitutional doping the Mg atoms in the top layer of an MgO surface with Eu atoms. In such a case, the ion-size difference would force the Eu or O atoms to find equilibrium positions in a roughened structure.

Alternatively, another possible structural alignment would be a 45° in-plane rotation of the EuO lattice relative to the underlying MgO orientation. Figure 6.1 c) shows a 45° rotated EuO layer on an MgO underlayer with the placement of a Eu ion on an oxygen bonding site. This configuration would remove the ion-size effect (a_{EuO} / 2 = 2.57 $<$ a_{MgO} / $\sqrt{2}$ = 2.91), reduce the lattice mismatch to 12% and could potentially improve the growth mode. How-

ever, anion-anion or cation-cation electrostatics makes the structure energetically unfavorable because the oxygen ions in the EuO overlayer sit atop oxygen ions in the underlying MgO surface. With these considerations in mind, any attempt to engineer the interface to minimize the electrostatic repulsion of like ions, while simultaneously maintaining an atomically smooth surface, could greatly improve the epitaxy.

To alleviate the interfacial electrostatic repulsion and stabilize EuO epitaxy on MgO(001), we propose a special TiO_2 template at the interface. Such an approach has been employed to produce high quality epitaxy of $BaTiO_3$ films on MgO(001) [346]. Figure 6.1 d) shows the stacking for subsequent depositions of a TiO_2 layer followed by EuO on MgO(001). Starting from left to right in Figure 6.1 d) is the MgO buffer layer, followed by a monolayer of TiO_2, and lastly, a single unit cell of EuO is shown rotated 45° relative to the MgO in-plane orientation. The displayed MgO lattice spacing is that of bulk MgO and the TiO_2 layer is shown lattice matched to the MgO. The EuO is shown with bulk EuO lattice constant. For the single monolayer of TiO_2, O atoms are positioned above Mg atoms. The Ti atoms and vacancy positions are located above the O atoms of the MgO layer. This configuration allows for the subsequent EuO layer to be positioned such that the Eu atoms are located above the vacant positions in the TiO_2 layer, while the O atoms are located above the Ti atoms. Within this EuO/TiO_2/MgO(001) interface, all nearest neighbor ions have opposite charge to produce attractive Coulomb forces for an energetically stable interface. Specifically, there are no O-O or Eu-cation nearest neighbor bonds. Thus, the TiO_2 interfacial layer eliminates

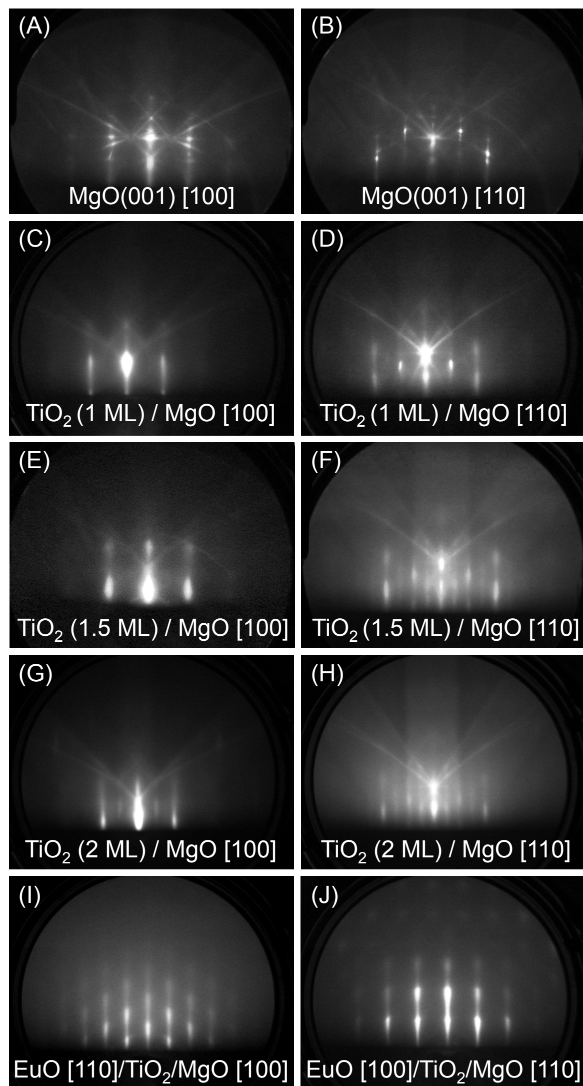

Figure 6.2: RHEED patterns for the 10 nm MgO buffer layer in the a) MgO(001)[100] and b) MgO(001)[110] directions. c) and d) are the RHEED patterns for 1 ML TiO_2 monolayer on MgO(001) in the [100] and the [110] directions, respectively. e) and f) are the RHEED patterns for 1.5 ML TiO_2 in the [100] and the [110] directions. g) and h) are the RHEED patterns for 2 ML TiO_2 in the [100] and the [110] directions. Final RHEED patterns for a 5 nm EuO film on TiO_2 (2 ML) showing i) EuO(001)[110] // MgO(001)[100] and j) EuO(001)[100] // MgO(001)[110].

the ion-size effect and electrostatic problems described for the growth of EuO directly onto MgO(001).

6.4 Results and Discussion

Figure 2 shows the RHEED patterns for TiO_2 monolayers on MgO(001). Figure 6.2 d) and b) show the 10 nm MgO/MgO(001) buffer layer pattern along the [100] and [110] directions, respectively. Figure 6.2 c), e), and g) are the RHEED images for oxidized Ti layers of 1, 1.5, and 2 ML along the [100] direction, while Figure 6.2 d), f), and h) are the corresponding TiO_2 monolayers along the [110] direction of MgO. The main features of the oxidized Ti patterns remain that of MgO with a slight broadening of the outer diffraction rods. In the RHEED image of 2 ML TiO_2/MgO(001)[100] (Figure 6.2 g)) the underlying MgO structure is readily visible with the important addition of inner streaks between the main MgO(001)[100] rods. As discussed previously, the TiO_2 layer is comprised of both Ti sites and vacant sites above the underlying oxygen atoms. Thus, the unit cell periodicity is increased to twice the size creating diffraction rods of half-spacing in the [100] direction. Equivalently, this TiO_2 layer can be perceived as a TiO rock salt surface of identical unit cell with the MgO lattice, but missing the face-centered Ti atoms [349]. This would then be a 2×2 reconstructed TiO surface producing diffraction streaks inside the MgO [100] rods. However, in no instances were inner streaks seen for the case of 1 ML oxidized Ti. Interestingly, as seen in Figure 6.2 d) and f), inner rods appeared for 1.5 and 2 ML of oxidized Ti along the [110] direction. This suggests decreased periodicity of the 2×2 reconstructed TiO_2, possibly from an ordered stacking effect or superstructure causing increased periodicity in the k-space lattice along the [110] direction. The subsequent RHEED patterns of a 5 nm EuO film grown on 2 ML

TiO_2/MgO(001) in the adsorption-controlled regime are shown in Figures 6.2 i) and j). These final films have an in-plane orientation of EuO(001)[110] // MgO(001)[100] and are thus 45° rotated. Importantly, as Fig 6.1 b) and Fig 6.1 d) illustrate, the ion-size effect is eliminated since the rotated EuO lattice has a smaller unit cell than the underlying TiO_2 template. While, generally, EuO growths on 1 ML TiO_2 surfaces resulted in polycrystalline films, deposition on 1.5 ML TiO_2 surfaces produced high quality EuO single crystal films of identical growth behavior and evolution to depositions on 2 ML TiO_2 (see Fig 6.3 a) and 6.3 b)). This is interesting since the 1.5 ML TiO_2 RHEED only shows part of the features seen in the 2 ML RHEED, suggesting that the 1.5 ML TiO_2 still has the critical structure of the 2×2 reconstructed TiO layer. Because of this result, and in combination with the desire to keep the TiO_2 interface as thin as possible, the 1.5 ML TiO_2 layer will be used throughout the remainder of this study.

To further examine the growth of EuO on the TiO_2 layer, the time evolution of a line cut across the RHEED pattern is monitored along the MgO(001)[110] in-plane crystal direction over the first 10 minutes of EuO growth. A line cut is obtained by plotting the intensity of the image against the CCD cameras horizontal pixel position and therefore crosses several diffraction rods. The initial line cut of 1.5 ML TiO_2 (in MgO(001)[110] direction) is shown at the top of Figure 6.3 c). After 20 seconds (dashed line (C1)), the Eu flux is introduced and immediately the RHEED begins to change. After the RHEED pattern is stabilized, oxygen is introduced into the chamber (dashed line (C2)), and the RHEED pattern changes to that of EuO(001)[100]. During this period, the RHEED quickly shifts (1 minute) to that of bulk

EuO indicating epitaxy within 1 ML with the introduction of oxygen. The final line cut (1 nm EuO) is shown below the time lapse. Analysis of the final EuO/TiO_2 line cut compared to the MgO lattice constant gives a EuO lattice parameter of 0.513 ± 0.006 nm. For comparison, the time evolution for direct deposition of EuO on the MgO buffer layer is shown in Figure 6.2 d). As indicated by dashed line (D1), elemental Eu flux is directed onto the MgO(001) substrate held at 500 °C. During this period, the RHEED pattern remains that of MgO, indicating that Eu is re-evaporating and not bonding to the surface. Once oxygen is leaked into the system (dashed line (D2)), the time evolution of the RHEED pattern consists of a fading out of the MgO(001)[110] pattern followed by a gradual recovery to a EuO(001)[110] pattern over several minutes ($\sim$2 nm). The diffraction rods increase in intensity over the subsequent 20 minutes of the growth.

Several key differences are immediately apparent between the two growths. First, comparative analysis of the diffraction pattern peak positions in the final line cuts between EuO/TiO_2/MgO and EuO/MgO demonstrates that EuO epitaxy on the TiO_2 is rotated 45-degree in-plane with respect to MgO, while the direct growth on MgO is cube-on-cube. Second, the evolution from the initial line cut to single crystal EuO takes place at a faster rate for the deposition on TiO_2/MgO and indicates fast strain relaxation for 45° rotated EuO in agreement with observations of EuO growth on Ni [286]. Third, during the distillation period, before the introduction of an oxygen partial pressure, the re-evaporation for each surface is distinctly different. While in both cases the opening of the Eu shutter decreases the RHEED intensity, on bare MgO buffer layer, the incident Eu flux re-evaporates leaving

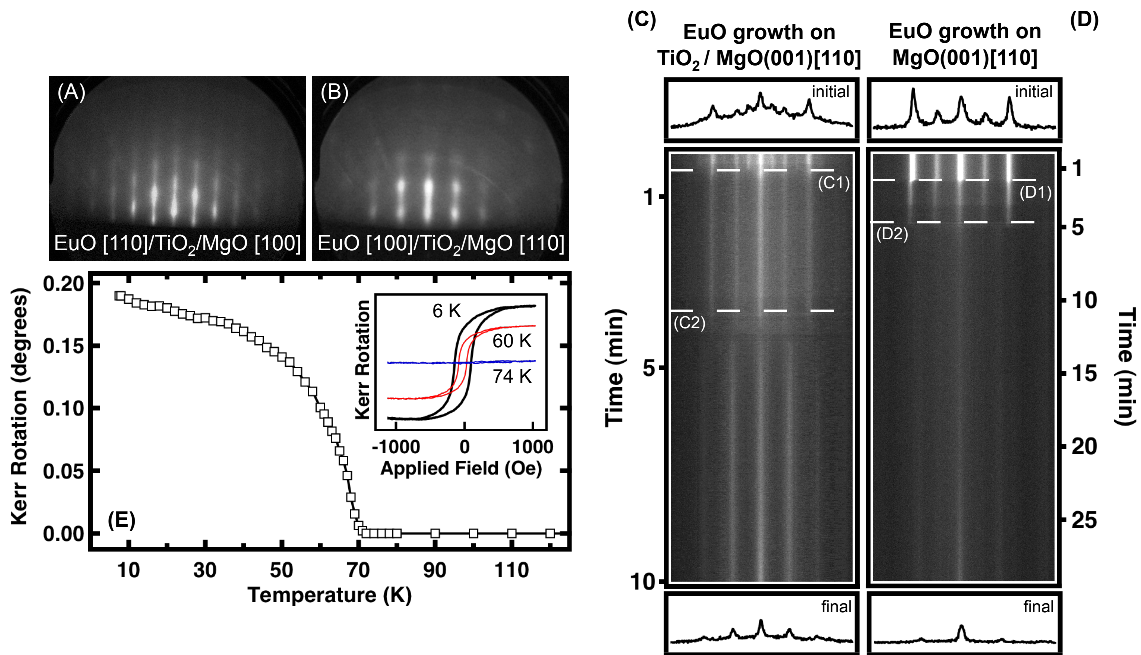

Figure 6.3: Time Evolution and Magnetic Properties of EuO Growth on TiO_2/MgO and MgO. a) and b) are the RHEED patterns for a 5 nm EuO thin film deposited on TiO_2 (1.5 ML)/MgO (10 nm)/MgO(001) along EuO(001)[110] // MgO(001)[100] and EuO(001)[100] // MgO(001)[110], respectively. c) is the time evolution of the initial 10 minutes EuO growth on TiO_2 (1.5 ML)/MgO. The initial and final line cuts are shown above and below, respectively. In Fig. 6.2 c), the peaks in the initial line cut correspond to diffraction rods seen in the 1.5 ML TiO_2 RHEED pattern (Fig. 6.2 f)), while the final line cut corresponds to the diffraction rods seen for EuO [100] // MgO [110] (Fig. 6.3 b)). (C1) (dashed line) indicates when the Eu flux is incident on the TiO_2 layer and (C2) (dashed line) indicates the introduction of O_2 into the system. d) The time evolution of direct deposition of EuO on MgO (10 nm)/MgO(001) in the MgO [110] direction and the peaks in the initial line cut shown above correspond to the diffraction rods in Fig. 6.2 b). (D1) (dashed line) indicates when the Eu flux is incident on the MgO and (D2) (dashed line) indicates the introduction of O_2. Below d) is the final line cut of EuO after 30 minutes of growth directly on the MgO buffer layer. e) Temperature dependence of the measured MOKE angle (degrees) taken at 0 Oe (remanence) for EuO (5 nm)/TiO_2/MgO(001). Inset shows representative hysteresis loops for T = 6 K (Black), T = 60 K (Red or grey) and T = 74 K (Blue or dark grey)

the MgO(001)[110] RHEED pattern unaltered. However, on the TiO_2, the incident flux only re-evaporates after an initial time period for which the inner diffraction streaks associated with the TiO_2 are lost but the overall MgO diffraction positions in the RHEED pattern are maintained. Lack of bonding and full re-evaporation at 500 °C on bare MgO suggests, in

agreement with the discussion in section 6.3, that there is some additional interfacial energy at the EuO/MgO interface that inhibits Eu bonding. Interestingly, this is not seen for Eu deposition on either the TiO_2/MgO or YSZ [241] at elevated temperatures. At this point, while the in-plane rotation, in conjunction with the TiO_2 RHEED pattern and lack of re-evaporation, would suggest that we have successfully reduced the interfacial energy at the interface by limiting electrostatic effects, one possibility that cannot be ruled out is Eu-Ti-O reactivity at the interface and that the lack of re-evaporation is due to some complex composition.

To investigate the magnetic properties of the EuO within the MgO cap (2 nm)/EuO (5 nm)/TiO_2 (1.5 ML)/MgO (10 nm)/MgO(001) structure, the magneto-optic Kerr effect (MOKE) is measured *ex situ* in an optical flow cryostat with variable temperature control. Longitudinal MOKE was measured with a p-polarized 635 nm diode laser and an incident angle near 45 degrees with respect to an applied in-plane magnetic field (H). Figure 6.3 e) inset shows representative M-H hysteresis loops at T = 6 K with a coercivity (H_c) of 117 Oe and ratio (M_r/M_s) between magnetization remanence (M_r) and saturation (M_s) of 0.53. Representative loops at T = 60 K and T = 74 K are also shown. In Figure 6.3 e), M_r is plotted (in degrees) as a function of temperature. Starting at 6 K, the Kerr rotation at remanence is 0.19 degrees and decreases with increasing temperature, following typical Curie-Weiss behavior down to the transition temperature at 69 K, the bulk T_C value for EuO.

We next investigate the interfacial structure and material quality at the interface between EuO and the 1.5 ML TiO_2/MgO stacking in the following manner. 1.5 ML TiO_2 is grown

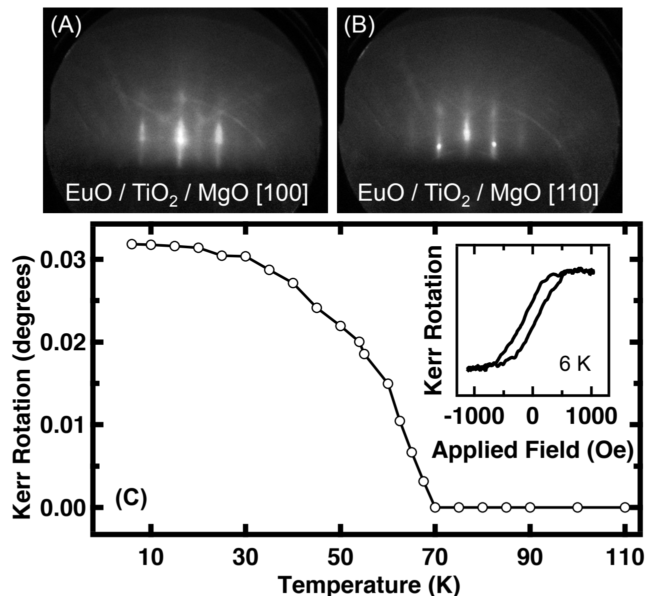

Figure 6.4: Magnetic Characterization of Ultrathin EuO. RHEED patterns for Eu deposition on the TiO_2 layer without leaking O_2 into the system in the a) MgO(001)[100] and b) MgO(001)[110] directions. c) Temperature dependence of the MOKE signal measured at saturation and the insert shows a representative hysteresis loop at T = 6 K.

on an MgO buffer layer and maintained at 500 °C. Next, a Eu flux is exposed to the heated TiO_2 without introducing an oxygen partial pressure. Unlike the case for Eu flux incident on the bare MgO, the RHEED pattern immediately changes (Fig. 6.4 a) and 6.4 b)), indicating bonding of Eu atoms to the TiO_2 surface. Furthermore, the faint streaks between the underlying MgO(001) [100] RHEED pattern (Fig 6.4 a)) indicates layer-by-layer epitaxial growth of EuO(001)[110] // MgO(001)[100] in the ultrathin limit. As in the case of oxygen-free growth of EuO on YSZ(001) [241], the oxygen atoms are believed to be supplied by the substrate. After a few minutes, the RHEED pattern stabilizes indicating steady state re-evaporation of the incoming Eu flux and thus the growth is terminated. The short time frame and visible

underlying MgO RHEED pattern suggests that at most, only a few monolayers of material are deposited.

The sample is then capped with 3 nm MgO and MOKE measurements are performed as shown in Fig 6.4 c). Hysteresis loops taken at 6 K (Fig 6.4 c) inset) clearly show ferromagnetic behavior with H_c = 98 Oe and M_r/M_s = 0.24. A temperature dependence of the magnetization remanence shows the transition temperature to be 69 K, indicating that the initial growth mode for Eu flux incident on the TiO_2/MgO interface is EuO and not a reacted Eu-Ti-O compound. Interestingly, the fact that T_C is equal to the bulk value suggests that the resulting film thickness is large enough to avoid finite size effects, which should decrease T_C [350]. Furthermore, these magnetic results shed light on the initial growth mode seen in the RHEED time evolution (Fig 6.3 c)). The reconstruction streaks immediately fade once the Eu flux is incident upon the TiO_2 surface. This occurs because the TiO_2 layer minimizes the electrostatic interactions between the EuO and MgO layers and creates nucleation sites for subsequent EuO epitaxy. The ability for Eu atoms to find a favorable binding site in the 2×2 reconstructed TiO (see Fig 6.1 d)), results in the formation of EuO with oxygen supplied by the substrate.

6.5 Conclusion

In conclusion, electrostatic interactions at the interface between EuO and MgO can greatly determine the growth sequence of the EuO layer. To improve the epitaxy of EuO on MgO,

a TiO_2 interfacial template was introduced and shown to alleviate like-ion repulsion and decrease the structural mismatch between EuO and MgO. Furthermore, the initial growth sequence is drastically different with the TiO_2 interface than on the bare MgO as demonstrated by in-plane rotation and fast strain relaxation. Also, the addition of the TiO_2 layer allows for substrate-supplied oxidation leading to ultrathin ferromagnetic EuO films. Such a template could be an avenue for combining emerging materials onto MgO such as $EuTiO_3$ or other rock salt magnetic oxides in single crystal heterostructures

Chapter 7

Integration of the Ferromagnetic Insulator EuO with graphene

7.1 Introduction

The exchange proximity interaction (EPI) has been predicted to exist at the interface between a ferromagnetic insulator (FMI) and graphene, originating from an overlap of electronic wavefunctions [190, 210]. In particular, the ferromagnetic insulator EuO has been theoretically estimated to induce a spin splitting in graphene of the order 5 meV [190]. EPI has been suggested for novel spintronic device functionality in a wide variety of applications such as induced magnetism in graphene [190, 228, 218, 184], controllable magnetoresistance [190, 212, 351, 230], gate tunable manipulation of spin transport [210, 199], gate tunable exchange bias [213], spin transfer torque [239, 229], as well as being a necessary requirement

for the observation of the quantized anomalous Hall effect in graphene [207, 222]. While theoretical predictions have been numerous, EPI at the FMI/graphene interface has yet to be experimentally observed.

EuO is a model FMI as it exemplifies an isotropic Heisenberg ferromagnet [174]. EuO has a half filled 4*f* shell which determines the magnetic properties leading to a magnetization of 7 Bohr magnetons per Eu atom. Further, because the 4*f* shell is electrically inert due to its localized orbitals, the unoccupied exchange split $5d$ band governs the charge transport characteristics and exchange overlap in stoichiometric EuO. However, part of the reason that EPI has yet to be observed in the EuO/graphene system is due to the difficulty in materials synthesis of high quality stoichiometric EuO thin films. EuO is not thermodynamically stable and readily converts to nonmagnetic Eu_2O_3 [287]. Furthermore, oxygen deficient EuO_{1-x} exhibits a metal to insulator transition [177] with a conductive ferromagnetic phase [179, 181]. In typical materials synthesis techniques such as reactive molecular beam epitaxy (MBE), maintaining stoichiometry by flux matching generally leads to the formation of either Eu_2O_3 or EuO_{1-x}. In order to possibly realize EPI in graphene, a critical first step is the integration of high quality stoichiometric EuO thin films with graphene.

Only recently, through the development of a special growth regime, have reliable stoichiometric films been readily produced [181, 240, 241, 242, 243]. The regime can be understood as follows: a high-purity elemental Eu flux is incident upon a heated substrate maintained at a temperature for which the incident Eu atoms re-evaporate off the substrate surface (i.e. distillation). Notably, distillation is highly substrate dependent and works well on certain

oxides [241, 243], but fails in the case of direct growth on GaAs [242]. Once distillation is achieved, the introduction of a small oxygen partial pressure allows for the formation of EuO while excess Eu atoms are re-evaporated. This ensures proper stoichiometry of the EuO film [181, 240, 241, 242, 243]. If the oxygen partial pressure is increased, the EuO growth rate increases until a critical O_2 pressure is reached and Eu_2O_3 forms. In this way, the growth rate is determined by the oxygen pressure and is termed adsorption-controlled (distillation) and oxygen-limited. To date there is no evidence that stoichiometric EuO can be integrated with sp^2 bonded carbon based materials.

In this study, we employ reactive MBE to investigate the deposition of EuO thin films onto graphene. First, we examine the viability of Eu distillation for sp^2 bonded carbon materials by examining highly-oriented pyrolitic graphite (HOPG) substrate, which allows for standard thin film characterization techniques such as Auger spectroscopy, reflection high energy electron diffraction (RHEED), and x-ray diffraction (XRD). Within the distillation and oxygen-limited regime, stoichiometric EuO(001) is shown to grow epitaxially on HOPG(0001) substrate. Such films are shown to be uniform and flat by *ex-situ* atomic force microscopy (AFM). Further, EuO is integrated onto mechanically exfoliated graphene flakes as well as large area graphene grown by chemical vapor deposition (CVD). Raman spectroscopy after EuO deposition on exfoliated graphene exhibits the absence of a D peak, indicating that, despite the high temperatures of deposition, EuO thin films do not induce significant defects to the underlying graphene. This is supported by four point resistivity measurements that indicate only a slight reduction of mobility. Also, we investigate the magnetic properties of

EuO on HOPG and CVD graphene and find a Curie temperature (T_C) of 69 K, the bulk EuO value. This advance in materials synthesis allows for future studies of EPI at FMI/graphene interfaces.

7.2 Results and Discussion

First, we establish the growth parameters by investigating EuO growth on HOPG using Auger spectroscopy, RHEED, and XRD. Fresh surfaces of HOPG (SPI, grade ZYA) are obtained by peeling with 3M scotch tape and subsequently loaded into the UHV growth chamber and annealed at 600 °C for 30 min. Auger spectroscopy for a pristine HOPG surface is shown in Fig. 7.1 (top curve). The spectrum is characterized by a peak at 272 eV identifying carbon. Since the temperature required for efficient Eu distillation is highly substrate dependent, we cannot rely on previous results for distillation temperatures based on oxide substrates [181, 240, 241, 243]. Therefore, we first investigated the optimal re-evaporation temperature on HOPG. Without introducing a partial pressure of molecular oxygen, an incident Eu flux (8-9 Å/min.) is introduced to the substrate, which is maintained at a fixed temperature. Fig. 7.1 shows Auger spectra for Eu metal deposited at room temperature (RT), 450 °C, 500 °C, 550 °C, and 600 °C. For each substrate temperature, Eu is deposited for the time equivalent to produce a 5 nm Eu film at RT. Eu Auger peaks at 83, 104, 124, and 138 eV can be seen in the RT spectrum of Fig. 7.1. As the substrate temperature is increased, the relative peak height of Eu to C decreases indicating a smaller amount of Eu material on

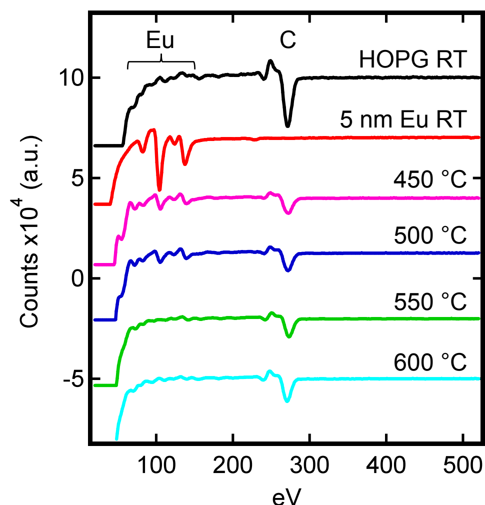

Figure 7.1: Auger Spectroscopy of Eu Deposited on HOPG at Several Different Substrate Temperatures. Pristine HOPG (black) shows a carbon peak at 272 eV. 5 nm Eu deposited at room temperature (red) shows Eu peaks only. At higher growth temperatures a combination of Eu and C peaks are present. Above 550 °C there is no evidence of Eu in the spectrum.

HOPG. This indicates the onset of re-evaporation of the Eu atoms. For the case of 550 °C and 600 °C, the Auger spectra shows only the carbon peak at 272 eV and no evidence of Eu material. Therefore, full distillation of Eu on HOPG is achieved above 550 °C.

Once in the distillation regime, the introduction of an oxygen flux smaller than the elemental Eu flux should produce stoichiometric EuO films. We investigate the formation of EuO on HOPG substrate by maintaining the substrate at 550 °C for distillation and then introduce a molecular oxygen partial pressure ($P_{O_2} = 1.0 \times 10^{-8}$ Torr) into the UHV system. *In-situ* RHEED images probe the sample surface crystalline structure. Fig. 7.2 a) and b) show the RHEED patterns for HOPG and the EuO layer after 5 nm of growth, respectively. The RHEED pattern for the HOPG substrate is unaltered upon in-plane rotation. This is expected since HOPG has out-of-plane (0001) orientation but has in-plane rotational disorder. The RHEED pattern of the EuO layer shows double streak features and in-plane rotation has

no effect on the RHEED pattern, similar to the HOPG substrate. Examination of the EuO RHEED diffraction rods indicates EuO(001) with a superposition of both [100] and [110] in-plane orientations [243]. We can better understand the growth evolution of the EuO film by examining the time lapse of a line cut of the RHEED pattern. A typical line cut, as depicted in Fig. 7.2 a) (red dashed line), samples the intensity of several diffraction rods across the RHEED pattern. Fig. 7.2 d) displays the time evolution of a line cut for EuO growth on HOPG in the distillation and oxygen-limited regime. Between 0 min. and dashed line d1, the high intensity streaks correspond to the diffraction rods as seen in Fig. 7.2 a) of the pristine HOPG pattern. Dashed line d1 indicates the introduction of Eu flux, during which time the HOPG diffraction rods remain unchanged as Eu re-evaporates off the HOPG surface. A partial pressure of oxygen ($P_{O_2} = 1.0 \times 10^{-8}$ Torr) is leaked into the chamber at dashed line d2. The subsequent time evolution shows a smooth transition from HOPG streaks to EuO indicating epitaxial growth.

Eu_2O_3 can be grown by increasing the O_2 partial pressure to 3×10^{-7} Torr. The Eu_2O_3 RHEED pattern is displayed in Fig. 7.2 c) and shows a clear distinction from the oxygen-limited growth which produces EuO. We further investigate the difference between the two oxygen regimes by looking at their respective Auger data as shown in Fig. 7.2 e). An oxygen peak at 510 eV is present for both samples. To our knowledge this is the first report on Auger spectroscopy for EuO. Taking the Eu 104 eV peak, EuO has a Eu:O peak ratio of 6.63, while Eu_2O_3 has a Eu:O ratio of 4.34 indicating increased oxygen content in Eu_2O_3. Comparison of the ratios 6.63/4.34 = 1.53 to the expected Eu:O/Eu_2:O_3 = 1.5 is in close

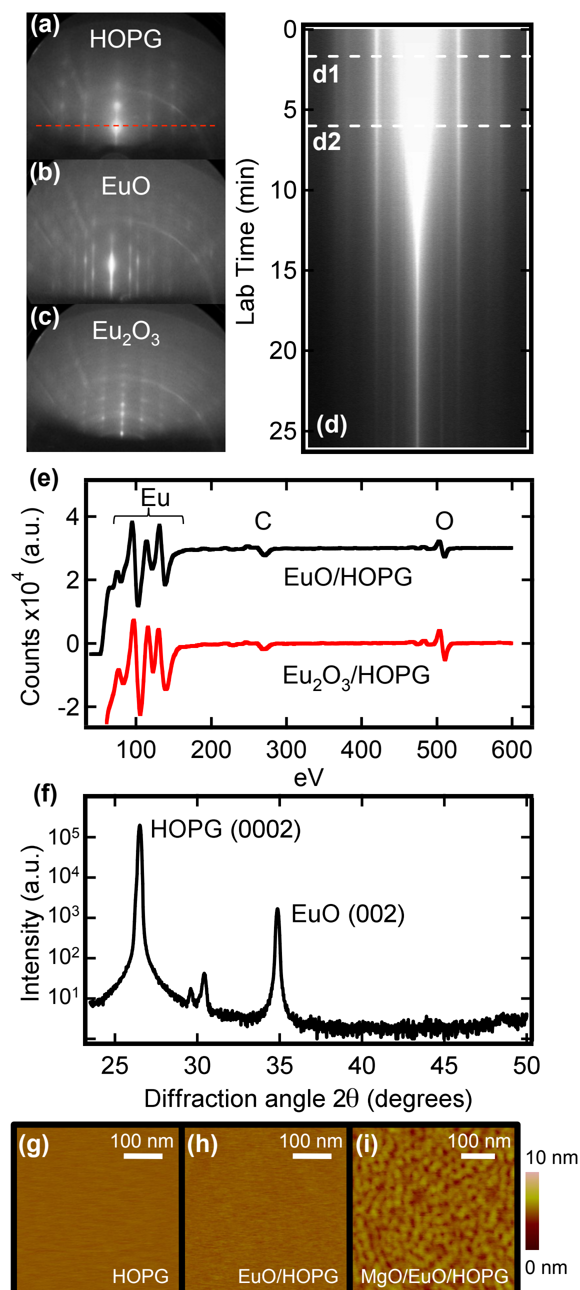

Figure 7.2: Characterization of EuO Thin Films on HOPG. a)-c) RHEED patterns for pristine HOPG, 5nm EuO deposited on HOPG, and Eu_2O_3 on HOPG. d) Time evolution of dashed red curve in a). Dashed line d1 indicates the opening of the Eu shutter and incidence of Eu flux to the substrate. Dashed line d2 signifies the introduction of molecular oxygen into the chamber. e) Auger spectroscopy of EuO/HOPG and Eu_2O_3/HOPG. f) XRD θ-2θ scan showing the HOPG (0002) peak and EuO (002) peak. g)-i) *ex-situ* AFM scans for peeled HOPG, EuO(5 nm)/HOPG(0001), and MgO(2 nm)/EuO(5 nm)/HOPG(0001) in order from left to right.

agreement. However, it should be noted that while this analysis is useful in verifying oxygen content between the two growths (i.e. EuO vs. Eu_2O_3), it is not sufficient for determining precise stoichiometry of the EuO oxidation state.

Ex-situ XRD θ-2θ scans, Fig. 7.2 f), serve to elucidate the structure of EuO deposited on HOPG. For XRD measurements, approximately 50 nm EuO was grown on HOPG and capped with 3 nm polycrystalline Al. A clear EuO (002) peak is seen in the θ-2θ scan and there are no other peaks associated with another EuO orientation indicating that entire EuO film is oriented (001), in agreement with the RHEED analysis. There are no detectable peaks associated with Eu_2O_3. There are two small peaks at 29.63 $^\circ$ and 30.43 $^\circ$ associated with Eu_3O_4 (040) and (320), possibly due to oxidation through the thin capping layer.

It is generally expected that FCC materials (EuO, Ni, etc..) would favor (111) orientations with hexagonal materials due to the surface symmetry. However, the RHEED and XRD data clearly indicate the orientation EuO(001)/HOPG(0001) is preferred. In the absence of other factors, the orientation preference may be partly explained by the lattice mismatch between EuO and graphene. EuO has a bulk lattice constant of 0.514 nm and 0.246 nm for graphite, leading to a lattice mismatch of 4.3% for EuO(001)/HOPG(0001) growth orientations. The mismatch for EuO(111)/HOPG(0001) is either 10% or 17% depending on the ratio of relative lattice spacings (i.e. 1:4 or 1:3 for EuO:graphene). However, while mismatch considerations might suggest a favorable orientation, it cannot explain the lack of symmetry between the rock salt surface and graphene. Previous work [243] has shown lattice mismatch to be less of a key factor for EuO epitaxy than other growth concerns. Surface energies, which are lowest

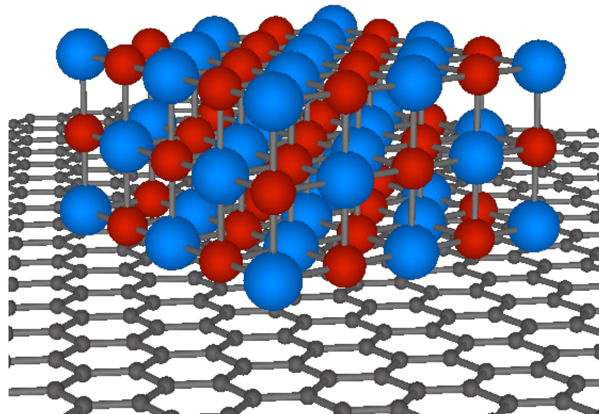

Figure 7.3: Schematic of EuO Crystal on Graphene. VESTA drawing of EuO(001) on graphene surface. Blue atoms correspond to europium, red to oxygen, and grey to carbon.

for (100) rock salt surfaces [352], are likely relevant and may provide a possible explanation for the observed growth orientation. A schematic for the structure is displayed in 7.3.

To investigate the surface morphology of the EuO films, we have performed *ex-situ* AFM on peeled HOPG(0001) substrate, a EuO(5 nm)/HOPG(0001) film, and a MgO(2 nm)/EuO(5 nm)/HOPG(0001) bilayer. The resulting AFM scans are displayed in Fig. 7.2 g), h), and i), with rms roughness values 0.1 nm, 0.2 nm, and 0.5 nm, respectively. It must be noted that the EuO surface is likely oxidized to Eu_2O_3 during the *ex-situ* measurement. In any case, the scans clearly show that the films are uniform, relatively flat, and pinhole free. This is crucial for possible use as a gate dielectric.

Due to EuO's large magneto-optic response [176], the magneto-optic Kerr effect (MOKE) serves as a sensitive probe of the magnetic behavior of the sample. Linearly polarized light is reflected off the sample surface and the resulting polarization rotates an amount, θ_K, which is proportional to the magnetization of the film. The sample structure is Al (2 nm)/EuO (5

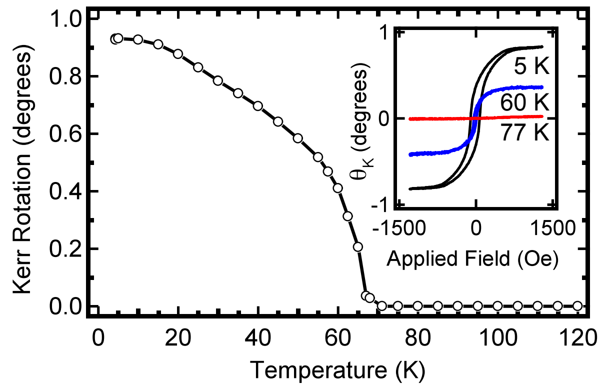

Figure 7.4: Temperature Dependence of the Magnetization of EuO/HOPG. Data is obtained through the Magneto-optic Kerr effect (MOKE). Inset shows several characteristic hysteresis loops at different temperatures.

nm)/HOPG(0001) and is measured in an optical flow cryostat separate from the UHV growth chamber. Fig. 7.4 inset shows magnetic hysteresis loops measured at 5 K, 60 K, and 71 K. At 5 K, the remanence (M_R/M_S) is 0.37, the coercive field (H_C) is 87 Oe, and the saturation Kerr rotation is 0.93 degrees. Fig. 7.4 shows a temperature dependence of the saturation magnetization with T_C = 69 K, the bulk value for EuO.

While EuO/HOPG serves as a useful system for examining the epitaxy of EuO on sp^2 bonded carbon and allows for the use of standard thin film characterization techniques, realization of EPI at EuO/graphene interfaces requires direct integration of EuO on either exfoliated or CVD graphene. Graphene flakes are mechanically exfoliated onto 300 nm SiO_2/Si substrate using standard techniques [41]. Single layer (SLG), bilayer (BLG), and trilayer (TLG) flakes are identified under an optical microscope and confirmed by Raman spectroscopy [353]. A 5 nm EuO film is deposited on top of exfoliated graphene flakes on SiO_2 and capped with 2 nm MgO. Fig. 7.5 a) shows an optical microscope image of pristine

graphene flakes while Fig. 7.5 b) shows the same flakes after EuO deposition with noticeable darkening of the graphene flakes. Raman spectroscopy (535 nm laser) of EuO/graphene for several flake thicknesses is shown in Fig. 7.5 c). Several key features are immediately apparent for EuO deposited onto graphene flakes. First, we do not observe a D peak above the noise level of the measurement. The D peak is typically associated with induced disorder [310, 354, 355] suggesting that the deposition process does not induce significant defects when compared with reports for oxide growth by PLD, e-beam, and sputter deposition [356]. Second, the G peak shrinks in relative size compared with features above 2200 cm^{-1} due to decreased signal from the impeding EuO overlayer. Lastly, the spectra exhibit a significant modification around the graphene 2D peak. To better understand this behavior, we compare with single crystal EuO on lattice-matched YSZ(001) [241, 242]. Fig. 7.5 d) shows the Raman spectra for EuO/SLG and EuO/YSZ around the graphene 2D peak. The features are nearly identical, indicating they are not related to graphene phonon modes.

Raman spectroscopy is a useful technique for investigating external effects on graphene such as doping, strain, and defects [354, 355, 356, 357, 358, 359, 360, 361, 362]. A closer examination of the graphene G peak for 5 nm EuO deposited on SLG (Fig. 7.5 e)) shows blue shifting of the G peak by 14 cm^{-1}, from 1581 cm^{-1} to 1595 cm^{-1}. We also note blue shifts for EuO/BLG and EuO/TLG of 10 cm^{-1} and 6 cm^{-1}, respectively. Both charge doping and induced strain could possibly explain the blue shifted G peak after EuO deposition [357, 358, 359, 360, 361, 362]. For SLG, while a shift of 14 cm^{-1} would suggest an induced charge doping greater than 6×10^{12} cm^{-2}, an increase in the carrier concentration of that

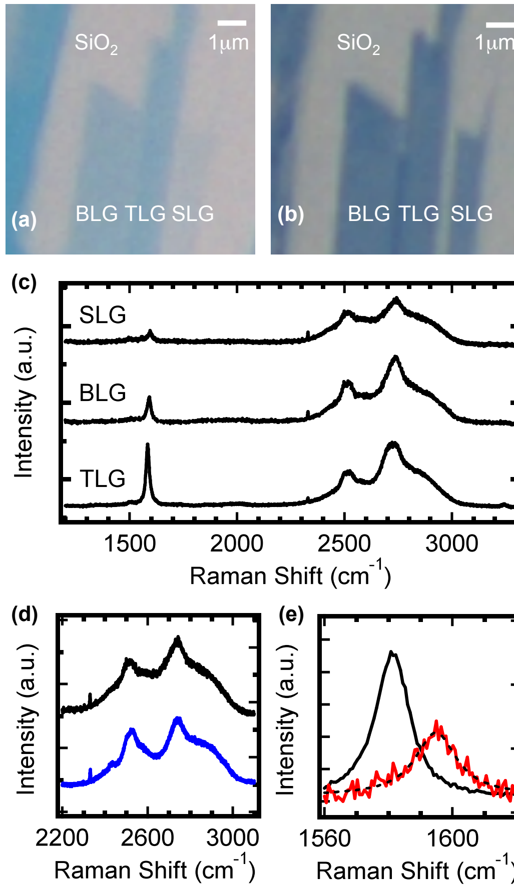

Figure 7.5: EuO Thin Films Deposited on Exfoliated Graphene Flakes. a) Optical microscope image of SLG, BLG, and TLG on SiO_2/Si substrate before EuO deposition. The scale bar indicates 1 μm. b) Optical microscope image of of the same sample after EuO deposition. c) Raman spectroscopy of EuO deposited on single layer, bilayer, and trilayer graphene. d) Raman spectroscopy of EuO/SLG (black) compared to EuO/YSZ(001) (blue) in the region around the 2D peak. e) Raman spectroscopy of the G band for pristine SLG (black) compared to EuO/SLG (red) with the intensities scaled for ease of viewing. Dashed black line is a Lorentzian fit to the G peak for EuO deposited on SLG.

magnitude is expected to decrease the FWHM by approximately 8 cm^{-1} [357]. Interestingly, for EuO deposited on graphene flakes, the FWHM of the G peak is 13 cm^{-1} for pristine graphene and 15 cm^{-1} with EuO, making charge doping unlikely as the sole cause of the G peak shift. Alternatively, the shift could be caused by strain and is comparable to that reported for annealed SiO_2/graphene/SiO_2 [359]. The 2D peak would shed light on this issue, but is not accessible due to the EuO overlayer.

Next, we discuss the effect of an EuO overlayer on charge transport. Graphene devices are fabricated using standard e-beam lithography techniques with Ti/Au (10 nm/60 nm) electrodes [51]. The resistivity is measured using 1 μA excitation at 11 Hz AC for lock-in detection in a four point geometry. Fig. 7.6 shows the resistivity for pristine SLG (black curve) with charge neutrality point at V_{CNP} = 8 V. The device is then loaded into the MBE chamber for growth of 2 nm EuO followed by a 2 nm MgO capping layer. The charge neutrality point after growth (red curve) is V_{CNP} = -2 V. The electron mobility can be determined from the slope of the conductivity ($\mu = \Delta\sigma/e\Delta n$). The carrier concentration, n, is determined from the relation $n = -\alpha(V_G - V_{CNP})$, where $\alpha = 7.2 \times 10^{10}$ V^{-1}cm^{-2} for 300 nm SiO_2 gate dielectric. The resulting electron mobility for pristine SLG and EuO/SLG are $\mu_e = 4600$ cm^2/Vs and $\mu_e = 4080$ cm^2/Vs, respectively. Thus, the deposition of EuO on the graphene surface, does not significantly decrease the mobility.

Lastly, we investigate the magnetic properties of EuO/graphene. For this, we employ large-area graphene which has been demonstrated to produce high-quality films with large grains [48], and is therefore desirable for MOKE characterization which has a spot size with

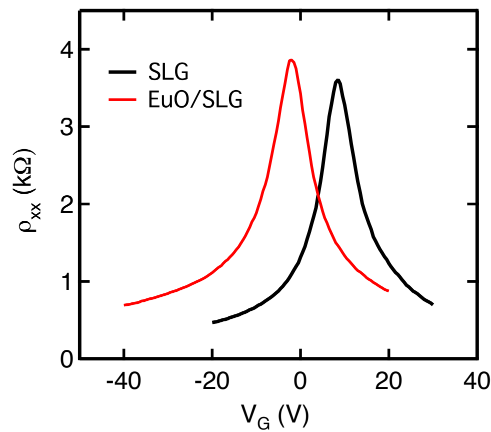

Figure 7.6: Gate Dependent Resistivity for EuO/graphene. Au/Ti Hall geometry device is patterned on exfoliated graphene flakes. Black curve corresponds to pristine graphene and red curve for the same device with MgO(2 nm)/EuO(2 nm) overlayer.

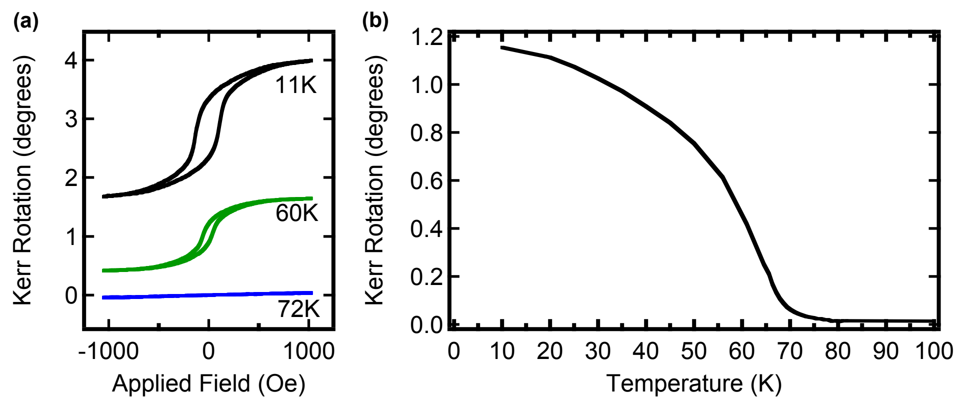

Figure 7.7: MOKE for EuO Grown on CVD Graphene. a) Several characteristic hysteresis loops at different temperatures for 5 nm EuO deposited onto CVD graphene on SiO_2/Si. b) Temperature dependence of the magnetization measured in degrees.

$\sim$40 μm diameter. Large area graphene is grown by chemical vapor deposition on copper foil and subsequently transferred to SiO_2/Si [48]. Next, 5 nm EuO thin film with 2 nm MgO capping layer is deposited on the CVD graphene in the distillation and oxygen-limited regime. Fig. 7.7 a) shows several MOKE hysteresis loops taken at 11 K, 60 K, and 72 K. As typical with EuO thin films, we observe a large Kerr rotation above 1 degree, which subsequently decreases in magnitude as the temperature is increased towards the Curie temperature of 69 K as shown in Fig. 7.7 b).

7.3 Conclusion

We have investigated the integration of the ferromagnetic insulator EuO with graphene. Using Auger spectroscopy, we find that distillation (re-evaporation) of Eu from the graphene surface occurs for temperatures above 550 °C. Employing the distillation and oxygen-limited regime, EuO was deposited on HOPG and graphene. The structural, chemical, and magnetic properties of these heterostructures were investigated by RHEED, XRD, AFM, Raman, Auger, and MOKE. EuO films grow epitaxially on honeycomb carbon with (001) orientation and the EuO does not induce significant defects in the exfoliated graphene. The growth technique presented here, demonstrates a significant materials advance in the field of oxide growth on graphene, which is notoriously difficult due to the chemically inert nature of the sp^2 surface. EuO films exhibit ferromagnetism with a Curie temperature of 69 K, equal to the bulk value. The excellent structural and magnetic properties combined with the direct in-

tegration without the aid of a buffer layer is a key advance towards experimental observation of the exchange proximity effect at the EuO/graphene interface.

7.4 Experimental Methods

Elemental europium metal (99.99%) is evaporated from a low temperature thermal cell. After proper degassing, a Eu background pressure below 4×10^{-9} Torr is maintained for rates between 8-9 Å/min. Molecular oxygen (99.999%) is leaked into the chamber and the partial pressure is determined by leaking in an amount P_{O_2} above the background pressure as measured by an ion gauge. Typically, a partial oxygen pressure of 1×10^{-8} Torr is used for which 30 min. growth time produces films approximately 5 nm thick [242]. The substrate temperature is monitored by a thermocouple located on the platen face. The UHV MBE chamber has a base pressure of $\sim 1 \times 10^{-10}$ Torr and is equipped with *in-situ* RHEED. Samples are transferred to an adjacent chamber for 3 keV Auger spectroscopy with a base pressure less than 5×10^{-9} Torr. XRD measurements were performed at UCSB MRL Central Facilities. Longitudinal MOKE is performed in an optical flow cryostat with a *p*-polarized laser beam (635 nm) and an incidence angle of 45 degrees with respect to the in-plane magnetization direction. The laser intensity is 100 μW focused to a spot size of $\sim$40 μm in diameter. Large-area graphene is produced by low pressure CVD as reported by Li, *et al.* [48]. 25 μm thick Cu foil (Alfa Aesar, item No. 13382) is loaded into a tube furnace and heated to 1035 $^\circ$C. After a 10 min. anneal in H_2 with a flow rate of 2 sccm and pressure, $P_{furnace}$= 2.5×10^{-2} mbar,

7 sccm of CH_4 is introduced for a total pressure of 1.4×10^{-1} mbar. After cooling down and removal from the furnace, the Cu is etched away with iron nitrate and transferred onto SiO_2/Si substrate with the aid of poly-methyl methacrylate (PMMA) as mechanical support. The PMMA is removed with acetone at room temperature and followed by IPA cleaning. Before EuO growth, the large area graphene sample is annealed at 600 $^\circ$C under UHV condition.

Reprinted (adapted) with permission from (*ACS Nano*, 2012, **6** (11), pp 1006310069). Copyright (2012) American Chemical Society.

Chapter 8

Magnetic Moment Formation in Graphene Detected by Scattering of Pure Spin Currents

8.1 Introduction

Many fascinating predictions have been made regarding magnetism in graphene including the formation of magnetic moments from dopants, defects, and edges [315, 316, 363, 364, 320, 317, 322, 365]. While several experimental techniques provide insight into this problem [330, 309, 329, 328, 327, 325, 324, 326, 332, 333, 165, 366, 367], lack of clear evidence for magnetic moment formation hinders development of this nascent field. Studies based on bulk magnetometry [330, 309, 329, 328, 327, 325, 324, 326] directly measure mag-

netic properties, but because it measures the total magnetic moment (not just the signal from graphene) it is difficult to rule out artifacts from environmental magnetic impurities. Transport [332, 333, 165] and scanning tunneling microscopy (STM) [366, 367] locally probe the graphene, but so far these measurements have been charge-based, so data are subject to various interpretations [334]. Thus, in order to convincingly demonstrate the formation of magnetic moments inside graphene due to dopants and defects, it is essential to employ techniques that directly probe the intrinsic spin degree-of-freedom of the magnetic moment while ensuring the signal originates from the graphene sheet under investigation.

Here, we utilize pure spin currents to demonstrate that hydrogen adatoms and lattice vacancies generate magnetic moments in single layer graphene. Pure spin currents are injected into graphene spin valve devices and clear signatures of magnetic moment formation emerge in the non-local spin transport signal as hydrogen adatoms or lattice vacancies are systematically introduced in an ultrahigh vacuum (UHV) environment. Specifically, introduction of these point defects generate a characteristic dip in the non-local signal as a function of magnetic field. This feature is due to scattering (relaxation) of pure spin currents by localized magnetic moments in graphene and is explained quantitatively by a phenomenological theory based on spin-spin exchange coupling between conduction electrons and magnetic moments. Furthermore, we observe effective exchange fields due to this spin-spin coupling, which are of interest for novel phenomena and spintronic functionality [190, 210, 199, 207] but have not been seen previously in graphene. This work provides the strongest and most clear evidence for magnetic moment formation in graphene to date, and does so for the following reasons:

(1) certainty that the signal comes from the graphene flake, (2) as a spin-dependent measurement, it directly probes the magnetic moments spin degree of freedom, (3) systematic *in-situ* measurement with appropriate control experiments, (4) comprehensive phenomenological theory developed in conjunction with the experimental data, and (5) the observation of similar effects resulting from hydrogen and vacancies, which are structurally and chemically dissimilar, thereby supporting the mechanism predicted for both systems based on removal of p_z-orbitals from the π-band. Lastly, these results demonstrate a method for utilizing localized magnetic moments to manipulate conduction electron spins and demonstrate magnetic field effect behavior as demonstrated by gate tunability of the effective g-factor.

8.1.1 The Proposed Experiment

For a systematic investigation, the spin transport measurement is first performed on a pristine single layer graphene (SLG) spin valve as a control measurement. Then, dopants/defects are controllably introduced to the SLG and the measurement is repeated. The sample remains in UHV during the entire process. Therefore, observed signatures of magnetic moment formation are caused by the adsorbed hydrogen or lattice vacancies. A schematic of the proposed experiment is displayed in Fig. 8.1.

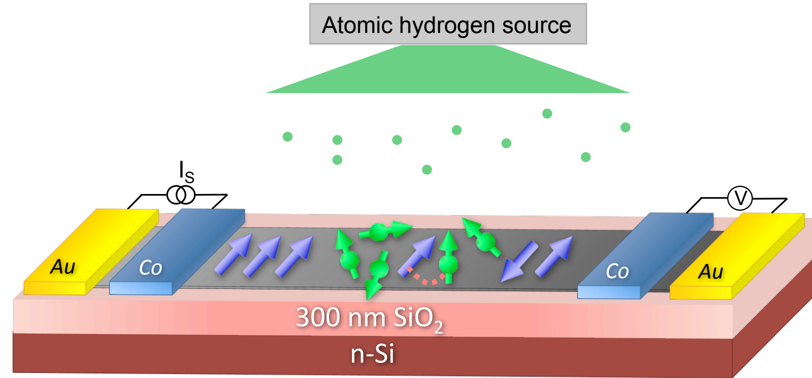

Figure 8.1: Schematic of the *in-situ* deposition of H and Interaction with the Spin Current. The magnetic moments (green arrows) induced by hydrogen doping interact (red dashed line) via exchange with the injected spins (blue arrows) diffusing along the graphene channel.

8.2 Spin Transport in Pristine Graphene

Experiments are performed on non-local SLG spin valves [29, 32, 25] (Fig. 8.2 a)) consisting of two outer Au/Ti electrodes (a and d) and two ferromagnetic (FM) Co electrodes that make contact to SLG across MgO/TiO_2 tunnel barriers (b and c). The Co electrodes are capped with 5 nm Al_2O_3 to protect from hydrogen exposure. The tunnel barrier and capping layer are present only at the site of the FM electrodes, leaving the rest of the graphene uncovered. The device is fabricated on a SiO_2/Si substrate (300 nm thickness of SiO_2) where the Si is used as a back gate. Details of device fabrication are published elsewhere [71, 25, 34].

The charge and spin transport properties of pristine SLG spin valves are measured at 15 K using lock-in techniques. The gate dependent resistivity (ρ_G) of a representative sample A (black curve in Fig. 8.2 b)) exhibits a maximum at the gate voltage (V_G) of 0 V, which defines the Dirac point ($V_D = 0$ V). This sample exhibits mobility (μ) of 6105 cm^2/Vs. To investigate spin transport in the SLG device (Fig. 8.2 a)), a current (I) is applied between electrodes b

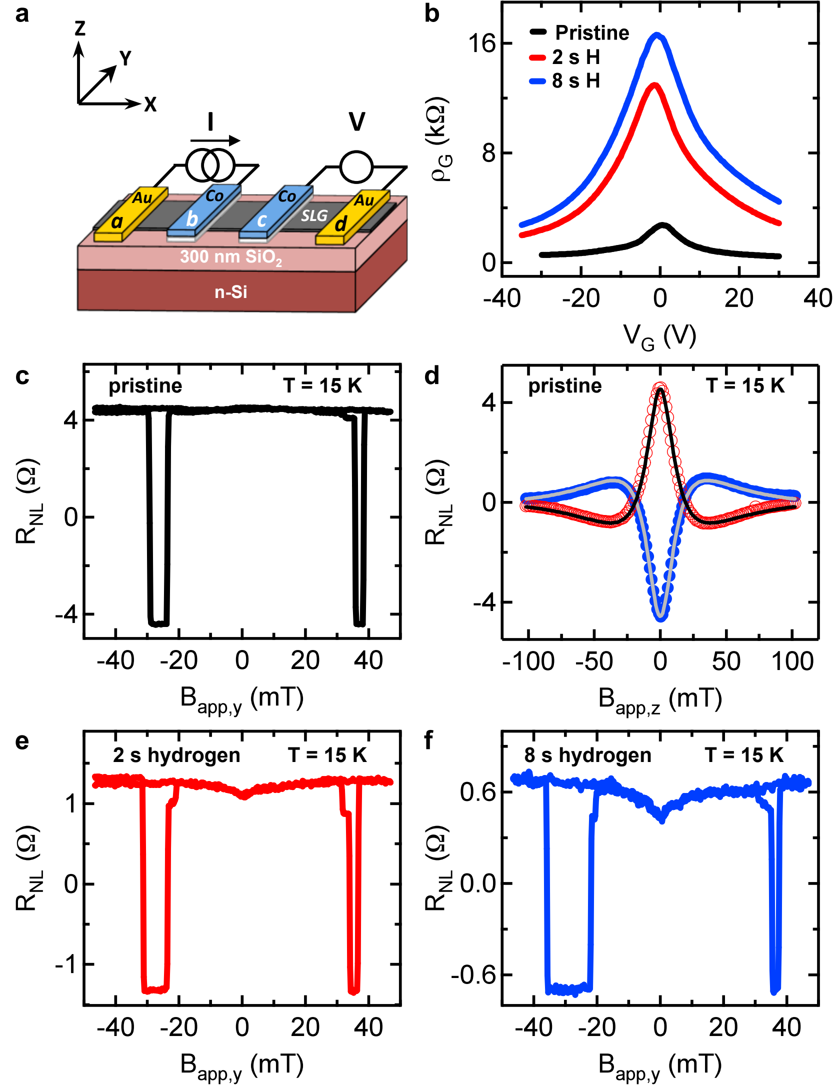

Figure 8.2: The Effect of Hydrogen Exposure on Charge and Spin Transport in SLG at 15 K. a) Schematic illustration of the non-local spin valve device. b) Gate dependent resistivity for the pristine graphene (black) and following exposure to atomic hydrogen for 2 s (red) and 8 s (blue). Upon hydrogen doping, the Dirac point shifts from 0 V to -1 V. c) Non-local spin transport measurement for pristine graphene. d) Hanle spin precession measurement on pristine graphene. e), f) Non-local spin transport measurements after atomic hydrogen exposure for 2 s and 8 s, respectively. Both curves exhibit a dip in R_{NL} at zero applied field, which is caused by spin relaxation induced by localized magnetic moments.

and a, injecting spin-polarized carriers into graphene directly below the FM injector, b. The spin population diffuses along the sample as a pure spin current (x-axis) and the spin density is measured at the FM spin detector, c, as a voltage difference (V) between electrodes c and d. An applied magnetic field ($B_{app,y}$) along the electrode magnetization direction (y-axis) is used to control the relative orientation of spin injector and detector magnetizations. For parallel alignment, the measured non-local resistance ($R_{NL} = V/I$) is positive whereas for antiparallel alignment R_{NL} is negative. The non-local spin signal is defined as the difference between parallel and antiparallel states ($\Delta R_{NL} = R_{NL}^{P} - R_{NL}^{AP}$). A typical scan of R_{NL} as a function of $B_{app,y}$ (Fig. 8.2 c)) displays discrete jumps as the electrode orientation changes between parallel and antiparallel. This sample exhibits a ΔR_{NL} of 8.8 Ω (sample A with $V_G - V_D$ = -15 V). A constant spin-independent background is subtracted from all R_{NL} data presented in this study. Out-of-plane magnetic fields are applied to generate spin precession, and the resulting data (Fig. 8.2 d), red for parallel, blue for antiparallel) are fit by the standard Hanle equation [32, 25] (solid curves) to determine the spin lifetime (τ_{so} = 479 ps) and diffusion coefficient (D = 0.023 m^2/s). The corresponding spin diffusion length is $\lambda = \sqrt{D\tau^{so}}$ = 3.3 μm. Based on these values and a non-local spin signal of 8.8 Ω, the spin polarization of the junction current (P_J) is calculated to be 20% [31].

8.3 Hydrogen Doping of Graphene Spin Valves

A commercial Omicron source is used to expose SLG spin valve devices to atomic hydrogen at 15 K. Diatomic hydrogen is cracked inside a tungsten capillary tube that is heated by electron bombardment. The amount of hydrogen introduced to the chamber is controlled via a leak valve, which is tuned to maintain a chamber pressure of 1×10^{-6} torr (the base pressure of the chamber is below 1×10^{-9} torr). The heating power of the Omicron source is determined by the high voltage (HV) applied to the capillary and the emission current between capillary and filament (I_{em}). We use the parameters HV=1 kV and I_{em}=80 mA. The distance from source to sample is 100 mm. A shutter positioned between the SLG spin valve and hydrogen source is used in order to control the exposure time. Additionally, deflector plates are used to steer any charged ions away from the sample.

The exposure of SLG spin valves to atomic hydrogen substantially modifies charge transport properties, such as ρ_G and μ (Fig. 8.2). We obtain an order of magnitude estimate for the hydrogen concentration based upon the changes in charge transport properties assuming adsorbed hydrogen induces resonant scattering. Comparing with previous experimental work on resonant scattering in graphene via fluorine doping [165] and lattice vacancies [161], the hydrogen concentration is estimated to be on the order of 0.1% for 8 s hydrogen exposure to sample A. This indicates samples are in the dilute limit of hydrogen coverage.

Atomic hydrogen is introduced to spin valve devices at 15 K at a chamber pressure of 1×10^{-6} torr. Following 2 s hydrogen exposure, the gate dependent ρ_G (red curve in Fig. 8.2b)

is dramatically increased. An additional 6 s of exposure (8 s total) further increases ρ_G (blue curve of Fig. 8.2 b)) and decreases the mobility to 495 cm^2/Vs. Based on the change in the resistivity, we make an order of magnitude estimate for the hydrogen coverage of 0.1%. Accompanying the changes in charge transport are also changes in spin transport. Figures 8.2 e) and 8.2 f) display R_{NL} of sample A at $V_G - V_D$ = -15 V as a function of $B_{app,y}$ following 2 s and 8 s of exposure, respectively. The initial ΔR_{NL} of 8.8 Ω is reduced to 2.6 Ω after 2 s of hydrogen exposure and further reduced to 1.4 Ω after 8 s. Interestingly, the R_{NL} scans exhibit a dip centered at zero applied field. The dip in R_{NL} is prevalent for both up and down sweeps of $B_{app,y}$ at all measured gate voltages and has been reproduced on multiple samples following hydrogen exposure. The ratio of the dip magnitude to ΔR_{NL} is found to increase with increasing hydrogen exposure (comparing Fig. 8.2 e) and 8.2 f)), indicating the dip feature is dependent on the amount of adsorbed hydrogen.

8.4 Origin of the Dip in R_{NL}: Control Experiments

To understand the origin of the dip in R_{NL}, we examine the expression for non-local resistance generated by spin transport [31],

$$R_{NL}^{(P/AP)} = \pm 2R_G e^{\frac{-L}{\lambda}} \prod_{i=1}^{2} \left(\frac{P_J \frac{R_i}{R_G}}{1-P_J^2} + \frac{P_F \frac{R_F}{R_G}}{1-P_F^2} \right) \times \left[\prod_{i=1}^{2} \left(1 + \frac{2\frac{R_i}{R_G}}{1-P_J^2} + \frac{2\frac{R_F}{R_G}}{1-P_F^2} \right) - e^{\frac{-2L}{\lambda}} \right]^{-1} \quad (8.1)$$

where $R_G = \rho_G \lambda / w$ is the spin resistance of graphene, w is the graphene width, $R_F = \rho_F \lambda_F / A_J$ is the spin resistance of the cobalt, ρ_F is the cobalt resistivity, λ_F is the cobalt spin

diffusion length, A_J is the junction area, P_F is the spin polarization of cobalt, R_1 and R_2 are the contact resistances of the spin injector and detector, respectively, and L is the distance from injector to detector. This equation shows that the spin density at the detector electrode depends on both charge and spin properties. First, we confirm that the SLG resistivity does not change with magnetic field, so the dip is not related to changes in charge transport (8.4.1). Also, we verify that the dip is not related to hydrogen-induced changes to the magnetic properties of the FM electrodes. Specifically, the effect of hydrogen exposure is reversible upon thermal cycling to room temperature and the anisotropic magnetoresistance of the Co electrodes are not affected by hydrogen exposure (8.4.3). Next, we perform minor loop analysis on sample B (Fig. 8.8 a)) by reversing the magnetic field sweep immediately after the first magnetization reversal. The inversion of the dip in the antiparallel state (red curve) proves that the dip is due to increased spin relaxation at low fields. Furthermore, we rule out hyperfine coupling to nuclear spins as the origin of this increased spin relaxation (8.4.2).

8.4.1 Excluding Field-Dependent Resistivity Effects

Equation 8.1 shows that changes in the resistivity of graphene could change the spin density at the detector electrode. Thus, magnetic field dependent changes to the graphene resistivity could in principle produce variations in R_{NL}. To investigate this possibility in hydrogen-doped graphene, gate dependent ρ_G measurements are performed on sample B at three distinct in-plane magnetic fields (Fig. 8.3). The three curves are indistinguishable, showing that the applied magnetic field has no effect on the measured ρ_G of hydrogen-doped

samples. As presented in the Figs. 8.2 e), f) and 8.8 a), b), the R_{NL} signal increases by tens of mΩ as the magnetic field is increased away from $B_{app,y}$= 0 mT, corresponding to an increase of several percent. If this change is due to a magneto-resistance effect, the gate dependent resistivity curves measured at discrete in plane fields must also differ by hundreds of Ω to kΩ and will be clearly detected in the scan presented in Figure 8.3. As evident in Fig. 8.3, ρ_G vs. V$_G$ is unaffected by the applied magnetic field, confirming the source of the measured dip in R_{NL} does not stem from any magnetoresistance effects.

For completeness, we present a detailed scan of the four point (4pt.) resistance vs. $B_{app,y}$ performed on Sample C and compare it to the field dependence of non-local resistance. Fig. 8.4 a displays a large dip feature on a hydrogen doped graphene sample at T=15 K and associated minor loop to verify the signal is due to spin scattering. On this sample, the R_{NL} signal at $B_{app,y}$=0 mT is 24% of the high field value. In Fig. 8.4 b), we show the in-plane field dependence ($B_{app,y}$) of the 4pt resistance. The noise level of the data is 8-10 Ω while 4pt Resistance is 7535 Ω which is 0.1% of the signal and no dip feature is observed. 8.4 c) compares the relative change in resistances, $\Delta R_{NL}/R_{NL}$ (left axis) and 4pt $\Delta R/R$ (right axis), normalized to the high field values. The data shows there is no field dependence in the charge transport of hydrogen-doped graphene, therefore excluding variations in ρ_G as the source of the measured dip in R_{NL}.

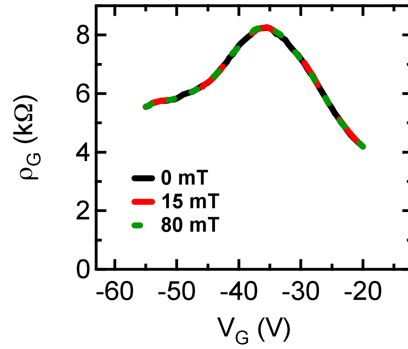

Figure 8.3: Investigating the Source of the Dip Measured in R_{NL}: Changes in Resistivity. Gate-dependent ρ_G of SLG after hydrogen exposure measured at several discrete in-plane applied magnetic fields. The applied field has no effect on the charge transport behavior of the graphene device.

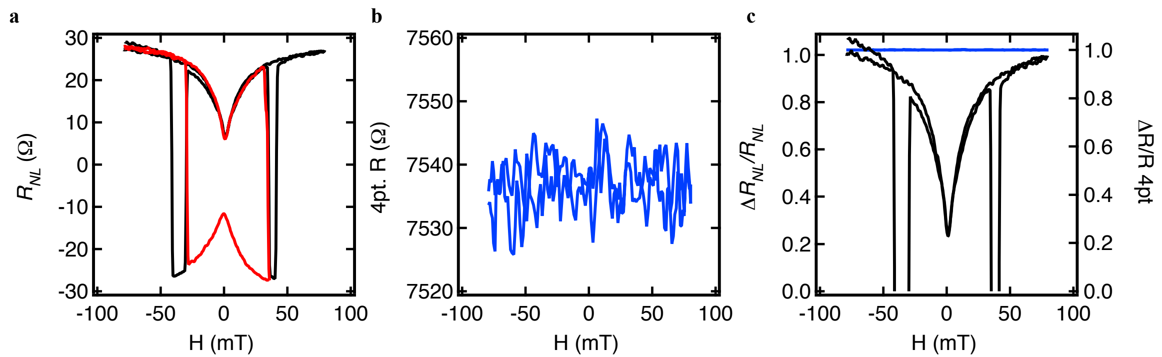

Figure 8.4: Comparison of Percent Change for R_{NL} and Resistivity. a) Non-local MR (R_{NL}) (black curve) and corresponding minor loop (red curve) for hydrogen doped graphene sample C at T = 15 K. b) Four point (4pt.) resistance of the same graphene channel as a function of the in-plane applied field ($B_{app,y}$)). Noise level is 8-10 Ω for 7.5 kΩ or 0.1% of the signal. c) Relative change of R_{NL} (black) and the 4pt Resistance (blue).

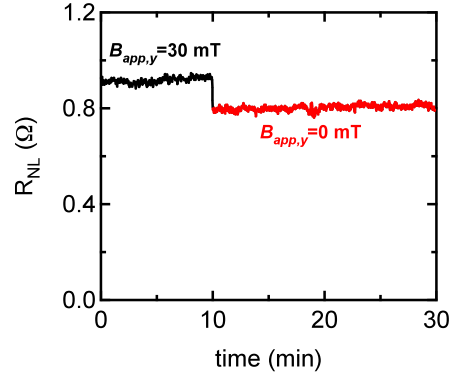

Figure 8.5: Test of Nuclear Spin Effects. The non-local spin transport signal is measured for 10 min while $B_{app,y}$=30 mT (black). This ensures any possible nuclear spins will reach steady state. The field is ramped to zero, and held constant for the following 20 min (red). The observed response excludes hyperfine coupling to nuclear spins as the origin of the dip in R_{NL}.

8.4.2 Excluding Nuclear Spin Effects

We investigate the possibility that the observed dip in the non-local resistance originates from hyperfine coupling between conduction electrons and nuclear spins. In graphene, this scenario is unlikely due to the small abundance of intrinsic nuclear spins in carbon (>98% of carbon is ^{12}C, which has no nuclear spin) and a lack of contact hyperfine coupling in the p_z-orbitals that make up the conduction and valence bands. Nevertheless, investigating the situation is necessary because the adsorption of hydrogen on graphene may alter the hyperfine coupling. Two effects that could in principle alter the non-local resistance include hyperfine coupling to dynamically polarized nuclear spins [368, 369] and organic magnetoresistance (OMAR) [370, 371].

The effect of OMAR has previously been observed in carbon C_{60} and functionalized carbon-based polymers [370, 371]. OMAR originates from hyperfine induced spin mixing

between singlet and triplet states and manifests itself as a magnetic field dependent resistivity. However, as shown in Fig. 8.3, resistivity does not change as a function of applied in-plane magnetic field. This confirms OMAR is not responsible for the observed dip in R_{NL}.

The effect of dynamic nuclear polarization (DNP) was demonstrated clearly by Salis *et al.* [369] and Chan *et al.* [368] who investigated GaAs non-local spin valves at low temperatures. Specifically, Salis et al. observed a dip in R_{NL} at zero applied magnetic field, similar to the dip we observe in hydrogen-doped graphene. They attributed their dip to precessional spin dephasing caused by hyperfine coupling to dynamically polarized nuclear spins. To determine whether such nuclear spin effects are present in hydrogen-doped graphene we perform a series of tests.

Test 1: Nuclear spin relaxation times are typically long ($\sim$minutes), and therefore, slow dynamics at this time scale are a characteristic of effects related to DNP. This is manifested in non-local spin transport data as a "lab time" dependence [369]. In our investigation of hydrogen-doped graphene, we do not observe a lab time dependence or a magnetic field ramp rate dependence.

Test 2: A characteristic feature of hyperfine coupling to the nuclear spin bath through DNP is the nuclear field's linear dependence on the applied field [369]. Specifically, at zero field the nuclear spin bath depolarizes slowly over time. The depolarization of the nuclear spin bath is evident in R_{NL} data as the gradual decrease and eventual disappearance (after a few minutes) of the dip when the applied field is set to zero (Figure 1 of Salis *et al.* [369]). We perform this test on hydrogen-doped graphene spin valves, as shown in Fig. 8.5. First, the

magnetic field is held at -30 mT for 10 minutes to ensure any possible nuclear spin transients reach steady state. The R_{NL} is measured continuously during this period and exhibits a value of $\sim$0.92 Ω. Then the magnetic field is quickly reduced to zero, coinciding with the immediate drop of R_{NL} to $\sim$0.80 Ω. This drop occurs because $B_{app,y}$=0 mT is at the center of the dip in R_{NL}. The R_{NL} is measured over the following 20 minutes, for which the observed value remains unchanged at $\sim$0.80 Ω. This indicates that the magnitude of the dip is independent of lab time. If the dip were due to hyperfine coupling to dynamically polarized nuclear spins, then the magnitude of the dip would gradually decrease to zero (i.e. R_{NL} would increase back to $\sim$0.92 Ω). Because this behavior is not observed, the dip in R_{NL} cannot be due to DNP.

Test 3: For the case of DNP, applying a constant out-of-plane magnetic field during a non-local spin transport measurement (in-plane field scan) results in a characteristic feature of nuclear depolarization and repolarization as the in-plane field crosses zero (Figure 1 of Chan *et al.* [368]). We perform this measurement on hydrogen-doped graphene and observe no evidence of depolarization/repolarization features. Together, these three tests show that the dip in R_{NL} is not due to hyperfine coupling to dynamically polarized nuclear spins.

The above investigations of OMAR and DNP conclusively exclude the possibility of hyperfine coupling with nuclear spins as the source of the observed dip in the non-local spin transport.

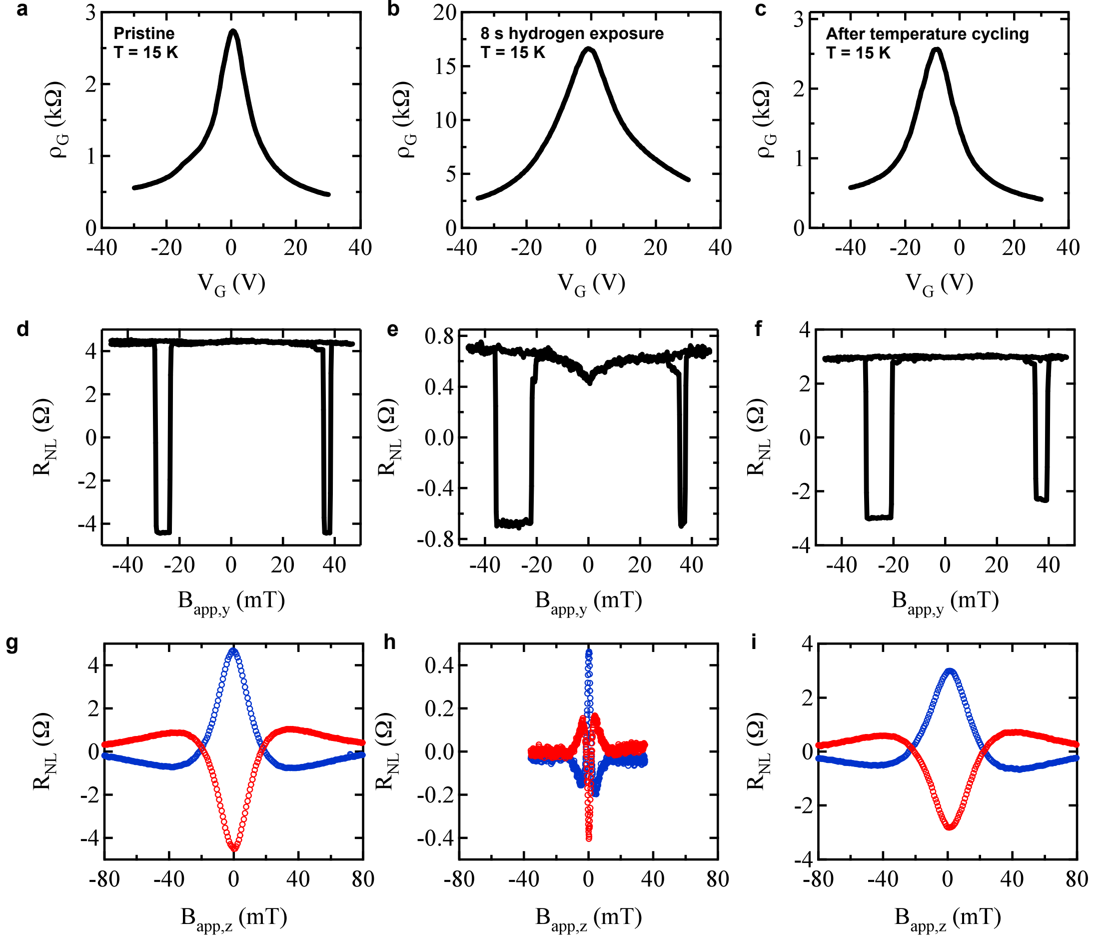

Figure 8.6: Reversibility of effects due to hydrogen doping of SLG. a) Gate dependent resistivity for pristine SLG at T=15 K. Data set corresponds to sample A. b) Gate dependent resistivity after 8 s hydrogen exposure at T=15 K. c) Gate dependent resistivity at T=15 K, measured after hydrogen exposure at 15 K followed by warming to room temperature and subsequent cooling to 15 K. d) R_{NL} for pristine SLG. e) R_{NL} after 8 s hydrogen exposure. f) R_{NL} after temperature cycling. g) Hanle spin precession data for pristine SLG. Blue (red) data is for parallel (antiparallel) magnetizations. h) Hanle spin precession data after 8 s hydrogen exposure. i) Hanle spin precession data after temperature cycling. All R_{NL} and spin precession data are measured at $V_G - V_D$=-15 V.

8.4.3 Excluding Changes in Magnetization of the Electrodes

Here we examine the possibility that the observed behavior in R_{NL} after hydrogen exposure is caused by spurious changes to the magnetic electrodes. It is known that hydrogen adsorption onto ferromagnetic materials can alter their magnetic properties [372, 373, 374, 375, 376]. In the present experiment, following the standard fabrication procedure for tunneling contacts to graphene as discussed in previous work [374], the magnetic electrodes are capped with 5 nm Al_2O_3. Also, we note that in the R_{NL} data presented in this work, the coercive fields of the electrodes remain unchanged after hydrogen exposure.

Further it is known that the bonding energy for hydrogen adsorption on transition metals is several eV ($\sim$2.6 eV for Co [376]), suggesting that H-Co chemisorption would be robust to temperature cycling. Here we observe that the behavior in R_{NL} and spin precession data after the introduction of atomic hydrogen at T=15 K is reversible upon temperature cycling (Fig. 8.6). At cryogenic temperatures, exposure of SLG graphene spin valves to hydrogen dramatically alters the charge and spin properties. The gate dependent resistivity increases, whereas the magnitude of R_{NL} decreases and exhibits a dip at low field. The observed dip is due to an increase in the spin scattering. Also, precession measurements exhibit a narrowing of the Hanle curve. Next, the sample is warmed to room temperature and subsequently re-cooled to T=15 K. The spin and charge transport properties are then re-measured. We have found that the charge transport properties of the gate dependent resistivity and mobility nearly recover to the pristine values. For instance, for sample A, the mobility is μ=6105 cm^2/Vs for pristine graphene. After 8 s hydrogen exposure the mobility decreases to μ=495 cm^2/Vs. After

temperature cycling, the mobility recovers to μ=5450 cm^2/Vs. The recovery indicates the effect of hydrogen is removed through desorption, cluster formation, or a combination of the two. After temperature cycling, the spin signal R_{NL} contains no indication of a dip near low field and has increased to 5.95 Ω. Also, the spin precession data broadens and conventional Hanle analysis (equation 8.17) yields τ^{so}=353 ps and D=0.022 m^2/s. As mentioned above, changes in the Co electrodes should persist after temperature cycling and so cannot explain the observed behavior. Upon re-hydrogenation at cryogenic temperatures the key features (dip in R_{NL}, narrowed Hanle curve) return. Fig. 8.6 summarizes the changes in resistivity, R_{NL}, and spin precession upon temperature cycling.

To comprehensively verify that changes in magnetism of the Co electrodes is not the cause of the observed dip, we fabricate Co wires in the same fashion as for tunnel barrier contacts to graphene. Three 300 nm wide Co wires with equal length (L=200 μm) and 80 nm thick are oriented at 0 °, 45 °, and 90 ° with respect to an in-plane applied field. Figure 8.7 shows the magnetoresistance plotted as ΔR/R (%) vs. $B_{app,y}$ for the three different orientations before and after 20 s hydrogen exposure. We note that 20 s hydrogen exposure is significantly more than typically needed to generate observable effects in R_{NL}. As can be seen in Fig. 8.7, no effect is seen in the magnetoresistance of the Co wires upon hydrogen exposure. The switching fields and shape remain unchanged along with the anisotropy behavior. Therefore, we rule out effects of alterations in the Co wire magnetization as a possible source for the origin of the observed dip at zero field in R_{NL}.

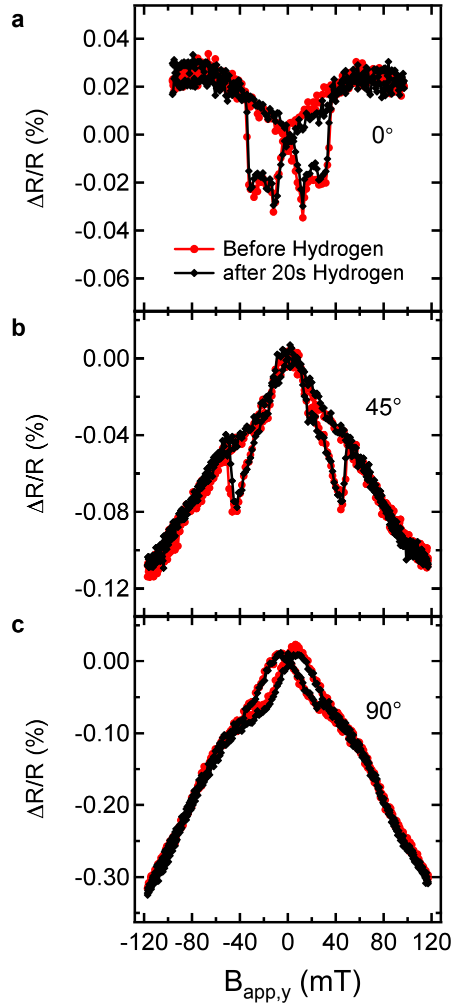

Figure 8.7: Magnetoresistance of Co Wires Before and After Hydrogen Exposure at T=10 K. a) ΔR/R (%) of a single Co wire measured before hydrogen exposure (red circles) for a wire oriented along $B_{app,y}$ (0 °). The wires were fabricated using standard e-beam lithography and angle evaporation in the same fashion as for producing tunnel barrier electrodes on SLG. The observed features are due to anisotropic magnetoresistance (AMR) and reflect the magnetization of the Co wire. No effect is observed after 20 s of hydrogen exposure (black diamonds). b) ΔR/R (%) of a Co wire oriented 45 ° with respect to $B_{app,y}$ before hydrogen exposure (red circles) and after 20 s exposure (black diamonds). c) ΔR/R (%) of a Co wire oriented 90 ° with respect to $B_{app,y}$ before hydrogen exposure (red circles) and after 20 s exposure (black diamonds). In all cases the wires are oriented in-plane.

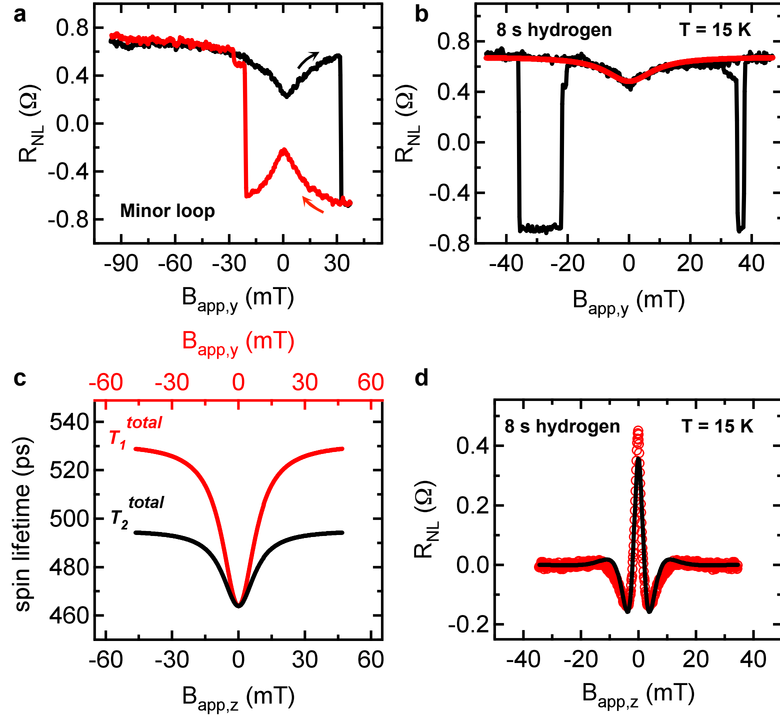

Figure 8.8: Minor Loop of Hydrogen-doped Graphene and Analysis of R_{NL}. a) A minor loop scan shows that the dip in R_{NL} for parallel alignment (black) becomes a peak for antiparallel alignment (red), indicating the feature is due to increased spin relaxation, as opposed to an artifact of the background level. b) Fitting the dip in R_{NL} based on the model of spin relaxation by paramagnetic moments (data in black, fit in red). c) Field dependence of longitudinal (red) and transverse (black) spin lifetimes. (d) Hanle precession data following 8 s hydrogen exposure (red) is fit using equation 9.1 (black curve).

8.5 Effective Exchange Field Model

8.5.1 Single Spin-Moment Model

As we discuss in the following, emergence of the dip following hydrogen adsorption identifies magnetic moment formation in graphene. The dip in R_{NL} is a characteristic feature of spin relaxation from exchange coupling with localized magnetic moments, and can be illustrated from a simple textbook example of two coupled spins in a magnetic field. The

Hamiltonian is given by $H = A_{ex}\vec{S}_e \cdot \vec{S}_M + g_e\mu_B\vec{S}_e \cdot \vec{B}_{app} + g_M\mu_B\vec{S}_M \cdot \vec{B}_{app}$, where $\vec{S}_e$ is the conduction electron spin, $\vec{S}_M$ is the spin of the magnetic moment, g_e and g_M are the respective g-factors, and A_{ex} is the exchange coupling strength [377, 378]. Due to the presence of the exchange coupling, the individual spins are not conserved; only the total spin $\vec{S}_{tot} = \vec{S}_e + \vec{S}_M$ is conserved. For the case where both $\vec{S}_e$ and $\vec{S}_M$ are spin-$\frac{1}{2}$, the quantum mechanical eigenstates in zero magnetic field are the well-known singlet ($S_{tot} = 0$) and triplet ($S_{tot} = 1$) spin states [379]. At higher magnetic fields the Zeeman terms dominate and the two spins decouple so that the magnitudes and z-components of $\vec{S}_e$ and $\vec{S}_M$ become good quantum numbers, similar to the Paschen-Back effect [379]. Thus, the dip in R_{NL} is qualitatively explained by the non-conservation of $\vec{S}_e$ at low fields due to the presence of exchange coupling with magnetic moments.

8.5.2 Interaction of an Electron Spin With Many Induced Moments

To quantitatively model the experiment, we consider electron spins $\vec{S}_e$ moving in an effective magnetic field of randomly positioned local magnetic moments $\vec{S}_M$ of filling density η_M. Each electron feels the average spin interaction

$$\begin{aligned} H_e &= \eta_M A_{ex}\vec{S}_e \cdot \langle\vec{S}_M\rangle + g_e\mu_B\vec{S}_e \cdot \vec{B}_{app} \\ &= g_e\mu_B\vec{S}_e \cdot (\overline{\vec{B}}_{ex} + \vec{B}_{app}) \end{aligned} \quad (8.2)$$

and

$$\overline{\vec{B}}_{ex} = \eta_M A_{ex} \langle \vec{S}_M \rangle / g_e \mu_B \tag{8.3}$$

where $\overline{\vec{B}}_{ex}$ is the effective exchange magnetic field, g_e is the electron g-factor, μ_B is the Bohr magneton, and A_{ex} is the strength of the exchange coupling between $\vec{S}_e$ and $\vec{S}_M$. The averaging $\langle ... \rangle$ is over the ensemble of magnetic moments. The effective exchange field $\overline{\vec{B}}_{ex}$ contributes to the Larmor frequency and enhances the electron g-factor.

As the spins diffuse through the lattice they experience varying magnetic moments which results in varying Larmor frequencies. In the local frame associated with the electrons this can be described by a time-dependent, randomly fluctuating magnetic field, $\vec{B}_{ex}(t) = \overline{\vec{B}}_{ex} + \Delta\overline{\vec{B}}_{ex}(t)$ with the rms value given by the time average

$$(\Delta B_{ex}^{rms})_\alpha^2 = \langle [\Delta B_{ex,\alpha}(t)]^2 \rangle_t \tag{8.4}$$

$$(\Delta B_{ex}^{rms})^2 = (\Delta B_{ex}^{rms})_x^2 + (\Delta B_{ex}^{rms})_y^2 + (\Delta B_{ex}^{rms})_z^2 \tag{8.5}$$

where α is an xyz component index. The time scale of the fluctuation is given by a correlation time τ_c defined by

$$\langle \Delta\vec{B}_{ex}(t) \cdot \Delta\vec{B}_{ex}(t - t') \rangle_t \propto \exp(-t'/\tau_c) \tag{8.6}$$

Spin relaxation resulting from a randomly fluctuating magnetic field has been solved in the review article by J. Fabian [20, Section IV.B.2] and is mathematically analogous to

the D'yakanov-Perel model [92]. For the non-local spin signal geometry, the injected spin polarization and the applied magnetic field lie along the same axis (y-axis) and the spin relaxation rate is given by longitudinal spin relaxation equation IV.36 of [20] The equation is rewritten using $\omega_\alpha = g_e\mu_B \Delta B_{ex,\alpha}/\hbar$ and $\omega_0 = g_e\mu_B \overline{B}_{total}/\hbar = g_e\mu_B(B_{app,y} + \overline{B}_{ex,y}/\hbar)$ to yield,

$$\frac{1}{\tau_1^{ex}} = \frac{(\Delta B)^2}{\tau_c}\frac{1}{(B_{app,y} + \overline{B}_{ex,y})^2 + \left(\frac{\hbar}{g_e\mu_B\tau_c}\right)^2} \tag{8.7}$$

where $(\Delta B)^2 = (\Delta B_{ex})_z^2 + (\Delta B_{ex})_z^2$. In other words, precession around randomly fluctuating exchange fields along the x- and z-axes induce spin relaxation. Equation (8.7) also shows that the spin relaxation is suppressed by a large applied magnetic field. Intuitively, this occurs because the precession axis is defined by the large applied field (along y-axis) and fluctuating fields along the x- and z-axes have very little ability to tilt the precession axis. This peak in spin relaxation at low magnetic fields produces the observed dip in R_{NL}.

The presence of the average exchange field $\overline{B}_{ex,y}$ in equation (8.7) shows that the spin relaxation is maximized when the $B_{app,y} + \overline{B}_{ex,y} = 0$, or $B_{app,y} = -\overline{B}_{ex,y}$. Because $\overline{B}_{ex,y}$, is proportional to the magnetization, paramagnetic moments will generate a dip in R_{NL} centered at zero applied field while ferromagnetic ordering will generate a hysteretic dip centered away from zero applied field. The observed dip (Figs. 8.2 e), f) and 8.4) is centered at zero applied field and is not hysteretic, signifying the observed magnetic moments are paramagnetic.

For paramagnetic moments, $\overline{B}_{ex,y}$ takes the form of the Brillouin function (B_J) and is given by

$$\overline{B}_{ex,y} = \eta_M A_{ex} \langle S_{M,y} \rangle / g_e \mu_B = \eta_M A_{ex} J B_J(\xi) / g_e \mu_B \tag{8.8}$$

$$B_J(\xi) = \frac{2J+1}{2J} \coth\left(\frac{2J+1}{2J}\xi\right) - \frac{1}{2J} \coth\left(\frac{1}{2J}\xi\right) \tag{8.9}$$

where J is the total angular momentum quantum number of the magnetic moment, $\xi = \frac{J g_e \mu_B}{k_B \mathrm{T}} B_{app,y}$, k_B is Boltzmanns constant, and T is temperature. For our experiments at T=15 K, this reduces to $\xi = J g_e B_{app,y} / (22.32 \text{ Tesla})$. Thus, for the values of $B_{app,y}$ in our experiments $\xi \ll 1$ so that $B_J \approx (J+1)\xi/3J$ to yield

$$\overline{B}_{ex,y} = \frac{\eta_M A_{ex} J(J+1)}{3\mu_B} \left(\frac{B_{app,y}}{22.32 \text{ Tesla}}\right) \tag{8.10}$$

Thus, the total field can be written as

$$B_{total} = B_{app,y} + \overline{B}_{ex,y}$$

$$= B_{app,y} + \frac{\eta_M A_{ex} J(J+1)}{3\mu_B} \left(\frac{B_{app,y}}{22.32 \text{ Tesla}}\right)$$

$$= \left(1 + \frac{\eta_M A_{ex} J(J+1)}{3\mu_B (22.32 \text{ Tesla})}\right) B_{app,y} = \frac{g_e^*}{g_e} B_{app,y} \tag{8.11}$$

where the g_e^* is the enhanced g-factor due to the presence of the exchange field. Substituting this into equation (8.7) yields the expression for spin relaxation from paramagnetic moments in the linear regime,

$$\frac{1}{\tau_1^{ex}} = \frac{(\Delta B)^2}{\tau_c}\frac{1}{\left(\frac{g_e^*}{g_e}B_{app,y}\right)^2 + \left(\frac{\hbar}{g_e\mu_B\tau_c}\right)^2} = \frac{\frac{(\Delta B)^2}{\tau_c}\left(\frac{g_e}{g_e^*}\right)^2}{(B_{app,y})^2 + \left(\frac{\hbar}{g_e^*\mu_B\tau_c}\right)^2} \tag{8.12}$$

Thus, the longitudinal spin relaxation rate is a Lorentzian with a peak at zero applied field.

For the Hanle geometry, the injected spin polarization is along the y-axis and the applied magnetic field is along the z-axis. In this case the spin relaxation rate is given by transverse spin relaxation equation IV.38 in [20] The equation is rewritten using $\omega_\alpha = g_e\mu_B\Delta B_{ex,\alpha}/\hbar$ (for $\alpha = x, y, z$) and $\omega_0 = g_e\mu_B\overline{B}_{total}/\hbar$ = $g_e\mu_B(B_{app,z} + \overline{B}_{ex,z})/\hbar$ to yield

$$\frac{1}{\tau_2^{ex}} = \frac{1}{2}\left[\frac{(\Delta B)^2}{\tau_c\left(\frac{\hbar}{g_e\mu_B\tau_c}\right)^2}\right] + \frac{1}{2}\left[\frac{(\Delta B)^2}{\tau_c}\frac{1}{(B_{app,z} + \overline{B}_{ex,z})^2 + \left(\frac{\hbar}{g_e\mu_B\tau_c}\right)^2}\right] \tag{8.13}$$

where the fluctuating field is assumed to be isotropic: $(\Delta B_{ex})_x^2 = (\Delta B_{ex})_y^2 = (\Delta B_{ex})_z^2$. For paramagnetic moments, this becomes

$$\frac{1}{\tau_2^{ex}} = \frac{1}{2}\left[\frac{\frac{(\Delta B)^2}{\tau_c}\left(\frac{g_e}{g_e^*}\right)^2}{\left(\frac{\hbar}{g_e^*\mu_B\tau_c}\right)^2}\right] + \frac{1}{2}\left[\frac{\frac{(\Delta B)^2}{\tau_c}\left(\frac{g_e}{g_e^*}\right)^2}{(B_{app,z})^2 + \left(\frac{\hbar}{g_e^*\mu_B\tau_c}\right)^2}\right] \tag{8.14}$$

8.6 Application of the Exchange Field Model to Experimental R_{NL} and Hanle Data

In Brief

To quantitatively analyze the experimental data, we must consider that a conduction electron will interact with many localized magnetic moments. Thus, the terms in the Hamiltonian involving the conduction electron are given by $H_e = \eta_M A_{ex} \vec{S}_e \cdot \langle \vec{S}_M \rangle + g_e \mu_B \vec{S}_e \cdot \vec{B}_{app} = g_e \mu_B \vec{S}_e \cdot \left(\overline{\vec{B}}_{ex} + \vec{B}_{app} \right)$ where η_M is the filling density of magnetic moments. The averaging $\langle \cdots \rangle$ is over the ensemble of magnetic moments and the effective field generated by the exchange interaction is $\overline{\vec{B}}_{ex} = \frac{\eta_M A_{ex} \langle \vec{S}_M \rangle}{g_e \mu_B}$. As the spins diffuse through the lattice they experience varying magnetic moments which results in varying Larmor frequencies. In the local frame associated with the electrons this can be described by a time-dependent, randomly fluctuating magnetic field, $\vec{B}_{ex}(t) = \overline{\vec{B}}_{ex} + \Delta \vec{B}_{ex}(t)$. For the R_{NL} measurements, the longitudinal spin relaxation due to a fluctuating field is given by [20],

$$\frac{1}{\tau_1^{ex}} = \frac{(\Delta B)^2}{\tau_c} \frac{1}{\left(B_{app,y} + \overline{B}_{ex,y} \right)^2 + \left(\frac{\hbar}{g_e \mu_B \tau_c} \right)^2} \tag{8.15}$$

where ΔB is the rms fluctuation and τ_c is the correlation time.

The spin relaxation rate due to the exchange field is described by a Lorentzian curve which depends explicitly on the applied field, $B_{app,y}$, resulting in strong spin relaxation at low fields and suppressed spin relaxation at high fields. Due to the presence of $\overline{B}_{ex,y}$ in

equation 8.15, ferromagnetic ordering will produce a dip in R_{NL} that is centered away from zero and is hysteretic, while paramagnetic ordering will produce a non-hysteretic dip centered at zero field. Thus, the magnetic moments measured in these experiments are paramagnetic. The total longitudinal spin lifetime, T_1^{total}, of conduction electrons is dependent on both the usual spin relaxation due to spin orbit coupling (τ_{so}) and longitudinal spin relaxation from the exchange field (τ_1^{ex}), such that $\left(T_1^{total}\right)^{-1} = \left(\tau_1^{ex}\right)^{-1} + \left(\tau^{so}\right)^{-1}$. We apply the above model to the non-local spin transport data presented in Fig. 8.2 f) (sample A) and fit using equation (8.1), $\lambda = \sqrt{DT_1^{total}}$, and equation (8.15). The resulting fit (red line in Fig. 8.8 b)) replicates the shape and magnitude of the dip measured in R_{NL} (black line in Fig. 8.8 b)). The field dependent T_1^{total} (Fig. 8.8 c)), exhibits a minimum of 464 ps at zero field and increases asymptotically towards τ_{so} = 531 ps for large $B_{app,y}$. The values obtained for ΔB and τ_c are 6.78 mT and 192 ps, respectively. The field-dependent spin relaxation following atomic hydrogen exposure, which emerges as a dip in R_{NL}, is a clear signature of paramagnetic moment formation.

Spin precession measurements provide further evidence for the presence of magnetic moments. Figure 8.8 d) shows spin precession data for sample A (8 s exposure, $V_G - V_D$ = -15 V) with FM electrodes in the parallel alignment state. The Hanle curve has considerably narrowed compared to the precession measurements obtained prior to hydrogen adsorption (Fig. 8.2 d)). The sharpening of the Hanle curve results from the presence of an exchange field. The injected spins precess around a total field $B_{tot} = B_{app,z} + \overline{B}_{ex,z}$ (along z-axis) that includes not only the applied field, but also the exchange field from the paramagnetic

moments. At 15 K and $B_{app,z} < 100$ mT, the magnetization is proportional to the applied field so that $\overline{B}_{ex,z} = kB_{app,z}$, where k is a proportionality constant. Thus, the spins precess about B_{tot} with frequency $\omega = g_e\mu_B B_{tot}/\hbar = g_e(1+k)\mu_B B_{app,z}/\hbar = g_e^*\mu_B B_{app,z}/\hbar$. To properly account for the enhanced g-factor induced by the magnetic moments, the Hanle equation must be modified to

$$R_{NL} = S\int_0^\infty \frac{e^{-L^2/4Dt}}{\sqrt{4\pi Dt}} \cos\left(\frac{g_e^*\mu_B B_{app,z}t}{\hbar}\right) e^{-t/T_2^{total}} dt \tag{8.16}$$

where T_2^{total} is the transverse spin lifetime. As shown in Fig. 8.8 c), the T_2^{total} is related to, but different from T_1^{total}. Using the field dependent T_2^{total}, the precession data (red circles of Fig. 8.8 d)) is fit to equation 9.1 (black line) to yield a value of $g_e^* = 7.13$. Physically, $g_e^* > 2$ corresponds to an enhanced spin precession frequency resulting from the exchange field. The dramatic narrowing of the Hanle peak combined with the emergence of a dip in R_{NL} provides the most direct evidence to date for the formation of magnetic moments in graphene due to the adsorption of atomic hydrogen.

In Detail

The spin relaxation, diffusion coefficient, and interfacial spin polarization of the pristine sample are determined though analysis of R_{NL} and spin precession measurements. Fitting of

spin precession data to the Hanle equation

$$R_{NL} = S\int_0^\infty \frac{e^{-L^2/4Dt}}{\sqrt{4\pi Dt}}\cos\left(\frac{g_e\mu_B}{\hbar}B_{app,z}t\right)e^{-t/\tau^{so}}dt \tag{8.17}$$

provides values of spin lifetime (τ^{so}), diffusion coefficient (D), Hanle amplitude (S), and spin diffusion length ($\lambda = \sqrt{D\,\tau^{so}}$). For pristine graphene, the electron g-factor, g_e, is assumed to be 2. It should be noted that in the case of pristine graphene, the longitudinal spin relaxation (τ_1^{so}) and transverse spin relaxation (τ_2^{so}) due to spin orbit coupling are equivalent ($\tau_1^{so} = \tau_2^{so} = \tau^{so}$) [32]. Data measured on sample A (Fig. 8.2 d)), yields τ^{so}=479 ps, D=0.023 m^2/s and λ=3.3 μm for the channel length, L=5.25 μm. The corresponding R_{NL} data is fit with the non-local resistance equation (eq. 8.1) [31],

$$R_{NL}^{(P/AP)} = \pm 2R_G e^{\frac{-L}{\lambda}} \prod_{i=1}^{2}\left(\frac{P_J\frac{R_i}{R_G}}{1-P_J^2}+\frac{P_F\frac{R_F}{R_G}}{1-P_F^2}\right)\times\left[\prod_{i=1}^{2}\left(1+\frac{2\frac{R_i}{R_G}}{1-P_J^2}+\frac{2\frac{R_F}{R_G}}{1-P_F^2}\right)-e^{\frac{-2L}{\lambda}}\right]^{-1} \tag{8.18}$$

to obtain the interfacial spin polarization, P_J, for the graphene device.

In the above equation, R_G is the graphene spin resistance defined by, $R_G = \rho_G\lambda/w$, where ρ_G is the resistivity and w is the graphene width. $R_{1,2}$ denotes the contact resistances of injector and detector electrodes, P_F is the ferromagnetic electrode spin polarization (assumed to be 0.35 for cobalt), and $R_F = \rho_F\frac{\lambda_F}{l_j w}$ is the spin resistance of the ferromagnet, where $\rho_F = 5.8 \times 10^{-8}$ Ωm is the resistivity of cobalt, l_j=50 nm is the effective spin injector contact length of the ferromagnetic electrode and is determined by the fabrication procedures (see [25, 34] for details), and lastly, λ_F is the spin diffusion length of the ferromagnet, taken to

be 38 nm in cobalt. The measured ΔR_{NL}=8.8 Ω for Sample A (Fig. 8.2 c)) corresponds to a P_J=0.20 for parameters λ=3.3 μm, ρ_G=898 Ω, w=2.3 μm, R_1=15.76 kΩ, and R_2=4.00 kΩ. The contact resistances are measured in a three terminal geometry [71] and are found to be unaffected by hydrogen exposure. The measured value of 20% interfacial spin polarization is comparable to previously reported values for efficient spin injection into SLG through tunneling contacts [71]. P_J is assumed to remain constant throughout hydrogen exposure, a reasonable assumption since the graphene at the site of spin injection is protected by the electrode, the hydrogen does not alter the cobalt (see section 8.4.3), and contact resistances remain unchanged.

As discussed above, exposure to atomic hydrogen results in the formation of magnetic moments, detected as a dip in R_{NL}. Additionally, a sharpened Hanle curve signifies enhanced precession of injected spins due to the presence of an exchange field caused by the moments. The exchange field is not accounted for in the standard Hanle equation (8.17), preventing direct determination of τ^{so} and D through Hanle fitting. Instead, the Einstein relation

$$D = \frac{\sigma}{e^2 \nu} \tag{8.19}$$

is employed to obtain D for hydrogen-doped samples, where ν denotes the density of states and e is the electron charge. Assuming ν is unchanged by exposure to hydrogen, which is reasonable in the dilute limit, the diffusion coefficient of hydrogen-doped samples D_{hyd} is determined from the pristine diffusion coefficient $D_{pristine}$ and the conductivities of hydrogen-

doped (σ_{hyd}) and pristine ($\sigma_{pristine}$) graphene.

$$\frac{D_{hyd}}{D_{pristine}} = \left(\frac{\sigma_{hyd}}{e^2\nu}\right) / \left(\frac{\sigma_{pristine}}{e^2\nu}\right) = \frac{\sigma_{hyd}}{\sigma_{pristine}} \tag{8.20}$$

The change in conductivity from 1.113 mS to 0.143 mS following hydrogen exposure results in D_{hyd}=0.0029 m^2/s.

The longitudinal spin lifetime is evaluated by examining R_{NL} for the hydrogen-doped sample. As shown in equation (8.12) the spin relaxation rate arising from the presence of magnetic moments is described by a Lorentzian centered at $B_{app,y}$=0, and can be fit using the general form

$$\frac{1}{\tau_1^{ex}} = \Gamma \frac{\gamma^2}{(B_{app,y})^2 + \gamma^2} \tag{8.21}$$

The total longitudinal spin lifetime, T_1^{total}, depends on both τ_1^{ex} and τ^{so} through the relation

$$\frac{1}{T_1^{total}} = \frac{1}{\tau^{so}} + \frac{1}{\tau_1^{ex}} \tag{8.22}$$

subsequently affecting the spin diffusion length λ

$$\lambda = \sqrt{D\,T_1^{total}} = \sqrt{D\left(\frac{1}{\tau^{so}} + \frac{1}{\tau_1^{ex}}\right)^{-1}} = \sqrt{D\left(\frac{1}{\tau^{so}} + \Gamma\frac{\gamma^2}{(B_{app,y})^2 + \gamma^2}\right)^{-1}}. \tag{8.23}$$

The field dependent λ directly translates to a field dependence in the non-local resistance causing the experimentally observed dip in R_{NL} at zero applied field. Values for τ^{so}, Γ,

and γ are determined by fitting the measured R_{NL} data to the non-local resistance equation (8.18), where λ is field dependent and defined by equation (8.23). The best fit to sample A is obtained by τ^{so}=531 ps, Γ=2.73$\times 10^8$ s^{-1}, and γ=8.32 mT and is displayed as the red curve in Fig. 8.8 b), using, R_F=0.019 Ω, ρ_G=6.99 kΩ R_1=15.76 kΩ, R_2=4.00 kΩ, P_J=0.20, P_F=0.35, and L=5.25 μm. The field dependent values of T_1^{total} are displayed as the red curve in Fig. 8.8 c). Clearly, this model explains the data well and may also be relevant for dip features observed recently in metallic lateral spin valves [380].

Following the determination of τ^{so}, Γ, and γ, the spin precession data for the hydrogen-doped sample is analyzed in order to obtain values for g_e^*. The standard Hanle equation (8.17) must be modified to account for precession induced by both the applied field and the exchange field ($B_{ex,z}$) produced by magnetic moments as well as the field dependent transverse spin lifetime T_2^{total}, where $\frac{1}{T_2^{total}} = \frac{1}{\tau^{so}} + \frac{1}{\tau_2^{ex}}$. For the Hanle geometry, the spin relaxation rate from the magnetic moments is given by equation (8.14). Thus, in terms of the Lorentzian parameters Γ and γ, the total spin relaxation rate is,

$$\frac{1}{T_2^{total}} = \frac{1}{\tau^{so}} + \frac{\Gamma}{2}\left(1 + \frac{\gamma^2}{(B_{app,z})^2 + \gamma^2}\right) \tag{8.24}$$

For comparison, Fig. 8.8 c) displays the total longitudinal spin lifetime T_1^{total} (red curve) and total transverse spin lifetime T_2^{total} (black curve) for hydrogen-doped graphene sample A.

The modified Hanle equation is dependent on T_2^{total} and takes the form

$$R_{NL}=S\int_0^{\infty}\frac{e^{-L^2/4Dt}}{\sqrt{4\pi Dt}}e^{-t\left[\frac{1}{\tau^{so}}+\frac{\Gamma}{2}\left(1+\frac{\gamma^2}{(B_{app,z})^2+\gamma^2}\right)\right]}\times\cos\left(\frac{g_e\mu_B}{\hbar}(B_{app,z}+\overline{B}_{ex,z})t\right)dt \quad (8.25)$$

For paramagnetic moments, $\overline{B}_{ex,z}$ is described by the Brillouin function. Additionally, $\frac{JB_{app,z}}{(22.32\text{Tesla})} \ll 1$, so that $\overline{B}_{ex,z}$ can be represented by the low field approximation

$$\overline{B}_{ex,z}=\frac{\eta_M A_{ex}J(J+1)}{3\mu_B\,(22.32\text{ Tesla})}B_{app,z} \quad (8.26)$$

resulting in,

$$R_{NL}=S\int_0^{\infty}\frac{e^{-L^2/4Dt}}{\sqrt{4\pi Dt}}e^{-t\left[\frac{1}{\tau^{so}}+\frac{\Gamma}{2}\left(1+\frac{\gamma^2}{(B_{app,z})^2+\gamma^2}\right)\right]} \quad (8.27)$$
$$\times\cos\left[\frac{g_e\mu_B}{\hbar}\left(B_{app,z}+\frac{\eta_M A_{ex}J(J+1)}{3\mu_B}\left(\frac{B_{app,z}}{22.32\text{ Tesla}}\right)\right)t\right]dt$$

which simplifies to,

$$R_{NL}=S\int_0^{\infty}\frac{e^{-L^2/4Dt}}{\sqrt{4\pi Dt}}e^{-t\left[\frac{1}{\tau^{so}}+\frac{\Gamma}{2}\left(1+\frac{\gamma^2}{(B_{app,z})^2+\gamma^2}\right)\right]}\times\cos\left(\frac{g_e^*\mu_B}{\hbar}B_{app,z}t\right)dt \quad (8.28)$$

with,

$$g_e^*=g_e\left[1+\frac{\eta_M A_{ex}J(J+1)}{3\mu_B(22.32\text{ Tesla})}\right] \quad (8.29)$$

Fitting of precession data to equation (8.28) yields values for Hanle amplitude (S) and g_e^*. In the fit, fixed parameters are: Γ=2.73$\times$10^8 s^{-1} and γ=8.32 mT, as determined by analysis of non-local resistance, D=0.0029 m^2/s from the Einstein relation, and L=5.25 μm. The best fit of Hanle data (presented in Fig. 8.8 d)) results in a g_e^* value of 7.13. We take a reasonable value for the exchange coupling of $A_{ex} \sim 1$ eV and the paramagnetic spin of $J = 1/2$ expected for the unpaired electrons due to hydrogen adatoms on graphene. Using the value g_e^*=7.13, we can independently estimate the fractional filling density of hydrogen induced magnetic moments to be $\eta_M \sim 1$ % using equation (8.29). This is in reasonable agreement with the order of magnitude estimate of 0.1% determined from the resistivity for 8 s hydrogen exposure to sample A.

The correlation time (τ_c) and the rms fluctuations in exchange field (ΔB) are determined by comparing equations (8.12) and (8.21) to give

$$\tau_c = \frac{\hbar}{g_e^* \mu_B} \frac{1}{\gamma} \tag{8.30}$$

$$(\Delta B)^2 = \gamma \left(\frac{g_e^*}{g_e} \right) \frac{\hbar \Gamma}{g_e \mu_B} \,. \tag{8.31}$$

Using g_e^*=7.13 from the Hanle fit and Γ=2.73$\times$10^8 s^{-1} and γ=8.32 mT from the non-local fit, we obtain values of τ_c=192 ps and $(\Delta B)^2$=4.59$\times$10^{-5} T^2 (or $\Delta B = \sqrt{(\Delta B_{ex,x})^2 + (\Delta B_{ex,z})^2}$ = 6.78 mT).

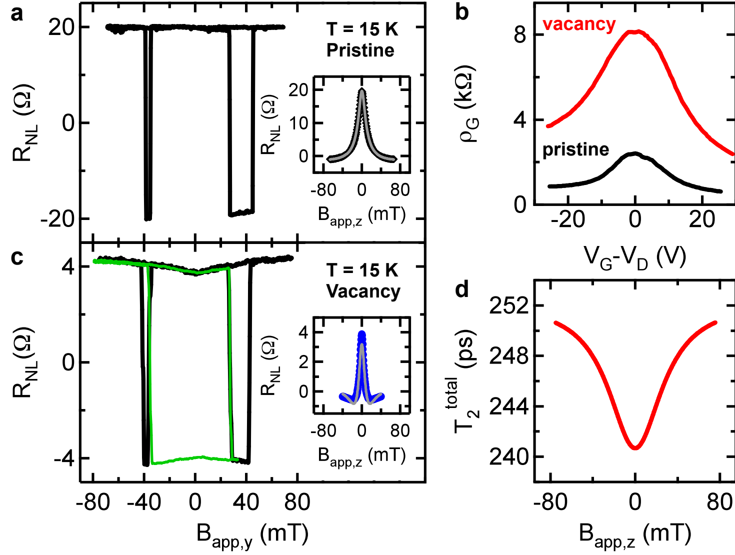

Figure 8.9: The Effect of Lattice Vacancies on Charge and Spin Transport in SLG at 15 K. a) Non-local spin transport data in pristine graphene with ΔR_{NL}=38.9 Ω. Hanle precession data (inset) yields values of τ^{so}= 859 ps and D=0.023 m^2/s. b) Gate dependent ρ_G for pristine graphene (black) and following lattice vacancy formation via Ar-sputtering (red). c) Non-local spin transport data in SLG containing vacancies. After Ar-sputtering, ΔR_{NL} is decreased to 8.2 Ω and exhibits a dip at zero applied field. The minor loop (green) confirms the observed dip is a spin dependent effect, caused by paramagnetic moment formation. The best fit to the Hanle precession data (inset) yields g_e^*=5.86. d) The field dependent T_2^{total} used to fit the Hanle data in c).

8.7 Magnetic Moments Generated by Lattice Vacancies

We investigate the effect of lattice vacancy defects in graphene. Several theoretical works suggest the similarity of magnetism due to vacancies and hydrogen-doping [315, 364], as both should create magnetic moments in graphene due to the removal/hybridization of p_z-orbitals. It is therefore reasonable to expect that similar effects will be observable in graphene spin transport following the introduction of lattice vacancies. To induce vacancies on pristine SLG spin valves, *in-situ* Ar-sputtering is performed at a sample temperature of 15 K. Argon partial pressures of 1×10^{-6} torr and energies between 100 eV and 500 eV combined with

short sputtering times (several seconds) produce dilute lattice vacancies. Prior to exposure to Ar-sputtering, the SLG device exhibits a ΔR_{NL} of 38.9 Ω at $V_G - V_D$=20 V and displays no dip in non-local resistance at zero applied field (Fig. 8.9 a)). Fitting of the corresponding precession data (inset of Fig. 8.9 a)) results in values of τ^{so}=859 ps and D=0.023 m^2/s for the pristine SLG device. The black (red) curve presented in Fig. 8.9 b) displays ρ_G before (after) sputtering. After the introduction of vacancies, the resistivity is substantially increased and the mobility is reduced from 4945 cm^2/Vs to 949 cm^2/Vs. Ar-sputtering results in a large decrease in the magnitude of ΔR_{NL} as well as the emergence of a dip in R_{NL} at zero applied field (Fig. 8.9 c)). The minor loop, shown in green, indicates the observed dip is due to a decrease in the spin signal at low fields, signifying the formation of paramagnetic moments. The Hanle data (Fig. 8.9 c) inset) narrows following Ar-sputtering. The Hanle data combined with fitting the dip in R_{NL} yields values of g_e^*=5.86, ΔB=13.9 mT, τ_c=64.1 ps, and the field dependent T_2^{total} shown in Fig. 8.9 d). Given the very different chemical and structural properties of lattice vacancies compared to adsorbed hydrogen, the observation of similar features in the spin transport data provide strong evidence that the magnetic moments are created by the removal of p_z orbitals from the π-band, as predicted theoretically.

8.8 Properties of the Exchange Field

In this section, we discuss properties of the exchange field stemming from the formation of magnetic moments with the introduction of hydrogen. Specifically, we examine the relation

between the exchange field and narrowing of the Hanle curve, and we investigate the gate dependence and accuracy of g_e^*.

8.8.1 Exchange Field and Narrowing of the Hanle Curve

Conventional Hanle analysis, as described at the beginning of section 8.6, consists of fitting spin precession data to the Hanle equation (8.17), yielding values for the spin lifetime (τ^{so}), the diffusion coefficient (D), and the amplitude (S). This relies on the assumption, g_e^*=2, and the absence of an exchange field. In conventional Hanle analysis, a narrowing of the Hanle curve is typically associated with an increase of the spin lifetime. Therefore, a valid question is whether the observed narrowing in the spin precession data after hydrogen doping is due to an enhanced spin lifetime instead of the emergence of an exchange field. Comprehensive analysis comprising the full data set (conductivity, non-local spin resistance (R_{NL}), and Hanle spin precession) provides compelling evidence that the narrowing of the Hanle curve is due primarily to an exchange field as opposed to enhanced spin lifetime. First, an increase in the spin lifetime cannot explain the observed dip in R_{NL}, while a fluctuating exchange field explains the dip and lineshape very well (see sections 8.5.2 and 8.6). Second, conventional Hanle analysis (g_e^*=2) of the hydrogen-doped sample A yields values for the diffusion coefficient that are inconsistent with the values obtained from the conductivity (differ by a factor of $\sim$6) and values for spin lifetime T_2^{total} that are inconsistent with the values obtained from the non-local spin resistance (differ by factor of 5-60). These inconsistencies can be resolved if an exchange field is present ($g_e^* > 2$). Key features of the full data

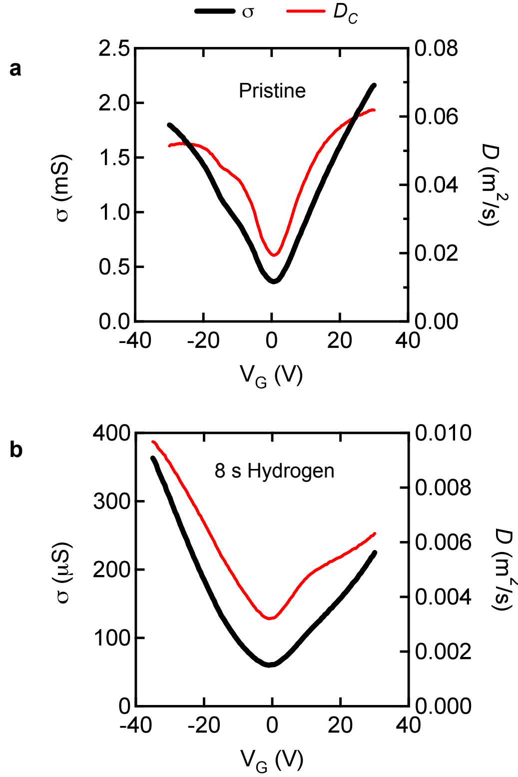

Figure 8.10: Conductivity and Calculated Diffusion Coefficient for Pristine and Hydrogen-doped SLG at 15 K. a) Gate dependent conductivity for pristine graphene (black curve) plotted on the left axis and the calculated diffusion coefficient, D_C (red curve), plotted on the right axis. b) Gate dependent conductivity for 8 s hydrogen exposure of SLG (black curve) plotted on the left axis and D_C (red curve) plotted on the right axis.

set emerge only after hydrogen doping and are best explained with a single effect, providing strong evidence for the presence of exchange fields.

In the following, we provide a detailed analysis of the discussion outlined above. First, we investigate the Hanle spin lifetime, $T_2^{total} = \tau^{so}$, without any consideration of an exchange field (i.e. g_e^*=2). Fig 8.11 a) and 8.11 c) show the gate dependence of Hanle lifetimes obtained from fitting spin precession data using Hanle equation (8.17) for pristine and 8 s hydrogen exposure to sample A, respectively. As can be seen in Fig. 8.11 c), when the Hanle fit parameters D and T_2 are allowed to vary, best-fit values yield long spin lifetimes. Values of

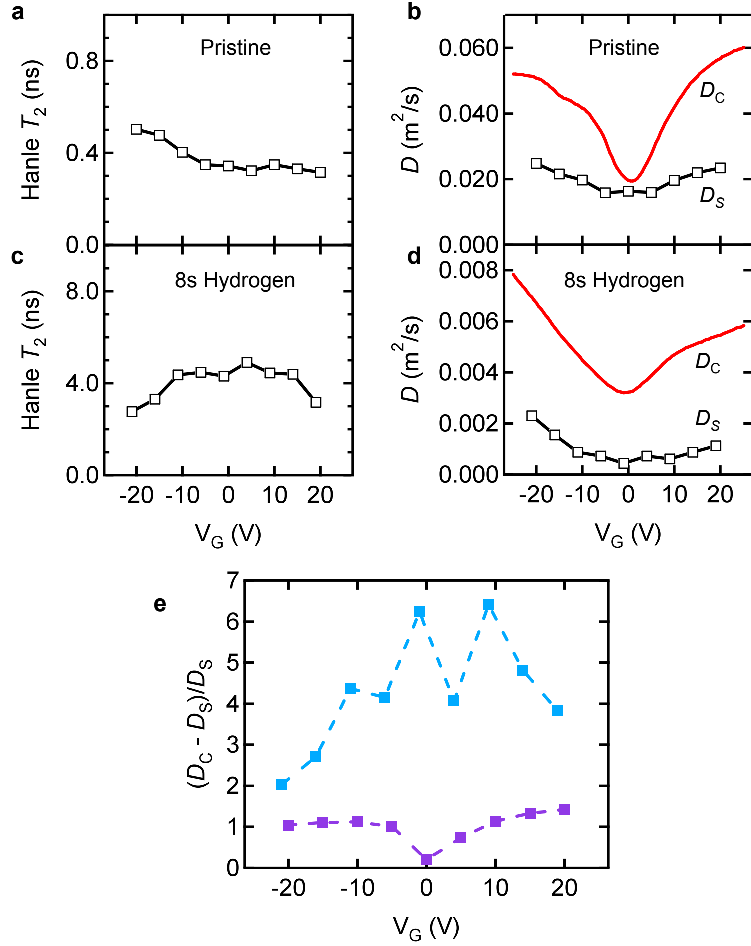

Figure 8.11: Conventional Hanle Fitting Assuming g_e^*=2 (No Exchange Field). a) Gate dependence of the Hanle spin lifetime for pristine SLG obtained by the Hanle equation. b) Gate dependence of the diffusion coefficients D_S (black open squares), obtained from the Hanle equation and the calculated diffusion coefficient, D_C (red curve), obtained by calculation from the conductivity and the broadened DOS for pristine SLG. c) Gate dependence of the Hanle spin lifetime for 8 s hydrogen exposure obtained by the conventional Hanle method. d) Gate dependence of the diffusion coefficients D_S (black open squares), obtained from the Hanle equation, and D_C (red curve) for 8 s hydrogen-doped SLG. e) Relative difference between D_S and D_C for pristine (purple solid squares) and 8 s hydrogen-doped (light blue solid squares) graphene.

D from the Hanle fit are denoted as D_S and are displayed (black open squares) in Fig. 8.11 b) and 8.11 d) for pristine and 8 s hydrogen-doped SLG.

Alternatively, one can use the gate-dependent conductivity to determine D via the Einstein relation (8.19),

$$D = \frac{\sigma}{e^2 \nu}$$

where σ is the experimentally measured conductivity, e is the electron charge, and ν is the broadened density of states (DOS). This value of diffusion coefficient is denoted as D_C. Spatial fluctuations of the Fermi level due to inhomogeneities in the SiO_2/Si substrate lead to broadening of the DOS. For Gaussian broadening [70], the DOS is

$$\nu(E) = \frac{g_v g_s 2\pi}{h^2 v_F^2} \left[\frac{2b}{\sqrt{2\pi}} e^{-\frac{E^2}{2b^2}} + E \,\mathrm{erf}\left(\frac{E}{b\sqrt{2}} \right) \right] \tag{8.32}$$

where g_v is the valley g-factor, g_s is the electron spin g-factor, h is Plancks constant, v_F=1$\times$10^6 m/s is the Fermi velocity, and b is the Gaussian broadening parameter. In Figure 8.10 a) and 8.10 b) we show the conductivity (black curve) for both pristine and 8 s hydrogen exposure, respectively. These conductivity curves correspond with the resistance data of sample A as shown in Fig. 8.2 b). We find reasonable agreement for b=100 meV and use this throughout the remainder of this section for D_C. On the right axis of Figures 8.10 a) and 8.10 b) we plot the calculated diffusion coefficient (red curve) (b=100 meV) for pristine and 8 s hydrogen, respectively. We have found that a broadening parameter between 75 and 125 meV, which is reasonable for graphene on SiO_2/Si substrate [70, 154], gives generally similar results for the present discussion.

We next examine the difference between these two methods for determining the diffusion coefficient. Figure 8.11 b) and 8.11 d) plots D_S (black open squares) and D_C (red curve) for the pristine sample and the hydrogen-doped sample as a function of gate voltage, respectively. Interestingly, D_S is much smaller than D_C for the hydrogen-doped sample, particularly when compared to the pristine sample. To quantify this, we plot the relative difference $(D_C - D_S)/D_S$ in Figure 8.11 e) and find it to be as large as $\sim$6 for the hydrogen-doped sample. On the other hand, the relative difference is less than $\sim$1 for the pristine sample. Therefore, for the hydrogen-doped sample, the values of D determined from the conventional Hanle method (D_S) and the charge transport measurement (D_C) are inconsistent. There are two possible explanations for the appearance of a large discrepancy in D_S and D_C upon hydrogen doping. First, a system with an exchange field and increased effective g-factor yields a very low value of D_S when fit using conventional Hanle with g_e^*=2. Alternatively, it is well known that D_S and D_C can differ drastically if there are significant electron-electron interactions present in the system [381]. As discussed below, we find that the presence of an exchange field also resolves other inconsistencies generated by conventional Hanle fitting.

We now consider values of spin lifetime determined by the in-plane R_{NL} data and compare it to values determined from conventional Hanle fitting assuming no exchange field. Following the same procedure outlined in section 8.6 from equation (8.18) to (8.23), we obtain values of τ^{so} based on best fits to the high field data of R_{NL}. The method utilized in section 8.6 takes the diffusion coefficient, D_S, from the conventional Hanle fitting of the *pristine* sample, then scales it based on the Einstein relation according to equation (8.20). In this

section, we denote this value as D_{SS}. The resulting spin lifetime values from R_{NL} are plotted in Figure 8.11 b) as a function of gate voltage and labeled "D_{SS}". Alternatively, best-fit values for the gate dependence of spin lifetime using the calculated diffusion coefficient, D_C, given by equations (8.19) and (8.32), are plotted in Figure 8.12 b) (blue open diamonds) and labeled "D_C". The light blue shaded region in the range of 300-600 picoseconds represents the values of spin lifetime consistent with the non-local resistance data and is labeled "R_{NL}". We compare this with the spin lifetimes determined by conventional Hanle fitting. The spin lifetime from the conventional Hanle fitting for 8 s hydrogen exposure displayed in Figure 8.11 c) is re-plotted in Figure 8.12 b) and labeled "D_S" (black open squares). Alternative values for spin lifetime are obtained by performing the Hanle fit with the diffusion coefficient as a fixed parameter given by D_C (and g_e^*=2). The resulting spin lifetime as a function of gate voltage is plotted in Figure 8.12 b) and labeled "D_C" (black open diamonds). The grey shaded region between 3 and 33 nanoseconds represents the values of spin lifetime consistent with the Hanle data assuming g_e^*=2 and is labeled "*Conventional Hanle*". Based on Figure 8.12 b), the spin lifetime determined by conventional Hanle analysis (with g_e^*=2) is inconsistent with the spin lifetimes determined by non-local resistance.

To summarize, with the introduction of atomic hydrogen (or lattice vacancies) to SLG, conventional Hanle fitting with the assumption of g_e^*=2 yields two inconsistencies: (i) values of D_S that are improbably low when compared to D_C and (ii) values of spin lifetime that are too large compared to values obtained from the non-local resistance. Notably, both of these inconsistencies can be alleviated if $g_e^* > 2$. This can be understood by considering the

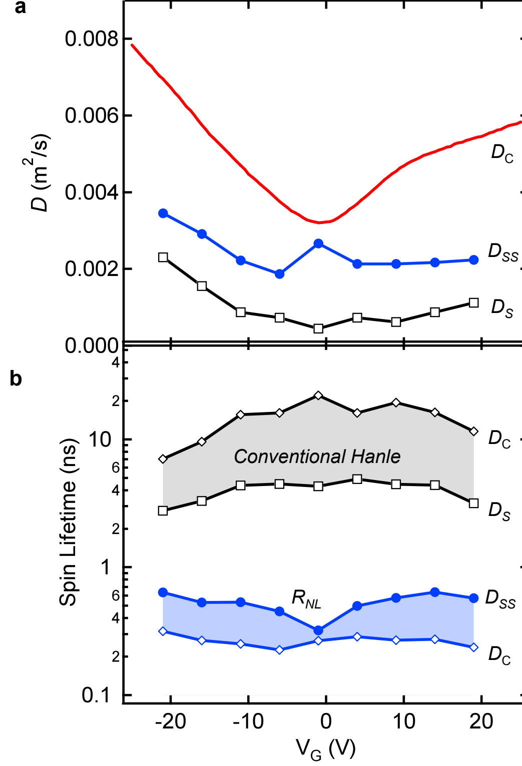

Figure 8.12: Comparison of the Spin Lifetimes. a) Gate dependence of the diffusion coefficients D_S (black open squares), D_C (red curve), and D_{SS} (blue solid circles) for 8 s hydrogen-doped graphene. b) Gate dependence of spin lifetimes for graphene after hydrogen exposure. Grey shaded region represents spin lifetimes by conventional Hanle fitting with D_C (black open diamonds) and D_S (black open squares) without taking the possibility of magnetic moments into account (g_e^*=2). A maximum T_2 of 33 ns is obtained at the charge neutrality point (V_G= -1 V) for D_C=0.0032 m^2/s. Blue shaded region represents spin lifetimes consistent with the in- plane R_{NL} data. Best fits solutions for τ^{so} using D_C (blue open diamonds) and D_{SS} (blue solid circles) according to the procedure outlined in section 8.6.

symmetries of the Hanle equation (8.33),

$$R_{NL} = S \int_0^\infty \frac{e^{-L^2/4D_S t}}{\sqrt{4\pi D_S t}} \cos\left(\frac{g_e^* \mu_B}{\hbar} B_{app,z} t\right) e^{-t/T_2} dt. \tag{8.33}$$

This equation is invariant under the transformation $g_e^* \rightarrow c\, g_e^*$, $T_2 \rightarrow T_2/c$, $D_S \rightarrow c\, D_S$, $S \rightarrow c\, S$, where c is a constant. For a given parameter set (g_e^*, T_2, D_S, S), the transformed

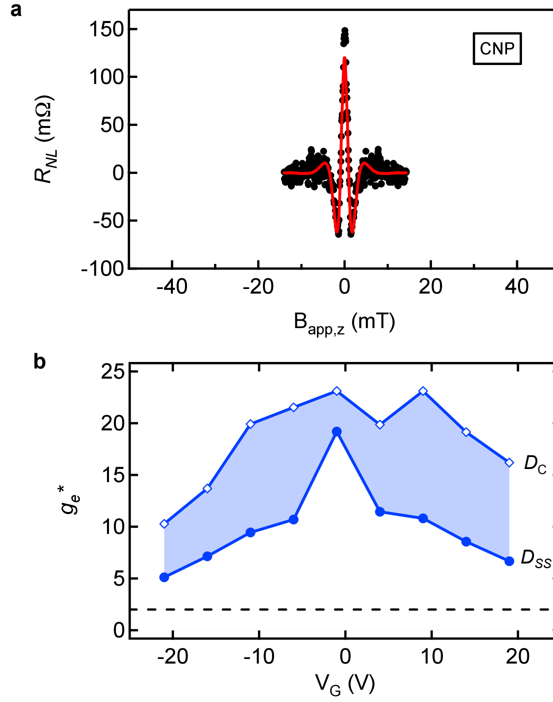

Figure 8.13: Gate Dependence of the Enhanced Precession due to the Exchange Field. a) Hanle precession data at the charge neutrality point (V_G=-1 V) for 8 s hydrogen exposure at T=15 K. A sharp increase in the observed precession due to the exchange field is seen at the charge neutrality point. Best fit to the Hanle equation (red curve) taking into account the Lorentzian shape of the spin lifetime and the scaled diffusion coefficient, D_{SS}, yields an effective g-factor, g_e^*=19.2. b) Gate dependence of g_e^* for both D_C (blue open diamonds) and D_{SS} (blue solid circles).

parameter set $(c\, g_e^*, T_2/c, c\, D_S, c\, S)$ will generate the same Hanle curve. Therefore, if we begin with a conventional Hanle fit that assumes g_e^*=2, a transformation that increases g_e^* (i.e. $c > 1$) has the effect of decreasing T_2 and increasing D_S. This simultaneously alleviates the discrepancies in spin lifetime and diffusion coefficient mentioned earlier, and therefore provides strong evidence for the presence of exchange fields.

The discussion above highlights several key points about the analysis of Hanle data. In the presence of an exchange field, g_e^* becomes a free parameter and the fitting parameters cannot be determined uniquely from the Hanle data alone. Therefore, it becomes necessary

to analyze the in-plane R_{NL} data and the Hanle data together (as detailed in section 8.6) in order to determine key parameters such as spin lifetime and g_e^*. The nature of this data set, with *in-situ* doping, makes it straightforward to apply this analysis, but this may not be true in other studies utilizing Hanle spin precession. Consequently, it brings to light an important question about the use of Hanle fitting in general: how does one tell whether changes in the Hanle curve are due to changes in spin lifetime or g_e^*? Fortunately, the above analysis leads to a useful rule of thumb: If values of D_C and D_S are similar for conventional Hanle fitting, this provides support for the assumption that g_e^*=2. This is important for future Hanle studies of spin relaxation in order to recognize when changes in spin precession data are due to changes in spin lifetime. For systems with an exchange field, this analysis motivates the need for alternative experimental techniques that can independently measure g_e^* and T_2, such as electrically-detected electron spin resonance (ESR) and time resolved spectroscopies.

8.8.2 Gate Dependence and Accuracy of g_e^*

In this section we examine the gate dependence of the effective electron g-factor, g_e^*, due to the presence of an exchange field. Following the procedure of section 8.6, g_e^* values are obtained by Hanle fits to the spin precession data for 8 s hydrogen exposure to sample A using equation 8.28. Figure 8.13 a) shows the spin precession data (black closed circles) at the charge neutrality point (CNP) (V_G=-1 V) where the fastest precession is observed. The best fit solution (Fig. 8.13 a) red curve) to the spin precession data by equation 8.28 is determined through the free parameters S and g_e^*. Fig. 8.13 b) displays the gate dependence

of g_e^* for both D_{SS} (blue solid circles) and D_C (blue open diamonds). The minimum value is g_e^*=5.1 obtained at V_G=-21 V and the maximum is g_e^*=19.2 at the CNP assuming D_{SS}. For D_C, the minimum g_e^* value is 10.3 for V_G= -21 V and the maximum is g_e^*=21.1 at the CNP. Uncertainty of the D value leads to uncertainty in g_e^*, again highlighting the need for techniques in graphene spintronics to directly measure g_e^* and T_2.

We can now examine the viability of performing Hanle analysis in the absence of consideration of R_{NL} data. This is important for experiments in which the contacts might induce additional spin relaxation or in apparatus for which the in-plane field cannot be applied. Next, we can fit the 8 s hydrogen doped spin precession data for Sample A using only D_C as a fixed parameter and allowing S, T_2, and g_e^* to vary. It must be noted that this analysis ignores the field dependence of T_2, but that does not significantly diminish the importance of this approach since the field dependence of T_2 is small when compared to the effect of g_e^* on the Hanle curve shape. In Fig. 8.14 b) we plot the resulting g_e^* (green curve) compared to the previous gate dependence determined using D_{SS} and D_C and Fig. 8.14 a) shows the resulting T_2 values in comparison with the other approaches from Fig. 8.12. It is a great result that the g_e^* values from this approach lie on top of the blue shaded region. This verifies that differences between D_C and D_S signify the presence of an effective g-factor. Interestingly, the best fit T_2 suggests a slight increase in τ_{so}, which may possibly be caused by DP mechanism which is expected to be important in SLG [88, 89, 84]. This analysis approach does not require any input from R_{NL} data and has recently been shown to be extremely useful in

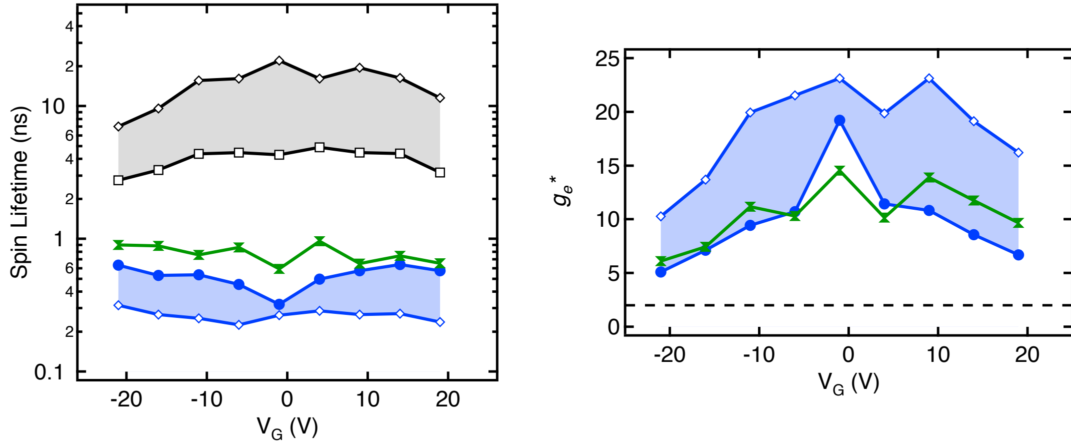

Figure 8.14: Analysis of Hanle Spin Precession Data Without Consideration of R_{NL} Data. a) Gate dependence of spin lifetimes of the Hanle only approach plotted in green. Grey shaded region represents spin lifetimes by conventional Hanle fitting with D_C (black open diamonds) and D_S (black open squares) without taking the possibility of magnetic moments into account (g_e^*=2). b) Gate dependence of the enhanced precession due to the exchange field. Analysis of the Hanle data only assuming a value of D_C is plotted in green compared to g_e^* for both D_C (blue open diamonds) and D_{SS} (blue solid circles). The green curve falls within the expected range indicating that this approach is valid.

understanding the behavior of doped and defected graphene [382, 383], as well as graphene on SiC [383, 78, 79].

8.9 Conclusion

In conclusion, clear signatures of magnetic moment formation are observed in both the non-local spin transport and Hanle precession data, which emerge only after exposure to atomic hydrogen or lattice vacancies. The technique used here, which investigates magnetic moment formation through the scattering of pure spin currents has significant advantages over other experimental attempts to investigate magnetism in graphene. The results and tech-

niques presented here are important for future developments in magnetism and spintronics. In particular, the combination of improvements in tunneling contacts for spin injection into graphene and the ability to perform these measurements *in-situ* with molecular beam epitaxy have been crucial in the completion of this important work.

The investigation by spin-spin interactions is an entirely new way of looking at the induced moments and sheds light on the nature of these magnetic moments and is not expected according to the current theoretical understanding of magnetic moment formation in graphene. For flat graphene, symmetry forbids hybridization of the σ and π bands thus making exchange coupling between conduction spins and the localized moment not possible. These results clearly demonstrate such exchange coupling and has motivated re-examination of the nature of the induced moments as discussed in a recent Castro Neto paper [384].

Further, the observed behavior in the Hanle data can only be explained by the presence of an exchange field. Numerous theorists have examined the possibility of exchange fields as well as their impact on gate tunable magnetism, quantized anomalous Hall effect, the spin rotator, and spin filter as discussed in Chapters 3 and 7. Yet, there have been no experimental signatures of exchange coupling or fields in graphene for any type of system (impurity, proximity, etc...) until now. Our results demonstrate the first observation of exchange fields in graphene. Further, this is the first system to incorporate a spin transistor device with magnetic graphene and demonstrate control over the exchange coupling and exchange field with a back gate. Not only does this work demonstrate new and unexpected spin physics, but it also opens the door to a new area of research that has appeal for both fundamental and ap-

plied physicists and engineers. Very recently, Nair et al., [331] (on the arxiv) have reported a doping effect on the magnetic moments introduced into graphene 'laminates' which seems to qualitatively agree with the results presented here.

Chapter 9

Effect of *in-situ* Deposition of Mg Adatoms on Spin Relaxation in Graphene

9.1 Introduction

Graphene's gate tunable transport, tabletop relativistic physics, chemical attributes, and mechanical properties have interested researchers in a wide variety of fields [44, 45, 43, 385]. In particular, graphene is a candidate material for spintronics due to its weak hyperfine coupling and low intrinsic spin-orbit (SO) coupling strength (Δ_{SO}) [61, 62, 63, 32], which should theoretically lead to long spin lifetimes. Beyond scientific interest, recent progress in large area production by chemical vapor deposition [48, 49] combined with significant advances in efficient spin injection by improved tunneling contacts [71, 77] has greatly improved the potential for advanced information processing utilizing spin-based logic [386]. In particu-

lar, the introduction of efficient tunneling contacts has increased the observed spin lifetime by an order of magnitude (to $\sim$1 nanosecond in exfoliated graphene) by lengthening the escape time due to the back-flow of electrons into the ferromagnetic leads [71, 75, 72]. While graphene remains a highly promising candidate for carbon based spintronics, the observed spin lifetimes are still well below the theoretical expectations and the nature of spin relaxation remains an open question.

In graphene, two possible spin relaxation mechanisms are discussed in the literature: the Elliot-Yafet (EY) mechanism, for which the spin relaxation time (τ_s) is proportional to the momentum scattering time (τ_p), and the D'yakonov-Perel (DP) mechanism, for which $\tau_s \propto \tau_p^{-1}$ [75, 72, 83, 84, 85, 86, 87, 88, 70, 69, 89]. Complicating the situation are the many possible sources of spin relaxation in experiments on SiO_2 substrate including charged impurity (CI) scatterers [83, 84], Rashba SO coupling due to adatoms [85, 93, 86], ripples [87, 88], and edge effects [84, 69]. Early experiments on spin transport in exfoliated graphene were able to take advantage of the tunable carrier concentration (n) and observe a linear relationship between τ_s and τ_p, thus suggesting EY [70, 72]. However, recent theoretical studies have shown that DP is expected to dominate over EY [88, 89] and that Elliot's approach applied to graphene predicts $\tau_s = (\epsilon_F)^2\tau_p/(\Delta_{SO})^2$ [84], for which both Fermi energy ϵ_F and τ_p depend on carrier concentration, thus highlighting the need for experiments that can tune τ_p at fixed carrier concentration, n.

In this work we systematically introduce CI scatterers on non-local single-layer graphene (SLG) spin valves with high quality tunneling contacts. The experiment takes place in an

ultra-high vacuum (UHV) deposition chamber with *in-situ* measurement capability at cryogenic temperatures. All measurements and doping are performed in the same chamber at T=12 K and the sample is never exposed to air. We choose Mg adsorbates as the CI scatterer since elements with low atomic weight should introduce minimal SO coupling. This substantially improves on earlier doping studies that utilized heavy atoms (Au) and ohmic contacts for shorter spin lifetimes ($\tau_s \sim 100$ ps) [171], which are dominated by contact induced spin relaxation [71]. We find that doping with Mg causes large shifts in the charge neutrality point (CNP), indicating significant charge transfer to the graphene layer, accompanied by increased momentum scattering. Spin transport measurements, however, indicate minimal effect on the spin relaxation despite pronounced changes in charge transport. These results indicate that CI scattering is not an important source of spin relaxation in SLG in the current regime of spin lifetimes of $\sim$1 ns.

9.2 Results and Discussion

Graphene flakes are obtained by mechanical exfoliation of HOPG (SPI, ZYA) onto 300 nm SiO_2/Si. SLG flakes are identified under an optical microscope and confirmed by Raman spectroscopy. The graphene flakes are electrically contacted using standard bilayer (PMMA/MMA) e-beam lithography and lift-off procedures. First, outer Au/Ti electrodes (60 nm/8 nm) are defined and deposited by e-beam evaporation to serve as spin insensitive reference contacts. The sample is then annealed for 3 hours in UHV at 150°C immediately

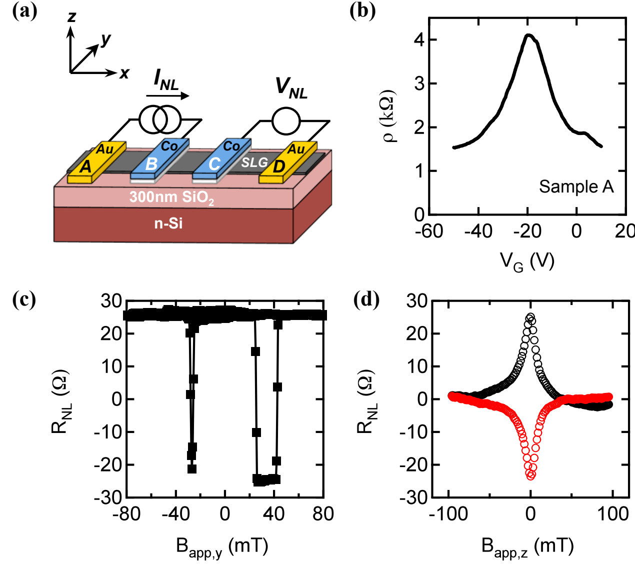

Figure 9.1: Spin Transport in Pristine Graphene. a) Device schematic of the non-local spin valve geometry with inner Co electrodes (blue) and outer Au electrodes (yellow). b) Gate dependent resistivity for sample A at $T = 12$ K. c) R_{NL} for pristine SLG at $V_G = 0$ V. d) Hanle spin precession data in parallel (black) and anti-parallel (red/grey) configuration between electrodes B and C for pristine SLG at $V_G = 0$ V. A constant spin-independent background has been subtracted.

prior to the second lithography step, which defines the inner ferromagnetic electrodes. Angle evaporation is utilized to deposit sub-monolayer TiO_2, which serves as a diffusion barrier for the 0.9 nm MgO tunnel barrier, and 80 nm Co. These tunneling contacts are deposited in a molecular beam epitaxy (MBE) chamber with base pressure of 1×10^{-10} torr. The electrodes are then capped with 5 nm Al_2O_3. A detailed description for the fabrication of tunneling contacts is described elsewhere [72].

Charge and spin transport measurements at T=12 K are performed on non-local devices as shown in Fig. 9.1 a). The gate dependent resistivity of pristine SLG (sample A) is shown in Fig. 9.1 b) with maximum resistivity at the charge neutrality point, $V_{CNP} = -20$ V. The mobility is calculated by taking the slope of the conductivity ($\mu = \Delta\sigma/e\Delta n$) where the carrier

concentration, n (positive for holes), is determined using the relation $n = -\alpha(V_G - V_{CNP})$ and $\alpha = 7.2 \times 10^{10}$ $V^{-1}cm^{-2}$ for 300 nm SiO_2 gate dielectric. The resulting electron and hole mobilities are $\mu_e = 1774$ cm^2/Vs and $\mu_h = 1508$ cm^2/Vs, respectively. For spin transport measurements, an AC current, $I_{NL} = 1$ μA (11 Hz), is applied to inject spin-polarized carriers into SLG at electrode B. This spin polarization diffuses through the graphene channel along the x-axis to electrode C. A non-local voltage, V_{NL}, is detected using standard lock-in techniques between electrodes C and D due to the accumulation of spins beneath electrode C. The detected voltage, V_{NL}, is proportional to the spin-dependent chemical potential difference between electrodes C and D [32]. The non-local resistance, $R_{NL} = V_{NL}/I_{NL}$, depends on the relative orientation of the two inner ferromagnetic electrodes and is positive (negative) for parallel (antiparallel) alignment. An external magnetic field, $B_{app,y}$, is applied along the electrode easy axis (y-axis) and is used to control the relative alignment of the magnetic electrodes. A typical sweep of $B_{app,y}$ for sample A at $V_G = 0$ V ($n = -1.44 \times 10^{12}$ cm^{-2}) is shown in Figure 9.1 c), for which the spin signal $\Delta R_{NL} = R_{NL}^{P} - R_{NL}^{AP}$ is 50.5 Ω. The dimensions of the graphene spin channel for sample A are defined by the channel length $L = 2.2$ μm and width $w = 2.4$ μm. The spin lifetime can be determined from Hanle spin precession measurements in which a magnetic field, $B_{app,z}$, is applied out of plane allowing the injected spins to precess around $B_{app,z}$. At large fields, the ensemble spin population dephases as $B_{app,z}$ is increased due to a distribution of arrival times at electrode C. In the tunneling limit,

the ensemble spin precession can be fit using the Hanle equation [32, 72],

$$R_{NL} \propto \int_0^\infty \frac{e^{-L^2/4Dt}}{\sqrt{4\pi Dt}} \cos\left(\frac{g\mu_B B_{app,z} t}{\hbar}\right) e^{-t/\tau_s} dt \tag{9.1}$$

where D is the diffusion coefficient, g is the electron g-factor, μ_B is the Bohr magneton, and $\hbar$ is the reduced Planck's constant. Figure 9.1 d) shows characteristic Hanle curves for parallel and antiparallel alignment for $n = -1.44 \times 10^{12}$ cm^{-2}, where best fits to the Hanle equation yield the diffusion coefficient $D = 0.058$ m^2/s, spin lifetime $\tau_s = 1.10$ ns, and spin diffusion length $\lambda_s = 8.0$ μm.

Next, Mg adsorbates are deposited *in-situ* in the UHV MBE chamber with base pressure 3×10^{-10} torr while the sample is maintained at T=12 K. Elemental Mg (99.99%) is evaporated from an effusion cell at a rate of 0.055 Å/min calibrated by a quartz crystal monitor and corresponds to a doping rate of 0.02% of a monolayer (ML) per second, where 1 ML is defined as 1.908×10^{15} atoms/cm^2. After 1 s Mg deposition, the charge and spin transport are re-measured. Figure 9.2 summarizes the effect on the charge transport on sample A following Mg doping. Figure 9.2 a) shows conductivity σ vs. V_G for Mg doping of sample A up to 7 s deposition time. After 7 s of Mg doping, V_{CNP} has shifted to $V_G = -70$ V. This indicates that Mg donates electrons to the graphene, consistent with other work on transition metals [148, 51, 144]. Figure 9.2 b) displays V_{CNP} for each doping time and demonstrates a linear relation between charge transfer and Mg coverage at a rate of -1438 V/ML. Also, Mg doping introduces CI scattering which decreases the conductivity and the mobility. Figure

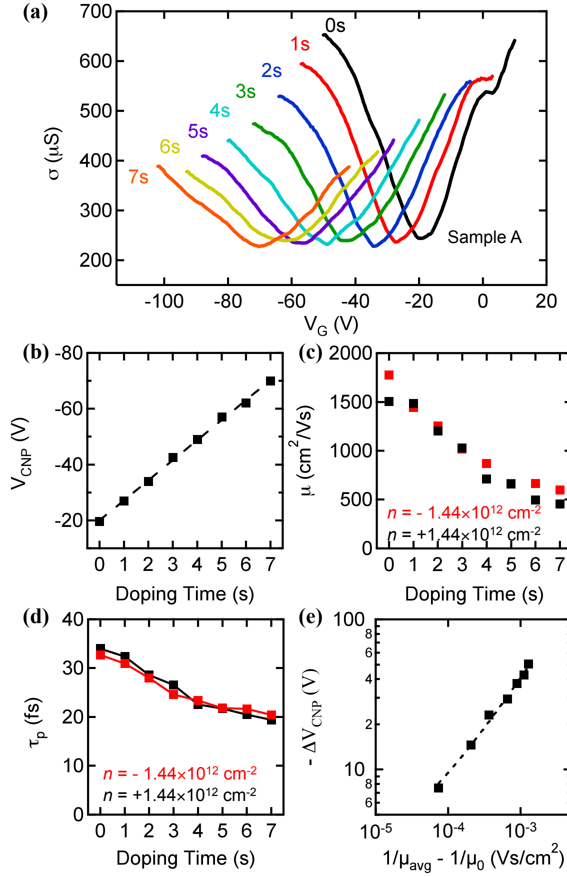

Figure 9.2: Effect on Charge Transport by Mg Doping. a) Gate dependent conductivity as the SLG (sample A) is systematically doped up to 7 s with Mg adsorbates at T=12 K. b) Charge neutrality point (CNP) plotted against the Mg doping time. c) Electron (red/grey) and hole (black) mobility as a function of Mg coverage. d) Calculated momentum scattering time for electrons (red/grey) and holes (black) as a function of Mg coverage. e) Shift in the charge neutrality point, $-\Delta V_{CNP}$, plotted against the change in inverse mobility. The dashed line is a power law fit (best fit exponent $b = 0.72$).

9.2 c) displays the effect of systematic Mg doping on the electron and hole mobilities. For undoped graphene, the mobility is $\mu_e = 1774$ cm^2/Vs and and $\mu_h = 1508$ cm^2/Vs, and decreases to $\mu_e = 599$ cm^2/Vs and $\mu_h = 453$cm^2/Vs after 7 s deposition time. The momentum

scattering time can be determined using Boltzmann transport theory [50],

$$\tau_p = \frac{h\sigma}{e^2 v_F \sqrt{n\pi g_s g_v}} \tag{9.2}$$

where h is Planck's constant, e is the electron charge, $v_F \sim 1 \times 10^6$ m/s is the Fermi velocity, and $g_e = 2$ and $g_v = 2$ are the spin and valley degeneracies. Fig. 9.2 d) shows τ_p vs. Mg doping for electrons and holes at $n = \pm 1.44 \times 10^{12}$ cm^{-2}. With increasing Mg coverage, the momentum scattering time decreases due to increased CI scattering. Lastly, we investigate the nature of Mg morphology on the graphene surface. Figure 9.2 e) shows the shift in charge neutrality point plotted against $1/\mu_{avg} - 1/\mu_0$, where μ_{avg} is the average of the electron and hole mobilities and μ_0 is the average electron and hole mobility for pristine graphene. The dashed line is a power law fit of $-\Delta V_{CNP} \propto (1/\mu_{avg} - 1/\mu_0)^b$, for which values of $1.2 < b < 1.3$ indicates a $1/r$ scattering potential for point-like scatterers [387, 159, 51, 144]. The best fit value of $b = 0.72$ indicates that the Mg adatoms do not transfer charge as well as they add momentum scattering when compared to point-like scatterers. This suggests the possibility of clustering even at cryogenic temperatures [51, 144]. This does not introduce a theoretical difficulty because the relationship $\tau_s = (\epsilon_F)^2 \tau_p / (\Delta_{SO})^2$ for EY scattering in SLG has been shown to hold for a wide variety of scattering sources including weak scatterers, strong scatterers (i.e. vacancies), CI scatterers, and clusters [84]. Lastly, we note that the gate dependent resistance curves exhibited no measurable change as a function of time in between Mg depositions.

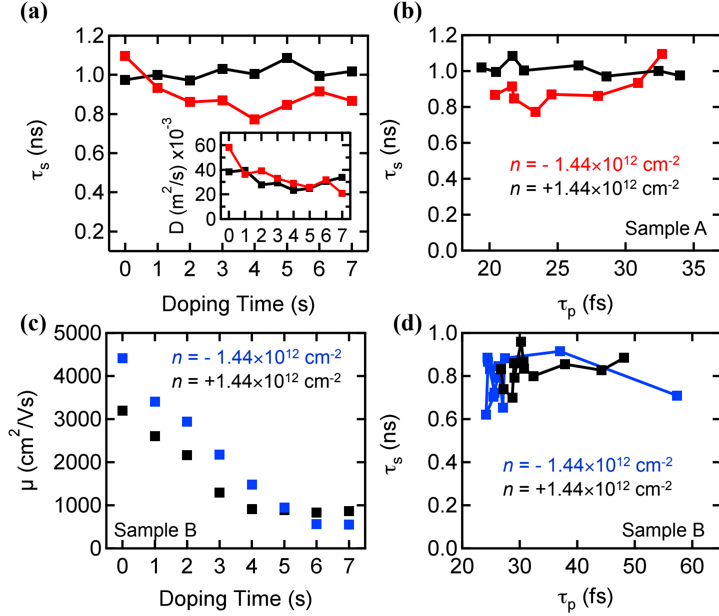

Figure 9.3: Effect on Spin Transport by Mg Adatoms. a) Hanle spin lifetime for sample A plotted against Mg coverage. Inset is the diffusion coefficient obtained from the Hanle fit as a function of Mg coverage at T=12 K. b) Hanle spin lifetime for sample A plotted against the calculated momentum scattering times for each doping. c) Electron (blue/grey) and hole (black) mobility as a function of Mg coverage for sample B at T=12 K. d) Hanle spin lifetime for sample B plotted against the calculated momentum scattering times.

We now turn to the effect on spin relaxation in SLG by Mg doping. After each Mg deposition at 1 s intervals, Hanle spin precession measurements were performed for $n = \pm 1.44 \times 10^{12}$ cm^{-2}. The resulting fits to the Hanle curves yield values for τ_s and D which are plotted against Mg doping time in Figure 9.3 a) and 9.3 a) inset, respectively. The diffusion coefficient decreases with increasing Mg coverage starting at 0.058 m^2/s (0.038 m^2/s) for pristine graphene and decreases to 0.021 m^2/s (0.033 m^2/s) for 7 s doping time for electrons (holes). This is in agreement with the observed charge transport behavior for which momentum scattering increases with Mg doping. Interestingly, the spin lifetimes (Fig. 9.3 a)) shows minimal variation, without a significant trend for electrons and holes. In Figure

9.3 b) we plot the Hanle spin lifetime for sample A against the momentum scattering time calculated from the conductivity using Eq. 9.2 from Boltzmann transport theory for sample A. With increasing Mg doping, τ_p decreases from ~ 35 fs to ~ 20 fs, but the spin relaxation time is constant for holes (black squares) while decreasing only slightly for electrons (red/grey squares). This experiment was repeated on several samples and in general τ_s does not display any substantial variations as a function of τ_p. For instance, results for a sample with higher initial mobility (sample B) are summarized in Fig. 9.3 c) and 9.3 d). Figure 9.3 c) displays the change in mobility for electrons and holes under Mg doping. For sample B, the mobility decreases from 4415 cm^2/Vs (3200 cm^2/Vs) for the pristine spin valve to 598 cm^2/Vs (1290 cm^2/Vs) after 7 s Mg doping for electrons (holes). In Fig. 9.3 d), we show τ_s displayed against the momentum scattering times for sample B at $n = \pm 1.44 \times 10^{12}$ cm^{-2}. Here, τ_s is near 800 ps and stays relatively unchanged as τ_P decreases from ~ 60 fs to ~ 24 fs.

As Fig. 9.3 b) and 9.3 d) show, τ_s does not vary substantially as τ_p is varied by CI scattering. This is in agreement with and goes beyond recent reports on CI scattering by organic-ligand bound nanoparticles, which are able to reversibly tune the mobility and momentum scattering [97]. However, due to the relatively large size (~ 13 nm, which is over 50 lattice constants) of the nanoparticles used in that study, it is not possible to draw conclusions for atomic-scale CI scatterers such as surface adatoms and impurities in the SiO_2 substrate. In contrast, Mg adsorbates are able to probe the atomic-scale regime. With the agreement between two quite different experiments (Mg adsorbates deposited in UHV and organic-ligand

bound nanoparticles deposited by drop casting) probing different length scales of the scattering potential, it is clear that spin relaxation in graphene is not determined by CI scattering despite its importance for momentum scattering.

It is also worth mentioning that this result is not incompatible with the early experiments showing a linear relation between τ_s and D by tuning the carrier concentration [70, 72]. While Mg adsorbates modify τ_p by introducing CI scattering and possibly local Rashba SO coupling, there are many alternative sources which might contribute to EY (i.e. weak scatterers, resonant scattering, phonon scattering) which could still present themselves as the carrier concentration is tuned leading to $\tau_s \sim D$. Thus, EY spin relaxation originating from sources other than CI scattering is still viable.

Some other possibilities to consider are DP spin relaxation in spatially inhomogeneous Rashba SO fields. It has recently been proposed that this type of SO coupling can result in a competition between EY-like and DP-like scaling behavior to yield unconventional scaling between τ_s and τ_p [86]. Another possibility is that the spin lifetime is limited by contact effects such as inhomogeneous stray fields [96]. Due to its atomically thin nature, this could have a larger effect for graphene compared to semiconductor or metallic spin transport systems that are typically much thicker.

9.3 Conclusion

In conclusion, we have investigated charge and spin transport in SLG by systematically introducing CI scatterers in the form of Mg adsorbates. The introduction of Mg was shown to transfer electrons to the SLG and decrease the momentum scattering time. Despite pronounced changes in momentum scattering, no significant variation was seen in spin relaxation. This indicates that CI scattering is not an important source of spin relaxation in SLG in the current regime of spin lifetimes ($\sim$1 ns).

Chapter 10

Appendix A: Growth Recipes

10.1 Introduction

In this section I will outline the step-by-step growth procedures for a variety of growths to serve as a guide to other group members. All detailed recipes were developed in the Kawakami group main chamber for growths on 'Adrian's' sample platen (pocket). 'Jared's' pocket registers similar sample thermocouple temperatures.

10.2 Mg Distillation and MgO Homoepitaxy

10.2.1 A (Recent) Growth Perspective on MgO

Our group has looked for various ways to grow flat crystalline MgO. Before I joined the group, several key results had already been achieved for FPP projects and graphene spintron-

ics. Yan Li developed a reactive growth using elemental Mg and molecular oxygen which she was able to deposit single crystal on GaAs. However, through her work on FPP, these films were shown to have Mg-rich interfaces [48]. Wei-Hua Wang, Wei Han, and Kyle Pi had demonstrated that by using a single crystal MgO target, e-beam MgO can grow flat on HOPG and graphene with a small amount of Ti seeding [388]. This led directly to huge success in achieving high quality tunneling spin injecting contacts to graphene [71]. Lastly, and most relevant for what follows, Jared Wong and Richard Chiang showed that annealing MgO(001) substrate can often bring contaminants to the surface of the MgO substrate and that metals growths (Co, Fe, Ag) directly on bare MgO substrate resulted in contaminated films. Therefore, they developed a recipe for growing homoepitaxial MgO buffer layers that were flattest at around 350 °C [289]. The RHEED patterns of the underlying MgO substrate is vastly improved after adding a 10 nm buffer layer of e-beam MgO (see Fig. 10.1). For the e-beam MgO deposition on Ge, following Jared's approach with homoepitaxy, Wei discovered that there is an optimal temperature around 250 °C where the films demonstrate best crystallinity and smoothness [342]. This work directly led to my realization that the same should be true for Si and GaAs. And both recipes for e-beam MgO growth on Si demonstrate an optimal temperature for best crystallinity and smoothness. We have since learned, mainly from experience with EuO, that the reason for this optimal temperature is most likely related to a distillation effect.

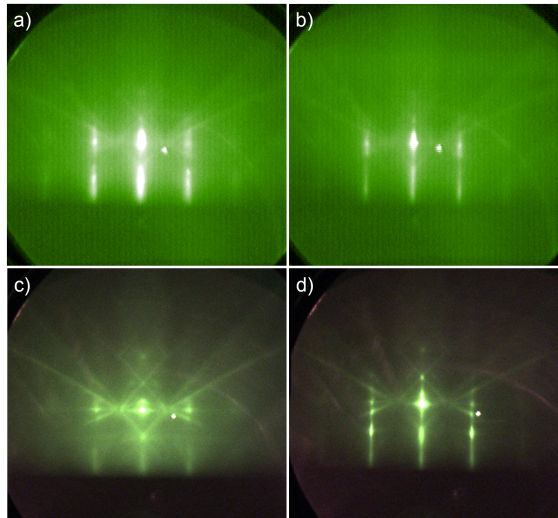

Figure 10.1: Homoepitaxy of e-beam MgO on MgO(001). a) RHEED pattern of MgO(001) substrate along [100]. This substrate has been DI rinsed and annealed at 600 °C for 30 min. Annealing greatly improves the RHEED quality. b) 10 nm homoepitaxy of e-beam MgO at 350 °C on the substrate shown in a). Images taken in 2010. c) RHEED images of MgO(001) along [100] after annealing at a steeper rocking angle using the new CCD camera. Image is from May 2011. d) Subsequent homoepitaxy of 10 nm MgO(001) along [100]. Sharpened streaks, spots, and Kikuchi lines indicated improvement in the crystalline surface. The anomalous spot in each image is a hole in the phosphorous screen. The screen was eventually replaced (after these images were taken) with a STAIB phosphorous screen with Al coating, which significantly reduces IR background from the heater. Images are taken at 15 keV.

10.2.2 Mg Distillation

At UHV pressures, Mg evaporates at reasonably low temperatures (< 500°C). Using a low temperature effusion cell, I have followed the procedure for investigating distillation as developed for Eu. Fig. 10.2 illustrates this procedure. Fig. 10.2 a) shows a 4 nm e-beam MgO buffer layer on MTI Corp. MgO(001) substrate. The substrate has been treated by deionized (DI) water rinse followed by 600 °C anneal in UHV. A 4 nm MgO e-beam buffer layer is deposited at 350 °C. The sample is then heated to 500 °C for distillation testing. At 500 °C, the Mg cell is opened under UHV condition (no molecular oxygen leak). If the MgO

RHEED pattern remains precisely unaltered, except for some possibility of a slight decrease in intensity, then Mg is under distillation condition. Fig. 10.2 b) displays the MgO buffer layer exposed to the Mg flux rate of what is supposed to be 4 Å/min as calibrated by the quartz crystal monitor. The RHEED pattern remains unaltered indicating that Mg has zero sticking probability to MgO at above 500 °C. The sample is then cooled to 300 °C and this temperature is maintained for $\sim$10 min. Again the RHEED pattern is unaltered, indicating distillation. The sample is then subsequently cooled to 200 °C and then 150 °C, which both indicate distillation, despite being below the temperature of evaporation according to the thermal cell. At 55 °C (Fig. 10.2 f)), we see that the RHEED pattern is altered by increased Mg sticking probability and resulting Mg overlayer. The Mg cell is then closed and the sample is heated to 150 °C, where the Mg overlayer RHEED pattern begins to undergo changes possibly due to re-evaporation or atomic diffusion and smoothing associated with annealing process. Heating to 300 °C, as shown in Fig. 10.2 h) returns the sample to it's original RHEED pattern of the MgO buffer layer, demonstrating full re-evaporation of the deposited Mg layer of approximate thickness $\leq$ 8 nm. This is a remarkable result.

We can then understand the excellent quality of e-beam MgO homoepitaxy in the following way. In the e-beam source, electrons bombard the source crystalline MgO target and dissociate Mg and O which normally leads to MgO with oxygen vacancies. However, deposition at elevated temperatures allows for surface diffusion of any Mg atoms, as well as distillation of excess Mg, leading to stoichiometric films.

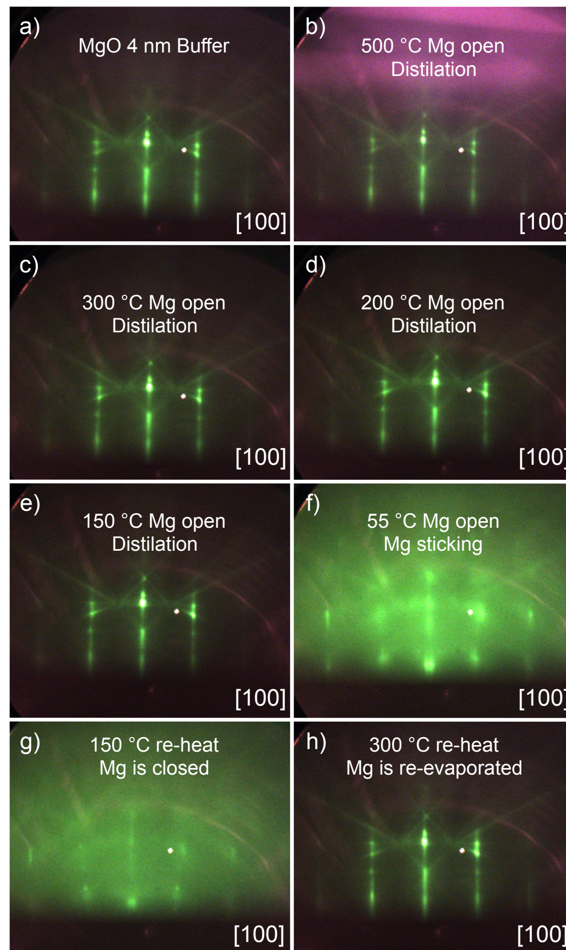

Figure 10.2: Evolution of Mg Distillation. a) MgO (4 nm) e-beam buffer layer grown at 350 °C on MgO(001). b) same 4 nm MgO buffer layer exposed to a Mg flux at 500 °C. c) - d) The substrate temperature is the decreased sequentially with stops at 300 °C (c), 200 °C (d), 150 °C (e), and 55 °C (f). The sticking probability of Mg increases below 150 °C allowing for the growth of a metallic Mg overlayer. After 20 minutes of deposition at 55 °C, the Mg shutter is closed. g) The sample is then re-heated to 150 °C and the Mg overlayer pattern begins to change. h) The original MgO e-beam buffer layer pattern returns after post annealing the Mg/MgO system to 300 °C. This can be understood as re-evaporation of the Mg overlayer.

10.2.3 MgO Homoepitaxy by rMBE

While e-beam MgO homoepitaxy provides excellent single crystal MgO surfaces for growth studies, the e-beam style of deposition is limited by growth rate and total thickness. The higher the rate of e-beam deposition (higher the power), the more oxygen vacancies are in-

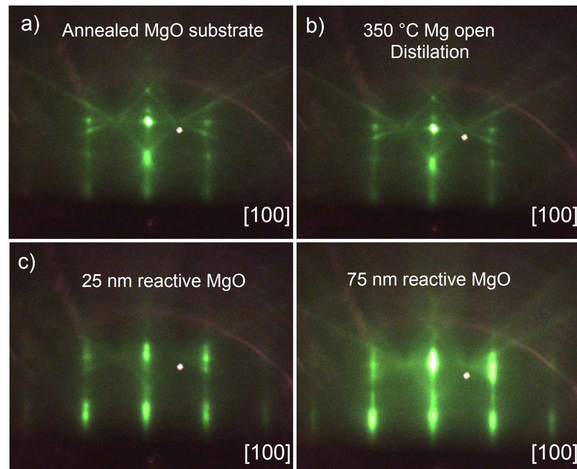

Figure 10.3: Homoepitaxy of Reactively Grown MgO on MgO(001). a) Annealed MgO(001) substrate. b) MgO substrate maintained at 350 °C and with incident Mg flux in distillation mode. c) 25 nm reactive growth of MgO through oxidation of elemental Mg flux. d) Final RHEED pattern of 75 nm rMBE MgO homoepitaxial film on MgO(001).

troduced. Also, e-beam rates in our MBE chamber, generally never exceed 3 Å/min because the source will run out of material very quickly. For this same reason, thick films above 10 nm are not experimentally realistic. For instance, while doing growth studies that involve 10 nm buffer layers, running out of MgO is the main reason for chamber vents, on the order of every 2 months. For each vent, it takes 1.5 - 2 weeks to get the chamber back up and fully running with clean material leading to a down time of 20%, which is not good for research. On the other hand, thermal evaporation sources of the high temperature variety, need refilling approximately every 2 vents ($\sim$4 – 6 months depending on usage). The low temperature effusion cells require filling at most once per year. Therefore, having thermal sources is desirable if thicker MgO films are needed. With the discovery of Mg distillation, it then became feasible to grow thick ($>$ 100 nm) films, with only a moderate decrease in quality from the e-beam MgO growths.

Fig. 10.3 shows the RHEED patterns for rMBE homoepitaxy of MgO on MgO(001) substrate. The substrate is first DI rinsed and the subsequently UHV annealed at 600 °C for 1 hour (Fig. 10.3 a)). The sample is then cooled to RT to take a Mg deposition rate, which was determined to be 4.1 Å/min. The sample is then heated to 350 °C and the temperature is allowed to stabilize. Next, the Mg shutter is opened and the incident Mg flux, in distillation condition, re-evaporates off the substrate surface leaving the RHEED pattern unaltered (Fig. 10.3 b)). The growth commences with the introduction of an oxygen partial pressure. Growth in the distillation regime for MgO differs, and is in fact simpler, from that of EuO growth. As MgO is the thermodynamically stable oxide [287], there is no need to worry about other oxidation states, and therefore no need to worry about limiting the oxygen content supplied during the growth. Therefore, we can simply overpressure with oxygen such that the flux of oxygen exceeds the Mg flux supplied to the substrate. For the reactive growth shown in Fig. 10.3 c) and d), $P_{O_2} \sim 1 \times 10^{-7}$ Torr. After 75 nm of growth. To terminate the growth, since there is no concern for over-oxidation of the MgO overlayer, the Mg shutter is first closed. (This is opposite of EuO growth termination). The total chamber pressure increases from 1.0×10^{-7} to 1.6×10^{-7} Torr, indicating that at 4.1 Å/min of Mg, about $\sim 5 \times 10^{-8}$ Torr molecular oxygen partial pressure is needed to fully oxidize the incoming Mg flux. The final homoepitaxial MgO film of 75 nm is shown in figure 10.3 d). The RHEED indicates some islanding, and that the e-beam MgO produces higher quality crystalline surfaces (compare with fig. 10.1 d) and 10.2 a)), but that the growth by rMBE is really quite good.

10.2.4 Recipes for MgO Homoepitaxy

Homoepitaxy of e-beam MgO buffer layers

1. Rinse MgO(001) substrate with DI water ($\sim$ several seconds). Substrate is usually 10 mm x 10 mm x 0.5 mm double side polished from MTI corp.

2. Blow dry with nitrogen.

3. Mount with Ta foil on corners to Thermionics sample platen (pocket).

4. Load into load-lock and pump down. Once pumped, Transfer to main chamber.

5. Take initial RHEED images along MgO(001) [100] and [110]. Pattern should appear slightly blurry.

6. Anneal in UHV at 600 °C for 1 hour. (Optional: Anneal in O_2 partial pressure of $\sim 5 \times 10^{-8}$ – 1×10^{-7} Torr.) Cool to RT when done.

7. Take post-anneal RHEED images along MgO(001) [100] and [110]. RHEED patterns should be much improved, but there should be some obvious broadening of the diffraction streaks.

8. Warm up e-beam MgO cell to deposition power. HV = 4.8 kV. Emission $>$ 8 mA. 17mA is maximum power and usually means you are out of MgO and the e-beam is now punching through the MgO crystal to the Ta crucible and your samples will be contaminated with Ta. This can be verified checking for Ta in Auger spectroscopy data.

9. Move sample into deposition monitor position (beyond x = 1.9 inches) and load in deposition monitor. Take MgO rate. When done, close MgO shutter, wheel out the deposition

monitor, and return sample to growth position (x = 1.3 inches). Typical MgO rate is ~ 1 – 1.5 Å/min with a background pressure of $\sim 1 \times 10{-}8$ Torr.

10. Heat substrate to $T_S = 350$°C ($T_M \sim 440$°C) and allow temperature to stabilize. Temperature stabilization is certain once T_M is constant.

11. Deposit 10 nm e-beam MgO, which should take $\sim$ 1 - 1.5 hours. Close MgO shutter at end of growth and turn off e-beam power supply.

12. Cool sample to RT and take final RHEED patterns along MgO(001) [100] and [110].

Homoepitaxy of Reactive MgO Layers

1. Rinse MgO(001) substrate with Di water ($\sim$ several seconds). Substrate is usually 10 mm x 10 mm x 0.5 mm double side polished from MTI corp.

2. Blow dry with nitrogen.

3. Mount with Ta foil on corners to Thermoinics sample platen (pocket).

4. Load into load-lock and pump down. Once pumped, Transfer to main chamber.

5. Warm up Mg cell to growth temperature.

6. Take initial RHEED images along MgO(001) [100] and [110]. Pattern should appear slightly blurry.

7. Anneal in UHV at 600 °C for 1 hour. (Optional: Anneal in O_2 partial pressure of $\sim 5 \times 10^{-8}$ – 1×10^{-7} Torr.) Cool to RT when done.

8. Take post-anneal RHEED images along MgO(001) [100] and [110]. RHEED patterns should be much improved, but there should be some obvious broadening of the diffraction streaks.

9. Move sample into deposition monitor position (beyond x = 1.9 inches) and load in deposition monitor. Take Mg rate. When done, close Mg shutter, wheel out the deposition monitor, and return sample to growth position (x = 1.3 inches). Typical Mg rate can be anywhere between $\sim$ 1 – 8 Å/min depending on the desired final thickness and available growth time. We have found that 4 Å/min produces good film quality.

10. Heat substrate to $T_S = 350$ °C ($T_M \sim 440$ °C) and allow temperature to stabilize. Temperature stabilization is certain once T_M is constant.

11. Open Mg shutter and allow for Mg distillation for a few minutes to allow the cell and system to come into steady state.

12. Open O_2 leak valve and stabilize oxygen partial pressure depending on Mg deposition rate. Typically 1×10^{-7} Torr should suffice for an Mg rate of $\sim$ 4 Å/min. Deposit for the desired time and monitor the total chamber pressure to make sure the oxygen partial pressure remains stable.

13. Terminate growth by closing the Mg shutter and oxygen leak valve. The order is irrelevant. This is because closing the oxygen leak first, with Mg flux still incident on the sample, will just result in Mg distillation. On the other hand, closing the Mg first, with oxygen still in the chamber, does not over-oxidize the MgO film as it is already stoichiometric and thermo-

dynamically stable. However, closing the Mg shutter first will tell you the amount of oxygen partial pressure that was used for full conversion. For instance, if the total pressure during growth is 1.0×10^{-7} Torr, and then the growth is terminated my closing the Mg shutter, the resulting chamber pressure may increase to 1.3×10^{-7} Torr, indicating that only 3×10^{-8} Torr was needed for achieving stoichiometric growth.

14. Cool sample to RT and take final RHEED patterns along MgO(001) [100] and [110].

10.3 MgO on Semiconductors by e-beam Deposition

10.3.1 MgO on GaAs(001)

There are several GaAs substrates that have been involved in growths here at UCR. We have examined substrates provided by three sources: i) collaboration with the Awschalom group at UC Santa Barbara, ii) AXT, inc., and iii) MTI Corporation. The samples provided by the Awschalom group are by far the best in terms of versatility, crystalline quality, and spin properties. GaAs supplied by AXT has shown to have moderate spin lifetimes of several nanoseconds (see Fig. 10.4). MTI substrates show characteristic semiconducting properties, but time resolved TRKR measurements showed no spin signals. The substrates provided by Awschalom's group are best for high quality optical studies of spin dynamics, the AXT substrate is acceptable for large wafer (>1 cm) spin injection for experiments such as the slow muons projects. Much of the substrate preparation, growth, and subsequent processing for optical experiments, is discussed in detail in Yan Li's Ph.D. thesis [389] and will not be

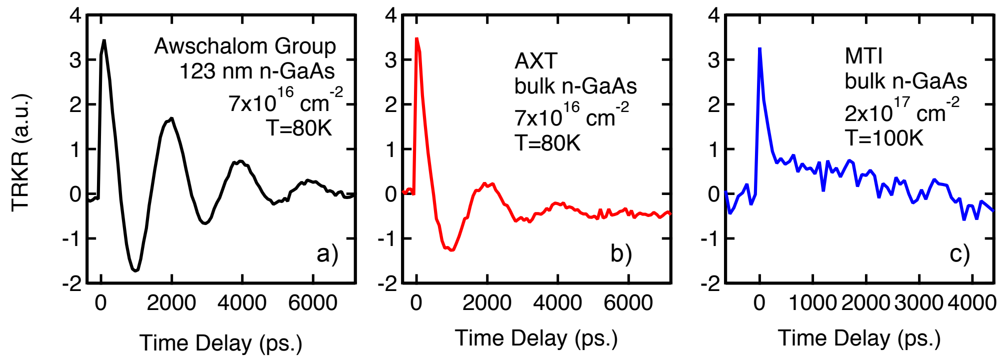

Figure 10.4: Comparison of Spin Lifetimes by TRKR on Different GaAs Substrates. a) Time resolved Kerr rotation (TRKR) measurements tuned to the band gap of GaAs at T = 80 K on a sample of n-GaAs with optimal doping of 7×10^{16} cm^{-2}. The sample structure is MgO 2(nm) / n-GaAs (123 nm) / $Al_xGa_{1-x}As$ (400 nm) / GaAs(001). The applied field of $B = 900$ Oe allows for the optically injected spin population to precess, which generates the oscillations observed in the data. b) TRKR measured on bulk substrate from AXT for $B = 900$ Oe. There is a slight decrease in spin lifetime as can bee seen in the faster decoherence (faster damping of the oscillating curve) as a function of time. c) TRKR measured on bulk n-GaAs from MTI for $B = 900$ Oe. There is no evidence for optical spin orientation.

discussed here. Below I will briefly outline the step-by-step procedure for growing e-beam MgO on 2x4 reconstructed GaAs surfaces. 2x4 reconstructed surfaces can be achieved on samples provided by the Awschalom group which are As capped. Desorbing of the arsenic cap and subsequent annealing to $\sim$ 420 °C yields 2x4 reconstructed surfaces. See [390] for a review on GaAs reconstructed surfaces.

Recipe

1. Cleave the GaAs(001) substrate provided by Awschalom's group. The substrate has the following structure As / n-GaAs* / $Al_xGa_{1-x}As$ (400 nm) / GaAs(001). the n-GaAs* layer can be of varying thickness and doping upon request. Over the years Shawn Mack has been generous in providing samples to our group. Common doping is usually between 1×10^{16}

cm^{-2} and 1×10^{19} cm^{-2} depending on the desired spin-based application. Similarly the thickness can vary, depending on the application and desired depletion region [103, 391, 102, 392, 393]. A typical sample, for which the only concern is high quality optical spin experiments, consists of 123 nm with optimal doping for longest spin lifetime [103] of $\sim 10^{16}$ cm^{-2}. The $Al_xGa_{1-x}As$ acts as an etch stop for TRFR experiments. For more detail see ref. [389]. Note: cleaving As capped GaAs may be toxic and a face mask should be worn. All dust should be properly disposed of.

2. Mount with Ta foil on corners to Thermoinics sample platen (pocket).

3. Gently wipe the sample face clean with IPA using a lens tissue. Never wipe with the same part of the lens tissue. The point is to remove any dust from the cleaving process. Re-wiping with the same lens tissue could scratch the surface by scraping the already removed dust particles back along the surface.

4. Blow dry with nitrogen.

5. Load into load-lock and pump down.

6. Once pumped, transfer onto the buffer heater or into the main chamber for desorbing of As capping layer. Note: in previous years, desorption of the As capping layer was done in the buffer chamber at ∼320 °C according to the buffer heater thermocouple. However, recently, due to a teaching experience mishap, the buffer heater now sits further back in the buffer heater port. Desorbing As in the buffer heater now seems to contaminate GaAs samples and so desorbing As should take place in the main chamber. The reason for the current problem

in the buffer chamber is due to desorbing of gasses off the buffer chamber port walls during annealing, which doesn't seem to affect other annealing procedures (i.e. Graphene device annealing at 150 °C), but does affect the GaAs As desorbing. An advantage of desorbing in the main chamber is that the RHEED pattern can be carefully monitored to find the exact temperature for desorption and reconstruction.

7. In the main chamber, heat the GaAs substrate to 350 °C ($T_M \sim 440$°C). At this temperature the As cap should desorb and the chamber pressure will rise. Wait for full desorption of the As layer. The chamber pressure should decrease to $\sim 1 \times 10^{-9}$ Torr. Monitor the RHEED pattern, which should appear after desorption. There should be no RHEED pattern before that As cap is desorbed.

8. Cool the sample to RT and re-orient the sample along [110] or [1$\bar{1}$0] direction.

9. Heat substrate to $T_S = 350$ °C ($T_M \sim 440$ °C).

10. In 10 °C increments, heat the substrate until 2x4 reconstruction is achieved. The RHEED patterns for 2x4 reconstructed GaAs are shown in section 5.3, figures 5.2 a) and 5.2 b).

11. Cool the sample to RT and take RHEED along GaAs(001) [110] and GaAs(001) [1$\bar{1}$0] direction.

12. Warm up MgO cell to deposition power. HV = 4.8 kV. Emission $>$ 8 mA. 17mA is maximum power and usually means you are out of MgO and the e-beam is now punching through the MgO crystal to the Ta crucible and your samples will be contaminated with Ta. This can be verified checking for Ta in Auger spectroscopy data.

13. Move sample into deposition monitor position (beyond x = 1.9 inches) and load in deposition monitor. Take MgO rate. When done, close MgO shutter, wheel out the deposition monitor, and return sample to growth position (x = 1.3 inches). Typical MgO rate is ~ 1 – 1.5 Å/min with a background pressure of $\sim 1 \times 10^{-8}$ Torr.

14. Heat to $T_S = 300$ °C ($T_M \sim 390$ °C).

15. Deposit 2 nm e-beam MgO. Close MgO shutter at end of growth and turn off e-beam power supply.

16. Cool sample to RT and take final RHEED patterns along MgO(001) [110] // GaAs(001) [$1\bar{1}0$] and MgO(001) [100] // GaAs(001) [100].

10.3.2 MgO on Si(001) for Al/Fe/MgO/Si Collaboration with OSU

This is the growth recipe for the silicon spin injection collaboration with the Center for Emergent Materials (CEM) at The Ohio State University. Samples of commercial silicon on insulator (SOI) are shipped from OSU to UCR for growth. Measurements are performed at OSU. Note: For safety, **all etching processes for silicon should be done in the UCR Cleanroom at the specified Acid bench**. The cleanroom has proper safety equipment and clothing coverings including special gloves for working with HF, aprons for working with acids, and face masks. **You must get proper cleanroom and acids bench training by cleanroom facilities personnel AND special training for this particular etch from an older grad student before using this procedure.** Additional note: The cleanroom nitrile gloves sometimes have holes in them even though they should not. Be sure to wear two pairs

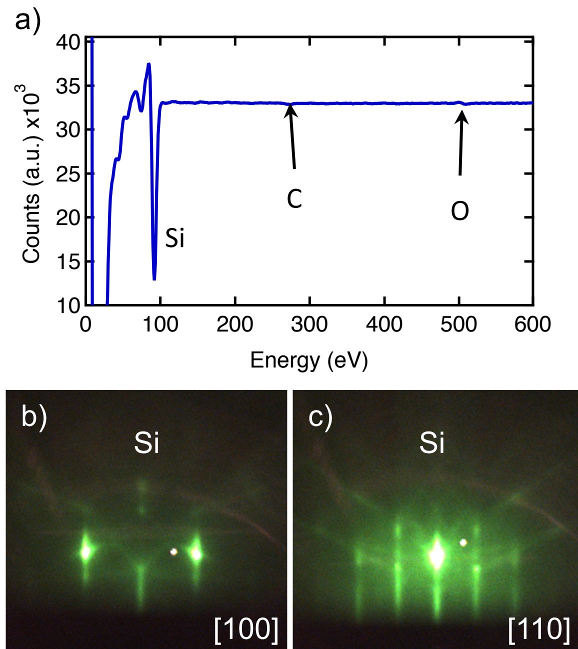

Figure 10.5: RHEED and Auger of Si. a) Auger spectroscopy of UHV annealed p-Si (SOI). p-SOI substrate was prepared as described in this recipe. RHEED of p-Si (SOI) along c) Si(001) [100] and d) Si(001) [110].

of nitrile gloves and bring an extra pair into the cleanroom in case you wish to dispose of the top pair and replace with a fresh set of gloves. Also, cleanliness of acid etching is extremely important and the beakers used for Si etching should only be used for this procedure, should be properly labeled, and kept separate from other stored beakers. This last one will keep people from using them accidentally for something else. We have had trouble with cross contamination of beakers affecting the subsequent growths.

Recipe

Si Substrate Preparation

A) Pre-clean the beakers before etching.

0. *Prep for later growths by taking Fe and Al deposition rates before sample is in the chamber. Target rates: Fe* $\sim$ *1 – 2 Å/min, Al* $\sim$ *1 – 2 Å/min. Typical background pressures due to elemental vapor pressure are* $< 1 \times 10^{-9}$ *Torr for Fe, and* $< 2 \times 10^{-9}$ *Torr for Al. Rates can be taken during etching time in UCR cleanroom (takes about 1/2 hour) and during load lock pump down time (takes about 1/2 hour).*

1. In UCR cleanroom, rinse graduated cylinder, plastic funnel, 2 plastic beakers, 2 glass beakers, Teflon tweezers and small jar with water three times each. We have special equipment in the UCR cleanroom for this.

2. Mix the piranha solution (12 ml H_2SO_4 99% and 12 ml H_2O_2 30%) in the *piranha etch* glass beakers and let sit for a few minutes.

3. Pour the same piranha solution into the *piranha rinse* glass beaker and wait a few minutes.

4. Rinse both piranha beakers three times. The piranha solution can be poured into the cleanroom sink which is set up for acid disposal.

5. Mix the dilute HF solution (100 ml DI H_2O and 3 ml HF (hydrofluoric acid) 50%) in the *HF etch* plastic beaker and wait a few minutes.

6. Pour the HF solution into the *HF rinse* plastic beaker.

7. Rinse both HF beakers three times. The HF solution can be poured into the cleanroom sink.

B) Si substrate etch

1. Mix a new batch of acid solutions in the proper beakers. (Pihrana: H_2SO_4(99%) : H_2O_2(30%) 12 ml:12 ml. HF: DI H2O2(100%):FH(50%) 100 ml:3 ml.) Fill the rinse beakers and small glass jar with DI.

2. Spray the Si substrate with DI and blow dry with nitrogen gas.

3. Using Teflon tweezers, place sample into *piranha etch* solution. Etch for 2 minutes. (The piranha etch is a strong metals etch, which is meant to clean the surface of contaminants.)

4. Using Teflon tweezers, remove sample from *piranha etch* solution and place in *piranha rinse* beaker. Let sit 1 minute.

5. Using Teflon tweezers, remove sample from *piranha rinse* and place in *HF etch* solution. Etch in HF solution for 1 minute. (HF dip etches any SiO_2 on the surface leaving the surface H-passivated Si. Si is hydrophobic and so water should ball up on the surface.)

6. Using Teflon tweezers, remove sample from *HF solution* and place in *HF rinse* beaker.

7. Using Teflon tweezers, remove sample from *HF rinse* and place in *small jar*, which should be half filled with DI. Do not blow dry. Place the cap on the small jar and screw tightly. Be careful, the small jar cap is not really water tight and it will leak. Hold the small jar upright at all times and try not to splash the water inside around. The substrate should be kept in the DI water at all times during transport and never exposed to air. The purpose of the small water

filled jar is to keep the silicon surface from re-oxidizing in the time it takes between the HF dip in the cleanroom and loading into the load lock in our lab.

8. Clean all beakers with DI rinse in the acids sink 3 times and dry them with nitrogen gas and then with kimwipes. Put everything away in the proper place.

9. Carry the sample in the small jar with DI back to the main lab.

C) Substrate anneal and Auger characterization

1. Sample should currently be in small jar with DI water to protect from oxidation. Do not expose Si to air longer then 5 minutes.

2. Remove sample from small jar with DI.

3. Blow dry with nitrogen.

4. Mount with Ta foil on corners to Thermoinics sample platen (pocket).

5. Load into load-lock and pump down. Once pumped, transfer sample to buffer chamber.

6. Do Auger spectroscopy on the sample (0-600 eV at 1 mV sens., 600-2000 at 100 – 300 μV sens.). Confirm Si peaks and examine C and O content.

7. Transfer sample into main chamber. Take RHEED images along [100] and [110] at RT

8. Anneal under UHV conditions at $T_S = 550$ °C ($T_M \sim 650$ °C) for 30 min. Annealing above 400 °C removes H-passivation.

9. Cool to RT and take RHEED images along [100] and [110].

10. Warm up auger with the sample still in the main chamber.

11. Transfer into the buffer chamber and do Auger spectroscopy (0-600 eV at 1 mV sens., 600-2000 at 100 – 300 μV sens.). It should be the same as before the anneal.

12. Transfer sample back into the main chamber.

e-beam MgO Growth on Si

1. After substrate anneal, subsequent Auger, and return of sample to main chamber, take RHEED images along Si(001) [100] and [110].

2. Warm up e-beam MgO cell to deposition power. HV = 4.8 kV. Emission $>$ 8 mA. 17mA is maximum power and usually means you are out of MgO and the e-beam is now punching through the MgO crystal to the Ta crucible and your samples will be contaminated with Ta. This can be verified checking for Ta in Auger spectroscopy data.

3. Move sample into deposition monitor position (beyond x = 1.9 inches) and load in deposition monitor. Take MgO rate. When done, close MgO shutter, wheel out the deposition monitor, and return sample to growth position (x = 1.3 inches). Typical MgO rate is $\sim$ 1 – 1.5 Å/min with a background pressure of $\sim 1 \times 10^{-8}$ Torr.

4. Heat substrate to $T_S = 200$ °C ($T_M \sim 270$ °C) and allow temperature to stabilize. Temperature stabilization is certain once T_M is constant.

5. Deposit 1.3 nm e-beam MgO at $T_S = 200$ °C. Close MgO shutter at end of growth and turn off e-beam power supply.

6. Cool sample to RT and take final RHEED patterns along MgO(001) [100] // Si(001) [100] and MgO(001) [110] // Si(001) [110] (Fig. 10.6). For MgO thicknesses below 2 nm, a RHEED pattern will be difficult to see. The growth is cube-on-cube.

7. Warm up auger while the sample is still in the main chamber.

8. Transfer into the buffer chamber and do Auger spectroscopy (0-600 eV at 1 mV sens., 600-2000 at 100 – 300 μV sens.). It should show clear Mg, Si, and O peaks.

9. Transfer sample back to main chamber.

Discussion and Analysis

200 °C is the optimal growth temperature of e-beam MgO on Si. This was determined by several growths at various substrate temperatures from the quality of the RHEED and AFM rms roughness. AFM on 2 nm e-beam MgO/Si(001) grown at 200 °C yielded an RMS roughness of 0.12 nm. At 2 nm, the MgO shows crystalline RHEED pattern (not shown) with cube-on-cube growth. For reference, growth at 400 °C resulted in rms roughness of 0.77 nm. RHEED images for the Si substrate and subsequent 1.3 nm MgO overlayer (as used in the Ohio state collaboration) is shown in figures 10.5 b) and 10.6 c), respectively. Of the three main semiconductors (Si, GaAs, Ge), MgO growth on Si is by far the worst. It has been reliably reported that growth of MgO on Si can result in interfacial oxidized Si, leaving at least 1 ML of SiO_x [338, 340]. Nevertheless, based on Yong Pu's work on spin injection in these samples, it has been determined that the materials we have provided give the lowest number of interfacial states in the reported literature for 3T spin injection experiments [394].

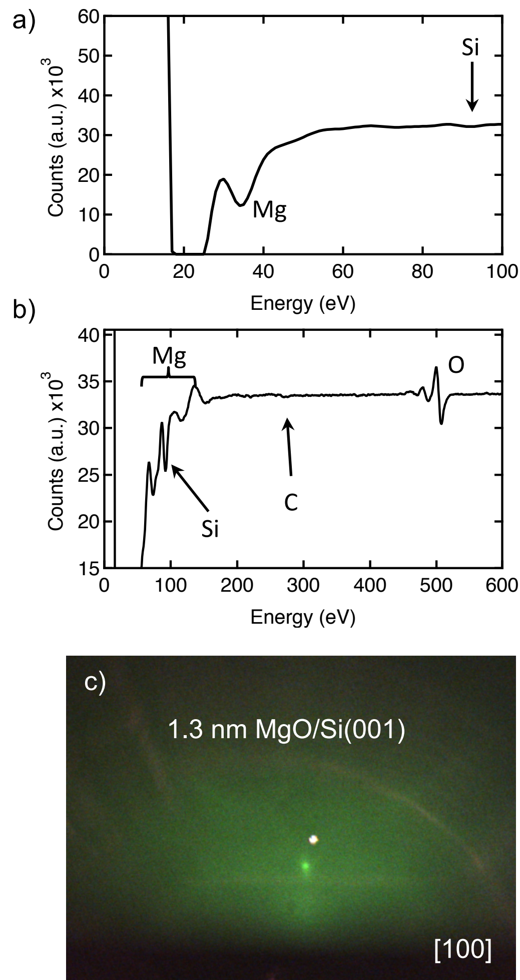

Figure 10.6: RHEED and Auger of e-beam MgO/Si. a) Auger spectroscopy of MgO (1.3 nm) / p-SOI(001). p-Si substrate was prepared as described in this recipe. b) RHEED MgO (1.3 nm) / Si(001) along [100].

Fe and Al Deposition on MgO/Si

Recipe

1. After e-beam MgO deposition, subsequent Auger, and return of sample to main chamber, take RHEED patterns along MgO(001) [100] // Si(001) [100] and MgO(001) [110] // Si(001) [110].

2. Deposit 10 nm elemental Fe at RT. P$_{MBE} < 1 \times 10^{-9}$ Torr.

3. Examine RHEED of Fe (10 nm) / MgO (2 nm) / Si(001).

4. Warm up auger while the sample is still in the main chamber.

5. Transfer into the buffer chamber and do Auger spectroscopy (0-800 eV at 1 mV sens.). It should show clear Fe peaks and possibly some remanence of the underlying Si, Mg, and O peaks.

Note: Auger spectroscopy at this point in the growth is critical to the subsequent fabrication based on wet etching at Ohio State as developed by Yong Pu. The slight oxidation of the Fe layer allows for smooth and sustained Al growth. Without the Auger step to slightly oxidize the Fe, the Al will not stick to the Fe layer and the resulting sample will come out looking too thin and "blue". These sample will not etch properly. The final film should look like an aluminum metal layer (i.e. the color should be that of aluminum (i.e. silvery-ish)).

6. Transfer sample back to main chamber.

7. Deposit 20 nm elemental Al at RT. P$_{MBE} < 2 \times 10^{-9}$ Torr.

8. Examine RHEED of Al (20 nm) / Fe (10 nm) / MgO (2 nm) / Si(001). It should be polycrystalline or amorphous.

9. Warm up auger while the sample is still in the main chamber.

10. Transfer into the buffer chamber and do Auger spectroscopy (0-800 eV at 1 mV sens., 800-2000 at 100 – 300 μV sens.). It should show Al peaks. The underlying MgO and Si should not be seen.

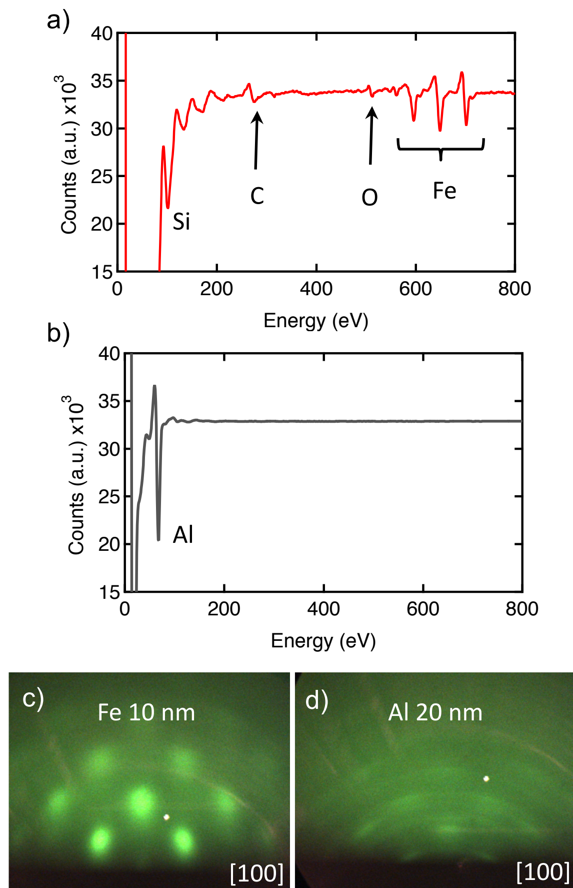

Figure 10.7: RHEED and Auger of Al/Fe/MgO/Si. a) Auger spectroscopy of Fe (10 nm) / MgO (1.3 nm) / p-SOI(001). b) Auger spectroscopy of Al (20 nm) / Fe (10 nm) / MgO (1.3 nm) / p-SOI(001). c) RHEED Fe (10 nm) / MgO (1.3 nm) / p-SOI(001) along [100]. d) RHEED Al (20 nm) / Fe (10 nm) / MgO (1.3 nm) / p-SOI(001) along [100].

10.4 EuO Growths on Various Substrates

Here I outline the growth procedures for growing EuO in the distillation and oxygen-limited regime on YSZ, EuO/MgO/GaAs, EuO/TiO_2/MgO, and EuO/HOPG. The main results of this work is summarized in chapters 6, 7, and 8.

10.4.1 EuO/YSZ(001)

Recipe

1. Warm up Eu cell to growth temperature to allow it to degas a bit during pump time.

Optional: Keep Eu cell at mid-range growth rate (2 Å/min) overnight for better degas.

2. Sonicate YSZ(001) substrate in Acetone for 10 minutes. YSZ(001) is generally 10 mm x 10 mm x 0.3 (or 0.5) mm double or single side polished from MTI corporation. Be careful, sometimes their substrates do not come oriented as advertised. Often it comes miscut with [100] not oriented along a cleaved plane. Optional: Sonicate additional 10 minutes in IPA.

3. Mount with Ta foil on corners to Thermoinics sample platen (pocket).

4. Load into load-lock and pump down.

5. While pumping, take Eu rate. Move manipulator into deposition monitor position (x $>$ 1.9). Wheel in deposition monitor. Eu rate should be between 8 and 9 Å/min. Pay close attention to the chamber pressure due to the Eu cell. When done, remove deposition monitor and put manipulator back into transfer position.

6. Transfer sample into main chamber.

YSZ has awful charging effect in the RHEED at low temperature. You will only get RHEED above 250 °C. Once you warm it up a bit, you can the orient it along an axis to monitor the sample during growth.

7. Oxygen anneal YSZ(001) substrate 600 °C at $P_{O_2} = 1 \times 10^{-7}$ Torr. Anneal for 3 hours and then close the O_2 leak.

8. Cool to RT. Take RHEED images while the sample is cooling. Below 250 °C, you may lose the RHEED pattern due to charging effect.

Optional Step: Once at RT, transfer the sample from the main chamber to the buffer chamber ($P_{buffer} < 5 \times 10^{-9}$ Torr). Run the TSP in the main chamber to remove any excess oxygen still remaining. even though this oxygen level should now be below 3×10^{-9} Torr, it can still affect the growth of EuO, which is very sensitive. Once done running the TSP, the main chamber pressure should now be the same base pressure from taking the Eu deposition rate earlier. Transfer sample back into the main chamber.

9. Take Eu rate again. Move manipulator into deposition monitor position (x $>$ 1.9). Wheel in deposition monitor. Eu rate should be between 8 and 9 Å/min. Pay close attention to the chamber pressure due to the Eu cell. When done, remove deposition monitor and put manipulator back into growth position (x = 1.3).

There are two reasons for this: i) remove excess oxygen from the chamber. The Eu acts effectively as a TSP. ii) After such a long oxygen anneal at high pressure it is a good idea to re-check the Eu rate is stable and has not dropped appreciably.

10. Heat substrate to $T_S = 450$ °C ($T_M \sim 540$ °C) and allow temperature to stabilize. Temperature stabilization is certain once T_M is constant.

11. Monitor RHEED along a particular axis. [100] often gives the better images, but [110] yields more information as those pesky Eu_2O_3 spots in the RHEED show up best along [110]. You can also set up a time lapse with high frame rate (1 picture every 0.25 seconds or faster) in order to try to obtain RHEED oscillations later. To do this you should be sure to crank

up the intensity on the initial RHEED image as it will fade as the first few monolayers are deposited. Eu deposited on YSZ forms EuO through oxidation supplied by the substrate. In the past I have seen up to 8 ML of growth this way by RHEED oscillations. You can analyze the time lapse after the data is recorded. It is a great improvement that we no longer have to try getting RHEED oscillations in real time with basically only one chance (per sample) to get it right.

12. Open the Eu shutter. This commences the growth of EuO (see Sec. 5.2). Monitor the chamber pressure carefully.

Upon opening the Eu shutter, the pressure will artificially spike due to Eu back heating. It takes $\sim$ 25 - 30 seconds per ML deposition of EuO through substrate supplied oxidation. The RHEED pattern will immediately begin to change. Wait at least 5 minutes for full distillation to occur. After this time the RHEED should be that of thin EuO lattice matched on the YSZ RHEED pattern. After the 5 minute wait time, the Eu vapor pressure, which is the dominant contributor to the current total chamber pressure, should have returned to close to the normal value (the pressure during at which the rate was taken with the deposition monitor).

13. Wait minimum 5 minutes for full distillation.

14. Leak molecular oxygen such that the partial pressure is P_{O_2} = 1 – 1.2×10^{-8} Torr above the chamber background pressure. Do NOT exceed this value.

15. Grow for the desired amount of time. At this Eu rate and oxygen pressure, EuO will deposit at a rate of $\sim$ 1.67 nm/min (or 5 nm per 30 minutes).

16. Terminate the growth by closing the oxygen leak valve. NEVER close the Eu shutter first.

17. Wait 10 minutes for the residual oxygen in the chamber to pump down. The Eu shutter should still be open, but despite the high flux rate, the Eu material is simply re-evaporating off the surface or depositing a little bit of EuO due to oxidation with the residual O_2.

18. Close the Eu shutter and turn the Eu cell back to base temperature ($T_{Eu} \sim 220$ °C).

19. Cool sample to RT and take final RHEED patterns along EuO(001) [100] // YSZ(001) [100] and EuO(001) [110] // YSZ(001) [110]. The charging effect should be minimal with the EuO overlayer.

20. The sample can be capped at RT by e-beam MgO or Al. 2 – 5 nm is sufficient. A double cap of MgO covered with Al (or Pd) is more effective.

10.4.2 EuO/MgO/GaAs(001)

This section presents a step-by-step recipe for realizing the growth results presented in section 5.3, which contains the relevant RHEED patterns and is also available in [242].

Recipe

1. Follow the recipe for growing MgO on GaAs(001) in section 10.3.1.

2. After MgO growth, take Eu rate. Move the manipulator into deposition monitor position ($x > 1.9$). Wheel in deposition monitor. Eu rate should be between 8 and 9 Å/min. Pay close attention to the chamber pressure due to the Eu cell. When done, remove deposition monitor

and put manipulator back into growth position (x = 1.3).

Optional Alternative Procedure: Take Eu rate along with step 13 of section 10.3.1. And instead of cooling the sample down after the MgO growth (i.e. skip step 16), heat the sample directly to 450 °C and begin EuO growth.

Note: The thickness of the e-beam MgO buffer layer can be altered if desired. I have achieved EuO growth on 0.8 nm MgO on GaAs.

3. Heat substrate to T_S = 450 °C ($T_M \sim 540$ °C) and allow temperature to stabilize. Temperature stabilization is certain once T_M is constant.

4. Open the Eu shutter. Unlike the case of YSZ, there should be no effect on the RHEED pattern of the underlying MgO buffer layer. Monitor the chamber pressure carefully.

5. Wait minimum 5 minutes for distillation and the chamber pressure to stabilize.

6. Leak molecular oxygen such that the partial pressure is P_{O_2} = 1 – 1.2×10^{-8} Torr above the chamber background pressure. Do NOT exceed this value.

7. Grow for the desired amount of time. At this Eu rate and oxygen pressure, EuO will deposit at a rate of $\sim$ 1.67 nm/min (or 5 nm per 30 minutes).

8. Terminate the growth by closing the oxygen leak valve. NEVER close the Eu shutter first.

9. Wait 10 minutes for the residual oxygen in the chamber to pump down. The Eu shutter should still be open, but despite the high flux rate, the Eu material is simply re-evaporating off the surface or depositing a little bit of EuO due to oxidation with the residual O_2.

10. Close the Eu shutter and turn the Eu cell back to base temperature ($T_{Eu} \sim 220$ °C).

11. Cool sample to RT and take final RHEED patterns along EuO(001) [100] // GaAs(001) [100] and EuO(001) [110] // GaAs(001) [$1\bar{1}0$] as shown in section 5.3, figures 5.2 e) and 5.2 f), respectively.

20. The sample can be capped at RT by e-beam MgO or Al. 2 – 5 nm is sufficient. A double cap of MgO covered with Al is more effective.

10.4.3 EuO/TiO_2/MgO(001)

This section presents a step-by-step recipe for realizing the growth results presented in section 6.4, which contains the relevant RHEED patterns and is also available in [243]. Also, the Methods section section 6.2) provides a comprehensive but concise description of the growth recipe.

Recipe

1. Follow the recipe for growing homoepitaxial 10 nm e-beam MgO buffer layers on MgO(001) in section 10.2.4.

2. With sample at RT and still in the main chamber, Take a Eu rate. Move manipulator into deposition monitor position ($x > 1.9$). Wheel in deposition monitor. Eu rate should be between 8 and 9 Å/min. Pay close attention to the chamber pressure due to the Eu cell. When done, close Eu shutter. Leave deposition monitor in place.

3. Turn on the Ti cell and let warm up. Turn up the filament first to 6 V, 4.4 A. Slowly put a little high voltage onto the grid of approximately 0.05 kV. There should be a current reading

on the power supply although it should be small (a few mA). Begin turning up the HV on the rod to $\sim$ 0.1 kV, there should be minimal current on the rod one or two mA. Slowly turn up the grid to $\sim$ 0.2 kV, and the rod to $\sim$ 2 – 3 kV. The current reading on the grid and rod should be about $\sim$ 60 mA and $\sim$ 15 – 20 mA, respectively.

4. Take Ti rate. This should be done as an immediate step before growing the Ti layer. The Ti e-beam rod source tends to decrease in rate over time and if you wait more than 1 hour between the taking the rate and actually growing the film, you may have a decreased rate by perhaps 20%. The rate should be somewhere between 0.6 – 1.0 Å/min. The cell background pressure should be $< 2 \times 10^{-9}$ Torr. When done, remove deposition monitor and put manipulator back into growth position (x = 1.3).

7. Deposit the desired amount of Ti for 1, 1.5, or 2 ML according to the TiO_2 plane as opposed to a monolayer of hexagonal Ti. For reference, 1 ML = 1.6 Å, 1.5 ML = 2.4 Å, and 2 ML = 3.2 Å. The numbers 1.6, 2.4, and 3.2 Å correspond to the amount of Ti to deposit based on hexagonal crystal structure. For instance, if you take a rate with the deposition monitor of 0.8 Å/min, you should deposit for exactly 2 minutes to achieve necessary number of Ti atoms for 1 ML of TiO_2 lattice matched to MgO. We have found that 2.1 Å of Ti is also reliable for producing the 2x2 TiO reconstruction with the additional higher periodic reconstruction. When done, turn off the Ti cell.

6. Heat substrate to $T_S = 500$ °C ($T_M \sim 610$ °C) and allow temperature to stabilize. Temperature stabilization is certain once T_M is constant.

7. Oxidize Ti layer at 500 °C at P_{O_2} = 1 – 5×10^{-8} Torr for 30 minutes. Close oxygen leak valve when done.

8. Cool sample to RT and take RHEED along MgO(001) [100] and MgO(001) [110] to look for special reconstructions in the MgO pattern. See section 6.4, figure 6.2.

9. Heat substrate to $T_S = 500$ °C ($T_M \sim 610$ °C) and allow temperature to stabilize. Temperature stabilization is certain once T_M is constant.

10. Open the Eu shutter. This commences the growth of EuO (see Sec. 6.4). Monitor the chamber pressure carefully.

Upon opening the Eu shutter, the pressure will artificially spike due to Eu back heating. It takes an estimated $\sim$ 25 - 30 seconds per ML deposition of EuO through substrate supplied oxidation. The RHEED pattern will immediately begin to change. Wait at least 5 minutes for full distillation to occur. After this time the RHEED should be to that displayed in section 6.4, figures 6.4 a) and 6.4 b). After the 5 minute wait time, the Eu vapor pressure, which is the dominant contributor to the current total chamber pressure, should have returned to close to the normal value (the pressure during at which the rate was taken with the deposition monitor).

11. Wait minimum 5 minutes for full distillation.

12. Leak molecular oxygen such that the partial pressure is P_{O_2} = 1 – 1.2×10^{-8} Torr above the chamber background pressure. Do NOT exceed this value.

13. Grow for the desired amount of time. At this Eu rate and oxygen pressure, EuO will deposit at a rate of $\sim$ 1.67 nm/min (or 5 nm per 30 minutes).

14. Terminate the growth by closing the oxygen leak valve. NEVER close the Eu shutter first.

15. Wait 10 minutes for the residual oxygen in the chamber to pump down. The Eu shutter should still be open, but despite the high flux rate, the Eu material is simply re-evaporating off the surface or depositing a little bit of EuO due to oxidation with the residual O_2.

16. Close the Eu shutter and turn the Eu cell back to base temperature ($T_{Eu} \sim 220$ °C).

17. Cool sample to RT and take final RHEED patterns along EuO(001) [100] // MgO(001) [110] and EuO(001) [110] // MgO(001) [100]. The EuO layer will be rotated 45 ° in-plane with respect to the underlying MgO substrate.

18. The sample can be capped at RT by e-beam MgO or Al. 2 – 5 nm is sufficient. A double cap of MgO covered with Al is more effective.

10.4.4 EuO/HOPG(0001)

Recipe

1. Warm up Eu cell to growth temperature to allow it to degas a bit during pump time.

Optional: Keep Eu cell at mid-range growth rate (2 Å/min) overnight for better degas.

2. Prepare fresh HOPG substrate. HOPG(0001) substrate is grade ZYA from SPI.

3. Place HOPG substrate on a clean flat surface and apply 3M scotch tape uniformly pressed over the HOPG substrate surface. Gently rub with your thumb over the tape surface to press the tape to the substrate. Use soft carbon tweezers for extra rubbing to fill any additional crevasses.

4. Peel the tape off the substrate to reveal a clean HOPG surface. *Note: Repeat steps 3 and 4 at least once more to be sure of a clean surface*

5. Mount with Ta foil on corners to Thermoinics sample platen (pocket).

6. Load into load-lock and pump down.

7. While pumping, take Eu rate. Move manipulator into deposition monitor position (x $>$ 1.9). Wheel in deposition monitor. Eu rate should be between 8 and 9 Å/min. Pay close attention to the chamber pressure due to the Eu cell. When done, remove deposition monitor and put manipulator back into transfer position.

8. Transfer sample into main chamber and examine the HOPG RHEED pattern. There is no need to examine different directions as HOPG has in-plane rotational disorder (see section 7.2, figure 7.2 a)).

9. Anneal in UHV at 600 °C for 1 hour.

10. Cool to $T_S = 550$ °C ($T_M \sim 670$ °C) and allow temperature to stabilize. Temperature stabilization is certain once T_M is constant.

11. Open the Eu shutter. The incoming Eu flux will re-evaporate off the sample surface (see Sec. 7.2) and the RHEED pattern will remain unaltered. Monitor the chamber pressure

carefully.

Upon opening the Eu shutter, the pressure will artificially spike due to Eu back heating. After the 5 minute wait time, the Eu vapor pressure, which is the dominant contributor to the current total chamber pressure, should have returned to close to the normal value (the pressure during at which the rate was taken with the deposition monitor).

12. Wait minimum 5 minutes for steady state of the Eu flux.

13. Leak molecular oxygen such that the partial pressure is P_{O_2} = 1 – 1.2×10^{-8} Torr above the chamber background pressure. Do NOT exceed this value.

14. Grow for the desired amount of time. At this Eu rate and oxygen pressure, EuO will deposit at a rate of $\sim$ 1.67 nm/min (or 5 nm per 30 minutes).

15. Terminate the growth by closing the oxygen leak valve. NEVER close the Eu shutter first.

16. Wait 10 minutes for the residual oxygen in the chamber to pump down. The Eu shutter should still be open, but despite the high flux rate, the Eu material is simply re-evaporating off the surface or depositing a little bit of EuO due to oxidation with the residual O_2.

17. Close the Eu shutter and turn the Eu cell back to base temperature ($T_{Eu} \sim 220$ °C).

18. Cool sample to RT and take final RHEED pattern (see section 7.2, figure 7.2 b)).

19. The sample can be capped at RT by e-beam MgO or Al. 2 – 5 nm is sufficient. A double cap of MgO covered with Al is more effective.

10.5 Co/Pd Superstructures for Perpendicular Media

Very thin Co and Pd repeated layers (superlattices) are known to demonstrate perpendicular magnetic anisotropy (PMA) [395, 396, 397, 398, 26]. Magnetic anisotropy simply refers to a preferred orientation of magnetization along different axis directions in a solid. For instance, if a system has a preferred orientation along one axis in the solid, that will be the configuration that minimizes the magnetic energy and is called the 'easy' axis. In the case of thin films, there are a wide variety of growth and materials parameters that allow for significant control over the magnetic anisotropy [138], and is therefore crucial for commercial applications. Some important applications include interlayer exchange coupling (IEC) [399, 400, 401, 402, 403, 138], spin transfer torque (STT) [404, 405, 406], giant magnetoresistance (GMR) [1, 2, 399] tunneling magnetoresistance (TMR) [5, 6, 27], and magneto-optic (MO) [407] recording. There are several types of sources for anisotropy in a magnetic system. They are due to the shape of material (shape anisotropy), the internal electric fields combined with spin-orbit coupling (magneto-crystalline anisotropy), and mechanical deformation like strain or stress (strain anisotropy), and symmetry-breaking at the interface (surface anisotropy). Like all interface effects, it is extremely sensitive to the the atomic scale structure, and therefore can be easily controlled and optimized for the desired application through MBE.

The relevant energy for surface anisotropy along the film normal is given by [397, 398, 138],

$$E_A = K_V \cos^2\theta \times d + K_S \cos^2\theta \tag{10.1}$$

where E_A is the surface anisotropy energy in units of erg/cm^{-2}, d is the thickness of the magnetic thin film, K_S is the interface or surface anisotropy term, θ is the angle between the axis and the magnetization, and K_V is the volume anisotropy term in units of erg/cm^{-3}. K_V is given by,

$$K_V = K_{shape} + K_{M-C} + K_{strain} \tag{10.2}$$

where K_{shape}, K_{M-C}, and K_{strain} are the shape, magneto-crystalline, and strain anisotropy terms. The shape anisotropy is caused by energy dependence along different directions from the boundary conditions of the dipolar field resulting from the magnetization. On the other hand, the spin-orbit interaction is responsible for magneto-crystalline anisotropy and strain anisotropy. For thick films we can ignore K_S and the easy direction can be determined by the magnitude and signs of the different bulk anisotropy terms. For the perpendicular axis chosen, $K_V > 0$ (< 0) corresponds to a preference for in-plane (out-of-plane) orientation of the magnetization. Generally, for thin films, the magneto-crystalline anisotropy is dominated by the shape anisotropy. Thus, along the perpendicular axis, $K_{shape} > 0$ and films typically have magnetizations in-plane. However, within the plane of the film, the magneto-crystalline anisotropy will be relevant as in the case of Fe films on 2x4 reconstructed GaAs(001) [389, 48, 390].

We can now add K_S back into consideration. Regardless of the origin of K_S, we can understand why PMA appears in very thin films through equation 10.1. First, it is necessary that the surface term K_S favors the perpendicular direction (i.e. $K_S < 0$). Second, there is a competition between K_S and K_V to determine the lowest energy axis. As the film thickness decreases, a crossover can occur where $\mid K_V \times d \mid < \mid K_S \mid$. Therefore, the surface anisotropy term dominates. This will orient the easy axis along the out-of-plane axis.

A comprehensive review of PMA in a variety of structures including Co, Fe, and Ni with various interlayers (Pt, Pd, Au, Cu, etc..) is presented in [398]. Perpendicular magnetic anisotropy was first discovered in (Co/Pd)$_n$ superlattices in 1985 [395] for structures with many repeats ($n \sim 100$) of thin Co (4 – 12 Å) and Pd ($\sim$ 33 – 80 Å) bilayers. The microscopic nature of PMA is considered to have several contributions to the surface anisotropy term [Johnson]:

$$K_S = K_N + K_{coh} + K_{inc} \tag{10.3}$$

where K_N is the Néel surface anisotropy [408], K_{coh} is the surface strain anisotropy, and K_{inc} is the incoherent anisotropy term. K_N arises due to particular orientations at the surface of the internal electric fields and spin-orbit coupling. This is essentially a surface modified version of the bulk magneto-crystalline anisotropy due to the lowering of symmetry [408]. Similarly, the magneto-elastic (strain/stress) contribution to the bulk value K_{strain} can also be significantly altered at the interface and produce a surface anisotropy. K_{coh} is the *coherent* part of the magneto-elastic surface anisotropy and appears for systems in which the lattice

mismatch is not too large, which allows for the layers to grow in a regime in which the magnetic layer experiences epitaxial tensile strain [397, 398]. On the other hand, when the lattice constants differ significantly (as is the case for Co/Pd), the layers will not grow strained, but can be characterized as epitaxial but with many dislocations. This is called *incoherent* and gives rise to the surface anisotropy term K_{inc}. Much of the behavior of the [(Co,Fe,Ni)/X]$_n$ bilayer superlattices, where X is a non-magnetic (usually a transition metal) element, can be reasonably explained with this model. The magneto-crystalline component to the surface anisotropy can be directly calculated, while the coherent and incoherent terms require some experimental input for the amount of strain induced through different growth techniques (i.e. sputter vs. MBE).

Interestingly, Co/Pd does not fall into the set of material systems that are easily explained through this model. It was shown by [409] that K_S is independent of the crystalline orientations of the Co/Pd bilayers, suggesting that the main source of anisotropy stems from K_{inc}. However, it has also been seen that K_S can be enhanced through annealing, which is associated with film smoothing [397]. This and other results would suggest a meaningful contribution from K_N [398, 410]. These issues were exacerbated by the difficulty in properly characterizing the structural quality for each group and each K_S experiment. At the time, advanced materials characterization techniques (RHEED) and magnetization measurements (SQUID) were less ubiquitous. In general the detailed microscopic origin of K_S is complex and depends strongly on the substrate, crystallinity, materials choice, roughness, and interdiffusion. Recent experiments provide new insights including the importance of

local anisotropy, grain structure, d-d orbital hybridization leading to enhanced orbital contributions, and induced magnetism in the adjacent Pd layers [411, 412]. Fortunately, regardless of the complex origin of K_S, (Co/Pd)$_n$ provides a robust, orientation independent, system to taking advantage of room temperature perpendicular magnetization for spintronics applications.

We are interested in taking advantage of perpendicular anisotropy for perpendicular spin injection into GaAs. The goal of this project is to inject spins electrically and then detect them via slow muons as discussed in ref. [413]. In plane spin injection is not possible as the muons are sensitive to spin polarization oriented along the surface normal to the substrate. Also, the muon detection signal is increased by having large substrates with injected spin carriers over a large region (1.5 cm x 1.5 cm) and therefore large substrates are desired. For this, we have used 7×10^{16} /cm-2 n-GaAs(001) that we buy in 2 inch wafers. As shown in figure 10.4, these AXT substrates provide acceptable spin properties for our purposes here.

AXT GaAs(001) substrates are prepared by a wet chemical digital etch. Prepare 30% H_2O_2 and a DI rinse beaker for the peroxide step. The peroxide serves to oxidize the surface. Next, prepare a beaker of HCL:H_2O (1:1) and a DI rinse beaker for the acid step as well. The hydrochloric acid etches the oxide. Using teflon tweezers dip the sample in the peroxide for 1 minute, then dip into the DI rinse for the peroxide step for 15 – 30 s. Blow dry with N_2 gas. Next, dip the sample into the HCL solution for 1 minute, and then into the DI rinse for the acid step for 15 – 30 s. Blow dry with N_2 gas and then repeat the process. This oxidize/etch procedure should be repeated three times, thus the term digital. The digital etch

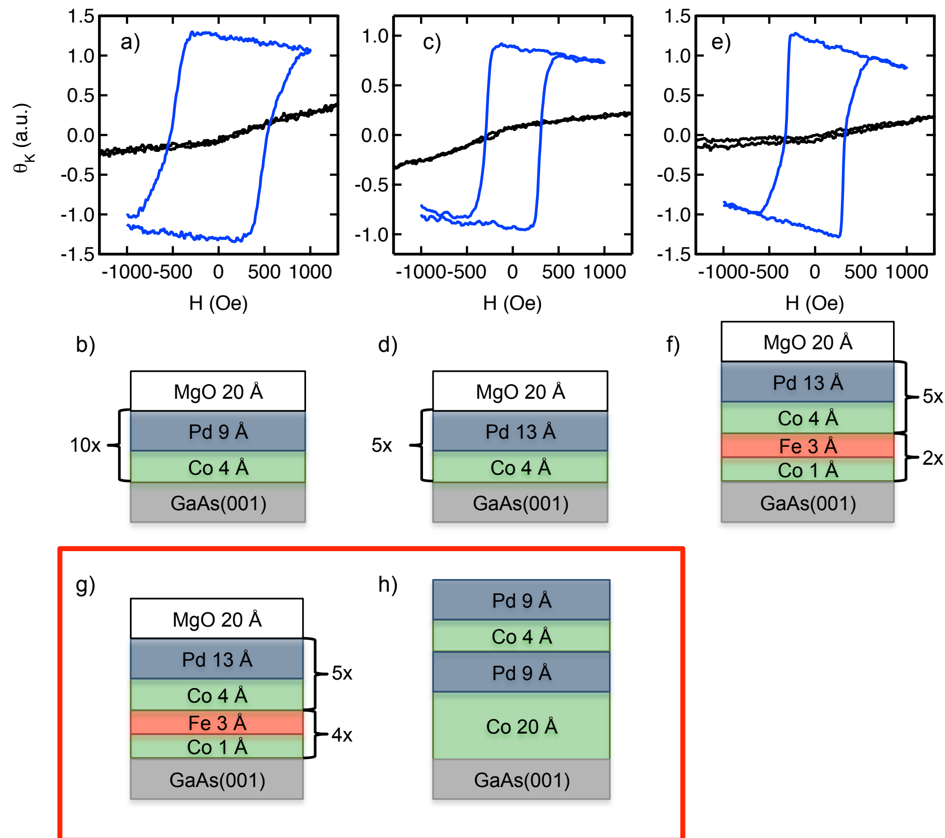

Figure 10.8: Comparison of Magnetic Behavior of Different Co/Pd Superlattices. a) Polar (blue curve) and longitudinal (black curve) MOKE plotted in arbitrary units. The data in a) corresponds to the structure shown in figure b). c) Polar (blue curve) and longitudinal (black curve) MOKE corresponding to the structure shown in figure d). e) Polar (blue curve) and longitudinal (black curve) MOKE corresponding to the structure shown in figure f). g) and h) The structures in the red box show structures that did not demonstrate PMA.

seems to produce better results than a single long peroxide and etch recipe. The sample is then annealed in UHV at 580 °C for 30 minutes.

Next, we investigate the Co/Pd growth and determine which bilayer repeats give PMA and the coercivity range we are looking for ($H_C < 500$ Oe). Fig. 10.8 shows the magnetic hysteresis loops as measured by polar MOKE at RT for several different Co/Pd superlattices. The hysteresis loop in fig. 10.8 a) (blue curve), which corresponds to the structure drawn in

10.8 b) with 4 ÅCo and 9 ÅPd repeated 10 times, demonstrates PMA with H_C = 520 Oe. A longitudinal MOKE scan (black curve) does not show any saturation in this field range indicating that the in-plane direction is a magnetically hard axis. The Co/Pd superlattice with 4 ÅCO and 13 ÅPd repeated 5 times, also demonstrated PMA with H_C = 300 Oe. Notably, the PMA (blue curves) demonstrated by these two structures shows high magnetic remanence (M_R = M_S), which is crucial for the upcoming muon experiments, which will seek to determine if there is spin injection at zero applied field. The diamagnetic background is likely due to the Pd layers.

For spin injection purposes, we are also concerned about the spin diffusion length in the spin injecting material. We do not wish to have Co/Pd bilayers directly at the interface as there is no spin polarization in the Pd layers which is expected to lead to lower spin injection efficiency. Therefore wee seek to have fully magnetic layers at the interface and the total thickness of these layers should approach the spin diffusion length in metals. For this, we would like to have at least 1 nm of magnetic material at the interface. We first investigate the now standard Co/Pd (4 Å/ 13 Å) 5 repeat structure with an additional Co/Fe (1 Å/3 Å) double bilayer at the interface as shown in fig. 10.8 f). The polar magnetic hysteresis loops for this structure is shown in 10.8 e) and is characterized by M_R = M_S, H_C = 320 Oe, and a slight twisting in the loop shape leading to an increase in the saturation field, H_S. This increase in M_S is directly related to relative increase in the volume anisotropy energy compared to the surface term due to the Co/Fe layers which do not contribute a significant contribution to the surface anisotropy term. However, the change in H_S is not large, and the magnetic

hysteresis loops still show excellent properties. We have also investigated increasing the amount of magnetic material at the interface by adding extra Co/Fe bilayers at the interface to create a total structure $[Co(4\ Å)/Pd(13\ Å)]_5/[Co(1\ Å)/Fe(3\ Å)]_4$ as shown in figure 10.8 g). And we also investigate a thick Co buffer layer at the interface underneath the standard Co/Pd structure (Fig. 10.8). These structures did not demonstrate perpendicular magnetization. Therefore, we have determined that the structure presented in figure 10.8 f) gives the best compromise of coercivity, saturation magnetization, and spin diffusion length, without compromising the magnetic remanence.

For the purposes of spin injection, it may also be desirable to improve the spin injection efficiency by adding an MgO tunnel barrier. We next investigate the magnetic properties of Co/Pd layers with the interfacial Co/Fe double bilayer on MgO grown on GaAs. The GaAs substrate is prepared as before with the peroxide/HCL digital etch. In order to protect the edges of the sample from edge deposition and therefore create electric shorts between the interface and the back of the sample, we employ a Ta foil mask system that protects all sides of the sample, but leaves the majority of the sample face open for materials growth. Also, the Ta foil mask is compatible with the GaAs substrate UHV anneal. 1.5 nm of e-beam MgO is deposited on the GaAs substrate at RT. Following this, the Co/Fe double bilayer and Co/Pd superstructure is grown on top. Next, a wedge shutter is wheeled in front of the sample to block one small $\sim \frac{1}{4}$ inch $\times \frac{1}{4}$ inch of the sample. Next 50 nm Pd is grown on top to act as a top electrical contact. The remaining $\sim \frac{1}{4}$ inch $\times \frac{1}{4}$ inch area of total metal thickness ~ 12 nm, is thin enough to allow for MOKE characterization. Lastly, the sample is flipped

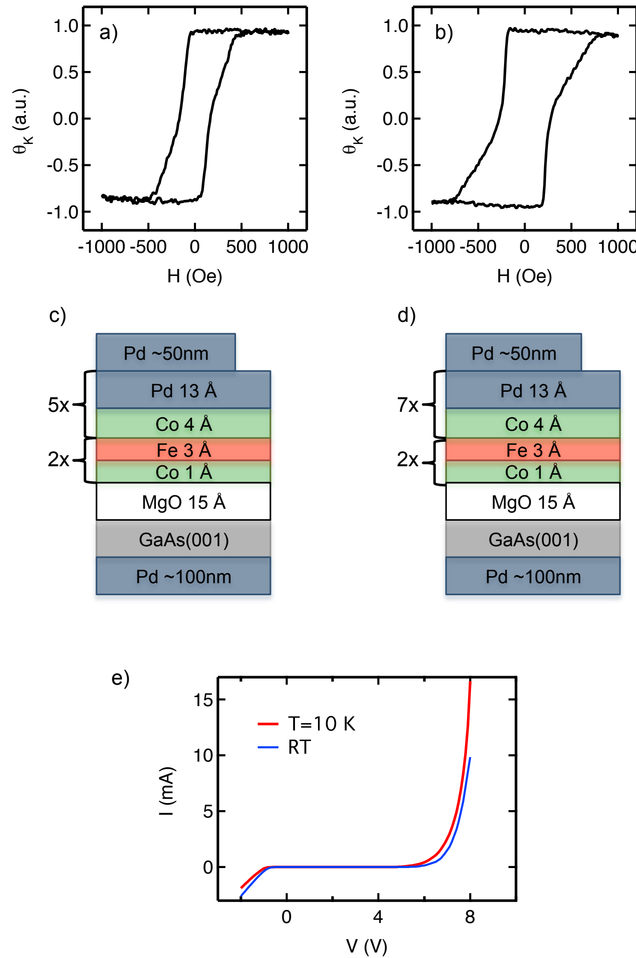

Figure 10.9: $[Co/Pd]_n/[Co/Fe]_m$ layers on MgO/GaAs(001) Characterization. a) Polar MOKE for 5 times repeated Co/Pd structure as shown in c) for growth on MgO (1.5 nm)/GaAs(001). b) Polar MOKE for 7 times repeated Co/Pd structure as shown in d) for growth on MgO (1.5 nm)/GaAs(001). e) DC I-V for these sample structures with a 50 nm Pd cap on top of the Co/Pd superstructure and 100 nm Pd layer grown on the unpolished back-side of the sample with forward bias applied relative to the $[Co/Pd/]_n/[Co/Fe]_m$/MgO/GaAs(001) interface.

over, carefully mounted so as to not scratch the front surface, and Ta foil masked off on the edges. It is then loaded back into the UHV growth chamber for 100 nm Pd contact grown on the back of the substrate. A sample of $[Co(4\ Å)/Pd(13\ Å)]_5/[Co(1\ Å)/Fe(3\ Å)]_4$/MgO (1.5 nm)/GaAs(001) is characterized by polar MOKE as shown in Fig. 10.9 a). The MOKE data

demonstrates that the PMA behavior has changed compared to growth in the absence of the MgO barrier. On MgO, the sample shows a much lower coercivity of H_C = 170 Oe. H_S = 500 Oe and noticeably, the magnetization switching is apparent close to zero field. This makes for an undesirable situation as the robustness of our mandatory condition, M_R = M_S, is on the cusp of not being met. Therefore, we can increase the low field magnetization stability and increase the difference in anisotropy between in-plane and out-of-plane, thus increasing the necessary field to switch the magnetization, by adding two extra bilayers of Co/Pd and create the structure $[Co(4\ Å)/Pd(13\ Å)]_7/[Co(1\ Å)/Fe(3\ Å)]_4$/MgO (1.5 nm)/GaAs(001) as shown in figure 10.9 d). The sample is grown with identical preparation, Ta masking, and Pd electrodes. Figure 10.9 b) shows the polar MOKE measurement which demonstrates increased stability at low field, increased coercivity (H_C = 270 Oe), and increased saturation field (H_S = 790 Oe). These magnetization characteristics meets the requirements that we are looking for. Next we can measure DC I-V on this sample structure. Fig. 10.9 e) shows I-V curve at RT and T=10K. Positive voltage corresponds to forward bias of the PMA interface.

In conclusion, we have investigated $(Co/Pd)_n/(Co/Fe)_m$ structures as a means for realizing perpendicular magnetic media for future projects that will investigate spin properties in n-GaAs via decay of spin-polarized slow muons. The magnetic properties were optimized for structures with and without an MgO barrier in order to maximize the remanence (M_R = M_S) and place the coercivity and saturation field in a moderate range that is accessible by reasonably low magnetic fields of $\sim$ 1000 Oe. The I-V curves demonstrate relatively temperature independent operation.

Bibliography

[1] M. N. Baibich, J. M. Broto, A. Fert, F. N. Van Dau, F. Petroff, P. Etienne, G. Creuzet, A. Friederich, and J. Chazelas, Physical Review Letters **61**, 2472 (1988).

[2] G. Binasch, P. Grünberg, F. Saurenbach, W. Zinn, et al., Physical Review B **39**, 4828 (1989).

[3] M. Julliere, Physics Letters A **54**, 225 (1975).

[4] P. M. Tedrow and R. Meservey, Physical Review Letters **26**, 192 (1971).

[5] S. S. P. Parkin, C. Kaiser, A. Panchula, P. M. Rice, B. Hughes, M. Samant, and S. H. Yang, Nature Materials **3**, 862 (2004).

[6] S. Yuasa, T. Nagahama, A. Fukushima, Y. Suzuki, and K. Ando, Nature Materials **3**, 868 (2004).

[7] A. Fert, Reviews of Modern Physics **80**, 1517 (2008).

[8] R. J. Epstein, F. M. Mendoza, Y. K. Kato, and D. D. Awschalom, Nature Physics **1**, 94 (2005).

[9] R. Hanson and D. D. Awschalom, Nature **453**, 1043 (2008).

[10] B. B. Buckley, G. D. Fuchs, L. C. Bassett, and D. D. Awschalom, Science **330**, 1212 (2010).

[11] S. A. Crooker, J. Brandt, C. Sandfort, A. Greilich, D. R. Yakovlev, D. Reuter, A. D. Wieck, and M. Bayer, Physical Review Letters **104**, 36601 (2010).

[12] A. J. Ramsay, Semiconductor Science and Technology **25**, 103001 (2010).

[13] Y. Li, N. Sinitsyn, D. L. Smith, D. Reuter, A. D. Wieck, D. R. Yakovlev, M. Bayer, and S. A. Crooker, Physical Review Letters **108**, 186603 (2012).

[14] M. W. Wu, J. H. Jiang, and M. Q. Weng, Physics Reports **493**, 61 (2010).

[15] S. A. Wolf, D. D. Awschalom, R. A. Buhrman, J. M. Daughton, S. von Molnar, M. L. Roukes, A. Y. Chtchelkanova, and D. M. Treger, Science **294**, 1488 (2001).

[16] I. Žutić, J. Fabian, and S. D. Sarma, Reviews of Modern Physics **76**, 323 (2004).

[17] S. A. Wolf, A. Y. Chtchelkanova, and D. M. Treger, IBM Journal of Research and Development **50**, 101 (2006).

[18] C. Felser, G. H. Fecher, and B. Balke, Angewandte Chemie International Edition **46**, 668 (2007).

[19] D. D. Awschalom and M. E. Flatté, Nature Physics **3**, 153 (2007).

[20] J. Fabian, A. Matos-Abiague, C. Ertler, P. Stano, and I. Zutic, Acta Phys. Slovaca **57**, 565 (2007).

[21] M. Bibes and A. Barthelemy, IEEE Transactions on Electronic Devices **54**, 1003 (2007).

[22] S. D. Bader and S. S. P. Parkin, Annu. Rev. Condens. Matter Phys. **1**, 71 (2010).

[23] M. Bibes, J. E. Villegas, and A. Barthelemy, Advances in Physics **60**, 5 (2011).

[24] S. Sanvito, Chemical Society Reviews **40**, 3336 (2011).

[25] W. Han, K. M. McCreary, K. Pi, W. H. Wang, Y. Li, H. Wen, J. R. Chen, and R. K. Kawakami, Journal of Magnetism and Magnetic Materials **324**, 369 (2012).

[26] J. Stöhr and H. C. Siegmann, *Magnetism: from fundamentals to nanoscale dynamics*, vol. 15 (Springer Heidelberg, 2006).

[27] S. Yuasa, A. Fukushima, H. Kubota, Y. Suzuki, and K. Ando, Applied Physics Letters **89**, 042505 (2006).

[28] S. Datta and B. Das, Applied Physics Letters **56**, 665 (1990).

[29] M. Johnson and R. H. Silsbee, Physical Review Letters **55**, 1790 (1985).

[30] F. J. Jedema, H. B. Heersche, A. T. Filip, J. J. Baselmans, B. J. van Wees, et al., Nature **416**, 713 (2002).

[31] S. Takahashi and S. Maekawa, Physical Review B **67**, 052409 (2003).

[32] N. Tombros, C. Jozsa, M. Popinciuc, H. T. Jonkman, and B. J. van Wees, Nature **448**, 571 (2007).

[33] K. M. McCreary, Ph.D. thesis, University of California, Riverside (2012).

[34] W. Han, Ph.D. thesis, University of California, Riverside (2012).

[35] Y. Fukuma, L. Wang, H. Idzuchi, S. Takahashi, S. Maekawa, and Y. Otani, Nature Materials **10**, 527 (2011).

[36] H. Idzuchi, Y. Fukuma, L. Wang, and Y. Otani, Applied Physics Letters **101**, 022415 (2012).

[37] F. J. Jedema, A. T. Filip, and B. J. Van Wees, Nature **410**, 345 (2001).

[38] Y. K. Takahashi, S. Kasai, S. Hirayama, S. Mitani, and K. Hono, Applied Physics Letters **100**, 052405 (2012).

[39] P. Laczkowski, L. Vila, V.-D. Nguyen, A. Marty, J.-P. Attané, H. Jaffrès, J.-M. George, and A. Fert, Physical Review B **85**, 220404 (2012).

[40] Y. Niimi, D. Wei, H. Idzuchi, T. Wakamura, T. Kato, and Y. Otani, Physical Review Letters **110**, 016805 (2013).

[41] K. S. Novoselov, A. K. Geim, S. V. Morozov, D. Jiang, Y. Zhang, S. V. Dubonos, I. V. Grigorieva, and A. A. Firsov, Science **306**, 666 (2004).

[42] A. K. Geim and K. S. Novoselov, Nature Materials **6**, 183 (2007).

[43] A. H. Castro Neto, F. Guinea, N. M. R. Peres, K. S. Novoselov, and A. K. Geim, Reviews of Modern Physics **81**, 109 (2009).

[44] K. S. Novoselov, A. K. Geim, S. V. Morozov, D. Jiang, M. I. Katsnelson, I. V. Grigorieva, S. V. Dubonos, and A. A. Firsov, Nature **438**, 197 (2005).

[45] Y. Zhang, Y.-W. Tan, H. L. Stormer, and P. Kim, Nature **438**, 201 (2005).

[46] E. J. H. Lee, K. Balasubramanian, R. T. Weitz, M. Burghard, and K. Kern, Nature Nanotechnology **3**, 486 (2008).

[47] A. K. Geim, Reviews of Modern Physics **83**, 851 (2011).

[48] X. Li, W. Cai, J. An, S. Kim, J. Nah, D. Yang, R. Piner, A. Velamakanni, I. Jung, E. Tutuc, et al., Science **324**, 1312 (2009).

[49] S. Bae, H. Kim, Y. Lee, X. Xu, J.-S. Park, Y. Zheng, J. Balakrishnan, T. Lei, H. R. Kim, Y. I. Song, et al., Nature Nanotechnology **5**, 574 (2010).

[50] Y. W. Tan, Y. Zhang, K. Bolotin, Y. Zhao, S. Adam, E. H. Hwang, S. D. Sarma, H. L. Stormer, and P. Kim, Physical Review Letters **99**, 246803 (2007).

[51] K. Pi, K. M. McCreary, W. Bao, W. Han, Y. F. Chiang, Y. Li, S.-W. Tsai, C. N. Lau, and R. K. Kawakami, Physical Review B **80**, 075406 (2009).

[52] K. I. Bolotin, F. Ghahari, M. D. Shulman, H. L. Stormer, and P. Kim, Nature **462**, 196 (2009).

[53] X. Du, I. Skachko, A. Barker, and E. Y. Andrei, Nature Nanotechnology **3**, 491 (2008).

[54] K. I. Bolotin, K. J. Sikes, Z. Jiang, M. Klima, G. Fudenberg, J. Hone, P. Kim, and H. L. Stormer, Solid State Communications **146**, 351 (2008).

[55] C. R. Dean, A. F. Young, I. Meric, C. Lee, L. Wang, S. Sorgenfrei, K. Watanabe, T. Taniguchi, P. Kim, K. L. Shepard, et al., Nature Nanotechnology **5**, 722 (2010).

[56] A. S. Mayorov, R. V. Gorbachev, S. V. Morozov, L. Britnell, R. Jalil, L. A. Ponomarenko, P. Blake, K. S. Novoselov, K. Watanabe, T. Taniguchi, et al., Nano Letters **11**, 2396 (2011).

[57] X. Du, I. Skachko, F. Duerr, A. Luican, and E. Y. Andrei, Nature **462**, 192 (2009).

[58] M. I. Katsnelson, K. S. Novoselov, and A. K. Geim, Nature Physics **2**, 620 (2006).

[59] A. F. Young and P. Kim, Nature Physics **5**, 222 (2009).

[60] N. Stander, B. Huard, and D. Goldhaber-Gordon, Physical Review Letters **102**, 26807 (2009).

[61] D. Huertas-Hernando, F. Guinea, and A. Brataas, Physical Review B **74**, 155426 (2006).

[62] H. Min, J. E. Hill, N. A. Sinitsyn, B. R. Sahu, L. Kleinman, and A. H. MacDonald, Physical Review B **74**, 165310 (2006).

[63] Y. Yao, F. Ye, X. L. Qi, S. C. Zhang, and Z. Fang, Physical Review B **75**, 041401(R) (2007).

[64] S. Chen, Q. Wu, C. Mishra, J. Kang, H. Zhang, K. Cho, W. Cai, A. A. Balandin, and R. S. Ruoff, Nature Materials (2012).

[65] E. W. Hill, A. K. Geim, K. S. Novoselov, F. Schedin, and P. Blake, IEEE Transactions on Magnetics **42**, 2694 (2006).

[66] M. Nishioka and A. Goldman, Applied Physics Letters **90**, 252505 (2007).

[67] W. H. Wang, K. Pi, Y. Li, Y. F. Chiang, P. Wei, J. Shi, and R. K. Kawakami, Physical Review B **77**, 020402 (2008).

[68] S. Cho, Y.-F. Chen, and M. S. Fuhrer, Applied Physics Letters **91**, 123105 (2007).

[69] M. Popinciuc, C. Jozsa, P. J. Zomer, A. Veligura, H. T. Jonkman, and B. J. van Wees, Physical Review B **80**, 214427 (2009).

[70] C. Józsa, T. Maassen, M. Popinciuc, P. J. Zomer, A. Veligura, H. T. Jonkman, and B. J. van Wees, Physical Review B **80**, 241403(R) (2009).

[71] W. Han, K. Pi, K. M. McCreary, Y. Li, J. J. I. Wong, A. G. Swartz, and R. K. Kawakami, Physical Review Letters **105**, 167202 (2010).

[72] W. Han and R. K. Kawakami, Physical Review Letters **107**, 047207 (2011).

[73] S. Jo, D. K. Ki, D. Jeong, H. J. Lee, and S. Kettermann, Physical Review B **84**, 075453 (2011).

[74] W. Han, W. H. Wang, K. Pi, K. M. McCreary, W. Bao, Y. Li, F. Miao, C. N. Lau, and R. K. Kawakami, Physical Review Letters **102**, 137205 (2009).

[75] T.-Y. Yang, J. Balakrishnan, F. Volmer, A. Avsar, M. Jaiswal, J. Samm, S. R. Ali, A. Pachoud, M. Zeng, M. Popinciuc, et al., Physical Review Letters **107**, 047206 (2011).

[76] T. Maassen, F. K. Dejene, M. H. D. Guimarães, C. Józsa, and B. J. van Wees, Physical Review B **83**, 115410 (2011).

[77] B. Dlubak, M. B. Martin, C. Deranlot, B. Servet, S. Xavier, R. Mattana, M. Sprinkle, C. Berger, W. A. D. Heer, D. Petroff, et al., Nature Physics **8**, 557 (2012).

[78] T. Maassen, J. J. van den Berg, N. IJbema, F. Fromm, T. Seyller, R. Yakimova, and B. J. van Wees, Nano Letters **12**, 1498 (2012).

[79] T. Maassen, J. J. van den Berg, E. H. Huisman, H. Dijkstra, F. Fromm, T. Seyller, and B. J. van Wees, Physical Review Letters **110**, 067209 (2013).

[80] M. H. D. Guimarães, A. Veligura, P. J. Zomer, T. Maassen, I. J. Vera-Marun, N. Tombros, and B. J. van Wees, Nano Letters **12**, 3512 (2012).

[81] I. Neumann, J. Van de Vondel, G. Bridoux, M. V. Costache, F. Alzina, C. M. S. Torres, and S. O. Valenzuela, Small **9**, 156 (2013).

[82] P. J. Zomer, M. H. D. Guimarães, N. Tombros, and B. J. van Wees, arXiv preprint arXiv:1209.1999 (2012).

[83] C. Ertler, S. Konschuh, M. Gmitra, and J. Fabian, Physical Review B **80**, 041405(R) (2009).

[84] F. Ochoa, A. H. Castro Neto, and F. Guinea, Physical Review Letters **108**, 206808 (2012).

[85] A. H. Castro Neto and F. Guinea, Physical Review Letters **103**, 026804 (2009).

[86] P. Zhang and M. W. Wu, Physical Review B **84**, 045304 (2011).

[87] D. Huertas-Hernando, F. Guinea, and A. Brataas, Eur. Phys. J. Spec. Top. **148**, 177 (2007).

[88] D. Huertas-Hernando, F. Guinea, and A. Brataas, Physical Review Letters **103**, 146801 (2009).

[89] P. Zhang and M. W. Wu, New Journal of Physics **14**, 033015 (2012).

[90] R. J. Elliott, Physical Review **96**, 266 (1954).

[91] Y. Yafet, Solid State Physics **14**, 1 (1963).

[92] M. I. D'yakonov and V. I. Perel, Sov. Phys. Solid State **13**, 3023 (1971).

[93] C. Weeks, J. Hu, J. Alicea, M. Franz, and R. Wu, Physical Review X **1**, 021001 (2011).

[94] K. M. McCreary, K. Pi, and R. K. Kawakami, Applied Physics Letters **98**, 192101 (2011).

[95] T. Maassen, I. J. Vera-Marun, M. H. D. Guimarães, and B. J. van Wees, Physical Review B **86**, 235408 (2012).

[96] S. P. Dash, S. Sharma, J. C. L. Breton, J. Peiro, H. Jaffrès, J.-M. George, A. Lemaître, and R. Jansen, Physical Review B **84**, 054410 (2011).

[97] W. Han, J.-R. Chen, D. Wang, K. M. McCreary, H. Wen, A. G. Swartz, J. Shi, and R. K. Kawakami, Nano Letters **12**, 3443 (2012).

[98] Y. Ohno, D. K. Young, B. a. Beschoten, F. Matsukura, H. Ohno, and D. D. Awschalom, Nature **402**, 790 (1999).

[99] R. Fiederling, M. Keim, G. Reuscher, W. Ossau, G. Schmidt, A. Waag, and L. W. Molenkamp, Nature **402**, 787 (1999).

[100] Y. K. Kato, R. C. Myers, A. C. Gossard, and D. D. Awschalom, Science **306**, 1910 (2004).

[101] S. A. Crooker, M. Furis, X. Lou, C. Adelmann, D. L. Smith, C. J. Palmstrøm, and P. A. Crowell, Science **309**, 2191 (2005).

[102] X. Lou, C. Adelmann, S. A. Crooker, E. S. Garlid, J. Zhang, K. S. M. Reddy, S. D. Flexner, C. J. Palmstrøm, and P. A. Crowell, Nature Physics **3**, 197 (2007).

[103] J. M. Kikkawa and D. D. Awschalom, Physical Review Letters **80**, 4313 (1998).

[104] F. Meier and B. P. Zakharchenya, *Optical orientation* (North-Holland Amsterdam, 1984).

[105] R. K. Kawakami, Y. Kato, M. Hanson, I. Malajovich, J. M. Stephens, E. Johnston-Halperin, G. Salis, A. C. Gossard, and D. D. Awschalom, Science **294**, 131 (2001).

[106] P. Kotissek, M. Bailleul, M. Sperl, A. Spitzer, D. Schuh, W. Wegscheider, C. H. Back, and G. Bayreuther, Nature Physics **3**, 872 (2007).

[107] H. Dery and L. J. Sham, Physical Review Letters **98**, 46602 (2007).

[108] H. J. Zhu, M. Ramsteiner, H. Kostial, M. Wassermeier, H.-P. Schönherr, and K. H. Ploog, Physical Review Letters **87**, 16601 (2001).

[109] H. C. Koo, J. H. Kwon, J. Eom, J. Chang, S. H. Han, and M. Johnson, Science **325**, 1515 (2009).

[110] A. Ohtomo and H. Y. Hwang, Nature **427**, 423 (2004).

[111] N. Reyren, M. Bibes, E. Lesne, J.-M. George, C. Deranlot, S. Collin, A. Barthélémy, and H. Jaffrès, Physical Review Letters **108**, 186802 (2012).

[112] J. Mannhart and D. G. Schlom, Science **327**, 1607 (2010).

[113] H. Y. Hwang, Y. Iwasa, M. Kawasaki, B. Keimer, N. Nagaosa, and Y. Tokura, Nature Materials **11**, 103 (2012).

[114] A. D. Caviglia, S. Gariglio, N. Reyren, D. Jaccard, T. Schneider, M. Gabay, S. Thiel, G. Hammerl, J. Mannhart, and J.-M. Triscone, Nature **456**, 624 (2008).

[115] N. Reyren, S. Thiel, A. D. Caviglia, L. F. Kourkoutis, G. Hammerl, C. Richter, C. W. Schneider, T. Kopp, A.-S. Rüetschi, D. Jaccard, et al., Science **317**, 1196 (2007).

[116] C. Bell, S. Harashima, Y. Kozuka, M. Kim, B. G. Kim, Y. Hikita, and H. Y. Hwang, Physical Review Letters **103**, 226802 (2009).

[117] M. Ben Shalom, M. Sachs, D. Rakhmilevitch, A. Palevski, and Y. Dagan, Physical Review Letters **104**, 126802 (2010).

[118] A. D. Caviglia, M. Gabay, S. Gariglio, N. Reyren, C. Cancellieri, and J.-M. Triscone, Physical Review Letters **104**, 126803 (2010).

[119] J. A. Bert, B. Kalisky, C. Bell, M. Kim, Y. Hikita, H. Y. Hwang, and K. A. Moler, Nature Physics **7**, 767 (2011).

[120] A. Tsukazaki, A. Ohtomo, T. Kita, Y. Ohno, H. Ohno, and M. Kawasaki, Science **315**, 1388 (2007).

[121] Y. Kozuka, M. Kim, H. Ohta, Y. Hikita, C. Bell, and H. Y. Hwang, Applied Physics Letters **97**, 222115 (2010).

[122] B. Jalan, S. Stemmer, S. Mack, and S. J. Allen, Physical Review B **82**, 081103 (2010).

[123] C. Sahin, G. Vignale, and M. E. Flatte, To Be Submitted (2013).

[124] J. Lee, N. Sai, and A. A. Demkov, Physical Review B **82**, 235305 (2010).

[125] Y. Wang, M. K. Niranjan, J. D. Burton, J. M. An, K. D. Belashchenko, and E. Y. Tsymbal, Physical Review B **79**, 212408 (2009).

[126] J. R. Arthur, Surface Science **500**, 189 (2002).

[127] M. A. Herman and H. Sitter, *Molecular beam epitaxy: fundamentals and current status* (Springer-Verlag Berlin, 1989).

[128] A. Y. Cho, Journal of Crystal Growth **111**, 1 (1991).

[129] A. Y. Cho, Journal of Crystal Growth **201–202**, 1 (1999).

[130] E. F. Schubert, Journal of Vacuum Science & Technology A: Vacuum, Surfaces, and Films **8**, 2980 (1990).

[131] E. F. Schubert, *Doping in III-V semiconductors* (Cambridge, UK: Cambridge University Press, 1993).

[132] N. L. Stormer, Reviews of Modern Physics **71**, 875 (1999).

[133] W. P. McCray, Nature Nanotechnology **2**, 259 (2007).

[134] D. C. Tsui, H. L. Stormer, and A. C. Gossard, Physical Review Letters **48**, 1559 (1982).

[135] M. F. Crommie, C. P. Lutz, D. M. Eigler, et al., Science **262**, 218 (1993).

[136] D. G. Schlom, J. H. Haeni, J. Lettieri, C. D. Theis, W. Tian, J. C. Jiang, and X. Q. Pan, Materials Science and Engineering: B **87**, 282 (2001).

[137] D. G. Schlom and C. H. Ahn, Nature **456**, 582 (2008).

[138] J. J. I. Wong, Ph.D. thesis, University of California, Riverside (2012).

[139] W. Braun, *Applied RHEED: reflection high-energy electron diffraction during crystal growth*, vol. 154 (Springer Verlag, 1999).

[140] C. C. Chang, Surface Science **25**, 53 (1971).

[141] F. Schedin, A. K. Geim, S. V. Morozov, E. W. Hill, P. Blake, M. I. Katsnelson, and K. S. Novoselov, Nature Materials **6**, 652 (2007).

[142] X. Dong, D. Fu, W. Fang, Y. Shi, P. Chen, and L. J. Li, Small **5**, 1422 (2009).

[143] X. Wang, X. Li, L. Zhang, Y. Yoon, P. K. Weber, H. Wang, J. Guo, and H. Dai, Science **324**, 768 (2009).

[144] K. M. McCreary, K. Pi, A. G. Swartz, W. Han, W. Bao, C. N. Lau, F. Guinea, M. I. Katsnelson, and R. K. Kawakami, Physical Review B **81**, 115453 (2010).

[145] D. B. Farmer, R. Golizadeh-Mojarad, V. Perebeinos, Y. M. Lin, G. S. Tulevski, J. C. Tsang, and P. Avouris, Nano Letters **9**, 388 (2008).

[146] Y. H. Lu, W. Chen, Y. P. Feng, and P. M. He, The Journal of Physical Chemistry B **113**, 2 (2008).

[147] J. Choi, H. Lee, K. Kim, B. Kim, and S. Kim, The Journal of Physical Chemistry Letters **1**, 505 (2009).

[148] G. Giovannetti, P. A. Khomyakov, G. Brocks, V. M. Karpan, J. Van den Brink, and P. J. Kelly, Physical Review Letters **101**, 26803 (2008).

[149] Z. Ni, Y. Wang, T. Yu, and Z. Shen, Nano Research **1**, 273 (2008).

[150] K. Zou, X. Hong, D. Keefer, and J. Zhu, Physical Review Letters **105**, 126601 (2010).

[151] L. A. Ponomarenko, R. Yang, T. M. Mohiuddin, M. I. Katsnelson, K. S. Novoselov, S. V. Morozov, A. A. Zhukov, F. Schedin, E. W. Hill, and A. K. Geim, Physical Review Letters **102**, 206603 (2009).

[152] J. Martin, N. Akerman, G. Ulbricht, T. Lohmann, J. H. Smet, K. Von Klitzing, and A. Yacoby, Nature Physics **4**, 144 (2007).

[153] Y. Zhang, V. W. Brar, C. Girit, A. Zettl, and M. F. Crommie, Nature Physics **5**, 722 (2009).

[154] A. Deshpande, W. Bao, F. Miao, C. N. Lau, and B. J. LeRoy, Physical Review B **79**, 205411 (2009).

[155] F. Xia, T. Mueller, R. Golizadeh-Mojarad, M. Freitag, Y. Lin, J. Tsang, V. Perebeinos, and P. Avouris, Nano Letters **9**, 1039 (2009).

[156] T. Mueller, F. Xia, M. Freitag, J. Tsang, and P. Avouris, Physical Review B **79**, 245430 (2009).

[157] J. Park, Y. H. Ahn, and C. Ruiz-Vargas, Nano Letters **9**, 1742 (2009).

[158] J. H. Chen, C. Jang, S. Adam, M. S. Fuhrer, E. D. Williams, and M. Ishigami, Nature Physics **4**, 377 (2008).

[159] S. Adam, E. H. Hwang, V. M. Galitski, and S. D. Sarma, PNAS **104**, 18392 (2007).

[160] E. H. Hwang, S. Adam, and S. Das Sarma, Physical Review Letters **98**, 186806 (2007).

[161] J.-H. Chen, W. G. Cullen, C. Jang, M. S. Fuhrer, and E. D. Williams, Physical Review Letters **102**, 236805 (2009).

[162] D. C. Elias, R. R. Nair, T. M. G. Mohiuddin, S. V. Morozov, P. Blake, M. P. Halsall, A. C. Ferrari, D. W. Boukhvalov, M. I. Katsnelson, A. K. Geim, et al., Science **323**, 610 (2009).

[163] Z. H. Ni, L. A. Ponomarenko, R. R. Nair, R. Yang, S. Anissimova, I. V. Grigorieva, F. Schedin, P. Blake, Z. X. Shen, E. H. Hill, et al., Nano Letters **10**, 3868 (2010).

[164] M. Wojtaszek, N. Tombros, A. Caretta, P. H. M. van Loosdrecht, and B. J. van Wees, Journal of Applied Physics **110**, 063715 (2011).

[165] X. Hong, S.-H. Cheng, C. Herding, and J. Zhu, Physical Review B **83**, 085410 (2011).

[166] F. Withers, M. Dubois, and A. K. Savchenko, Physical Review B **82** (2010).

[167] J. Moser, H. Tao, S. Roche, F. Alzina, C. M. S. Torres, and A. Bachtold, Physical Review B **81**, 205445 (2010).

[168] I. Childres, L. A. Jauregui, J. Tian, and Y. P. Chen, New Journal of Physics **13**, 025008 (2011).

[169] K. Pi, Ph.D. thesis, University of California, Riverside (2010).

[170] M. I. Katsnelson, F. Guinea, and A. K. Geim, Physical Review B **79**, 195426 (2009).

[171] K. Pi, W. Han, K. M. McCreary, A. G. Swartz, Y. Li, and R. K. Kawakami, Physical Review Letters **104**, 187201 (2010).

[172] B. T. Matthias, R. M. Bozorth, and J. H. Van Vleck, Physical Review Letters **7**, 160 (1961).

[173] J. H. Van Vleck, Journal of Applied Physics **39**, 365 (1968).

[174] A. Mauger and C. Godart, Physics Reports **141**, 51 (1986).

[175] F. Cardarelli, ed., *Materials Handbook: a concise desktop reference* (Springer-Verlag, London, 2008), 2nd ed.

[176] K. Y. Ahn and M. W. Shafer, Journal of Applied Physics **41**, 1260 (1970).

[177] M. R. Oliver, J. O. Dimmock, A. L. McWhorter, and T. B. Reed, Physical Review B **5**, 1078 (1972).

[178] Y. Shapira, S. Foner, and T. B. Reed, Physical Review B **8**, 2299 (1973).

[179] A. Schmehl, V. Vaithyanathan, A. Herrnberger, S. Thiel, C. Richter, M. Liberati, T. Heeg, M. Rockerath, L. F. Kourkoutis, S. Muhlbauer, et al., Nature Materials **6**, 882 (2007).

[180] T. Yamasaki, K. Ueno, A. Tsukazaki, T. Fukumura, and M. Kawasaki, Applied Physics Letters **98**, 082116 (2011).

[181] P. G. Steeneken, Ph.D. thesis, University of Groningen (2002).

[182] Y. Hajati, M. Zargar Shoushtari, and G. Rashedi, Journal of Applied Physics **112**, 013901 (2012).

[183] Y. Asano, T. Yoshida, Y. Tanaka, and A. A. Golubov, Physical Review B **78**, 014514 (2008).

[184] L. Dell'Anna and A. De Martino, Physical Review B **80**, 155416 (2009).

[185] L. Dell'Anna and A. De Martino, Physical Review B **79**, 045420 (2009).

[186] L. Dell'Anna and A. De Martino, Physical Review B **83**, 155449 (2011).

[187] E. Faizabadi, M. Esmaeilzadeh, and F. Sattari, The European Physical Journal B-Condensed Matter and Complex Systems **85**, 1 (2012).

[188] S. Grover, S. Ghosh, and M. Sharma, Modelling and Simulation in Materials Science and Engineering **20**, 045010 (2012).

[189] Y. Gu, Y. H. Yang, J. Wang, and K. S. Chan, Journal of Applied Physics **105**, 103711 (2009).

[190] H. Haugen, D. Huertas-Hernando, and A. Brataas, Physical Review B **77**, 115406 (2008).

[191] N. V. Hung, A. Bournel, P. Dollfus, and N. Van Lien, in *Journal of Physics: Conference Series* (IOP Publishing, 2009), vol. 187, p. 012037.

[192] Y. F. Hsu and G. Y. Guo, Physical Review B **81**, 045412 (2010).

[193] M. Khodas, I. A. Zaliznyak, and D. E. Kharzeev, Physical Review B **80**, 125428 (2009).

[194] Y. X. Li, The European Physical Journal B-Condensed Matter and Complex Systems **68**, 119 (2009).

[195] W. Liewrian, R. Hoonsawat, I. Tang, et al., Physica E: Low-dimensional Systems and Nanostructures **42**, 1287 (2010).

[196] W. Liewrian, I. Tang, R. Hoonsawat, et al., Physica E: Low-dimensional Systems and Nanostructures **44**, 327 (2011).

[197] J. Linder, A. M. Black-Schaffer, and A. Sudbø, Physical Review B **82**, 041409 (2010).

[198] J. F. Liu and K. S. Chan, Nanotechnology **22**, 395201 (2011).

[199] P. Michetti, P. Recher, and G. Iannaccone, Nano Letters **10**, 4463 (2010).

[200] P. Michetti and P. Recher, Physical Review B **84**, 125438 (2011).

[201] A. G. Moghaddam and M. Zareyan, Solid State Communications **149**, 1106 (2009).

[202] F. M. Mojarabian and G. Rashedi, Physica E: Low-dimensional Systems and Nanostructures (2011).

[203] N. Myoung and G. Ihm, Journal of Applied Physics **109**, 053716 (2011).

[204] V. H. Nguyen, A. Bournel, and P. Dollfus, Journal of Applied Physics **109**, 073717 (2011).

[205] Z. P. Niu, F. X. Li, B. G. Wang, L. Sheng, and D. Y. Xing, The European Physical Journal B-Condensed Matter and Complex Systems **66**, 245 (2008).

[206] Z. P. Niu, Journal of Physics: Condensed Matter **23**, 435302 (2011).

[207] Z. Qiao, S. A. Yang, W. Feng, W. K. Tse, J. Ding, Y. Yao, J. Wang, and Q. Niu, Physical Review B **82**, 161414 (2010).

[208] Z. Qiao, H. Jiang, X. Li, Y. Yao, and Q. Niu, Physical Review B **85**, 115439 (2012).

[209] M. Salehi, M. Alidoust, and G. Rashedi, Journal of Applied Physics **108** (2010).

[210] Y. G. Semenov, K. W. Kim, and J. M. Zavada, Applied Physics Letters **91**, 153105 (2007).

[211] Y. G. Semenov, J. M. Zavada, and K. W. Kim, Journal of Applied Physics **107**, 064507 (2010).

[212] Y. G. Semenov, J. M. Zavada, and K. W. Kim, Physical Review B **77**, 235415 (2008).

[213] Y. G. Semenov, J. M. Zavada, and K. W. Kim, Physical Review Letters **101**, 147206 (2008).

[214] M. Sharma and S. Ghosh, Journal of Physics: Condensed Matter **23**, 055501 (2011).

[215] B. Soodchomshom, I. Tang, R. Hoonsawat, et al., Physica C: Superconductivity **469**, 689 (2009).

[216] B. Soodchomshom, I. Tang, R. Hoonsawat, et al., Physica E: Low-dimensional Systems and Nanostructures **41**, 1310 (2009).

[217] B. Soodchomshom, I. Tang, R. Hoonsawat, et al., Physica C: Superconductivity **470**, 31 (2010).

[218] B. Soodchomshom, I. Tang, R. Hoonsawat, et al., Physics Letters A **372**, 5054 (2008).

[219] Q. Sun, Z. Jiang, Y. Yu, and X. C. Xie, Physical Review B **84**, 214501 (2011).

[220] Q. Sun and X. C. Xie, Physical Review Letters **104**, 66805 (2010).

[221] H. Y. Tian, Y. H. Yang, and J. Wang, The European Physical Journal B-Condensed Matter and Complex Systems **85**, 1 (2012).

[222] W. K. Tse, Z. Qiao, Y. Yao, A. H. MacDonald, and Q. Niu, Physical Review B **83**, 155447 (2011).

[223] Q. P. Wu, X. D. He, and Z. F. Liu, The European Physical Journal B-Condensed Matter and Complex Systems **85**, 1 (2012).

[224] Q. P. Wu, X. D. He, and Z. F. Liu, Physica E: Low-dimensional Systems and Nanostructures (2011).

[225] L. I. Xiao-Wei, Chinese Physics Letters **28**, 047401 (2011).

[226] Y. L. Yang, C. Bai, and X. D. Zhang, The European Physical Journal B-Condensed Matter and Complex Systems **72**, 217 (2009).

[227] H. X. Yang, A. Hallal, D. Terrade, X. Waintal, S. Roche, and M. Chshiev, Phys. Rev. Lett. **110**, 046603 (2013).

[228] T. Yokoyama, Physical Review B **77**, 073413 (2008).

[229] T. Yokoyama and J. Linder, Physical Review B **83**, 081418 (2011).

[230] Y. Yu, Q. Liang, and J. Dong, Physics Letters A **375**, 2858 (2011).

[231] F. Zhai and L. Yang, Applied Physics Letters **98**, 062101 (2011).

[232] Q. Zhang, K. S. Chan, and Z. Lin, Applied Physics Letters **98**, 032106 (2011).

[233] Q. Zhang, J. F. Liu, Z. Lin, and K. S. Chan, Journal of Applied Physics **112**, 073701 (2012).

[234] Q. Zhang, Z. Lin, and K. S. Chan, Journal of Physics: Condensed Matter **24**, 075302 (2012).

[235] Z. Y. Zhang, Journal of Physics: Condensed Matter **21**, 095302 (2009).

[236] Q. Zhang, D. Fu, B. Wang, R. Zhang, and D. Y. Xing, Physical Review Letters **101**, 47005 (2008).

[237] J. Zou and G. Jin, EPL (Europhysics Letters) **87**, 27008 (2009).

[238] J. Zou, G. Jin, and Y. Ma, Journal of Physics: Condensed Matter **21**, 126001 (2009).

[239] B. Zhou, X. Chen, H. Wang, K. H. Ding, and G. Zhou, Journal of Physics: Condensed Matter **22**, 445302 (2010).

[240] R. W. Ulbricht, A. Schmehl, T. Heeg, J. Schubert, and D. G. Schlom, Applied Physics Letters **93**, 102105 (2008).

[241] R. Sutarto, S. G. Altendorf, B. Coloru, M. Moretti Sala, T. Haupricht, C. F. Chang, Z. Hu, C. Schüßler-Langeheine, N. Hollmann, H. Kierspel, et al., Physical Review B **79**, 205318 (2009).

[242] A. G. Swartz, J. Ciraldo, J. J. I. Wong, Y. Li, W. Han, T. Lin, S. Mack, J. Shi, D. D. Awschalom, and R. K. Kawakami, Applied Physics Letters **97**, 112509 (2010).

[243] A. G. Swartz, J. J. I. Wong, I. V. Pinchuk, and R. K. Kawakami, Journal of Applied Physics **111**, 083912 (2012).

[244] A. G. Swartz, P. M. Odenthal, Y. Hao, R. S. Ruoff, and R. K. Kawakami, ACS Nano **6**, 10063 (2012).

[245] K. Momma and F. Izumi, J. Appl. Crystallogr. **41**, 653 (2008).

[246] T. Kasuya, Journal of Applied Physics **41**, 1090 (1970).

[247] C. E. Moore, *Atomic Energy Levels* (National Bureau of Standards Circular, 1958), no. 467 ed.

[248] L. Pauling, *The Nature of the Chemical Bond* (Cornell University Press, Ithaca, N.Y., 1960).

[249] G. Güntherodt, P. Wachter, and D. M. Imboden, Zeitschrift für Physik B Condensed Matter **12**, 292 (1971).

[250] N. J. C. Ingle and I. S. Elfimov, Physical Review B **77**, 121202 (2008).

[251] T. S. Santos, J. S. Moodera, K. V. Raman, E. Negusse, J. Holroyd, J. Dvorak, M. Liberati, Y. U. Idzerda, and E. Arenholz, Physical Review Letters **101**, 147201 (2008).

[252] M. J. Freiser, S. Holtzberg Methfessel, G. D. Petit, M. W. Shafer, and J. C. Suits, Helv. Phys. Acta **41**, 832 (1969).

[253] P. A. M. Dirac, *The Principles of Quantum Mechanics* (Clarendon, Oxford, 1947), 3rd ed.

[254] W. Heisenberg, Zeitschrift für Physik A Hadrons and Nuclei **49**, 619 (1928).

[255] N. W. Ashcroft and N. D. Mermin, *Solid State Physics* (Thomas Learning, Inc., 1976).

[256] C. Zener, Physical Review **81**, 440 (1951).

[257] O. W. Dietrich, A. J. Henderson, and H. Meyer, Physical Review B **12**, 2844 (1975).

[258] T. Kasuya, IBM Journal of Research and Development **14**, 214 (1970).

[259] O. W. Dietrich, J. Als-Nielsen, and L. Passell, Physical Review B **14**, 4923 (1976).

[260] W. Nolting, G. Borstel, and W. Borgiel, Physical Review B **35**, 7015 (1987).

[261] W. Liu, G. Hong, D. Dai, L. Li, and M. Dolg, Theoretical Chemistry Accounts: Theory, Computation, and Modeling (Theoretica Chimica Acta) **96**, 75 (1997).

[262] R. Schiller, W. Müller, and W. Nolting, Physical Review B **64**, 134409 (2001).

[263] R. Schiller and W. Nolting, Physical Review Letters **86**, 3847 (2001).

[264] R. Schiller and W. Nolting, Solid State Communications **118**, 173 (2001).

[265] J. Kunes, W. Ku, and W. E. Pickett, Journal of the Physical Society of Japan **74**, 1408 (2005).

[266] W. Söllinger, W. Heiss, R. T. Lechner, K. Rumpf, P. Granitzer, H. Krenn, and G. Springholz, Physical Review B **81**, 155213 (2010).

[267] X. Wan, J. Dong, and S. Y. Savrasov, Physical Review B **83**, 205201 (2011).

[268] H. Wang, C. Schuster, and U. Schwingenschlögl, Chemical Physics Letters **524**, 68 (2012).

[269] P. G. Steeneken, L. H. Tjeng, I. Elfimov, G. A. Sawatzky, G. Ghiringhelli, N. B. Brookes, and D. J. Huang, Physical Review Letters **88**, 47201 (2002).

[270] H. Miyazaki, T. Ito, H. J. Im, S. Yagi, M. Kato, K. Soda, and S. Kimura, Physical Review Letters **102**, 227203 (2009).

[271] P. Liu, J. A. C. Santana, Q. Dai, X. Wang, P. A. Dowben, and J. Tang, Physical Review B **86**, 224408 (2012).

[272] N. M. Souza-Neto, D. Haskel, Y. C. Tseng, and G. Lapertot, Physical Review Letters **102**, 57206 (2009).

[273] P. Liu and J. Tang, Physical Review B **85**, 224417 (2012).

[274] H. Miyazaki, H. J. Im, K. Terashima, S. Yagi, M. Kato, K. Soda, T. Ito, and S. Kimura, Applied Physics Letters **96**, 232503 (2010).

[275] S. G. Altendorf, A. Efimenko, V. Oliana, H. Kierspel, A. D. Rata, and L. H. Tjeng, Physical Review B **84**, 155442 (2011).

[276] S. G. Altendorf, N. Hollmann, R. Sutarto, C. Caspers, R. C. Wicks, Y. Y. Chin, Z. Hu, H. Kierspel, I. S. Elfimov, H. H. Hsieh, et al., Physical Review B **85**, 081201 (2012).

[277] T. Mairoser, A. Schmehl, A. Melville, T. Heeg, W. Zander, J. Schubert, D. E. Shai, E. J. Monkman, K. M. Shen, T. Z. Regier, et al., Applied Physics Letters **98**, 102110 (2011).

[278] T. Mairoser, A. Schmehl, A. Melville, T. Heeg, L. Canella, P. Böni, W. Zander, J. Schubert, D. E. Shai, E. J. Monkman, et al., Physical Review Letters **105**, 257206 (2010).

[279] M. Arnold and J. Kroha, Physical Review Letters **100**, 46404 (2008).

[280] P. Liu, J. Tang, J. A. Colón Santana, K. D. Belashchenko, and P. A. Dowben, Journal of Applied Physics **109**, 07C311 (2011).

[281] A. Melville, T. Mairoser, A. Schmehl, D. E. Shai, E. Monkman, J. W. Harter, T. Heeg, B. Hollander, J. Schubert, K. M. Shen, et al., Applied Physics Letters **100**, 222101 (2012).

[282] K. Y. Ahn, Applied Physics Letters **17**, 347 (1970).

[283] M. Muller, G. X. Miao, and J. S. Moodera, Journal of Applied Physics **105**, 07C917 (2009).

[284] E. Negusse, J. Dvorak, J. S. Holroyd, M. Liberati, T. S. Santos, J. S. Moodera, E. Arenholz, and Y. U. Idzerda, Journal of Applied Physics **105**, 07C930 (2009).

[285] M. Barbagallo, T. Stollenwerk, J. Kroha, N. J. Steinke, N. D. M. Hine, J. F. K. Cooper, C. H. W. Barnes, A. Ionescu, P. Monteiro, J. Y. Kim, et al., Physical Review B **84**, 075219 (2011).

[286] D. F. Forster, J. Klinkhammer, C. Busse, S. G. Altendorf, T. Michely, Z. Hu, Y. Y. Chin, L. H. Tjeng, J. Coraux, and D. Bourgault, Physical Review B **83**, 045424 (2011).

[287] G. V. Samsanov, ed., *The Oxide Handbook* (IFI/Plenum, New York, 1985), 2nd ed.

[288] N. Iwata, G. Pindoria, T. Morishita, and K. Kohn, Journal of the Physical Society of Japan **69**, 230 (2000).

[289] J. J. I. Wong, L. Ramirez, A. G. Swartz, A. Hoff, W. Han, Y. Li, and R. K. Kawakami, Physical Review B **81**, 094406 (2010).

[290] S. Wang, Y. Zhang, N. Abidi, and L. Cabrales, Langmuir **25**, 11078 (2009).

[291] M. Fiebig, Journal of Physics D: Applied Physics **38**, R123 (2005).

[292] T. Maruyama, Y. Shiota, T. Nozaki, K. Ohta, N. Toda, M. Mizuguchi, A. Tulapurkar, T. Shinjo, M. Shiraishi, S. Mizukami, et al., Nature Nanotechnology **4**, 158 (2009).

[293] M. Weisheit, S. Fähler, A. Marty, Y. Souche, C. Poinsignon, and D. Givord, Science **315**, 349 (2007).

[294] X. He, Y. Wang, N. Wu, A. N. Caruso, E. Vescovo, K. D. Belashchenko, P. A. Dowben, and C. Binek, Nature Materials **9**, 579 (2010).

[295] V. Garcia, M. Bibes, L. Bocher, S. Valencia, F. Kronast, A. Crassous, X. Moya, S. Enouz-Vedrenne, A. Gloter, D. Imhoff, et al., Science **327**, 1106 (2010).

[296] S. Valencia, A. Crassous, L. Bocher, V. Garcia, X. Moya, R. Cherifi, C. Deranlot, K. Bouzehouane, S. Fusil, A. Zobelli, et al., Nature Materials **10**, 753 (2011).

[297] J. J. I. Wong, A. G. Swartz, R. Zheng, W. Han, and R. K. Kawakami, Physical Review B **86**, 060409 (2012).

[298] P. M. Tedrow, J. E. Tkaczyk, and A. Kumar, Physical Review Letters **56**, 1746 (1986).

[299] S. Y. Huang, X. Fan, D. Qu, Y. P. Chen, W. G. Wang, J. Wu, T. Y. Chen, J. Q. Xiao, and C. L. Chien, Physical Review Letters **109**, 107204 (2012).

[300] T. Stehlin, M. Feller, P. Guyot-Sionnest, and Y.-R. Shen, Optics letters **13**, 389 (1988).

[301] Y. Fan, H. B. Zhao, G. Lüpke, A. T. Hanbicki, C. H. Li, and B. T. Jonker, Physical Review B **85**, 165311 (2012).

[302] R. J. Epstein, I. Malajovich, R. K. Kawakami, Y. Chye, M. Hanson, P. M. Petroff, A. C. Gossard, and D. D. Awschalom, Physical Review B **65**, 121202 (2002).

[303] Y. Li, Y. Chye, Y. F. Chiang, K. Pi, W. H. Wang, J. M. Stephens, S. Mack, D. D. Awschalom, and R. K. Kawakami, Physical Review Letters **100**, 237205 (2008).

[304] N. Nakagawa, H. Y. Hwang, and D. A. Muller, Nature Materials **5**, 204 (2006).

[305] M. Basletic, J.-L. Maurice, C. Carrétéro, G. Herranz, O. Copie, M. Bibes, É. Jacquet, K. Bouzehouane, S. Fusil, and A. Barthélémy, Nature Materials **7**, 621 (2008).

[306] S. S. A. Seo, Z. Marton, W. S. Choi, G. W. J. Hassink, D. H. A. Blank, H. Y. Hwang, T. W. Noh, T. Egami, and H. N. Lee, Applied Physics Letters **95**, 082107 (2009).

[307] A. Tsukazaki, S. Akasaka, K. Nakahara, Y. Ohno, H. Ohno, D. Maryenko, A. Ohtomo, and M. Kawasaki, Nature Materials **9**, 889 (2010).

[308] Q. Song, K. H. Chow, M. Egilmez, I. Fan, M. D. Hossain, R. F. Kiefl, S. R. Kreitzman, C. D. P. Levy, G. D. Morris, T. J. Parolin, et al., Physica B: Condensed Matter **404**, 619 (2009).

[309] O. V. Yazyev, Reports on Progress in Physics **73**, 056501 (2010).

[310] A. C. Ferrari, J. C. Meyer, V. Scardaci, C. Casiraghi, M. Lazzeri, F. Mauri, S. Piscanec, D. Jiang, K. S. Novoselov, S. Roth, et al., Physical Review Letters **97**, 187401 (2006).

[311] V. M. Pereira, F. Guinea, J. M. B. Lopes dos Santos, N. M. R. Peres, and A. H. Castro Neto, Physical Review Letters **96**, 36801 (2006).

[312] W.-M. Huang, J.-M. Tang, and H.-H. Lin, Physical Review B **80**, 121404 (2009).

[313] E. J. Duplock, M. Scheffler, and P. J. D. Lindan, Physical Review Letters **92**, 225502 (2004).

[314] P. O. Lehtinen, A. S. Foster, Y. Ma, A. V. Krasheninnikov, and R. M. Nieminen, Physical Review Letters **93**, 187202 (2004).

[315] O. V. Yazyev and L. Helm, Physical Review B **75**, 125408 (2007).

[316] D. W. Boukhvalov, M. I. Katsnelson, and A. I. Lichtenstein, Physical Review B **77**, 035427 (2008).

[317] M. A. H. Vozmediano, M. P. López-Sancho, T. Stauber, and F. Guinea, Physical Review B **72**, 155121 (2005).

[318] H. Kumazaki and D. Hirashima, Journal of Magnetism and Magnetic Materials **310**, 2256 (2007).

[319] J. J. Palacios, J. Fernández-Rossier, and L. Brey, Physical Review B **77**, 195428 (2008).

[320] B. Uchoa, V. N. Kotov, N. M. R. Peres, and A. H. Castro Neto, Physical Review Letters **101**, 026805 (2008).

[321] E. H. Lieb, Physical Review Letters **62**, 1201 (1989).

[322] L. Pisani, J. A. Chan, B. Montanari, and N. M. Harrison, Physical Review B **75**, 064418 (2007).

[323] O. V. Yazyev and M. I. Katsnelson, Physical Review Letters **100**, 047209 (2008).

[324] P. Esquinazi, D. Spemann, R. Hohne, A. Setzer, K.-H. Han, and T. Butz, Physical Review Letters **91**, 227201 (2003).

[325] L. Xie, X. Wang, J. Lu, Z. H. Ni, Z. Luo, H. Mao, R. Wang, Y. Wang, H. Huang, D. Qi, et al., Applied Physics Letters **98**, 193113 (2011).

[326] J. Cervenka, M. I. Katsnelson, and C. F. J. Flipse, Nature Physics **5**, 840 (2009).

[327] H. S. S. Ramakrishna Matte, K. S. Subrahmanyam, and C. N. R. Rao, Journal of Physical Chemistry C **113**, 9982 (2009).

[328] Y. Wang, Y. Huang, Y. Song, X. Zhang, Y. Ma, J. Liang, and Y. Chen, Nano Letters **9**, 220 (2009).

[329] M. Sepioni, R. R. Nair, S. Rablen, J. Narayanan, F. Tuna, R. Winpenny, A. K. Geim, and I. V. Grigorieva, Physical Review Letters **105**, 207205 (2010).

[330] R. R. Nair, M. Sepioni, I.-L. Tsai, O. Lehtinen, J. Keinonen, A. V. Krasheninnikov, T. Thomson, A. K. Geim, and I. V. Grigorieva, Nature Physics **8**, 199 (2012).

[331] R. R. Nair, I. Tsai, M. Sepioni, O. Lehtinen, J. Keinonen, A. V. Krasheninnikov, A. H. Castro Neto, A. K. Geim, I. V. Grigorieva, et al., arXiv preprint arXiv:1301.7611 (2013).

[332] A. Candini, C. Alvino, W. Wernsdorfer, and M. Affronte, Physical Review B **83**, 121401 (2011).

[333] J.-H. Chen, L. Li, W. G. Cullen, E. D. Williams, and M. S. Fuhrer, Nature Physics **7**, 535 (2011).

[334] J. Jobst and H. B. Weber, Nature Physics **8**, 352 (2012).

[335] H. Ott, S. J. Heise, R. Sutarto, Z. Hu, C. F. Chang, H. H. Hsieh, H.-J. Lin, C. T. Chen, and L. H. Tjeng, Physical Review B **73**, 094407 (2006).

[336] J. Lettieri, V. Vaithyanathan, S. K. Eah, J. Stephens, V. Sih, D. D. Awschalom, J. Levy, and D. G. Schlom, Applied Physics Letters **83**, 975 (2003).

[337] A. Fujimori, M. Grioni, and J. H. Weaver, Physical Review B **33**, 726 (1986).

[338] K. J. Hubbard and D. G. Schlom, Journal of Materials Research **11**, 2757 (1996).

[339] C. M. Boubeta, J. L. Menendez, J. L. Costa-Kramer, J. M. Garcia, J. V. Anguita, B. Bescos, A. Cebollada, F. Briones, A. V. Chernykh, I. V. Malikov, et al., Surface Science **482–485, Part 2**, 910 (2001).

[340] J. W. Reiner, A. M. Kolpak, Y. Segal, K. F. Garrity, S. Ismail-Beigi, C. H. Ahn, and F. J. Walker, Advanced Materials **22**, 2919 (2010).

[341] S. Yadavalli, M. H. Yang, and C. P. Flynn, Physical Review B **41**, 7961 (1990).

[342] W. Han, Y. Zhou, Y. Wang, Y. Li, J. J. I. Wong, K. Pi, A. G. Swartz, K. M. McCreary, F. Xiu, K. L. Wang, et al., Journal of Crystal Growth **312**, 44 (2009).

[343] X. Jiang, R. Wang, R. M. Shelby, R. M. Macfarlane, S. R. Bank, J. S. Harris, and S. S. P. Parkin, Physical Review Letters **94**, 056601 (2005).

[344] T. Sasaki, T. Oikawa, T. Suzuki, M. Shiraishi, Y. Suzuki, and K. Tagami, Applied Physics Express **2**, 053003 (2009).

[345] Y. Zhou, W. Han, L.-T. Chang, F. Xiu, M. Wang, M. Oehme, I. A. Fischer, J. Schulze, R. K. Kawakami, and K. L. Wang, Physical Review B **84**, 125323 (2011).

[346] R. A. McKee, F. J. Walker, E. D. Specht, G. E. Jellisen, and L. A. Boatner, Physical Review Letters **72**, 2741 (1994).

[347] D. M. Lind, S. D. Berry, G. Chern, H. Mathias, and L. R. Testardi, Physical Review B **45**, 1838 (1992).

[348] R. D. Shannon, Acta Crystallogr., Sect. A: Cryst. Phys. Diff., Theor. Gen. Crystallogr. **32**, 751 (1976).

[349] H. Kawanowa, D. Mori, Y. Gotohand, and R. Souda, Surf. Interface Anal. **36**, 1001 (2004).

[350] R. Rausch and W. Nolting, Journal of Physics: Condensed Matter **21**, 376002 (2009).

[351] J. Zou, G. Jin, and Y.-Q. Ma, Journal of Physics: Condensed Matter **21**, 126001 (2009).

[352] V. E. Henrich and P. A. Cox, *The surface science of metal oxides* (Cambridge university press, 1996).

[353] Y. Hao, Y. Wang, L. Wang, Z. Ni, Z. Wang, R. Wang, C. K. Koo, Z. Shen, and J. T. L. Thong, Small **6**, 195 (2009).

[354] A. Gupta, G. Chen, P. Joshi, S. Tadigadapa, and Eklund, Nano Letters **6**, 2667 (2006).

[355] L. M. Malard, M. A. Pimenta, G. Dresselhaus, and M. S. Dresselhaus, Physics Reports **473**, 51 (2009).

[356] B. Tang, H. Guoxin, and H. Gao, Applied Spectroscopy Reviews **45**, 369 (2010).

[357] S. Pisana, M. Lazzeri, C. Casiraghi, K. S. Novoselov, A. K. Geim, A. C. Ferrari, and F. Mauri, Nature Materials **6**, 198 (2007).

[358] A. Das, S. Pisana, B. Chakraborty, S. Piscanec, S. K. Saha, U. V. Waghmare, K. S. Novoselov, H. R. Krishnamurthy, A. K. Geim, A. K. Sood, et al., Nature Nanotechnology **3**, 210 (2008).

[359] Z. H. Ni, H. M. Wang, Y. Ma, J. Kasim, Y. H. Wu, and Z. X. Shen, ACS Nano **2**, 1033 (2008).

[360] Z. H. Ni, T. Yu, Y. H. Lu, Y. Y. Wang, Y. P. Feng, and Z. X. Shen, ACS Nano **2**, 2301 (2008).

[361] F. Ding, H. Ji, Y. Chen, A. Herklotz, K. Dörr, Y. Mei, A. Rastelli, and O. G. Schmidt, Nano Letters **10**, 3453 (2010).

[362] Z. Cheng, Q. Zhou, C. Wang, Q. Li, C. Wang, and Y. Fang, Nano Letters **11**, 767 (2011).

[363] J. Zhou, Q. Wang, Q. Sun, X. S. Chen, Y. Kawazoe, and P. Jena, Nano Letters **9**, 3867 (2009).

[364] D. Soriano, N. Leconte, P. Ordejon, J.-C. Charlier, J.-J. Palacios, and S. Roche, Physical Review Letters **107**, 016602 (2011).

[365] H. Lee, Y.-W. Son, N. Park, S. Han, and J. Yu, Physical Review B **72**, 174431 (2005).

[366] M. M. Ugeda, I. Brihuega, F. Guinea, and J. M. Gomez-Rodriguez, Physical Review Letters **104**, 096804 (2010).

[367] C. Tao, L. Jiao, O. V. Yazyev, Y.-C. Chen, J. Feng, X. Zhang, R. B. Capaz, J. M. Tour, A. Zettl, S. G. Louie, et al., Nature Physics **7**, 616 (2011).

[368] M. K. Chan, Q. O. Hu, J. Zhang, T. Kondo, C. J. Palmstrøm, and P. A. Crowell, Physical Review B **80**, 161206 (2009).

[369] G. Salis, A. Fuhrer, and S. F. Alvarado, Physical Review B **80**, 115332 (2009).

[370] T. D. Nguyen, Y. Sheng, M. Wohlgenannt, and T. D. Anthopoulos, Synthetic Metals **157**, 930 (2007).

[371] T. Nguyen, G. Hukic-Markosian, F. Wang, L. Wojcik, X.-G. Li, E. Ehrenfreund, and Z. Vardeny, Nature Materials **9**, 345 (2010).

[372] R. E. Dietz and P. W. Selwood, Journal of Applied Physics **30**, S101 (1959).

[373] M. Boudart, J. A. Dumesic, and H. Topsøe, Proceedings of the National Academy of Sciences **74**, 806 (1977).

[374] R. Vollmer, T. Gutjahr-Löser, J. Kirschner, S. van Dijken, and B. Poelsema, Physical Review B **60**, 6277 (1999).

[375] M. Weinert and J. W. Davenport, Physical Review Letters **54**, 1547 (1985).

[376] P. Nordlander, S. Holloway, and J. K. Nørskov, Surface Science **136**, 59 (1984).

[377] J. K. Furdyna, Journal of Applied Physics **64**, 29 (1988).

[378] G. Bastard and R. Ferreira, Surface Science **267**, 335 (1991).

[379] D. Griffiths, *Introduction to quantum mechanics* (Pearson Prentice Hall, Upper Saddle Riverer, NJ 07458, 2005), 2nd ed.

[380] G. Mihajlović, S. I. Erlingsson, K. Výborný, J. E. Pearson, S. D. Bader, and A. Hoffmann, Physical Review B **84**, 132407 (2011).

[381] C. Weber, N. Gedik, J. Moore, J. Orenstein, J. Stephens, and D. D. Awschalom, Nature **437**, 1330 (2005).

[382] M. Wojtaszek, I. J. Vera-Marun, T. Maassen, and B. J. van Wees, arXiv preprint arXiv:1209.2365 (2012).

[383] B. Birkner, D. Pachniowski, A. Sandner, M. Ostler, T. Seyller, J. Fabian, M. Ciorga, D. Weiss, and J. Eroms, Physical Review B **87**, 081405 (2013).

[384] M. A. Cazalilla, A. Iucci, F. Guinea, and A. H. Castro Neto, arXiv preprint arXiv:1207.3135 (2012).

[385] C. Lee, X. Wei, J. W. Kysar, and J. Hone, Science **321**, 385 (2008).

[386] H. Dery, H. Wu, B. Ciftcioglu, M. Huang, Y. Song, R. K. Kawakami, J. Shi, I. Krivorotov, I. Zutic, and L. J. Sham, IEEE Transactions on Electronic Devices **59**, 259 (2012).

[387] J. H. Chen, C. Jang, S. Adam, M. S. Fuhrer, E. D. Williams, and M. Ishigami, Nature Physics **4**, 377 (2009).

[388] W. H. Wang, W. Han, K. Pi, K. M. McCreary, F. Miao, W. Bao, C. N. Lau, and R. K. Kawakami, Applied Physics Letters **93**, 183107 (2008).

[389] Y. Li, Ph.D. thesis, University of California, Riverside (2010).

[390] G. Wastlbauer and J. A. C. Bland, Advances in Physics **54**, 137 (2005).

[391] A. T. Hanbicki, B. T. Jonker, G. Itskos, G. Kioseoglou, and A. Petrou, Applied Physics Letters **80**, 1240 (2002).

[392] Q. O. Hu, E. S. Garlid, P. A. Crowell, and C. J. Palmstrøm, Physical Review B **84**, 085306 (2011).

[393] K. Ando, S. Takahashi, J. Ieda, H. Kurebayashi, T. Trypiniotis, C. H. W. Barnes, S. Maekawa, and E. Saitoh, Nature Materials **10**, 655 (2011).

[394] Y. Pu, J. Beardsley, P. M. Odenthal, A. G. Swartz, R. K. Kawakami, P. C. Hammel, E. Johnston-Halperin, J. Sinova, and J. P. Pelz, in review (2013).

[395] P. F. Carcia, A. D. Meinhaldt, and A. Suna, Applied Physics Letters **47**, 178 (1985).

[396] F. J. A. Den Broeder, H. C. Donkersloot, H. J. G. Draaisma, and W. J. M. De Jonge, Journal of Applied Physics **61**, 4317 (1987).

[397] F. J. A. Den Broeder, W. Hoving, and P. J. H. Bloemen, Journal of Magnetism and Magnetic Materials **93**, 562 (1991).

[398] M. T. Johnson, P. J. H. Bloemen, F. J. A. Den Broeder, and J. J. De Vries, Reports on Progress in Physics **59**, 1409 (1996).

[399] S. S. P. Parkin, N. More, and K. P. Roche, Physical Review Letters **64**, 2304 (1990).

[400] S. S. P. Parkin, R. Bhadra, and K. P. Roche, Physical Review Letters **66**, 2152 (1991).

[401] M. D. Stiles, Journal of Magnetism and Magnetic Materials **200**, 322 (1999).

[402] R. K. Kawakami, E. Rotenberg, H. J. Choi, E. J. Escorcia-Aparicio, M. O. Bowen, J. H. Wolfe, E. Arenholz, Z. D. Zhang, N. V. Smith, and Z. Q. Qiu, Nature **398**, 132 (1999).

[403] R. K. Kawakami, E. Rotenberg, E. J. Escorcia-Aparicio, H. J. Choi, J. H. Wolfe, N. V. Smith, and Z. Q. Qiu, Physical Review Letters **82**, 4098 (1999).

[404] M. D. Stiles and A. Zangwill, Physical Review B **66**, 014407 (2002).

[405] J. C. Sankey, Y. T. Cui, J. Z. Sun, J. C. Slonczewski, R. A. Buhrman, and D. C. Ralph, Nature Physics **4**, 67 (2007).

[406] S. Mangin, D. Ravelosona, J. A. Katine, M. J. Carey, B. D. Terris, and E. E. Fullerton, Nature Materials **5**, 210 (2006).

[407] W. B. Zeper, Ph.D. thesis, Technical University Twente, The Netherlands (1991).

[408] L. Néel, J. Phys. Radium **15**, 225 (1954).

[409] B. N. Engel, C. D. England, R. A. Van Leeuwen, M. H. Wiedmann, and C. M. Falco, Physical Review Letters **67**, 1910 (1991).

[410] C. A. F. Vaz, J. A. C. Bland, and G. Lauhoff, Reports on Progress in Physics **71**, 056501 (2008).

[411] J. M. Shaw, H. T. Nembach, T. J. Silva, S. E. Russek, R. Geiss, C. Jones, N. Clark, T. Leo, and D. J. Smith, Physical Review B **80**, 184419 (2009).

[412] N. Nakajima, T. Koide, T. Shidara, H. Miyauchi, H. Fukutani, A. Fujimori, K. Iio, T. Katayama, M. Nỳvlt, and Y. Suzuki, Physical Review Letters **81**, 5229 (1998).

[413] K. Yokoyama, Ph.D. thesis, University of California, Riverside (2009).